ELECTROCHEMICAL AND MATERIAL CHARACTERIZATION OF A TCP CONVERSION COATING ON ALUMINUM ALLOY 7075-T6

By

Catherine Munson

A DISSERTATION

Submitted to
Michigan State University
in partial fulfillment of the requirements
for the degree of

Chemistry - Doctor of Philosophy

2017

ABSTRACT

ELECTROCHEMICAL AND MATERIAL CHARACTERIZATION OF A TCP CONVERSION COATING ON ALUMINUM ALLOY 7075-T6

By

Catherine Munson

The physical, chemical, and electrochemical properties of different variants of a commercial (SurTec 650) trivalent chromium process conversion coating formed on AA7075-T6 are reported on. Comparison of immersion and spray-on application was undertaken. Three different variants of the commercial TCP coating were studied: 650 E, C and V. ICP-OES revealed similar concentrations of Cr in all three coating baths. The concentrations of Zr, Zn, S (likely as sulfate) and Fe were different in the coating baths. The anti-corrosion properties of the 650E were similar for both immersion and spray applications. Furthermore, both application methods produced coatings similar in structure and performance to other commercial TCP coatings. The conversion coating had a nodular coating morphology. X-ray emission lines indicated that the compositions mainly differed through increased Cr and Ca in V and increased F and Zr in C. Raman spectroscopy indicates a slightly different chromium oxide bond present in the spray coated specimens, which needs to be verified and further examined. The coating roughness and pit depths were determined from profilometry to be statically higher than uncoated specimens for only the 650C composition, due to a less consistent and conformal coating, while 650E and V were equivalent to the uncoated specimens indicating a conformal and continuous film. The film thickness was determined from ellipsometry measurements to be between 40-90 nm for all specimens. Over a seven-day drying period, water contact angles on all films statistically increased from hydrophilic to hydrophobic regions, indicating better primer adhesion and more continuous films on specimens aged for longer time periods. All coating variants produced more

active OCPs (< -0.25 V vs Ag/AgCl), indicating cathodic protection, compared to uncoated AA7075 (-0.22 V) in Na_2SO_4. In NaCl, all coatings still provided significantly lower anodic (<1.5 μA/cm^2) and cathodic currents (<10 μA/cm^2) when compared to uncoated AA7075 (6.5 μA/cm^2 anodic and 25 μA/cm^2 cathodic). Overall, the best corrosion protection was found with both spray coated and immersion coated 650 E, of which the immersion coating provided the most reproducible protection. Accelerated degradation tests on coated samples showed that the immersion and spray coated 650 E protected against the most corrosion when compared to uncoated metals samples.

The accelerated degradation tests on a cross comparison of TCP and NCP coatings produced by various manufacturers showed that the 650 E composition performed just as well as the other TCP variants. Luster-On and Chemeon brand TCP coatings performed the best, which correlated with the highest Cr concentrations found in those coating baths.

ACKNOWLEDGEMENTS

This research was made possible by a grant from the Office of Naval Research (Sea-Based Aviation Program), N00014-15-1-2005 (William Nickerson, Program Officer). I would like to thank Dr. Nabil Zaki (Technical Advisor, SurTec, Inc.) for providing the degreaser, deoxidizer and TCP coating solutions, and for providing technical assistance. Thanks also go to Craig Matzdorf (NAVAIR) for his technical expertise on the coatings. I would also like to thank my family and friends for their support during this process.

TABLE OF CONTENTS

LIST OF TABLES viii

LIST OF FIGURES x

KEY TO ABBREVIATIONS xxi

CHAPTER 1: INTRODUCTION AND MOTIVATION FOR STUDIES 1
1.1. Alloy Properties and Composition 1
1.2. Surface Preparation 5
1.3. Coating Formation 5
1.4. Material Characterization 6
1.5. Electrochemical Characterization 8
1.6. Accelerated Degradation Tests 8
1.7. Motivations and Questions 9
REFERENCES 11

CHAPTER 2: FORMATION AND STRUCTURE OF DIFFERENT VARIANTS OF A COMMERCIAL TRIVALENT CHROMIUM PROCESS (TCP) COATING ON ALUMINUM ALLOY 7075-T6 15
2.1. Characterization Introduction 15
2.2. Material and Methods 17
2.2.1. Reagents 17
2.2.2. Specimen Preparation 18
2.3. Alloy and Coating Characterization 21
2.4. Calculations and Statistical Analysis 22
2.5. Results 23
2.5.1. Elemental composition of the different coating baths 23
2.5.2. Surface morphology and chemical composition of the pretreated and conversion coated specimens 23
2.5.3. TCP Coating Composition with Depth, Wettability and Thickness 36
2.6. Discussion 40
2.7. Conclusions 45
REFERENCES 47

CHAPTER 3: ELECTROCHEMICAL CHARACTERIZATION OF DIFFERENT VARIANTS OF A COMMERCIAL TRIVALENT CHROMIUM PROCESS (TCP) COATING ON ALUMINUM ALLOY 7075-T6 52
3.1. Electrochemical Introduction 52
3.2. Experimental 54
3.2.1. Reagents 54
3.2.2. Specimen Preparation 54
3.2.3. Alloy and Coating Characterization 56
3.2.4. Electrochemical Measurements 57

3.2.5. Thin-Layer Mist Degradation Test 58
3.3. Results 59
3.3.1. Open Circuit or Corrosion Potentials 59
3.3.2. Potentiodynamic Polarization Curves 62
3.3.3. Rotating Disk Voltammetry Studies of ORR 69
3.3.4. Polarization Resistance 71
3.3.5. Electrochemical Parameter Comparisons 76
3.3.6. Thin-Layer Mist Accelerated Degradation Test 80
3.4. Discussion 82
3.5. Conclusions 86
REFERENCES 88

CHAPTER 4: CROSS COMPARISON OF TCP- AND NCP-COATED AA7075-T6 DURING THIN-LAYER MIST AND SALT-SPRAY ACCELERATED DEGRADATION TESTING: SURFACE PROFILOMETRY AND OPTICAL MICROSCOPY 93
4.1. Introduction and Research Objectives 93
4.2. Experimental Procedures 93
4.2.1. ICP-OES Analysis of Coating Baths 93
4.2.3. Accelerated Degradation Tests 97
4.2.4. Visual Analysis 98
4.2.5. Optical Microscopy and Image Analysis 99
4.2.6. Contact Mode Scanning Profilometry 99
4.2.7. Statistical Analysis and Graphs 100
4.3. Cross Comparison Results 100
4.3.1. Coating Bath Elemental Analysis 100
4.3.2. Profilometry Analysis 103
4.3.3. Weight Change Analysis 114
4.3.4. Microscopy Analysis 116
4.3.5. Visual Analysis 120
4.4. Cross Comparison Discussion 136
4.5. Conclusions 138
REFERENCES 140

CHAPTER 5: CROSS COMPARISON OF TCP- AND NCP-COATED AA7075-T6 DURING SALT-SPRAY ACCELERATED DEGRADATION TESTING: SCANNING ELECTRON MICROSCOPY AND ENERGY DISPERSIVE X-RAY SPECTROSCOPY 146
5.1. Introduction and Research Objectives 146
5.2. Experimental Procedures 146
5.2.1. Scanning Electron Microscopy 146
5.2.3. Accelerated Degradation Tests 147
5.3. Cross Comparison Results 147
5.3.1. Scanning Electron Microscopy Analysis Before and After Accelerated Degradation Tests 147
5.4. SEM Cross Comparison Discussion 174
5.5. Cross Comparison Conclusions 176

CHAPTER 6: CONCLUSIONS AND FUTURE WORK 177
6.1. SurTec Characterization Conclusions 177
6.2. SurTec Electrochemical Characterization Conclusions 179
6.3. Cross Comparison Conclusions 179
6.4. Cross Comparison SEM Conclusions 180
6.5. Future Work 180

REFERENCES 182

LIST OF TABLES

Table 1. The elemental composition (wt.%) of AA7075-T6 as determined from quantitative XRF analysis. 18

Table 2. Comparison of electrochemical parameters for uncoated and immersion-coated AA7075-T6 specimens in oxygenated 0.5 M Na_2SO_4. Data are presented for 650 E, V, and C coatings. Values are reported as mean ± standard error of the mean (n=3). 77

Table 3. Comparison of electrochemical parameters for uncoated and immersion-coated AA7075-T6 specimens in oxygenated 3.5% NaCl. Data are presented for 650 E, V, and C coatings. Values are reported as mean ± standard error of the mean (n=3). 78

Table 4. Comparison of electrochemical parameters for uncoated and conversion-coated AA7075-T6 specimens in oxygenated 0.5 M Na_2SO_4. Data are presented for immersion and spray-coated 650 E. Values are reported as mean ± standard error of the mean (n=3). †TCP coating values are for Bonderite T5900 (Henkel)[17] in naturally-aerated 0.5 M Na_2SO_4. NR = not reported. 79

Table 5. Comparison of electrochemical parameters for uncoated and conversion-coated AA7075-T6 specimens in oxygenated 3.5% NaCl. Data are presented for immersion- and spray-coated 650 E. Values are reported as mean ± standard error of the mean (n=3). 80

Table 6. The elemental composition (ppm) of all coating baths as determined using ICP-OES analysis. 102

Table 7. Nominal values for the RMS surface roughness (over 1 mm^2) and average pit depth determined from profilometry maps. Data are presented for uncoated, TCP-coated, and NCP-coated AA7075-T6 before any testing. Values are presented as mean ± S.E.M (n=3). 106

Table 8. Nominal values for the surface roughness (over 1 mm^2) and average pit depth determined from contact profilometry maps. Data are presented for uncoated, TCP-coated, and NCP-coated AA7075-T6 after a 7-day salt-spray test. All panels were sonicated in nitric acid for 20 min to remove corrosion product. Values are presented as mean ±S.E.M (n=3). 110

Table 9. Nominal values for the surface roughness (over 1 mm^2) and average pit depth determined from contact profilometry maps. Data are presented for uncoated, TCP-coated, and NCP-coated AA7075-T6 after a 7-day thin-layer mist test. All panels were sonicated in nitric acid to remove corrosion product for 20 min. Values are presented as mean ±S.E.M (n=3). 113

Table 10. Pit density and pit diameter data for uncoated, Henkel, SurTec E, Chemeon, Luster-On, and NAVAIR NCP-coated AA7075-T6 after corrosion product removal with 20-min nitric

acid after 7-day thin-layer mist (TLM) and 7-day salt-spray (SS) tests. Values are presented as mean ±S.E.M (n=3). 119

LIST OF FIGURES

Figure 1. Elemental analysis of the city tap water (July 2016) used for specimen rinsing as determined by ICP-OES. Data are presented as mean ± S.E.M. for n ≥ 3. 19

Figure 2. Elemental analysis of SurTec 650 E (red), 650 V (blue), and 650 C (green) coating baths as determined by ICP-OES analysis. Data are presented as mean ± S.E.M. for n ≥ 3..... 20

Figure 3. (top) Secondary electron SEM micrographs and (bottom) EDXS elemental line profiles recorded along the red arrows for the AA7075-T6 alloy (A) as received, (B) after polishing, (C) after polishing + degreasing, and (D) after polishing + degreasing + deoxidation. All images are at approximately the same magnification as indicated by the scale bars. 24

Figure 4. (A) Secondary electron SEM micrograph of the conversion-coated AA7075-T6 alloy. (B) EDXS elemental line profiles taken along the red arrow that crosses a coating precipitate and an intermetallic particle (IMP). (C) X-ray emission data for the uncoated (shaded grey) and conversion-coated (red line) alloy recorded at the green arrow away from any intermetallic particles. The conversion coating was 650 E and it was spray applied. 26

Figure 5. Secondary electron SEM micrographs and EDXS elemental line profile data for immersion-coated AA7075-T6 specimens of (A) 650 E, (B) 650 V and (C) 650 C. The EDXS data were taken along the directional red arrows shown in each image. 28

Figure 6. Raman spectroscopy line profile data for immersion-coated specimens (AA7075-T6) of (A) 650 E, (B) 650 V and (C) 650 C. The spectral data were recorded approximately every 0.5 μm along the long red arrow directionally shown in each microscope image. The y-axis length in A is 17.3 μm, B is 22.6 μm and C is 24 μm..... 32

Figure 7. Secondary electron SEM micrographs and EDXS elemental line profile data for spray-coated AA7075-T6 specimens of (A) 650 E, (B) 650 V and (C) 650 C. The EDXS data were recorded directionally along the red line shown in each image. 33

Figure 8. Raman spectroscopy line profile data for spray-coated specimens (AA7075-T6) of (A) 650 E, (B) 650 V and (C) 650 C. The spectral data were measured every ca. 0.5 μm along the red arrow directionally shown in each micrograph..... 35

Figure 9. Auger electron spectroscopy depth profiles for AA7075-T3 specimens (A) immersion-coated and (B) spray-coated with 650 E. The top panels show full depth profiles while the bottom panels show expanded scale profiles over the top 20 nm of sputtering depth. The depth profiling was performed with Ar^+ at 10 keV. The sputter depth information is approximate as it is based on an Ar^+ sputter rate 6.2 nm/min for Ta_2O_5. 36

Figure 10. Static water contact angles on (A) immersion-coated and (C) spray-coated 650 E (red), 650 V (green), 650 C (blue), and uncoated (black) specimens. Film thickness, as determined from open air ellipsometry, for (B) immersion-coated and (D) spray-coated

specimens. The results are presented over a 7-day period of aging in the open laboratory atmosphere. Data are presented as mean ± standard error of the mean, n ≥3. 38

Figure 11. Schematic of the thin-layer mist (TLM) polypropylene test chamber and protocol: (A) specimen configuration during a test cycle and (B) reapplication of the 3.5% NaCl spray at the beginning of a test period. The polypropylene container was sealed during a test period but opened daily to re-apply the spray and to equilibrate with the laboratory air for 30 min at room temperature. The container was placed in an oven at 55 ^{o}C during the test. Each test cycle was 24 h over a 14-day period. 59

Figure 12. (A) Open circuit potential (OCP)-time transients for immersion-coated 650 E (red), 650 V (blue), 650 C (green), and uncoated AA7075-T6 (black) specimens in oxygenated 0.5 M Na_2SO_4. (B) Nominal values of the E_{corr} for the TCP-coated and uncoated specimens. Values are displayed as mean ± standard error of the mean (n = 3). Asterisk indicates data significantly different from the uncoated control ($p \leq 0.15$). 60

Figure 13. (A) OCP-time transients for immersion-coated 650 E (red), 650 V (blue), 650 C (green), and uncoated AA7075-T6 (black) specimens in oxygenated 3.5% NaCl. (B) Nominal values of Ecorr for the TCP-coated and uncoated specimens. Values are displayed as mean ± standard error of the mean (n = 3). Asterisk indicates data significantly different from the uncoated control ($p \leq 0.15$). 61

Figure 14. (A) Open circuit potential (OCP)-time transients for spray-coated 650 E (red), 650 V (blue), 650 C (green), and uncoated AA7075-T6 (black) specimens in oxygenated 0.5 M Na_2SO_4. (B) Nominal values of the E_{corr} for the TCP-coated and uncoated specimens. Values are displayed as mean ± standard error of the mean (n = 3). Asterisk indicates data significantly different from the uncoated control ($p \leq 0.15$). 61

Figure 15. (A) OCP-time transients for spray-coated 650 E (red), 650 V (blue), 650 C (green), and uncoated AA7075-T6 (black) specimens in oxygenated 3.5% NaCl. (B) Nominal values of Ecorr for the TCP-coated and uncoated specimens. Values are displayed as mean ± standard error of the mean (n = 3). Asterisk indicates data significantly different from the uncoated control ($p \leq 0.15$). 62

Figure 16. (A) Cathodic and (B) anodic potentiodynamic polarization curves for immersion-coated and uncoated AA7075-T6 specimens in oxygenated 0.5 M Na_2SO_4. (C) Plots of the nominal anodic (top, black, at -0.10 V) and cathodic (bottom, red, at -0.80 V) currents for the TCP-coated and uncoated alloys. Values are displayed as mean ± standard error of the mean (n = 3). Asterisk indicates data significantly different from the uncoated control ($p \leq 0.05$). 63

Figure 17. (A) Cathodic and (B) anodic potentiodynamic polarization curves for immersion-coated and uncoated AA7075-T6 specimens in oxygenated 3.5% NaCl. (C) Plots of the nominal anodic (top, black, at -0.65 V) and cathodic (bottom, red, at -0.80 V) currents for the TCP-coated and uncoated alloys. Values are displayed as mean ± standard error of the mean (n

= 3). Asterisk indicates data significantly different from the uncoated control ($p \leq 0.05$). 65

Figure 18. (A) Cathodic and (B) anodic potentiodynamic polarization curves for immersion-coated and uncoated AA7075-T6 specimens in oxygenated 0.5 M Na_2SO_4. (C) Plots of the nominal anodic (top, black, at -0.10 V) and cathodic (bottom, red, at -0.80 V) currents for the TCP-coated and uncoated alloys. Values are displayed as mean ± standard error of the mean (n = 3). Asterisk indicates data significantly different from the uncoated control ($p \leq 0.05$). 66

Figure 19. (A) Cathodic and (B) anodic potentiodynamic polarization curves for spray-coated and uncoated AA7075-T6 specimens in oxygenated 0.5 M Na_2SO_4. (C) Plots of the nominal anodic (top, black, at -0.10 V) and cathodic (bottom, red, at -0.80 V) currents for the TCP-coated and uncoated alloys. Values are displayed as mean ± standard error of the mean (n = 3). Asterisk indicates data significantly different from the uncoated control ($p \leq 0.05$). 67

Figure 20. Pitting or breakdown potentials, E_{pit}, for the TCP-coated and uncoated AA7075-T6 alloys in oxygenated 3.5% NaCl. Values are displayed as mean ± standard error of the mean (n = 3). Asterisk indicates data significantly different from the uncoated control ($p \leq 0.2$). 69

Figure 21. (A) Cathodic polarization curves for bare/uncoated (black) and TCP-coated (colored) AA7075-T6 disk electrodes in oxygenated 3.5% NaCl. The TCP coating was SurTec 650 E. The rotation rates were 500, 1000, 1500 and 2000 rpm. (B) Plots of the limiting current at -0.85 V, i_l, versus the rotation rate$^{1/2}$. Values are displayed as mean ± standard error of the mean (n = 3). 70

Figure 22. Plots of the limiting current at -0.85 V, i_l, versus the rotation rate$^{1/2}$ for TCP-coated AA2024-T3, 6061-T6 and 7075-T6 alloys in oxygenated 3.5% NaCl. The TCP coating was SurTec 650 E. The rotation rates were 500, 1000, 1500 and 2000 rpm. 71

Figure 23. Polarization resistance, R_p, determined from (A) Bode plots of the total impedance recorded at E_{corr} ($Z_{0.01Hz}$), (B) equivalent circuit fitting of Nyquist plots of the impedance data recorded at E_{corr}, and (C) linear polarization curves recorded at ± 25 mV vs. E_{corr} for immersion- coated and uncoated AA7075-T6 specimens in oxygenated 0.5 M Na_2SO_4. (D) Plots of the R_p values determined by the three methods for the coated and uncoated specimens displayed as mean ± standard error of the mean (n = 3). Asterisk indicates data significantly different from the uncoated control ($p \leq 0.05$)..... 73

Figure 24. Equivalent circuits used for fitting Nyquist plots of impedance data recorded at E_{corr} for uncoated (left) and TCP-coated (right) specimens..... 74

Figure 25. Polarization resistance determined from (A) Bode plots of the total impedance recorded at E_{corr} ($Z_{0.01\ Hz}$), (B) equivalent circuit fitting of Nyquist plots of the impedance data recorded at E_{corr}, and (C) linear polarization curves recorded at ± 25 mV vs. E_{corr} for

immersion-coated and uncoated AA7075-T6 specimens in oxygenated 3.5 % NaCl. (D) Plots of the R_p values determined by the three methods for the coated and uncoated specimens displayed as mean ± standard error of the mean (n = 3). Asterisk indicates data significantly different from the uncoated control ($p \leq 0.05$)..... 76

Figure 26. Optical micrographs of uncoated and TCP-coated specimens before and after exposure to a 14-day (336 h) thin-layer mist test (3.5 % NaCl, 55 ^{o}C). Image dimensions are 1 x 1 cm^2. 81

Figure 27. Elemental analysis of all TCP and NCP coating baths as determined by ICP-OES analysis. Data are presented as mean ± S.E.M. for n = 3..... 102

Figure 28. (A) Average pit depths (seen in the 1 mm^2 area) and (B) RMS roughness (over 1 mm^2) determined from contact profilometry. Data are presented for uncoated, TCP-coated, and NCP-coated AA7075-T6 before any testing or environmental exposure. Values are displayed as mean ± standard error of the mean (n = 3). Asterisks indicate data significantly different from the uncoated control ($P < 0.05$). 103

Figure 29. Surface profilometry maps of the TCP- and NCP-coated AA7075-T6 specimens as well as an uncoated control before any testing. The images were recorded over a 1 mm^2 area. The z-axis scale ranges from -17 μm (dark green) to 11.4 μm (light green)..... 104

Figure 30. Line scan profiles across the deepest pits visible for uncoated, TCP-coated, and NCP-coated AA7075-T6 specimens before any testing. 105

Figure 31. (A) Average pit depth (seen in the 1 mm^2 area) and (B) RMS roughness (over 1 mm^2) determined from contact profilometry. Data are presented for uncoated, TCP-coated, and NCP-coated AA7075-T6 after 7 days of a neutral salt-spray test. All panels were sonicated in nitric acid for 20 min to remove corrosion product. Values are displayed as mean ± standard error of the mean (n = 3). Asterisks indicate data significantly different from the uncoated control ($P < 0.05$)..... 106

Figure 32. Surface contact profilometry maps of the TCP- and NCP-coated AA7075-T6 specimens as well as an uncoated control after a 7-day neutral salt-spray test. The images were recorded over a 1 mm^2 area. All panels were sonicated in nitric acid for 20 min to remove corrosion product. The z-axis scale ranges from -17 μm (dark green) to 11.4 μm (light green). 107

Figure 33. Line profiles across the deepest pits visible on the maps shown in Figure 32. Data are presented for uncoated, TCP-coated, and NCP-coated AA7075-T6 after 7 days of a salt-spray test. All panels were sonicated in nitric acid to remove corrosion product for 20 min. 109

Figure 34. (A) Average pit depths (seen in the 1 mm^2 area) and (B) RMS surface roughness (over 1 mm^2) for uncoated, TCP-coated, and NCP-coated AA7075-T6 after 7 days of a thin-layer mist test. All panels were sonicated in nitric acid for 20 min to remove corrosion product.

Values are displayed as mean ± standard error of the mean (n = 3). Asterisks indicate data significantly different from the uncoated control (P < 0.05). 110

Figure 35. Surface contact profilometry maps of uncoated, TCP-, and NCP-coated AA7075-T6 specimens after a 7-day thin-layer mist test. The images were recorded over a 1 mm^2 area. All panels were sonicated in nitric acid for 20 min to remove corrosion product. The z-axis scale ranges from -17 μm (dark green) to 11.4 μm (light green)..... 111

Figure 36. Line profiles across the deepest pits visible on the maps shown in Figure 8. Data are presented for uncoated, TCP-coated, and NCP-coated AA7075-T6 after 7 days of a thin-layer mist test. All panels were sonicated in nitric acid for 20 min to remove corrosion product. 113

Figure 37. Weight loss data for uncoated, TCP-coated and NCP-coated AA7075-T6 panels after a 7-day neutral salt-spray test. All panels were ultrasonicated in nitric acid for 20 min to remove corrosion product. Panels used had a one square inch surface area. Values are displayed as mean ± standard error of the mean (n = 3 tested panels). Asterisks indicate data significantly different from the uncoated control (P < 0.05). 114

Figure 38. Weight loss data for uncoated, TCP-coated and NCP-coated AA7075-T6 panels after the 7-day thin-layer mist test. Panels used had a one square centimeter surface area. Values are displayed as mean ± standard error of the mean (n = 3). Asterisks indicate data significantly different from the uncoated control (P < 0.05). Double asterisks indicate data significantly different from the single asterisk data (P < 0.05). 116

Figure 39. Pit areas and pit densities were determined from optical micrographs measured over at least 3 imaging areas of 0.001 mm^2 in various spots across the overall 1 mm^2 panel surface. Data are presented for uncoated, TCP-coated, and NCP-coated AA7075-T6 panels after 7 days of a salt-spray test. All panels were sonicated in nitric acid for 20 min to remove corrosion product. Values are displayed as mean ± standard error of the mean (n = 3). Asterisks indicate data significantly different from the uncoated control (P < 0.05). 117

Figure 40. Pit areas and pit densities were determined from optical micrographs measured over at least 3 imaging areas of 0.001 mm^2 in various spots across the overall 1 mm^2 panel surface. Data are presented for uncoated, TCP-coated, and NCP-coated AA7075-T6 panels after 7 days of a thin-layer test. All panels were sonicated in nitric acid for 20 min to remove corrosion product. Values are displayed as mean ± standard error of the mean (n = 3). Asterisks indicate data significantly different from the uncoated control (P < 0.05). 119

Figure 41. Black and white images of replicate uncoated AA7075-T6 specimens before (Day 0), after 7 days of a neutral salt-spray test (Day 7), and after nitric acid dissolution of corrosion product (Post Nitric Acid). Red circles demark regions of corrosion product formation seen on day 7, and red arrows demark regions of surface pitting. Image size = one square inch (entire panel shown in image). 121

Figure 42. Black and white images of replicate NCP-coated (NAVAIR) AA7075-T6 specimens before (Day 0), after 7 days of a neutral salt-spray test (Day 7), and after nitric acid dissolution of corrosion product (Post Nitric Acid). Red circles demark regions of corrosion product formation seen on day 7, and red arrows demark regions of surface pitting. Image size = one square inch (entire panel shown in image). 122

Figure 43. Black and white images of replicate TCP-coated (Luster-On) AA7075-T6 specimens before (Day 0), after 7 days of a neutral salt-spray test (Day 7), and after nitric acid dissolution of corrosion product (Post Nitric Acid). Red circles demark regions of surface pitting. Image size = one square inch (entire panel shown in image). 123

Figure 44. Black and white images of replicate TCP-coated (Chemeon) AA7075-T6 specimens before (Day 0), after 7 days of a neutral salt-spray test (Day 7), and after nitric acid dissolution of corrosion product (Post Nitric Acid). Red circles demark regions of surface damage. Image size = one square inch (entire panel shown in image). 124

Figure 45. Black and white images of replicate TCP-coated (SurTec 650 E) AA7075-T6 specimens before (Day 0), after 7 days of a neutral salt-spray test (Day 7), and after nitric acid dissolution of corrosion product (Post Nitric Acid). Red circles demark regions of corrosion product formation seen on day 7, and red arrows demark regions of surface pitting. Image size = one square inch (entire panel shown in image). 125

Figure 46. Black and white images of replicate TCP-coated (Henkel) AA7075-T6 panels before (Day 0), after a 7-day neutral salt-spray test (Day 7), and after nitric acid dissolution of any corrosion product (After Nitric Acid). Red circle marks a region of slight surface damage. Image size = one square inch (entire panel shown in image). 126

Figure 47. Black and white images of replicate uncoated AA7075-T6 specimens before (Day 0), after 7 days of a thin-layer mist test (Day 7), and after nitric acid dissolution of corrosion product (Post Nitric Acid). Red circles demark regions of corrosion product formation seen on day 7, and red arrows demark regions of surface pitting. Image size = one square centimeter (entire panel shown in image). 127

Figure 48. Black and white images of replicate NCP-coated (NAVAIR) AA7075-T6 specimens before (Day 0), after 7 days of a thin-layer mist test (Day 7), and after nitric acid dissolution of corrosion product (Post Nitric Acid). Red circles demark regions of corrosion product formation seen on day 7, and red arrows demark regions of surface pitting. Image size = one square centimeter (entire panel shown in image). 128

Figure 49. Black and white images of replicate TCP-coated (Luster-On) AA7075-T6 specimens before (Day 0), after 7 days of a thin-layer mist test (Day 7), and after nitric acid dissolution of corrosion product (Post Nitric Acid). Red circles demark regions of corrosion product formation and surface pitting. Image size = one square centimeter (entire panel shown in image). 129

Figure 50. Black and white images of replicate TCP-coated (Chemeon) AA7075-T6 specimens before (Day 0), after 7 days of a thin-layer mist test (Day 7), and after nitric acid dissolution of corrosion product (Post Nitric Acid). No corrosion product or surface pitting was seen after the 7-day test. Image size = one square centimeter (entire panel shown in image). 130

Figure 51. Black and white images of replicate TCP-coated (SurTec 650 E) AA7075-T6 specimens before (Day 0), after 7 days of a thin-layer mist test (Day 7), and after nitric acid dissolution of corrosion product (Post Nitric Acid). Red circles demark regions of surface damage. Image size = one square centimeter (entire panel shown in image). 131

Figure 52. Black and white images of replicate TCP-coated (Henkel) AA7075-T6 specimens before (Day 0), after 7 days of a thin-layer mist test (Day 7), and after nitric acid dissolution of corrosion product (Post Nitric Acid). Red circles demark regions of surface pitting. Image size = one square centimeter (entire panel shown in image). 132

Figure 53. Comparison of optical images of the full 1 inch^2 surface area for NCP- and TCP-coated as well as uncoated AA7075-T6 before and after the 7-day neutral salt-spray test. Images for the panels after acid dissolution of any corrosion product are also presented. Red circles demark regions of corrosion product formation seen on day 7, and red arrows demark regions of surface pitting. 133

Figure 54. Comparison of optical images of the full 1 cm^2 surface area for NCP- and TCP-coated as well as uncoated AA7075-T6 before and after a 7-day thin-layer mist test. Images for the panels after acid dissolution of any corrosion product are also presented. Red circles demark regions of corrosion product formation seen on day 7, and red arrows demark regions of surface pitting. 134

Figure 55. Photographs of the full 1 cm^2 surface area for NCP-coated, TCP-coated, and uncoated AA7075-T6 before (Day 0), after 1 day (Day 1), and after 2 days (Day 2) of a thin-layer mist test. The droplet distribution is shown for the 3.5% NaCl spray immediately after application. Red arrows mark regions of corrosion initiation, seen after 1 day for uncoated specimens and after 2 days for NCP-coated specimens..... 136

Figure 56. Scanning electron micrographs of uncoated AA7075-T6. Top images show secondary electron micrographs and bottom images show back-scattered electron micrographs. Images on the left are before testing (Day 0), images in the center are major damaged regions after the 7-day neutral salt-fog exposure (ASTM B117) (Day 7- Damage), and images on the right are the same regions as the center panels after nitric acid sonication to remove corrosion product (Post Nitric-Damage). All images have a 100 µm scale bar in the bottom right..... 149

Figure 57. Scanning electron micrographs and corresponding energy dispersive x-ray spectral maps of uncoated AA7075-T6 before any testing. All images correspond to the 10 µm scale bar in the secondary electron (SE) image, next to the back-scattered (BSE) image. The element represented in each map is shown in the top left corner of each panel..... 150

Figure 58. Scanning electron micrographs and corresponding energy dispersive x-ray spectral maps for uncoated AA7075-T6 after a 7-day neutral salt-fog test. All image dimensions are indicted by the 10 µm scale bar in the secondary electron (SE) image. The element represented in each map is shown in the top left corner of the panel. 151

Figure 59. Scanning electron micrographs and corresponding energy dispersive x-ray spectral maps of uncoated AA7075-T6 after a 7-day neutral salt-fog test and subsequent removal of corrosion product with nitric acid. All image dimensions are indicated by the 10 µm scale bar in the secondary electron (SE) image. The element represented in each map is shown in the top left corner of the panel..... 152

Figure 60. Scanning electron micrographs of TCP-coated (Henkel) AA7075-T6. Top images show secondary electron micrographs and bottom images show back-scattered electron micrographs. Images on the left are before testing (Day 0), images in the center are the major damaged regions after the 7-day neutral salt-fog exposure (Day 7- Major Damage), and images on the right are damaged regions after nitric acid removal of corrosion product (Post Nitric- Damage). All images are the same magnification and have a 100 µm scale bar in the bottom right..... 153

Figure 61. Scanning electron micrographs and corresponding energy dispersive x-ray spectral maps of TCP-coated (Henkel) AA7075-T6 before salt-spray testing. All images and maps are scaled equivalently with the corresponding 10 µm scale bar seen in the secondary electron (SE) micrograph. The element represented in each map is shown in the top left corner of the panel. 154

Figure 62. Scanning electron micrographs and corresponding energy dispersive x-ray spectral maps of TCP-coated (Henkel) AA7075-T6 after a 7-day salt-spray test. All images and maps are scaled equivalently with the corresponding 10 µm scale bar seen in the secondary electron (SE) micrograph. The element represented in each map is shown in the top left corner of the panel. 155

Figure 63. Scanning electron micrographs and corresponding energy dispersive x-ray spectral maps of TCP-coated (Henkel) AA7075-T6 after a 7-day salt-spray test and nitric acid removal of corrosion product. All images are the same scale correspond to the 10 µm scale bar in the secondary electron (SE) image. The element represented in each map is shown in the top left corner of each panel..... 156

Figure 64. Scanning electron micrographs of TCP-coated (Luster-On) AA7075-T6. Top images show secondary electron micrographs and bottom images show back-scattered electron micrographs. Images on the left are before testing (Day 0), images in the center are major damaged regions after the 7-day test (Day 7- Major Damage), and images on the right are damaged regions after nitric acid sonication to remove corrosion product (Post Nitric-Damage). All images have a 100 µm scale bar in the bottom right..... 158

Figure 65. Scanning electron micrographs and corresponding energy dispersive x-ray spectral maps of TCP-coated (Luster-On) AA7075-T6 before testing. All images and maps are scaled equivalently with the corresponding 10 µm scale bar seen in the secondary electron (SE) micrograph. The element represented in each map is shown in the top left corner of each panel. 159

Figure 66. Scanning electron micrographs and corresponding energy dispersive x-ray spectral maps of TCP-coated (Luster-On) AA7075-T6 after a 7-day salt-spray test. All images and maps are scaled equivalently with the corresponding 10 µm scale bar seen in the secondary electron (SE) micrograph. The elements represented in each map are shown in the top left corner of each panel. 160

Figure 67. Scanning electron micrographs and corresponding energy dispersive x-ray spectral maps of TCP-coated (Luster-On) AA7075-T6 after a 7-day salt-spray test and nitric acid sonication to remove corrosion product. All images and maps are scaled equivalently with the corresponding 10 µm scale bar seen in the secondary electron (SE) micrograph. The elements represented in each map are shown in the top left corner of each panel. 161

Figure 68. Scanning electron micrographs of TCP-coated (Chemeon) AA7075-T6. Top images show secondary electron micrographs and bottom images show back-scattered electron micrographs. Images on the left are before testing (Day 0), images in the center are major damaged regions after the 7-day test (Day 7- Major Damage), and images on the right are damaged regions after nitric acid sonication to remove corrosion product (Post Nitric-Damage). All images have a 100 µm scale bar in the bottom right. 162

Figure 69. Scanning electron micrographs and corresponding energy dispersive x-ray spectral maps of TCP-coated (Chemeon) AA7075-T6 before testing. All images and maps are scaled equivalently with the corresponding 10 µm scale bar seen in the secondary electron (SE) micrograph. The element represented in each map is shown in the top left corner of each panel. 163

Figure 70. Scanning electron micrographs and corresponding energy dispersive x-ray spectral maps of TCP-coated (Chemeon) AA7075-T6 after a 7-day salt-spray test. All images and maps are scaled equivalently with the corresponding 10 µm scale bar seen in the secondary electron (SE) micrograph. The element represented in each map is shown in the top left corner of each panel. 164

Figure 71. Scanning electron micrographs and corresponding energy dispersive x-ray spectral maps of TCP-coated (Chemeon) AA7075-T6 after a 7-day salt-spray test and nitric acid sonication to remove corrosion product. The element represented in each map is shown in the top left corner of each panel. 165

Figure 72. Scanning electron micrographs of TCP-coated (SurTec E) AA7075-T6. Top images show secondary electron micrographs and bottom images show back-scattered electron micrographs. Images on the left are before testing (Day 0), images in the center are major damaged regions after the 7-day test (Day 7- Major Damage), and images on the right are

damaged regions after nitric acid sonication to remove corrosion product (Post Nitric-Damage). All images have a 100 µm scale bar in the bottom right. 166

Figure 73. Scanning electron micrographs and corresponding energy dispersive x-ray spectral maps of TCP-coated (SurTec E) AA7075-T6 before testing. All images correspond to the 10 µm scale bar in the secondary electron (SE) image, next to the back-scattered (BSE) image the element represented in each map is shown in the top left corner of each panel. 167

Figure 74. Scanning electron micrographs and corresponding energy dispersive x-ray spectral maps of TCP-coated (SurTec E) AA7075-T6 after a 7-day salt-spray test. All images correspond to the 10 µm scale bar in the secondary electron (SE) image, next to the back-scattered (BSE) image. The element represented in each map is shown in the top left corner of each panel. 168

Figure 75. Scanning electron micrographs and corresponding energy dispersive x-ray spectral maps of TCP-coated (SurTec E) AA7075-T6 after a 7-day salt-spray test and nitric acid sonication to remove corrosion product. All images and maps are scaled equivalently with the corresponding 10 µm scale bar seen in the secondary electron (SE) micrograph. The element represented in each map is shown in the top left corner of each panel. 169

Figure 76. Scanning electron micrographs of NCP-coated (NAVAIR) AA7075-T6. Top images show secondary electron micrographs and bottom images show back-scattered electron micrographs. Images on the left are before testing (Day 0), images in the center are major damaged regions after the 7-day test (Day 7- Major Damage), and images on the right are damaged regions after nitric acid sonication to remove corrosion product (Post Nitric-Damage). All images have a 100 µm scale bar in the bottom right. 170

Figure 77. Scanning electron micrographs and corresponding energy dispersive x-ray spectral maps of NCP-coated (NAVAIR) AA7075-T6 before testing. All images and maps are scaled equivalently with the corresponding 10 µm scale bar seen in the secondary electron (SE) micrograph. The element represented in each map is shown in the top left corner of each panel. 171

Figure 78. Scanning electron micrographs and corresponding energy dispersive x-ray spectral line scans along the red arrow. All images and maps are scaled equivalently with the corresponding 10 µm scale bar seen in the secondary electron (SE) micrograph. The elemental line scans are presented on the right for the red arrows going from 0 to 9 µm at the arrow tip. 172

Figure 79. Scanning electron micrographs and corresponding energy dispersive x-ray spectral maps of NCP-coated (NAVAIR) AA7075-T6 after a 7-day salt-spray test. All images and maps are scaled equivalently with the corresponding 10 µm scale bar seen in the secondary electron (SE) micrograph. The element represented in each map is shown in the top left corner of each panel. 173

Figure 80. Scanning electron micrographs and corresponding energy dispersive x-ray spectral maps of NCP-coated (NAVAIR) AA7075-T6 after a 7-day salt-spray test and nitric acid sonication to remove corrosion product. All images correspond to the 10 µm scale bar in the secondary electron (SE) image, next to the back scattered (BSE) image. The element represented in each map is shown in the top left corner of each panel. 174

KEY TO ABBREVIATIONS

AA	Aluminum alloy
ICP-OES	Inductively coupled plasma optical emission spectrometry
Na_2SO_4	Sodium sulfate
NaCl	Sodium chloride
R_p	Polarization resistance
TCP	Trivalent chromium process
OCP	Open circuit potential
NCP	Non-chromated process
IMP	Intermetallic particle
CCC	Chromate conversion coating

CHAPTER 1: INTRODUCTION AND MOTIVATION FOR STUDIES

1.1. Alloy Properties and Composition

Aluminum alloy (AA) 7075-T6 (UNS A97075) is widely used in aerospace applications due to its characteristic high strength combined with low weight.[1] This allows the manufacture of strong, yet light fuselage components for airplanes. When aluminum alloys are used as structural components, the main source of catastrophic failure is localized corrosion of the alloy, which often initiates at intermetallic particle (IMP) sites that are dispersed throughout the aluminum.[2] When aluminum alloys are used in the field, they must be protected from corrosion during exposure to the environment. This is accomplished using a multi-layer coating system that is generally composed of an initial conversion coating followed by a primer and a topcoat.

Traditional coatings currently used by the aerospace industry contain hexavalent chromium (Cr(VI)) as an active component of either the conversion coating and or primer. The primer and topcoat also contain volatile organic compounds (VOC) and hazardous air pollutants (HAP) with several heavy metals used for corrosion protection and color.[3] Hexavalent chromium is useful for corrosion preventive coatings due to ion migration into damaged regions and the formation of a protective chromium (III) hydroxide layer that blocks further corrosion damage. This process is commonly referred to as active corrosion protection. Environmental and health concerns are driving the aerospace industry to transition from chromated conversion coatings and primers to more environmentally-friendly coating systems.[3-4] Conversion coatings are thin, hydrated metal oxide films formed on a metal surface that ideally provide adhesion promotion with primers, anti-corrosion properties to the base metal, and a reservoir of inhibitor ions during the coating lifetime.[5-7] The end date for new applications using hexavalent chromium coatings is September 2017. To

this end, the Naval Air Systems Command (NAVAIR) has formulated some novel coating chemistries for metal finishing and developed associated application processes. Two of these for aluminum alloys are (i) non-chromated process (NCP) and (ii) trivalent chromium process (TCP) conversion coatings. NCP is a non-chromium, zirconium and zinc-based aqueous coating that can be applied by both immersion and spray.[3, 8] TCP is a non-chromated, trivalent chromium and zirconium-based coating that can also be applied by immersion or spray.[3, 9-10] Both have undergone field testing on some assets, however, much remains to be learned about the mechanism(s) by which these coatings inhibit corrosion on different alloys in a variety of test environments, and how combinations of these non-chromated conversion coatings and primers maintain high corrosion resistance and good physical properties.

TCP is the leading candidate to replace the chromate pretreatment conversion coatings on aerospace aluminum alloys.[3, 10-11] TCP has been licensed by several vendors and is currently marketed under different names: Bonderite M-Cr T5900 from Henkel, TCP-HF from Chemeon (formerly Metalast), 650 ChromitAL from SurTec and Aluminescent from Luster-on. These coating baths have chemical compositions that differ to some extent from the original NAVAIR formulation so, from a research perspective, each should be treated as a separate coating system. Generally speaking, while these commercial TCP coatings have been qualified for use, differences are often observed in their anti-corrosion properties on different aluminum alloys, particularly during accelerated degradation testing and environmental exposure. The morphology and chemical composition of a TCP coating will depend on the coating bath composition, the cleanliness of the alloy surface, the chemical composition of the alloy surface namely the number density of intermetallic phases present, and the alloy surface morphology (*i.e.*, pit size and density). Improvements in the TCP coating anti-corrosion performance could be realized with more

fundamental insight of the coating formation mechanism, the physical structure and chemical composition, and how the coating structure depends on the surface pretreatment of the alloy.

There has been limited published work to date on fundamental investigations of the TCP coating formation mechanism, the physical and chemical structure of the coating on different aluminum alloys, and correlation of these properties with the anti-corrosion behavior. Our group reported on the Bonderite M-Cr T5900 coating from Henkel on AA2024-T3, AA6061-T6 and AA7075-T6.[6, 12-13] Results on AA2024-T3 have shown that Henkel T5900 forms a 90-100 nm thick coating composed of hydrated zirconia ($ZrO_2 \bullet nH_2O$) co-precipitated with $Cr(OH)_3$. The coating is biphasic with the upper 60 nm comprised of Zr and Cr oxides and a fluoroaluminate interfacial layer formed extending some 40 nm away from the aluminum surface. The coating thickness tends to be greater on and around intermetallic particles (IMPs) due to enhanced reaction (precipitation) chemistry at these sites. The presence of the coating across all regions of an alloy with greater thickness around intermetallics is evidenced from EDXS line profile scans.[12] Transient formation of Cr (VI) is its possible migration into damaged regions on the aluminum alloy has been detected through Raman spectroscopy. It is proposed to form through an oxidation of Cr (III) by locally produced hydrogen peroxide (a product of the oxygen reduction reaction at Cu IMPs).[6,12-19,22,24] The TCP coating in low chloride-containing electrolytes provides both anodic and cathodic protection to the aluminum alloy surface as evidence by an increased polarization resistance, decreased anodic and cathodic polarization curve currents, and decreased damage during accelerated degradation testing when compared to an uncoated alloy control.

Prior work has shown that the conversion coating provides both anodic and cathodic protection on AA2024-T3, AA6061-T6, and AA7075-T6.[6, 12, 14] The Henkel T5900 TCP coating provided more cathodic inhibition on AA6061 and both cathodic and anodic inhibition on

AA7075, based on suppression of polarization curve currents.[14] These protective differences are expected to be inherent to each specific coating and alloy combination, with many of the factors already mentioned contributing to enhanced performance and corrosion inhibition mechanisms. However, to a first approximation, the basic barrier properties of the TCP coatings are expected to provide a similar basic level of corrosion protection across all the different commercial variants of the coating and aluminum alloy types.

There have also been some reports on the 650 ChromitAl from SurTec.[8-10, 15-19] Thompson, et. al. provided additional evidence that supports the biphasic structure of the coating on AA2024-T3. Using XPS analysis, the Zr and Cr present were identified as ZrO_2, $Cr(OH)_3$, $Cr_2(SO_4)_4$, and CrF_3, while the fluoroaluminate interfacial layer was purported to consist of mainly hydrated alumina.[16] Impedance spectroscopy has provided some evidence that the inner aluminum-rich layer is providing the most corrosion protection.[10] Enhancement of coating formation was observed around the S-phase intermetallic particles (Al_2CuMg IMPs), and is attributed, in part, to fluoride ion attack on Cu IMPs leading to localized corrosion and oxide formation.[10, 16] TCP coatings contain CrF_3 in addition to $Cr(OH)_3$ and Cr_2O_3, as detected with Raman spectroscopy.[18]

As mentioned, transient formation of hexavalent chromium, associated with active corrosion protection, has been detected in some coatings using Raman spectroscopy.[10, 12, 16, 18] As already discussed, the Henkel coating produced evidence of transient formation of Cr(VI) which will be discussed in further detail later in the introduction.[12] With the SurTec coating system, hexavalent chromium formation has been seen through trivalent chromium oxidation during exposure to NaCl droplets, supporting the belief that trivalent chromium could provide similar active corrosion prevention through migration similar to process that occurs with hexavalent chromium.[18] Evidence was not been seen for hexavalent chromium formation in de-aerated

solutions, which could be due to the lack of oxygen reduction to produce hydrogen peroxide, which supposedly oxidizes local trivalent chromium.[10]

1.2. Surface Preparation

The metal surface must be pretreated consistently to provide optimum conditions for conversion coating formation. Pretreatment often consists of multiple steps. In the laboratory, smut and surface roughness are removed by manual polishing. However, alloys being prepared for use on an aerospace asset will not receive any polishing the smooth the surface. Next, any cutting oils or grease is removed through the application of an alkaline degreasing agent that contains some type of surfactant. [20] After the surface is degreased, any remaining oxide layer is removed using a deoxidizer that is typically an acidic fluoride solution. Finally, once the surface is clean and low in surface oxygen, the conversion coating is applied by immersion, spray or brush application. Surface pretreatments, specifically the deoxidation step, can cause severe pitting and surface roughening that should be avoided.[21]

1.3. Coating Formation

The TCP coating formation process has been examined in our group[6, 22] and been found to occur by a mechanism similar to that known for the formation of chromate conversion coatings. The process initially involves the dissolution of the natural oxide layer and the underlying aluminum alloy. The dissolution of the oxide film[23] is associated with the following chemical reaction:

$$Al_2O_3 + 2nHF + (6-2n)H^+ \leftrightarrow 2AlF_n^{(3-n)+} + 3H_2O \quad (1)$$

The dissolution reaction for the metal[23] is associated with the following chemical reaction:

$$Al + nHF + (3-n)H^+ \leftrightarrow AlF_n^{(3-n)+} + \frac{3}{2}H_2 \quad (2)$$

The overall reactions involve the corrosion of the aluminum matrix by fluoride ions present in the coating bath that form an interfacial fluoroaluminate layer with potassium that is present in the coating baths (K_xAlF_{3+x}). Once the passivating and electrically insulating oxide layer is removed, the potential of the alloys shifts negatively to regions where cathodic reactions, in addition to metal corrosion, can occur. While the aluminum occurs (reaction 3), the oxygen reduction (reaction 4), and hydrogen evolutions reactions (reaction 5) commence. The oxygen reduction occurs primarily at Cu-rich intermetallic sites. Both reactions are shown below and they consume protons to produce in increase in the interfacial pH:

$$Al + 6F^- \rightarrow AlF_6^{3-} + 3e^- \quad (3)$$

$$O_2 + 2H_2O + 4e^- \rightarrow 4OH^- \quad (4)$$

$$2H^+ + 2e^- \rightarrow H_2 \quad (5)$$

The increase in interfacial pH drives the hydrolysis of hexafluorozirconate[12] species in the coating bathe to hydrated zirconia that precipitates on the surface to form an outer barrier layer:

$$ZrF_6^{2-} + 4OH^- \rightarrow ZrO_2 \cdot 2H_2O + 6F^- \quad (6)$$

This zirconium oxide formation co-precipitates with a mixture of chromium compounds including Cr_2O_3, $Cr(OH)_3$, $Cr(SO_4)_3$, and CrF_3.[6, 16] The chromium oxides are enhanced in regions around IMPs, due to increased localized oxygen reduction around these sites:[6]

$$Cr^{3+} + 3OH^- + 3e^- \leftrightarrow Cr(OH)_3 + 5OH^- \quad (7)$$

1.4. Material Characterization

The TCP coating baths contain fluorozirconate, which is similar to the chromate conversion coating baths, but does not contain any of the Cr(VI) salts. These are instead replaced with Cr(III)

salts, *e.g.* $Cr_2(SO_4)_3$. The actual composition of the commercial forms of TCP are proprietary. The elemental composition (inorganic content) of a NAVAIR non-chromate process (NCP) coating bath[24] has been determined through ICP-OES. The coating bath composition (inorganic and organic) is important to know as it is linked to the coating composition once formed.

The TCP films themselves have been characterized for thickness, morphological structure, and surface chemistry using a variety of different spectroscopic methods, of which ellipsometry[11], SEM and EDXS[6], XPS and Auger spectroscopy[16], and Raman spectroscopy[18] have been used. Ellipsometry results have supported the proposed mechanism of native Al oxide dissolution through fluoride and proton attack, and revealed that the coatings form with a thickness of around 100 nm (5-10 min coating time). [5, 11, 13] SEM and EDXS have revealed (using a different brands of TCP) increased amounts of coating precipitate (Zr, Cr, O, and F) around Cu IMPs. This is due to the increased rate of the oxygen reduction reaction at the Cu, as compared to the surrounding aluminum. This reaction consumes protons and the high rate leads to a steeper pH gradient around these sites.[6] It is the induced pH gradient that drives the formation of the coating. Similar SEM/EDXS results supporting this formation mechanism was seen with the SurTec brand of TCP on different aluminum alloys.[16]. XPS analysis has provided further support for the proposed formation mechanism and confirmed the presence of an Al, F and O interfacial layer underlying the outer Cr(III) and Zr oxide layer.[16] XPS and Auger electron spectroscopy data revealed this biphasic film structure with enriched signals for F, Al, and O in the interfacial region (~40 nm), and increased signals for ZrO_2 and Cr in the outer layer up to a thickness of ~100 nm.[6] Raman spectroscopy has detected CrF_3 present in the SurTec coating in addition to the $Cr(OH)_3$ and Cr_2O_3 usually seen for other TCP coatings.[13, 18] Additionally, Raman spectroscopy has revealed evidence for the transient formation of Cr(VI).[13, 25] Cr(VI) was found to form selectively near pits,

indicating the formation is driven by decreases in local pH and Al ion increases due to alloy corrosion.[25]

1.5. Electrochemical Characterization

Various TCP coatings on several different aluminum alloys have been studied electrochemically.[8-9, 26-31] On AA2024-T3, TCP coatings provide both anodic and cathodic corrosion protection through decreased polarization currents around the OCP, more noble OCPs when compared to uncoated AA2024-T3 (indicating more anodic protection than cathodic), and 10-fold increases in the polarization resistance.[12] The same brand of TCP provided similar anodic and cathodic protection when applied to AA7075-T6 with decreased currents around OCP, more noble OCPs, and a 10-fold increase in polarization resistance when compared to uncoated specimen. On AA6061-T6, the coating provided increased cathodic protection with a more active OCP, slight decreases in current around OCP, and greater than a 10-fold increase in polarization resistance.[14] We can expect the SurTec brand of TCP coating to perform in similar ways, providing decreased anodic and cathodic currents, more noble OCPs, and 10-fold increases in polarization resistance.

1.6. Accelerated Degradation Tests

Laboratory electrochemical tests provide information about whether or not a coating has a tendency to protect an aluminum alloy from corrosion. Accelerated degradation tests are performed as a follow-up to evaluate coating performance under conditions designed to simulate the service environment. Coating performance would best be performed in service, but that would require long testing periods and would not very cost effective if the coating does not perform well. There are a few ASTM standard test methods that are commonly used to evaluate corrosion protection: full immersion in salt solution[32], a thin layer of salt spray in an increased humidity

environment [24], and a salt-spray fog chamber.[33] Analysis of chromate conversion coatings (CCC) on various metals has revealed that the corrosion protection seen through EIS and electrochemical measurements is a good predictor of the corrosion protection observed during accelerated degradation tests.[34] Previous analysis of SurTec TCP and NCP conversion coatings on aluminum alloy during the full immersion, thin-layer mist, and salt-spray tests showed that the NCP coating reduced mass loss by 2x while the TCP coating reduced mass by 10x.[24]

After the accelerated degradation testing, the specimens are generally cleaned with concentrated nitric acid for 5-20 minutes to remove corrosion product from the surface. The degree of corrosion protection can be analyzed through changes in mass (with mass gain indicating corrosion product built up and mass loss indicating specimen damage due to corrosion). Additionally, specimens can be analyzed with SEM and Raman spectroscopy to determine if there are any increases in Cr (VI), specifically around damaged sites indicating possible active corrosion prevention.

1.7. Motivations and Questions

In this dissertation research, a systematic study of three versions of the SurTec TCP 650 conversion coating (E, V and C), applied to degreased and deoxidized AA7075-T6 by immersion and spray, was performed. The inorganic content in the coating baths was quantified by ICP-OES. The coating morphology and chemical composition were assessed by SEM and EDXS analysis. The elemental composition through the coating was determined by depth-profiling XPS. The presence of Cr(III)-O and Cr(VI)-O species in the coating was verified using Raman spectroscopy and specification vibrational modes for each. The coating thickness was measured by ellipsometry (in air) and the coating wettability was assessed by static water contact angle measurements. The electrochemical properties (including OCPs, polarization currents, and polarization resistances)

were assessed for all coating variants and application methods. Additionally, the performance of the coating was analyzed during accelerated degradation tests and compared to other brands of TCP (non-chromated) and a NAVAIR NCP (non-chromium) coating. Finally, an initial in-depth microanalysis of the coating failure initiation sites was conducted using SEM and EDXS. For these studies, the performance of five different TCP and NCP coatings (Henkel, SurTec, Chemeon, Luster-On TCPs and NAVAIR NCP) were compared.

We sought to answer several key questions:

1. What are the chemical composition differences in the coating baths and do these compositional differences lead to coatings with different physical and chemical properties?
2. Are the physical and chemical properties of the coatings different for immersion versus spray-on application?
3. Do the coatings produced through spray and immersion provide similar stand-alone corrosion protection?
4. What are the corrosion protection mechanisms (*i.e.* equivalent amounts of cathodic and anodic corrosion protection)?
5. Which coating composition provides the best corrosion protection, with specific attention to aggressive chloride ion attack?
6. Will the best performing coating variant and application method provide corrosion protection equivalent to other TCP and NCP coatings on the market when exposed to accelerated degradation testing?
7. How does the damage initiation on a SurTec TCP coating compare with other TCP and NCP coatings during an accelerated degradation test? Does damage initiate through similar mechanisms with the different brands on the same aluminum alloy?

REFERENCES

REFERENCES

1. Polmear, I. J., 2 - Physical metallurgy of aluminium alloys. In *Light Alloys (Fourth Edition)*, Polmear, I. J., Ed. Butterworth-Heinemann: Oxford, 2005; pp 29-96.

2. Birbilis, N.; Buchheit, R. G., Electrochemical characteristics of intermetallic phases in aluminum alloys - An experimental survey and discussion. *Journal of the Electrochemical Society* **2005,** *152* (4), B140-B151.

3. Costa, M., Toxicity and carcinogenicity of Cr(VI) in animal models and humans. *Critical Reviews in Toxicology* **1997,** *27* (5), 431-442.

4. Shanker, A. K.; Cervantes, C.; Loza-Tavera, H.; Avudainayagam, S., Chromium toxicity in plants. *Environment International* **2005,** *31* (5), 739-753.

5. Dardona, S.; Chen, L.; Kryzman, M.; Goberman, D.; Jaworowski, M., Polarization Controlled kinetics and composition of trivalent chromium coatings on aluminum. *Analytical Chemistry* **2011,** *83* (16), 6127-6131.

6. Li, L.; Swain, G. M., Formation and structure of trivalent chromium process coatings on aluminum alloys 6061 and 7075. *Corrosion* **2013,** *69* (12), 1205-1216.

7. La Scala, J., Non-Chromate/ no VOC conversion coatings. *SERDP Report* **2009**, 68.

8. Feng, Z.; Frankel, G. S.; Matzdorf, C. A., Quantification of accelerated corrosion testing of coated AA7075-T6. *Journal of The Electrochemical Society* **2014,** *161* (1), C42-C49.

9. Feng, Z.; Boerstler, J.; Frankel, G. S.; Matzdorf, C. A., Effect of surface pretreatment on galvanic attack of coated al alloy panels. *Corrosion* **2015,** *71* (6), 771-783.

10. Qi, J. T.; Hashimoto, T.; Walton, J. R.; Zhou, X.; Skeldon, P.; Thompson, G. E., Trivalent chromium conversion coating formation on aluminium. *Surface and Coatings Technology* **2015,** *280*, 317-329.

11. Dardona, S.; Jaworowski, M., In situ spectroscopic ellipsometry studies of trivalent chromium coating on aluminum. *Applied Physics Letters* **2010,** *97* (18), 181908.

12. Li, L.; Swain, G. P.; Howell, A.; Woodbury, D.; Swain, G. M., The formation, structure, electrochemical properties and stability of trivalent chrome process (TCP) coatings on AA2024. *Journal of The Electrochemical Society* **2011,** *158* (9), C274-C283.

13. Li, L.; Swain, G. M., Effects of aging temperature and time on the corrosion protection provided by trivalent chromium process coatings on AA2024-T3. *ACS Applied Materials & Interfaces* **2013,** *5* (16), 7923-7930.

14. Li, L.; Doran, K. P.; Swain, G. M., Electrochemical characterization of trivalent chromium process (TCP) coatings on aluminum alloys 6061 and 7075. *Journal of The Electrochemical Society* **2013,** *160* (8), C396-C401.

15. Qi, J.; Hashimoto, T.; Thompson, G. E.; Carr, J., Influence of water immersion post-treatment parameters on trivalent chromium conversion coatings formed on AA2024-T351 alloy. *Journal of The Electrochemical Society* **2016,** *163* (5), C131-C138.

16. Qi, J.; Hashimoto, T.; Walton, J.; Zhou, X.; Skeldon, P.; Thompson, G. E., Formation of a trivalent chromium conversion coating on AA2024-T351 alloy. *Journal of The Electrochemical Society* **2016,** *163* (2), C25-C35.

17. Qi, J.; Thompson, G. E., Comparative studies of thin film growth on aluminium by AFM, TEM and GDOES characterization. *Applied Surface Science* **2016,** *377*, 109-120.

18. Qi, J.; Walton, J.; Thompson, G. E.; Albu, S. P.; Carr, J., Spectroscopic studies of chromium vi formed in the trivalent chromium conversion coatings on aluminum. *Journal of The Electrochemical Society* **2016,** *163* (7), C357-C363.

19. Munson, C. A.; Swain, G. M., Structure and chemical composition of different variants of a commercial trivalent chromium process (TCP) coating on aluminum alloy 7075-T6. *Surface and Coatings Technology* **2017,** *315*, 150-162.

20. Committee, A. S. M. I. H., ASM Handbook, Volume 05 - Surface Engineering. ASM International.

21. Li, L.; Desouza, A. L.; Swain, G. M., Effect of deoxidation pretreatment on the corrosion inhibition provided by a trivalent chromium process (TCP) conversion coating on AA2024-T3. *Journal of The Electrochemical Society* **2014,** *161* (5), C246-C253.

22. Li, L.; Desouza, A. L.; Swain, G. M., In situ pH measurement during the formation of conversion coatings on an aluminum alloy (AA2024). *Analyst* **2013,** *138* (15), 4398-4402.

23. Xue, T.; Cooper, W. C.; Pascual, R.; Saimoto, S., Effect of fluoride ions on the corrosion of aluminium in sulphuric acid and zinc electrolyte. *Journal of Applied Electrochemistry* **1991,** *21* (3), 238-246.

24. Li, L.; Whitman, B. W.; Munson, C. A.; Estrada, R.; Matzdorf, C. A.; Swain, G. M., Structure and corrosion performance of a non-chromium process (NCP) Zr/Zn pretreatment conversion coating on aluminum alloys. *Journal of The Electrochemical Society* **2016,** *163* (13), C718-C728.

25. Ramsey, J. D.; McCreery, R. L., Raman microscopy of chromate interactions with corroding aluminum alloy 2024-T3. *Corrosion Science* **2004,** *46* (7), 1729-1739.

26. Feng, Z.; Frankel, G. S., Galvanic test panels for accelerated corrosion testing of coated Al alloys: Part 2—measurement of galvanic interaction. *CORROSION* **2014,** *70* (1), 95-106.

27. Feng, Z.; Frankel, G. S.; Abbott, W. H.; Matzdorf, C. A., Galvanic attack of coated Al alloy panels in laboratory and field exposure. *Corrosion* **2016,** *72* (3), 342-355.

28. Frankel, G. S.; Newman, R. C.; Jahnes, C. V.; Russak, M. A., On the Pitting resistance of sputter-deposited aluminum alloys. *Journal of The Electrochemical Society* **1993,** *140* (8), 2192-2197.

29. Guo, Y.; Frankel, G. S., Characterization of trivalent chromium process coating on AA2024-T3. *Surface and Coatings Technology* **2012,** *206* (19–20), 3895-3902.

30. Guo, Y.; Frankel, G. S., Active Corrosion inhibition of AA2024-T3 by trivalent chrome process treatment. *CORROSION* **2012,** *68* (4), 045002-1-045002-10.

31. Clark, W. J.; Ramsey, J. D.; McCreery, R. L.; Frankel, G. S., A galvanic corrosion approach to investigating chromate effects on aluminum alloy 2024-T3. *Journal of The Electrochemical Society* **2002,** *149* (5), B179-B185.

32. Standard practice for immersion testing of industrial protective coatings and linings. ASTM International: **2015.**

33. Standard practice for operating salt spray (Fog) apparatus. ASTM International: **2016.**

34. Leggat, R. B.; Taylor, S. R.; Zhang, W.; Buchheit, R. G., Corrosion performance of field-applied chromate conversion coatings. *CORROSION* **2002,** *58* (3), 283-291.

CHAPTER 2: FORMATION AND STRUCTURE OF DIFFERENT VARIANTS OF A COMMERCIAL TRIVALENT CHROMIUM PROCESS (TCP) COATING ON ALUMINUM ALLOY 7075-T6

2.1. Characterization Introduction

Multi-layer coating systems (conversion coating + primer + topcoat) are used to protect aerospace aluminum alloys from corrosion in service. Traditional coating systems contain hexavalent chromium (Cr(VI)) in both the conversion coating and primer, volatile organic compounds (VOC) and hazardous air pollutants (HAP) in both the primer and topcoat, as well as several heavy metals used for corrosion protection and color.[3] Environmental and health concerns are driving the aerospace industry to transition away from the chromated conversion coatings and primers to more environmentally-friendly coating systems.[3, 7, 35] Conversion coatings are thin, hydrated metal oxide films formed on a metal surface that ideally provide adhesion promotion with primers, anti-corrosion properties to the base metal, and a reservoir of inhibitor ions during the coating lifetime.[36] To this end, the Naval Air Systems Command (NAVAIR) has formulated some novel coating chemistries for metal finishing and developed associated application processes. Two of these for aluminum alloys are (i) non-chromated process (NCP) and (ii) trivalent chromium process (TCP) conversion coatings. NCP is a non-chromium, zirconium and zinc-based aqueous coating that can be applied by both immersion and spray.[24, 37] TCP is a non-chromated, trivalent chromium and zirconium-based coating that can also be applied by immersion or spray.[38] Both have undergone field testing on some assets, however, much remains to be learned about the mechanism(s) by which these coatings inhibit corrosion on different alloys in a variety of test environments, and how combinations of these non-chromated conversion coatings with primers maintain high corrosion resistance and good physical properties.

TCP is the leading candidate to replace the chromated pretreatment conversion coatings on aerospace aluminum alloys.[6, 10, 12-16, 29-30, 38-39] TCP has been licensed by several vendors and is currently marketed under different names: Bonderite M-Cr T5900 from Henkel, TCP-HF from Chemeon (formerly Metalast), 650 ChromitAL from SurTec and Aluminescent from Luster-on. These coating baths have chemical compositions that differ to some extent from the original NAVAIR formulation so, from a research perspective, each should be treated as a separate coating system. Generally speaking, while these commercial TCP coatings have been qualified for use in selected applications, differences are often observed in their anti-corrosion properties on aluminum alloys, particularly during accelerated corrosion testing and environmental exposure. The morphology and chemical composition of a TCP coating, and therefore the anti-corrosion properties, will depend on the coating bath composition, the cleanliness of the alloy surface, the chemical composition of the alloy surface namely the number density of intermetallic phases present, and the alloy surface morphology (*i.e.*, pit size and density). Improvements in the TCP coating's anti-corrosion performance could be realized with more fundamental knowledge regarding the physical structure and chemical composition of the coating, how the coating structure depends on the surface pretreatment of the alloy and the corrosion inhibition mechanism(s).

There has been limited published work to date on fundamental investigations of the TCP coating formation mechanism, the physical and chemical structure of the coating on different aluminum alloys, and correlation of these properties with the anti-corrosion behavior. We have reported such data for the Bonderite M-Cr T5900 coating from Henkel on AA2024-T3, AA6061-T6 and AA7075-T6.[12-14, 39b] There have also been some reports on the 650 ChromitAl from SurTec.[8-10, 15-16]

In this chapter, we report on a systematic study of three versions of the SurTec TCP coating (650 E, V and C) applied to degreased and deoxidized AA7075-T6 by immersion and spray. The inorganic content in the coating baths was quantified by ICP-OES. The coating morphology and chemical composition were assessed by SEM and EDXS analysis, respectively. The elemental composition through the coating was determined by depth-profiling AES. The presence of Cr(III)-O and Cr(VI)-O vibrational modes in the coating was verified by Raman spectroscopy. Finally, the coating thickness was measured by ellipsometry (in air) and the coating wettability was assessed by static water contact angle measurements. We sought to answer two key questions:

1) What are the chemical composition differences in the coating baths and do these compositional differences lead to coatings with different structure and composition?
2) Are the physical structure and chemical composition of the coatings different for immersion versus spray-on application?

Correlating the anti-corrosion properties of the coatings with their physical and chemical structure was also addressed during the work. These results will be reported in a separate chapter.

2.2. Material and Methods

2.2.1. Reagents

The 133 degreaser and 495L deoxidizer (SurTec, Inc., Brunswick, OH) were prepared to 4 wt. % and 20 vol. %, respectively. The 650 E (also known as the traditional chromitAl 650), V, and C TCP coating baths were prepared to 20 vol. %. The pH of the coating solution was adjusted to 3.85 using 0.1 M NaOH or 0.1 M H_2SO_4, as needed. All solutions were prepared using ultrapure water (Barnstead E-Pure) with a resistivity >17 MΩ·cm.

2.2.2. Specimen Preparation

The AA7075-T6 was obtained as a 2-mm thick sheet (www.onlinemetals.com), which was cut into 1 cm^2 specimens. The composition of the alloy was determined by x-ray fluorescence (XRF) using known sensitivity factors for the different elements. The measurements were made by energy dispersive x-ray fluorescence (Bruker S2 Ranger). The quantitative results are presented in Table 1. All values are within the expected range[40], except for Mg which is a little higher than expected for this alloy.

Table 1. The elemental composition (wt.%) of AA7075-T6 as determined from quantitative XRF analysis.

Elemental Composition (wt. %)	XRF	Expected Range
Cu	1.61 ± 0.02	1.2 - 2
Fe	0.25 ± 0.01	< 0.5
Mg	6.00 ± 0.06	2.1 - 2.9
Mn	ND	< 0.3
Si	0.33 ± 0.03	< 0.4
Zn	5.71 ± 0.06	5.1 - 6.1
Ti	0.04 ± 0.01	< 0.2
Cr	0.22 ± 0.01	0.18 - 0.28
Al	84.75 ± 0.27	87.1 - 91.4

Values are reported as mean ± standard error of the mean for n = 3 specimens. Known values are from the ASM material data sheet for AA7075-T6.[40] ND = not detected. Total mass balance = 98.91%.

The specimens were prepared for conversion coating by first wet sanding for 4 min using 1500 grit aluminum oxide paper to smooth the surface and to expose fresh alloy. This was followed by ultrasonic cleaning for 20 min in ultrapure water in a covered glass beaker. The specimens were then hand polished for 4 min using a 0.3-μm diameter alumina powder (Buehler) slurry on a felt polishing pad. The alumina slurry or paste was prepared by mixing the powder with ultrapure water directly on the polishing pad. The polished specimens were then ultrasonically cleaned for 20 min in ultrapure water in a covered glass beaker. After polishing, the specimens were degreased by a 5-min immersion in 4 wt. % SurTec 133 at 60°C in a glass beaker.

This is an alkaline (pH 9.0-9.5) and silicate-free degreaser that contains phosphate and borate surfactants. The specimens were gently agitated each minute of the cleaning. The specimens were then rinsed for 2 min under gently flowing city tap water, which contained ~0.1 ppm Zr, ~0.2 ppm Cu, Fe, Zn, ~0.4 ppm Al, and 30-45 ppm Ca, Mg, and S as determined using ICP-OES (Figure 1). This was followed by deoxidation for 2 min in 20 vol. % SurTec 495L at room temperature. The deoxidation was performed in a glass beaker without any specimen agitation. This fluoride-containing deoxidizer has a sulfuric acid base with added Fe salts. The specimens were then rinsed for 2 min under gently flowing city tap water. At this point, the pretreated specimens were dried under a stream of nitrogen and stored in a petri dish until further use. These specimens are referred to as "uncoated".

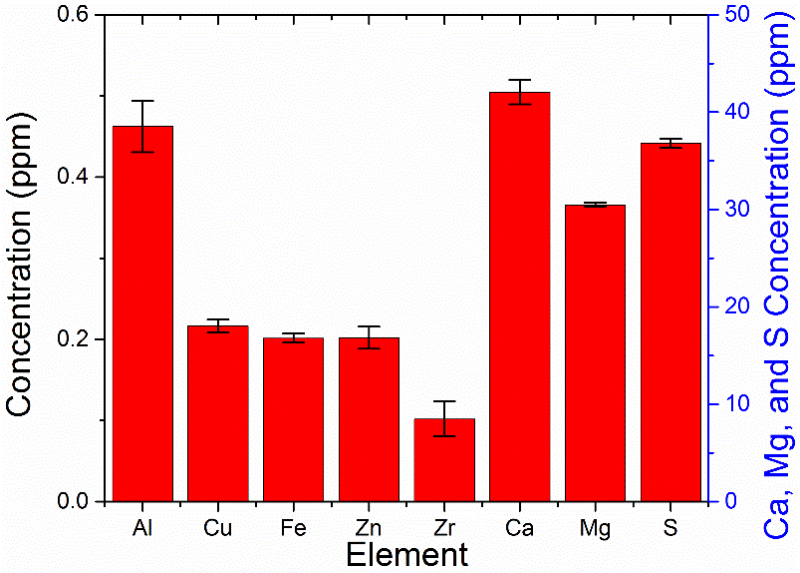

Figure 1. Elemental analysis of the city tap water (July 2016) used for specimen rinsing as determined by ICP-OES. Data are presented as mean ± S.E.M. for n ≥ 3.

The TCP coating was applied to degreased and deoxidized specimens by immersion or spray. Immersion-coated specimens were placed in a 20 vol. % 650 E, C, or V solution at 30°C for 4 min without any agitation. Spray-coated specimens were sprayed every 30 s for a 3-min

period at room temperature, ~21-25°C. These coating conditions were selected based on recommendations by the supplier. The spray coating was applied with a nebulizing spray bottle. The immersion-coated specimens were then rinsed by immersion in city tap water for 2 min followed by a final soak in ultrapure water for 30 s. The spray-coated specimens were then rinsed with a city tap water spray every 30 s for a 2-min period followed by a final immersion in ultrapure water for 30 s. The coated specimens were allowed to dry in the laboratory atmosphere overnight before further testing. The drying or aging was performed at room temperature in a covered petri dish.

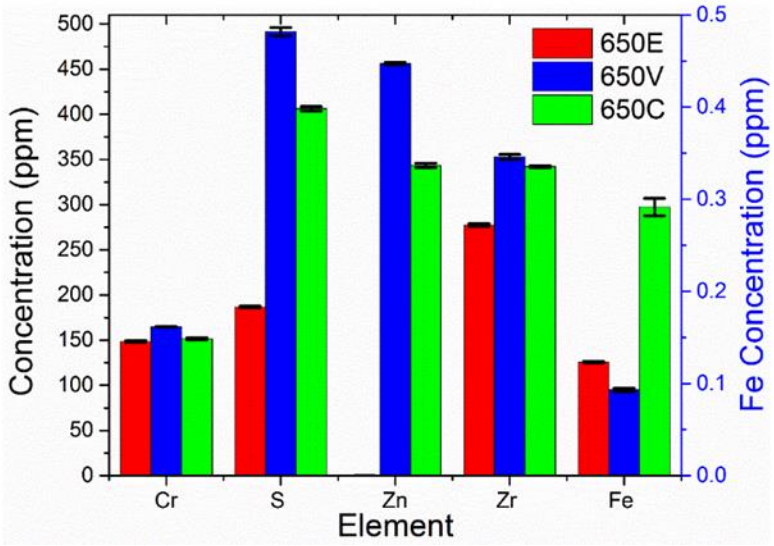

Figure 2. Elemental analysis of SurTec 650 E (red), 650 V (blue), and 650 C (green) coating baths as determined by ICP-OES analysis. Data are presented as mean ± S.E.M. for n ≥ 3.

Quantitative inorganic chemical analysis of the city tap water and the coating baths was performed on a Varian 710-ES ICP-OES. Quantitation was performed using response curves generated with external standards. The results for the coating bath composition are presented in Figure 2. The major chemical differences in the coatings are Zn in 650 V and C, the greater level of S in 650 V and C, and the greater level of Fe in 650 C. The Zr/Cr ratio is approximately 2:1 for all three coating variants. SurTec 650 (650 E) is the first-generation of the coating based on the

original NAVAIR formulation with Zr^{+4} and Cr^{+3} salts. 650 V is the second-generation of the coating with the same general composition as 650 E plus some added complexing agents. 650V is designed to produce a heavier coating than 650 E with more coloration for visible detection. 650 C is generally similar to 650 V in chemical composition, with some different complexing agents added. During the course of this work, it was learned that the 650 C has been discontinued from the company's product line.

2.3. Alloy and Coating Characterization

Scanning electron microscopy and energy dispersive x-ray analysis (EDXS) were performed using a field emission SEM (JEOL 7500F) with an energy dispersive x-ray microanalysis attachment. These studies were performed to assess the metallographic condition of the pretreated and coated specimen surfaces. The x-ray emission lines from EDXS spectra were used to determine the presence of the conversion coating (Zr, Cr, F and O) near intermetallic particles and away from these particles on the aluminum matrix. The measurements were made at the Center for Advanced Microscopy (MSU). Raman microprobe spectroscopy was performed using a Renishaw *inVia* Confocal Raman Microscope equipped with a Nd:YAG laser (45 W maximum power with 10% of this used at the specimen surface). The excitation line was at 523 nm. Raman spectroscopy was used principally to probe the coatings for the presence of Cr^{+3}-O ($Cr(OH)_3$) and Cr^{+6}-O (CrO_4^{2-} or $HCrO_4^-$) vibrational modes in the coating. Ellipsometry (in air) was performed using a VASE ellipsometer with a 75 W Xenon light source to determine the coating thickness. Static water contact angles were measured with an AST Products Video Contact Angle System 2000 with a 150 W light source to determine the coating wettability. Surface profilometry was performed on a NanoMap-500LS Contact Surface Profilometer at the Electrical

and Computer Engineering Testing Facility (MSU). The surface profilometry provided information on the specimen surface roughness, pit density, and pit dimensions.

2.4. Calculations and Statistical Analysis

Spectroscopic ellipsometry measures the change in polarization state of linearly polarized light upon reflection from a surface. The measured ellipsometry parameters are the amplitude ratio (tan Ψ) and the phase shift difference (Δ) of the parallel and perpendicularly polarized components of the reflected light (r_s and r_p). The parameters are defined through the expression, tan (Ψ) exp (Δ) = r_p/r_s. These measured responses depend on the optical properties (*e.g.*, refractive index, n) and coating thickness, d. Using model analysis and an iterative process, n and d are determined indirectly by calculating Ψ and Δ from known values of n and d until the calculated values of Ψ and Δ match the experimental values. tan (Ψ) and exp (Δ) are calculated using Fresnel equations.[18,25,26] Calculations of coating thickness, the phase and amplitude were fit to a Cauchy model to determine the refractive index (n) of the film: $n = A + B/\lambda^2 + C/\lambda^4$, where λ is the wavelength of incident light, and A, B, and C are the fitting parameters.[18,25,26] To calculate n, 600 nm was chosen as the wavelength, A, B, and C were determined from the experimental fit, and n was calculated according to the following equation:

$$n = A + \frac{B}{\lambda^2} + \frac{C}{\lambda^4} \qquad (8)$$

The nominal n value was 2.38 ± 0.13 for all film compositions, similar to those calculated for this coating as well as a different brand (Bonderite T5900) of TCP.[18,25,26] Using the Cauchy model and an initial proposed film thickness, a computer algorithm adjusts the parameters (A, B, C, and d = film thickness) until the lowest mean squared error is attained.

Any statistical differences reported were determined using the two-specimen t-test with a significance level of 0.05. All values are displayed as a mean ± the standard error of the mean for at least 3 specimens and graphed as the mean with error bars.

2.5. Results

2.5.1. Elemental composition of the different coating baths

The TCP coating baths have different chemical compositions as determined by ICP-OES analysis. The results are presented in Figure 2. The analysis was performed on the as-received coating bath solutions that were first diluted to 20 vol. % with ultrapure water followed by a second dilution to 10 vol. % with 0.48 M HNO_3. Quantitation was performed using external standards of each element prepared in the 0.48 M HNO_3. The results in Figure 2 represent the elemental concentrations in the 20 vol. % baths used for all coating applications. The Cr concentration is similar for all three coating baths at ~150 ppm. The nominal Zr concentration in all three baths is higher than the Cr concentration by about a factor of *ca.* 2x. The nominal Zr concentration is slightly greater in the 650 V and C (350 and 340 ppm) than in the 650 E (275 ppm) coating bath. 650 V and C contain significant levels of Zn while the Fe level is greatest in 650 C as compared to 650 E and V.

2.5.2. Surface morphology and chemical composition of the pretreated and conversion coated specimens

Inclusions or constituent particles in AA7075 (Al-Zn-Mg-Cu) can be classified as Fe- and Si-containing.[2, 41] Common particles include binary Al_2Cu and ternary Al_2CuMg phases in addition to Al_7Cu_2Fe, Al_3Fe and Mg_2Si.[2, 41] Figure 3 shows secondary electron SEM micrographs and corresponding EDXS elemental line profiles for the alloy (A) as received, (B) after polishing, (C) after polishing + degreasing and (D) after polishing + degreasing + deoxidation. The AA7075-T6

specimen, as received (no sanding or polishing), displays deep ridges from the rolling process with intermetallic particles (IMPs) distributed across the surface. One is indicated by the IMP marking (Fig. 3A). The corresponding EDXS elemental line profile reveals the presence of three IMPs consisting of Fe with some Cu and Cr. There is also background signal for Mg and Zn present consistent with their presence in the alloy (see Table 1). The image after polishing (Fig. 3B) reveals a considerably smoother surface with a slightly degraded IMP. The EDXS line profile reveals the Cu-Fe IMP in the center of the image. Not apparent in the image is the higher number density of small Cu particles decorating the surface, as compared to the as received panel.

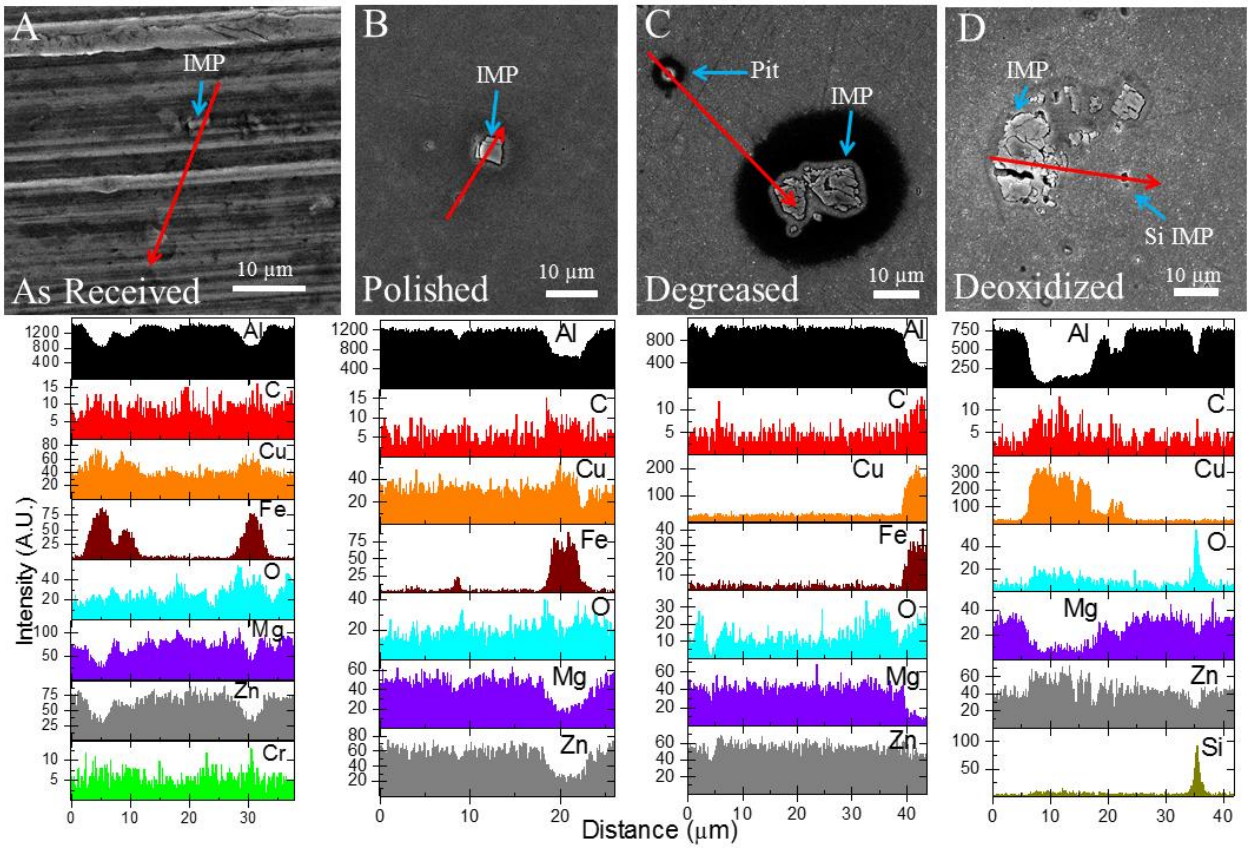

Figure 3. (top) Secondary electron SEM micrographs and (bottom) EDXS elemental line profiles recorded along the red arrows for the AA7075-T6 alloy (A) as received, (B) after polishing, (C) after polishing + degreasing, and (D) after polishing + degreasing + deoxidation. All images are at approximately the same magnification as indicated by the scale bars.

The SEM micrograph taken after polishing + degreasing (Fig. 3C) reveals a smooth surface with a damaged Fe-Cu particle (center) displaying cracks and partially dissolved edges. The SEM micrograph taken after polishing + degreasing + deoxidation (Fig. 3D), shows a greater level surface roughening and pitting after the pretreatment. There are also cracks and evidence for dissolution within the Cu-Zn particle seen in the center of the image. There is also the start of trenching around the IMPs in both images suggesting they are noble in potential relative to the Al matrix.[2, 41d, 42] During solution exposure, attack is mainly at the Al matrix phase and is ascribed to local galvanic attack of the more active matrix by the more noble particles.[2, 41d, 42] The dealloying within the intermetallic leaving behind a Cu-rich phase. EDXS data recorded across the center of the image reveals the large remaining phase is rich in Cu and Zn. There is also a second smaller particle composed of Si and O, likely from the dissolution of Mg from a Mg_2Si particle. The degreasing and deoxidation steps cause morphological and chemical changes on the alloy surface that are important to control for optimum conversion coating coverage. Ideally, one wants to minimize pitting and dissolution/redistribution of Cu particles over the surface during this pretreatment step. The EDXS data reveal the presence of C on all of the specimens particularly around the IMPs. This C likely exists as adsorbed carbonate species on the surface given that there is a general correlation between the C and O signal intensities.

Figure 4 shows (A) a secondary electron SEM micrograph of the conversion-coated alloy, (B) EDXS elemental line profiles recorded along the red arrow that crosses a coating precipitate particle and an IMP and (C) an EDXS spectrum recorded on the Al matrix at the green arrow away from any IMP. X-ray emission lines from the EDXS data (Fig. 4C) are presented for the uncoated or bare (grey shaded area) and the coated (red line) surface. The conversion coating was 650 E and it was spray applied.

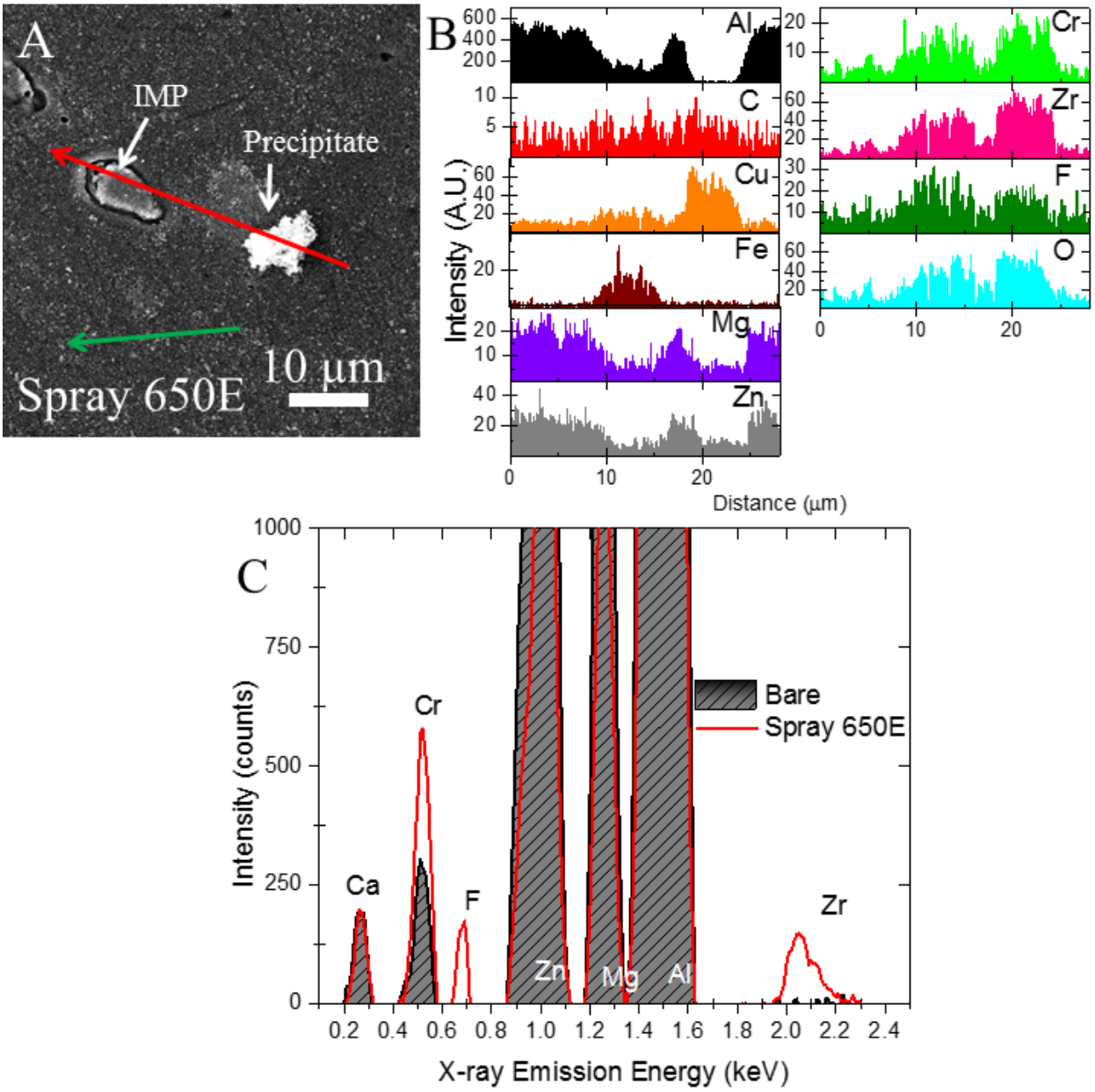

Figure 4. (A) Secondary electron SEM micrograph of the conversion-coated AA7075-T6 alloy. (B) EDXS elemental line profiles taken along the red arrow that crosses a coating precipitate and an intermetallic particle (IMP). (C) X-ray emission data for the uncoated (shaded grey) and conversion-coated (red line) alloy recorded at the green arrow away from any intermetallic particles. The conversion coating was 650 E and it was spray applied.

The SEM micrograph reveals one large IMP near the center-left of the image and a smaller one near the white precipitate (center-right). The white precipitate particle is a constituent of the TCP coating. The surface consists of small (sub-micron), white precipitate particles decorating all

regions of the surface. There is one large aggregate seen in the image that is 5-10 microns in diameter. Such large aggregates are not the norm however. The white coating precipitate particles also decorate the surface of the two IMPs seen in the center of the image. The EDXS elemental analysis data presented in Figure 4B reveal the larger IMP in the center-left of the image consists of Cu-Mg-Zn and the particle nearest the white precipitate is an Fe-Cu phase. The EDXS elemental line profile data also reveal the presence of the coating elements, Zr, Cr, O and F, in the large coating precipitate particle as well as on the surface of the two IMPs. There is clearly some coating enrichment (*i.e.*, greater coating thickness) on and around the intermetallic phases. To verify that the Al matrix was also coated, EDXS spectra were recorded away from any intermetallic phase on the coated and uncoated or bare alloy. A comparison of the emission lines for the coating elements are presented in Figure 4C. The data reveal increased signal intensities for the coating elements, Zr, F and Cr, on the spray-coated panel. Consistent with past results, this sprayed-on conversion coating forms over all regions of the alloy with some enrichment on and around intermetallic phases.[6, 10, 12-14, 16, 22, 39]

Figure 5 shows secondary electron SEM micrographs (top) and associated EDXS elemental data (bottom) for immersion-coated specimens of (A) 650 E, (B) 650 V and (C) 650 C. The formation of the coating is driven by a pH increase at the alloy interface due to the usual cathodic reactions of dissolved oxygen reduction and hydrogen evolution.[6, 10, 12-14, 16, 22, 39]

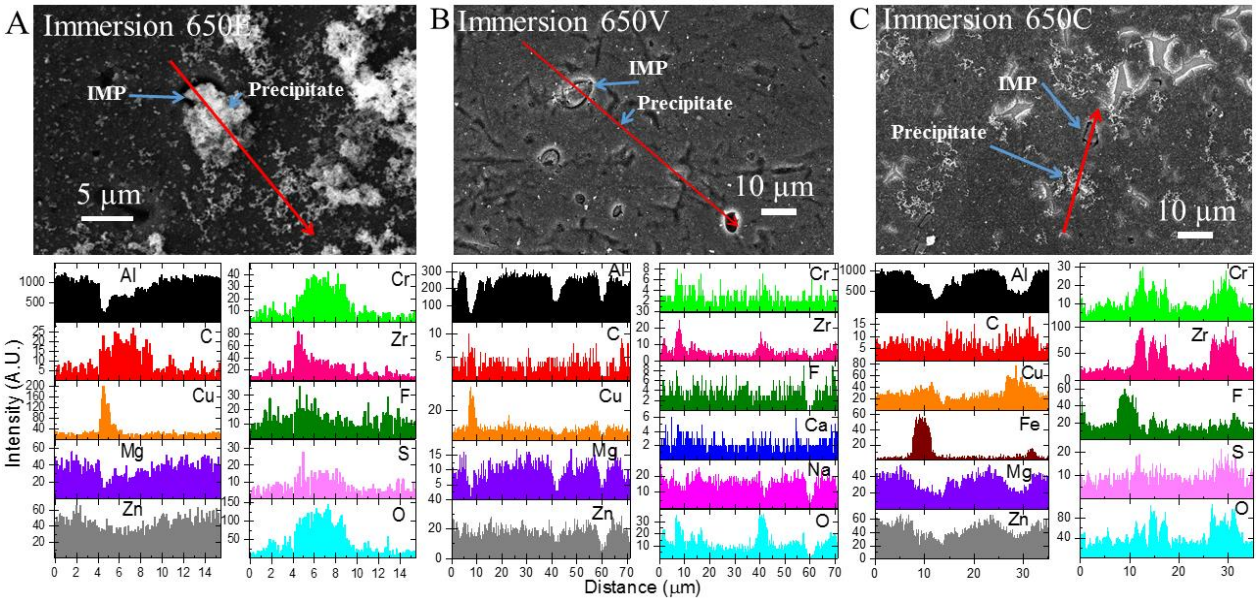

Figure 5. Secondary electron SEM micrographs and EDXS elemental line profile data for immersion-coated AA7075-T6 specimens of (A) 650 E, (B) 650 V and (C) 650 C. The EDXS data were taken along the directional red arrows shown in each image.

There are clear differences in the coating morphology/structure depending on the coating type. The 650 E coating (Fig. 5A) is characterized by small nodular precipitates that decorate the entire alloy surface. There is significant aggregation of coating particles on and around IMPs (*i.e.*, coating enrichment). Based on the distribution of precipitate particles, the coating appears to form over all regions of the surface. The EDXS elemental line profiles, recorded along the red arrow, show the alloy signals for Al, Mg, and Zn, which more or less track each other. This indicates these elements are dispersed within the aluminum matrix. The line profile also crosses a Cu-containing IMP. It is on and around this particle that the coating coverage, as evidenced by the accumulated white nodular features, is high. The coating enhancement around IMPs is likely due to the pH gradient that develops from the reduction of dissolved oxygen at these sites as compared to the surrounding Al matrix.[6, 10, 12-14, 16, 22, 39] The characteristic coating elements are all co-localized: Zr, Cr, O, and F. There is also some C detected, likely from adsorbed carbonate species present on the IMPs.

The 650 V coating (Fig. 5B) has a distinctly different morphology. There are some of the nodular precipitates decorating the surface, but these are fewer in number density than for the 650E coating. The alloy exhibits considerably more damage with numerous pits and what appears to be corrosion channels over the surface. Several IMPs are present in the region shown, each with a corrosion trench around the particle. This trenching occurs during the deoxidation step but also during the immersion coating. The cathodic activity of the Cu-containing IMP for oxygen reduction causes localized oxidation of the nearby Al matrix leading to the trenching.[2, 41b, 41d, 41e, 42b] The coating elements are co-localized: Zr, Cr, F, and O. The signal intensities for these elements are a factor of 10x less than the intensities on the 650E specimen, suggestive of a reduced nominal coating thickness. There are also trace amounts of Ca and Na co-localized with the coating elements. These elements are likely introduced during the final rinse with city tap water.

The 650 C (Fig. 5C) coating appears thicker than the 650 V coating. Evidence for this is the cracking and detachment seen in the center and upper right of the micrograph. The characteristic white coating precipitates decorate the alloy surface. These are far greater in number density than on the 650 V-coated specimen. The EDXS elemental line profile data reveal the metal alloy elements: Al, Mg, and Zn. Closer analysis of the Zn profile also reveals that the signal intensity tracks the signals for Zr and Cr as this coating bath contains Zn, unlike 650E. 650V contains an equivalent level of Zn in the coating bath but, apparently due to the thinness of the coating, was not detected. The line profile crosses two Fe and Cu-containing IMPs. Based on signal intensities, the particle on the lower end of the scan consists of more Fe than Cu, while the opposite is true for the particle on the upper end. There is coating enrichment around the two IMPs: Zr, Cr, Zn, F, and O. S is also co-localized in the coating as is some C. The S likely

originates from sulfate while the C likely comes from carbonate. This coating bath, unlike 650 E, contains relatively high levels of S and Zn (Fig. 2).

Raman imaging spectroscopy was performed on the immersion-coated specimens to probe for chromium species in the coating either as Cr(III)-O (*ca.* 530 cm^{-1}) or Cr(VI)-O (*ca.* 860 cm^{-1}). Raman spectroscopy has revealed the presence of both species in chromate conversion coatings formed on Al alloys, and on Cr(III)-O and transiently formed Cr(VI)-O species in TCP coatings on Al alloys. .[6, 16, 18, 39b] These peaks have been assigned based on the Raman spectra of reference compounds: K_2CrO_4, Cr_2O_3, $Cr(OH)_3$, CrF_3, $Cr_2(SO_4)_3$, and mixed Cr(III)/Cr(VI) oxides.[6, 16, 18, 39b] We previously reported on the transient formation of Cr(VI)-O species in TCP coatings on AA2024-T3, 6061-T6 and 7075-T6 after overnight exposure to the laboratory air[6, 12-13, 39b] Others have published similar findings for the SurTec 650 E coating.[16, 18] The transient formation of Cr(VI)-O species maybe linked to the formation of hydrogen peroxide generated by the reduction of dissolved oxygen at Cu-rich intermetallic sites.[6, 39b] The hydrogen peroxide then oxidizes local Cr(III)-O species in the TCP coating to Cr(VI)-O species according to the following two reactions:

$$O_2 + 2H^+ + 2e^- \rightarrow H_2O_2 \qquad (9)$$

$$3H_2O_2 + 2Cr^{+3} \rightarrow 2Cr^{+6} + 6OH^- \qquad (10)$$

Figure 6 shows characteristic Raman spectra recorded along the indicated line profile for the three SurTec coatings on AA7075-T6. Spectra were recorded with ~0.5 μm spacing along the red arrow in the accompanying optical micrographs. The immersion-coated specimens were aged overnight in the laboratory atmosphere prior to the measurements. The spectra are different for each of the coatings but the mapping indicates the Cr(III) and Cr(VI) oxospecies are localized within the coating. Figure 6A shows data for 650 E. The line profile crosses a white coating precipitate (see Fig. 5A) and at this particle peaks are seen at 543 cm^{-1} and 863 cm^{-1}. These peaks

are associated with the vibrational modes of Cr(III)-OH from $Cr(OH)_3$ and Cr(VI)-O from CrO_4^{2-}.[6, 16, 18, 25, 39b, 43] It is possible that the peak at 543 cm^{-1} could also be associated with Cr(III)-F modes of CrF_3,[18] which may also be a constituent of the TCP coating due to F^- sequestration in the interfacial region.[39a] It has been reported that solid CrF_3 exhibits a strong Raman peak at 538 cm^{-1}.[18] The aggregate particles that are characteristic of this and other TCP coatings consist of $ZrO_2 \bullet nH_2O$, $Cr(OH)_3/CrF_3$ and CrO_4^{2-}, and are present in the coating bath or form as occlusions during the coating precipitation process.[6, 16, 18, 25, 39b, 43] For 650 V (Fig. 6B), there is weak scattering intensity centered at 568 cm^{-1} along most of the length of the line scan. The slight blue shift in this peak from ~540 cm^{-1} could be due to the formation of Cr_2O_3 (Cr(III)-O). In one location, there are also peaks at 790 and 969 cm^{-1}. The 790 cm^{-1} peak is likely a downshifted mode reflective of Cr(VI)-O while the 960 cm^{-1} peak may be reflective of S-O bond from sulfate in the coating.[18] For 650 C (Fig. 6C), the signal-to-noise ratio of the spectral features is considerably lower indicating fewer Cr species in the scattering volume. There is a peak at 539 cm^{-1} with a companion at 882 cm^{-1}. This is likely due to the presence of a mixed Cr(III)/Cr(VI) oxide.[18, 25, 43] The 547 cm^{-1} peak is present along most of the length probed and could be reflective of $Cr(OH)_3$ or CrF_3.

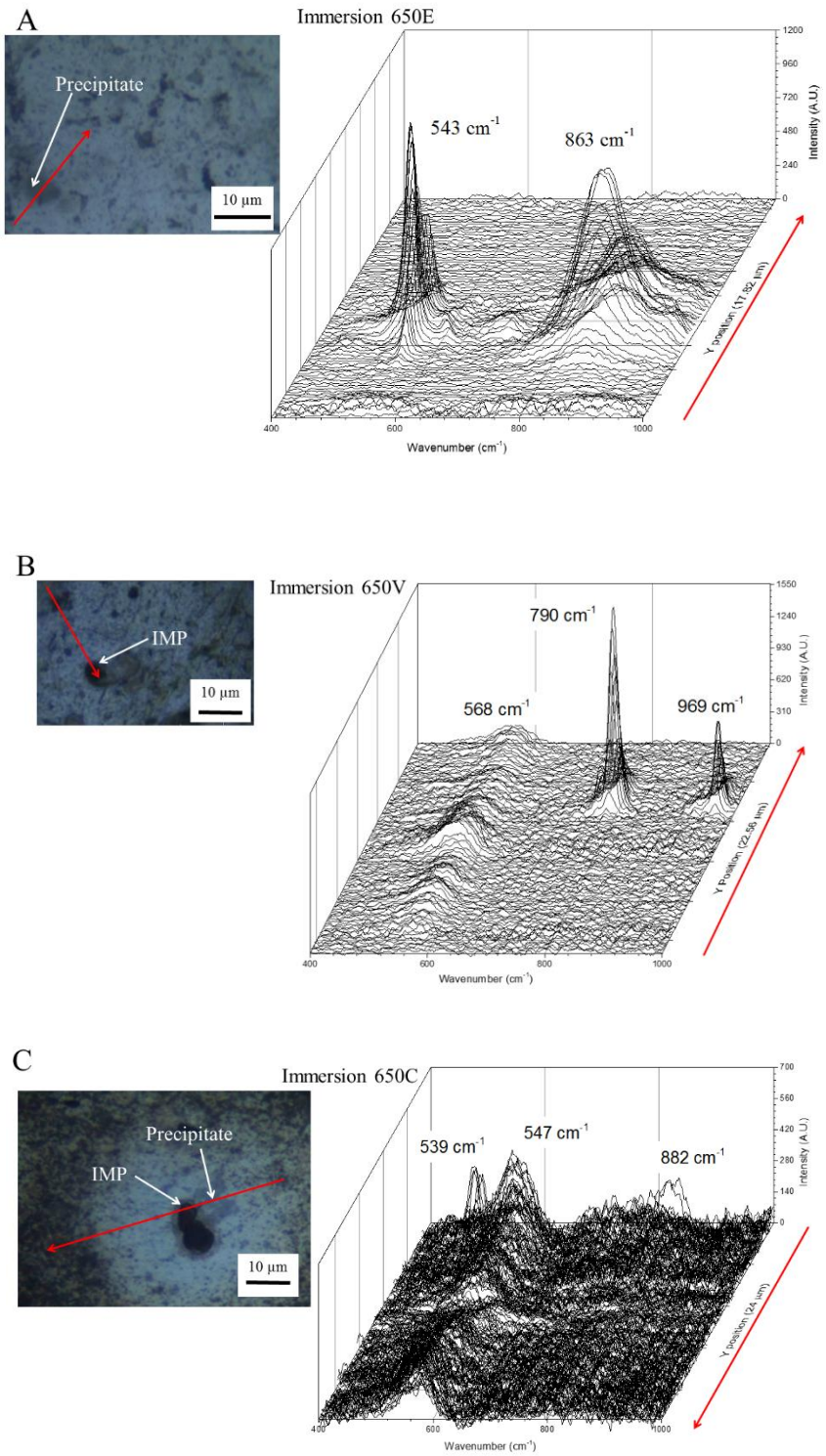

Figure 6. Raman spectroscopy line profile data for immersion-coated specimens (AA7075-T6) of (A) 650 E, (B) 650 V and (C) 650 C. The spectral data were recorded approximately every 0.5 µm along the long red arrow directionally shown in each microscope image. The y-axis length in A is 17.3 µm, B is 22.6 µm and C is 24 µm.

Figure 7 shows secondary electron SEM micrographs and associated EDXS elemental analysis data recorded along the red arrows for spray-coated specimens of (A) 650 E, (B) 650 V, and (C) 650 C.

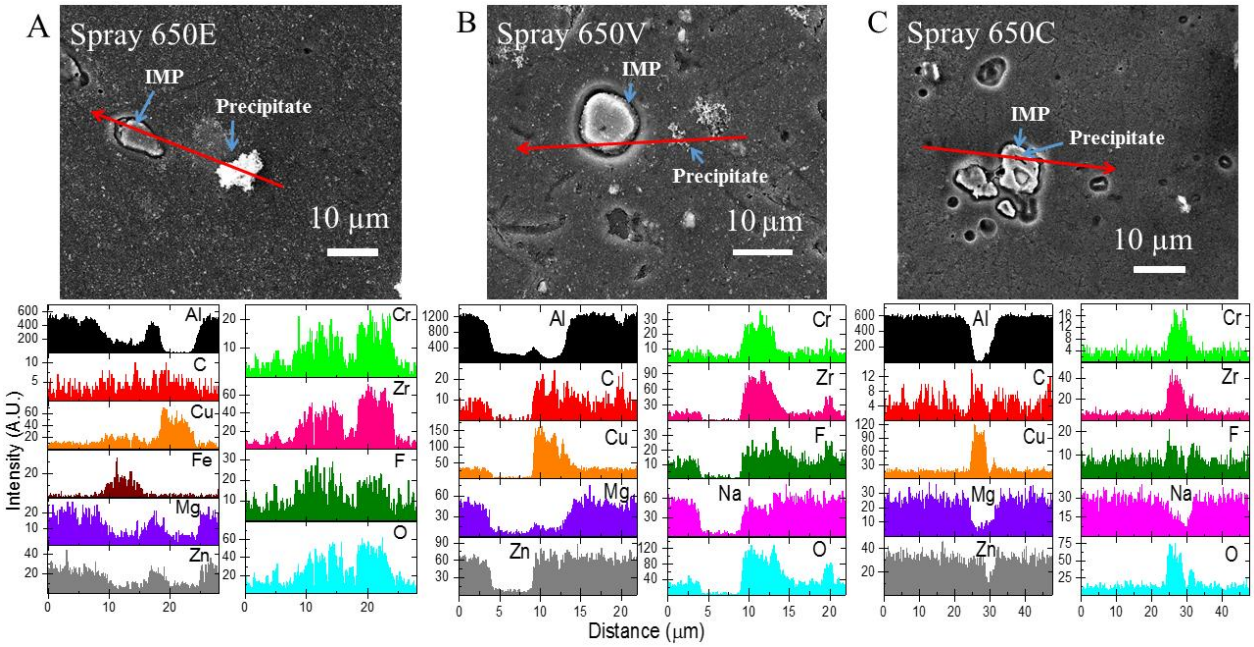

Figure 7. Secondary electron SEM micrographs and EDXS elemental line profile data for spray-coated AA7075-T6 specimens of (A) 650 E, (B) 650 V and (C) 650 C. The EDXS data were recorded directionally along the red line shown in each image.

The first observation is that there is much more pitting and trenching around intermetallic particles for all the sprayed coatings than for the immersion coatings. This is likely due to the thin solution layer for the spray application, which leads to a greater dissolved oxygen flux to the surface as compared to the immersion coating. The higher oxygen flux to the cathodic IMP sites drives the dissolution of the surrounding aluminum matrix.[2, 8-9, 41b, 41d, 41e, 42b] The second observation is the smoothness and homogeneity of the spray coatings as compared to the immersion coatings. The third observation is the relative absence of coating aggregates over the surface as compared to the immersion coatings. The far lower aggregate number for all the spray coated films could lead to better adhesion of primer layers. The coating morphology for 650 E and

C is distinctly different from their immersion counterparts. The 650 E coating (Fig. 7A) is characterized by the nodular precipitates decorating the surface, but these are far lower in number density than for the immersion-coated specimen. There is one large coating aggregate (white precipitate) particle in the center of the image. Several intermetallic phases are visible, two in the center of the image, and they are not as covered by the coating as they tend to be for the immersion-coated 650 E, specifically the nodular precipitates. The EDXS line profile data reveal the alloy elements (Al, Mg, Zn) and the coating elements (Zr, Cr, O, F) that are co-localized around the IMP and precipitate particle in the image. The particle labeled IMP is Fe-rich and the particle adjacent to the precipitate is Cu-rich. The coating elements (Zr, Cr, F and O) are all enriched around these sites. The 650 V spray-coated specimen (Fig. 7B) is characterized by a thin coating with a lower number of precipitate particles across the surface. The EDXS line profile indicates a co-localization of the coating elements (Zr, Cr, O, F) around the Cu-Zn IMP and a few visible precipitate particles in the center of the image. The 650 C spray-coated specimen (Fig. 7C) shows little to no visible coating precipitates on the aluminum or IMPs. Despite the limited visual indication of a coating, the EDXS data revealed the coating elements (Zr, Cr, O F) to be co-localized on and around the intermetallic particles in the center of the image. Surprisingly, there is no Zn detected in the 650 C and V coatings even though this element is present in the coating baths.

The spray-on coatings produce Raman spectral features in the 400-1000 cm^{-1} range that are different from was is seen for the immersion coatings. Figure 8A-C shows spectra for 650 E, V and C conversion coatings. For 650 E (Fig. 8A). Raman peaks are seen at 534, 788 and 963 cm^{-1}

for an aggregate of coating particles covering an intermetallic particle. The 534 cm^{-1} peak is attributed to Cr(III)-O as $Cr(OH)_3$. The peak at 788 cm^{-1} is due to Cr(VI)-O in an Al(III)/Cr(VI)

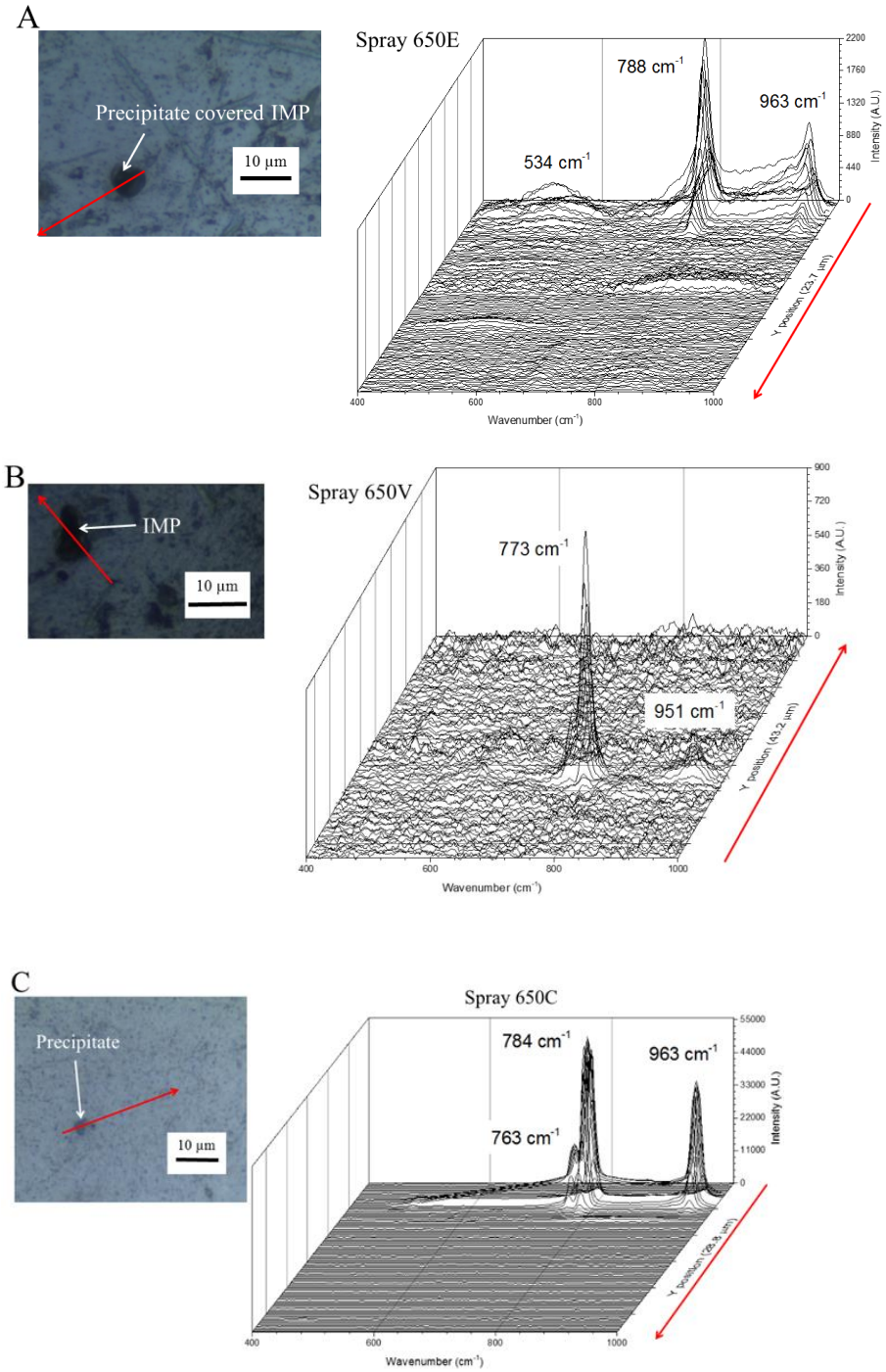

Figure 8. Raman spectroscopy line profile data for spray-coated specimens (AA7075-T6) of (A) 650 E, (B) 650 V and (C) 650 C. The spectral data were measured every *ca.* 0.5 µm along the red arrow directionally shown in each micrograph.

mixed oxide.[25, 39b, 43c] The Cr(VI)-O peak position shifts toward lower energy with increasing pH.[39b] The 963 cm^{-1} was not detected on the immersion coating and its origin is a bit unclear. Qi et al. have reported the presence of this peak in Raman spectra recorded for 650 E and have attributed this peak to S-O modes of sulphate possibly as $Fe_2(SO_4)_3$ or $Cr_2(SO_4)_3$ in the coating.[18] The Raman spectra for 650 V and C showed no evidence for any Cr(III)-O modes and only peaks at 770-790 cm^{-1} and 950-965 cm^{-1}.

2.5.3. TCP Coating Composition with Depth, Wettability and Thickness

Auger electron spectroscopy (AES) depth profiling was performed on the immersion- and spray-coated 650 E specimens to investigate the coating chemical composition with depth. Representative data are presented in Figure 9A and B.

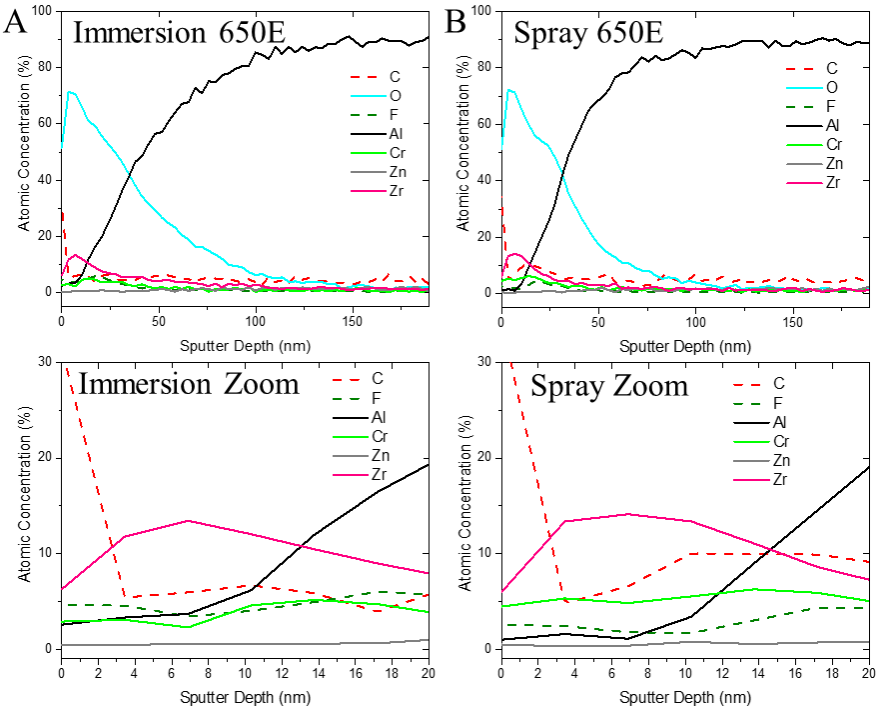

Figure 9. Auger electron spectroscopy depth profiles for AA7075-T3 specimens (A) immersion-coated and (B) spray-coated with 650 E. The top panels show full depth profiles while the bottom panels show expanded scale profiles over the top 20 nm of sputtering depth. The depth profiling was performed with Ar^+ at 10 keV. The sputter depth information is approximate as it is based on an Ar^+ sputter rate 6.2 nm/min for Ta_2O_5.

The measurement probes both the coating composition and the near-surface region of the Al alloy. We use the depth at which the Al signal reaches a constant value as the apparent coating thickness. Based on this, the immersion coating is *ca.* 100 nm thick while the spray coating is thinner at *ca.* 50 nm. This is in qualitative agreement with the SEM images for the two coated specimens (*vide supra*) and ellipsometry data (*vide infra*). The O signal decays to near zero at these same depths. Profiles for the primary coating elements (Zr, Cr, O, F) are shown. It can be seen that the Zr reaches a maximum concentration of 15 at. % in both coatings in the outer 30 nm. The concentration decays with further depth into the coating. Cr reaches a maximum concentration of 5 at. % in both coatings in the center 30 nm. There is an interfacial region in the 30-100 nm range where Al-O-F exists with some Zr. This interfacial region has been proposed previously.[5-6, 10-12, 16, 29, 39a] The F concentration increases slightly with depth for both coatings in the range from 3-6 at. % consistent with some sequestration in the interfacial region. Signals for S or Fe were not recorded. Overall, the results indicate that the elemental composition with depth is similar for both application methods. The spray-coated film (3 min) is thinner than the immersion-coated film (4 min). Both have an interfacial region rich in Al, O and F.

Figure 10 presents static water contact angles measured on (A) uncoated and immersion-coated and (C) uncoated and spray-coated specimens. The data were recorded over a 7-day period of aging after coating formation. The aging was performed in the open laboratory atmosphere.

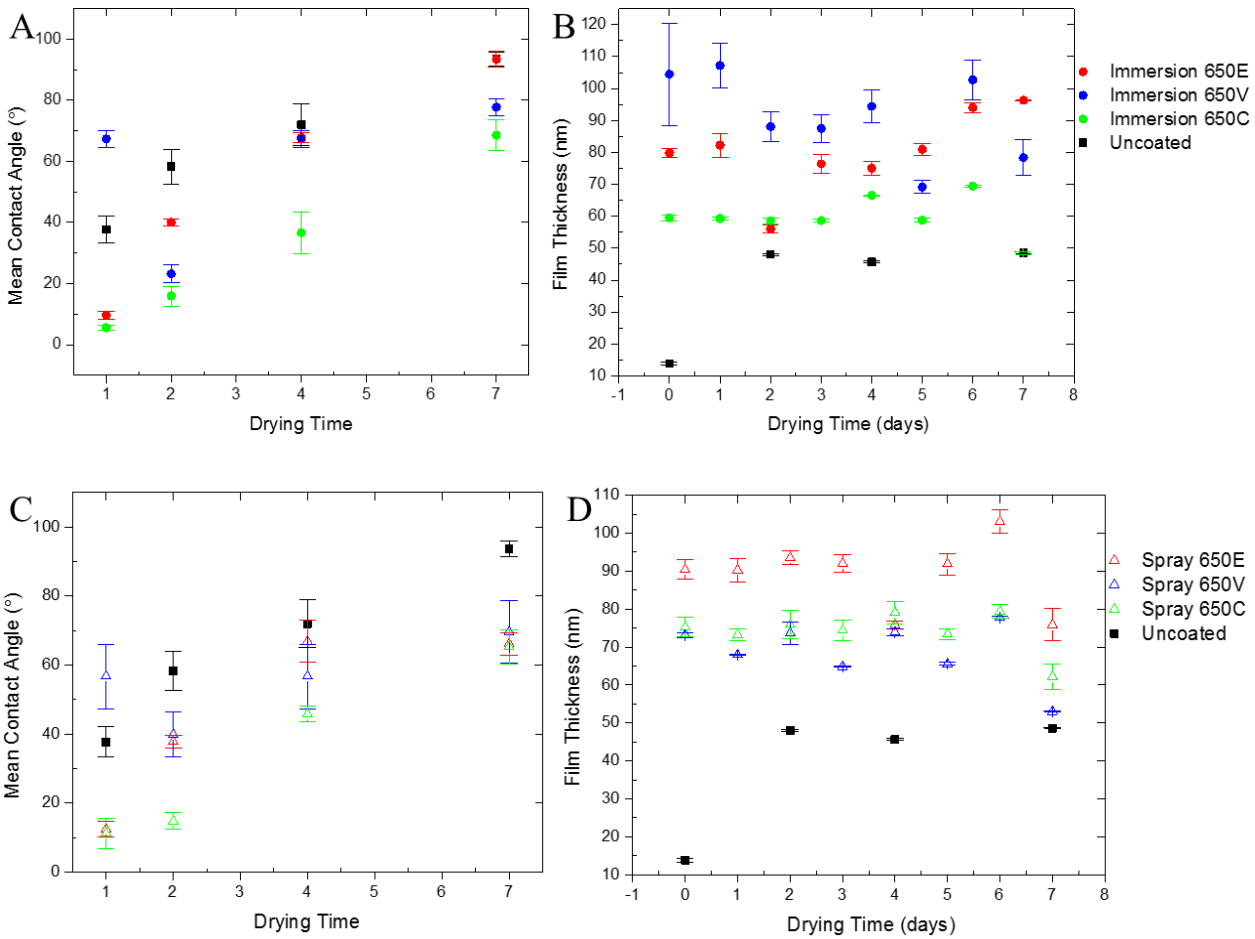

Figure 10. Static water contact angles on (A) immersion-coated and (C) spray-coated 650 E (red), 650 V (green), 650 C (blue), and uncoated (black) specimens. Film thickness, as determined from open air ellipsometry, for (B) immersion-coated and (D) spray-coated specimens. The results are presented over a 7-day period of aging in the open laboratory atmosphere. Data are presented as mean ± standard error of the mean, n ≥3.

Overall, the average of the leading and trailing edge contact angles (n ≥ 3) increased with aging time, consistent with the coating surface becoming progressively more hydrophobic. This is consistent with a changing surface chemistry over time. For both the immersion and spray coatings, 650 E and 650 C are quite hydrophilic (θ ~10°) at day 1, more so than 650 V (θ ~ 60-80°). There may be more organic content (*e.g.*, surfactants) or complexing agents in 650 V, which would explain the more hydrophobic character. All the coatings become progressively more hydrophobic with aging time, as evidenced by the trend of increasing contact angle. This trend has

been observed before for other TCP coatings on aluminum alloys.[13] At day 7, the most hydrophobic coating is 650 E formed by immersion. The other two coating exhibit contact angles in the 60-80° range. After 7 days, all three spray coatings have contact angles in the 60-80° range. The contact angle for an uncoated specimen (degreased and deoxidized AA7075-T6) was measured over the same time period as a control. The uncoated alloy becomes progressively more hydrophobic with aging time due to the formation of a passivating oxide layer. Some of the hydrophobic character may result from the adsorption of hydrocarbon contaminants in the laboratory air as there is carbon on the coating surface as evidenced in the AES depth profiles and EDXS elemental analysis.

The coating thickness was measured by ellipsometry (open air) and the results are presented for (B) immersion-coated and (D) spray-coated specimens. Generally, the coating thicknesses are relatively constant over the 7-day aging period. 650 E is the thickest of the coatings after the 7-day period when formed by both methods. At the 7-day point the mean thickness is 95 nm for the immersion coating and 75 nm for the spray-coating. The 95 nm is consistent with the thickness of this same SurTec coating[5, 11] on aluminum and Bonderite T5900 (Henkel) on AA2024-T3.[13] This is in contrast to the densification and thinning of Bonderite T5900 over the same time period.[13] The immersion-coated 650 E, C and V film thickness ranges from 80-100, 50-70 and 75-105 nm, respectively. At the 7-day point, the final mean thicknesses are 95, 50 and 75 nm for 650 E, C and V, respectively. For the spray coatings, the final mean thickness at the 7-day point was 75, 62 and 53 nm, respectively, for 650 E, C and V. The spray coating thicknesses are somewhat constant over the drying period but decrease in thickness on day 7. Overall, the thicknesses of the spray-coated films (3 min) is less than the immersion-coated films (4 min).

2.6. Discussion

The three most notable differences between the immersion and spray-on coatings are: (i) the much lower number of coating aggregate particles on the spray coatings, (ii) the smoother morphology for the spray coatings and (iii) the greater pitting and alloy surface damage for spray-coated specimens. Overall, the chemical composition and the elemental distribution of the primary coating elements is similar for all three TCP coatings applied by the two methods.

The major differences in the coating bath compositions, as determined from ICP-OES analysis, are (i) Zr/Cr levels are greater in 650 V and C, as compared to 650 E, (ii) 650 E contains undetectable levels of Zn while 650 V and C contain 350-450 ppm, (iii) the level of S, likely as sulfate as part of a chromium sulfate salt, in 650 E is 2-3x lower than the levels in 650 V and C, and (iv) the concentration of Fe (sub ppm) in 650 E and V is 2x lower than the level in 650 C. The reason for the added Fe is unclear. There is no detectable Ca or Mg in any of the coating baths. The higher concentrations of Zn in 650 V and C are supposed to be primarily for coating coloration. Based on discussions with the supplier, 650 V and C contain additional complexing agents that aid in the coloration. We did not measure the organic content in the coating baths. The 650 E has a chemical composition that most closely resembles the original NAVAIR TCP formulation.

The SEM and EDXS analysis reveal that all three conversion coatings form over all regions of the alloy surface with some coating thickening on and around intermetallic phases. The coating thickening is particularly true for 650 E formed by immersion. This coating consists of colloidal aggregates that are composed of Zr and Cr, based on EDXS analysis. Raman spectroscopy revealed that precipitates often contain a mixture of Cr(III)-O ($Cr(OH)_3$) and transiently formed Cr(VI)-O (CrO_4^{2-}) species. These aggregates may be occlusions that form during the coating precipitation process or pre-existing colloidal particles in the coating bath. It has been reported that $Zr(OH)_4$

(hydrated zirconia) can form stable mono-disperse colloidal particles in the pH 3-4 range.[19,43] Recall the pH of the coating baths is 3.85. The number density of these aggregates on the coated panels is greatest for 650 E and C. Very few are detected on the 650 V-coated surface. The conversion coating is primarily hydrated zirconia with localized regions of $Cr(OH)_3$ and transiently formed Cr^{+6} oxide. The also tends to be some sequestered fluoride within the coating, likely as part of a fluoroaluminate interfacial layer, such as $KAlF_4$.[6, 12] Based on the weaker EDXS signal intensities for the primary coating elements (Zr, Cr, O and F) for 650 V, this coating is thinner than the other two. This may be due to slower precipitation kinetics in this coating bath. One reason for this could be that the interfacial pH increase during the coating formation process is not as alkaline for this coating as it is for the other two.[22] The rate of hydrated zirconia precipitation strongly depends on the solution pH.[44] The coating formation kinetics were not investigated in this work. Cracking and delamination were observed for 650 C, something that has been reported before for 650 E.[10] Cracking or peeling was not observed on any of the 650 E-coated panels used in this work.

The spray-coated 650 E and V films are characterized by the presence of the aggregate particles decorating the alloy surface. There are very few aggregates in the 650 C coating. The presence of these apparently loosely bound aggregates may negatively impact primer adhesion. This remains to be studied. Overall, the number density of these particles is far lower on the spray-coated than on the immersion-coated films for all three variants. The primary coating elements are detected over all regions of the panel; on and around intermetallic phases and the surrounding aluminum matrix. A significant difference in the alloy surface between the two methods is the greater level of pitting and trenching around intermetallic particles seen after spray-coating. This is attributed to the thinner solution layer that results in a higher flux of dissolved oxygen to the

surface, particularly the cathodically-active intermetallic compounds. This should be considered when using spray application methods. Longer coating times may result in increased pitting and damage to the alloy surface and this could negatively impact the anti-corrosion properties of the conversion coating. The coating formation in both application methods is driven by a pH increase near the electrode surface due to activation of the aluminum (dissolution of the surface oxide layer) in the acidic fluoride bath and cathodic reactions that occur on the intermetallic compounds (dissolved oxygen reduction) and the activated aluminum (dissolved oxygen reduction and hydrogen evolution). The kinetics of dissolved oxygen reduction are expected to be more rapid at the Cu-rich intermetallic phases and this is expected to produce a more alkaline pH gradient in these regions. This is likely the reason for the increased coating thickness on and around these particles.

The AES profiling data reveal similar chemical compositions for both the immersion and spray coatings (650 E) with depth. The conversion coating (650 E) formed by both methods has a biphasic chemical composition with an outer layer rich in Zr and Cr and an interfacial layer that contains Al, O and F with some Cr. This same biphasic structure has been reported previously for this (650 E)[19,20] and other TCP conversion coatings on aluminum alloys.[12,16] The maximum Zr/Cr atomic ratio in both coatings is 3:1. This ratio is slightly larger than the ratio in the coating bath, ~2:1. This difference could be due to more rapid precipitation kinetics for hydrated zirconia ($ZrO_2 \bullet nH_2O$ or $Zr(OH)_4$) as compared to $Cr(OH)_3$. All three coatings were generally found to become more hydrophobic with aging time in air, presumably due to dehydration. This dehydration may produce a change in the molecular structure of the coating from $Zr(OH)_4$ to ZrO_2. Such a structural change would reduce the number of adsorbed water molecules and terminal OH functionalities to hydrogen bond with water. This trend of increasing hydrophobicity with aging

time is consistent with what has been reported for other (Bonderite T5900) TCP coatings.[18] The increased hydrophobicity may be an important issue to consider when priming these surfaces as changing surface wettability with time could affect aqueous-based primer adhesion.

Ellipsometry revealed the 650 E coating formed by immersion is *ca.* 95 nm thick for a 4-min (240 s) immersion. This is in good agreement with the thicknesses reported by others for this conversion coating on aluminum[25,26] and aluminum alloy.[45] This is also consistent with the *ca.* 100 nm thickness reported for Bonderite T5900 TCP on aluminum alloy.[18] The immersion-coated 650 E, C and V film thickness ranges from 80-100, 50-70 and 75-105 nm, respectively over a 7-day period of aging. At the 7-day point, the final mean thickness was 95, 50 and 75 nm for 650 E, C and V, respectively. For the spray coatings, the final mean thickness at the 7-day point was 75, 62 and 53 nm, respectively, for 650 E, C and V. The spray coating thicknesses are relatively constant over the drying period with a decrease seen on day 7. Overall, the thicknesses of the spray-coated films (3 min) is less than the immersion-coated films (4 min). No inferences can be made about the defect density or the micro-/nanoporosity of the different coatings from the data in hand. It is known that the molecular structure of precipitated zirconia depends on the solution pH.[44]

Finally, Raman spectroscopy provides evidence for the presence of localized Cr(III)-O and transiently formed Cr(VI)-O species in the coatings. For the three different TCP variants formed by immersion, the data clearly reveal the presence of localized Cr(III) and Cr(VI) species. For 650 E, there isolated regions in the coating where peaks at 543 and 863 cm^{-1} are co-localized. This is the case for the nodular precipitate particles that decorate the surface. For 650 V, there are larger regions in the coating where scattering at 568 cm^{-1} is detected along with peaks at 568, 790 and 969 cm^{-1}. Examples can be found where the co-localization of these bands is seen on and around intermetallic particles. For 650 C, the signal-to-noise ratio of the spectra is lower than that for 650

E and V due to its thinner nature. The coating is characterized by extended regions of scattering at 547 cm^{-1} on both the aluminum matrix and around intermetallic particles.

The results indicate that the coatings contain Cr(III)-O species as well as isolated regions of transiently formed Cr(VI)-O species. Although the equilibrium distribution of different Cr(VI)-O species, CrO_4^{2-}, $HCrO_4^-$ and $Cr_2O_7^{2-}$, is complex and depends on the local pH, the Cr(VI)-O bands are positioned in the 840–904 cm^{-1} range, which easily distinguishes them from the Cr(III)-O bands in the range of 520–580 cm^{-1}.[12,15,45,46] Reference spectra for Cr_2O_3 and $Cr(OH)_3$ exhibit peaks at 536 and 526 cm^{-1}, respectively. These two Cr(III) species have indistinguishable spectral features. The difference in band shape and peak position is due to differential states of hydration (*i.e.*, bond length).[15,37,38,47,48] CrF_3 exhibits scattering near 547 cm^{-1} so the low frequency mode could reflect the presence of $Cr(OH)_3$ as well as CrF_3.[36] In summary, the Cr(III) species is $Cr(OH)_3$ and the transiently formed Cr(VI) species is likely CrO_4^{2-} or $HCrO_4^-$.

The Raman spectral features are a little different for the spray-on coatings. Spectra obtained from the aggregate particles in 650 E, which are normally concentrated on and around intermetallic phases, exhibited bands at 534, 788 and 963 cm^{-1}. The 534 cm^{-1} peak is attributed to Cr(III)-O and the 788 cm^{-1} peak is ascribed to Cr(VI)-O as part of a mixed Al(III)/Cr(VI) mixed oxide.[49] The Cr(VI)-O mode in this mixed oxide shifts to lower energy with increasing solution pH.[15] The origin of the band at 963 cm^{-1} has not been conclusively established yet. It is present in all of the TCP coating variants formed by spray. Qi et al. have reported the presence of this peak in Raman spectra recorded for 650 E and have attributed it to S-O modes of sulphate possibly as $Fe_2(SO_4)_3$ or $Cr_2(SO_4)_3$ in the coating.[36] The Raman spectra for 650 V and C showed no evidence for any Cr(III)-O modes and only peaks at 770-790 cm^{-1} and 950-965 cm^{-1}.

2.7. Conclusions

Three different TCP coating variants (SurTec 650 E, V and C) formed by immersion and spray on AA7075-T6 were characterized for morphology, coating chemistry, film thickness, and hydrophobicity. The following are the key findings:

1. The Cr concentration is similar for all three coating baths at ~150 ppm. The nominal Zr concentration in all three baths is higher than the Cr concentration by about a factor of *ca.* 2x. The nominal Zr concentration is slightly greater in 650 V and C (350 and 340 ppm) than in 650 E (275 ppm). 650 V and C contain significant levels of Zn while the Fe level is greatest in 650 C as compared to 650 E and V.

2. The conversion coatings (immersion or spray) form over all regions of the alloy surface with some thickening on and around intermetallic particles. Based on EDXS elemental signal intensities, greater coating thickness is observed for 650E and C. The 650 C coating is characterized by cracks and delamination while the other two are devoid of these defects.

3. Conversion coatings formed by spray are characterized fewer coating aggregate particles that their immersion-coated counterparts. A significant difference is the increased alloy pitting and trenching around intermetallic particles when the coatings are spray applied. Care should be taken regarding the duration of the formation process when applying these conversion coatings by spray.

4. AES depth profiling indicates the 650 E conversion coating (immersion and spray) consists of a biphasic structure. An outer layer (30-50 nm) exists that is rich in Zr and Cr. There is also an interfacial region (~50 nm) rich in Al, O, F and some Cr. The maximum Zr/Cr atomic concentration ratio is *ca.* 3:1 in the coatings.

5. The conversion coatings (immersion or spray) become more hydrophobic over a 7-day aging period in the laboratory air. For both the immersion and spray-on coatings, 650 E and 650 C are quite hydrophilic ($\theta \sim 10^o$) at day 1, more so that 650 V ($\theta \sim 60\text{-}80^o$). Static water contact angles at day 7 are $60\text{-}90^o$ for all the coatings.

6. Ellipsometry data indicate 650 E is the thickest of the three coatings. At the 7-day point, the final mean thicknesses of the immersion coatings are 95, 50 and 75 nm for 650 E, C and V, respectively. For the spray coatings, the final mean thickness at the 7-day point was 75, 62 and 53 nm, respectively, for 650 E, C and V.

7. Raman spectroscopic imaging reveals the presence of localized regions of Cr(III)-O species (*e.g.*, $Cr(OH)_3$) with some of these regions also containing transiently-formed Cr(VI)-O species (*e.g.*, CrO_4^{2-}, $HCrO_4^-$). The Cr(III)/Cr(VI) species are often present in the coating aggregate particles that decorate the surface and the intermetallic particles. These particles are potential reservoirs of Cr(VI).

REFERENCES

REFERENCES

Reprinted from Surface & Coatings Technology, 315, Catherine A. Munson, Greg M. Swain, Structure and chemical composition of different variants of a commercial trivalent chromium process (TCP) coating on aluminum alloy 7075-T6, 150-162, Copyright (2017), with permission from Elsevier.

1. J. LaScala, Non-chromate/No-VOC coating systems for DoD applications, (WP-1521), Final Report, SERDP, **2009.**

2. M. Costa, Toxicity and Carcinogenicity of Cr(VI) in Animal Models and Humans. *Critical Rev. Toxicol.* **1997**, *27*, 431-442.

3. S. Mishra and R. N. Bharagava, Toxic and genotoxic effects of hexavalent chromium in environment and its bioremediation strategies. *J. Environ. Sci. Health C. Environ. Carcinog. Ecotoxicol. Rev.* **2016**, *34*, 1-32.

4. R. L. Twite and G. P. Bierwagen, Review of alternatives to chromate for corrosion protection of aluminum aerospace alloys. *Prog. Org. Coat.* **1998**, *33*, 91-100.

5. M. W. Kendig and R. G. Buchheit. Corrosion inhibition of aluminum and aluminum alloys by soluble chromates, chromate coatings, and chromate-free coatings. *Corrosion* **2003**, *59*, 379 -400.

6. H. Guan and R. G. Buchheit. Corrosion protection of aluminum alloy 2024-T3 by vanadate conversion coatings. *Corrosion* **2004**, *60*, 284-296.

7. C. A. Matzdorf, W. C. Nickerson, Jr., E. N. Beck, A. S. Schwartz and J. L. Green, U.S. Patent Application Publication, *Non-Chromium Coatings for Aluminum*, US2007/0095436 A1, **May 3, 2007**.

8. L. Li, B. W. Whitman, C. A. Munson, R. Estrada, C. A. Matzdorf and G. M. Swain. Structure and corrosion performance of a non-chromium process (NCP) Zr/Zn pretreatment conversion coating on aluminum alloys. *J. Electrochem. Soc.* **2016**, *163*, C1-11.

9. S. L. Suib, J. LaScala, W. Nickerson, A. Fowler and N. Zaki, Determination of hexavalent chromium in NAVAIR trivalent chromium process (TCP) coatings and process solutions, *Metal Finishing* **2009**, *107*, 28, 31-34.

10. A. Iyer, W. Willis, S. Frueh, W. Nickerson, A. Fowler, J. Bames, L. Hagos, J. Escarsega, J. La Scala and S.L. Suib. Characterization of NAVAIR trivalent chromium process (TCP) coatings and solutions, *Plat. and Surf. Fin.*, **2010,** *5*, 32-42.

11. X. C. Dong, P. Wang, S. Argekar and D. W. Schaefer. Structure and composition of trivalent chromium process (TCP) films on Al alloy, *Langmuir* **2010**, *26*, 10833-10841.

12. L.L. Li, G. P. Swain, A. Howell, D. Woodbury and G. M. Swain. The formation, structure, electrochemical properties and stability of trivalent chromium process (TCP) coatings on AA2024, *J. Electrochem. Soc.* **2011**, *158*, C274-283.

13. Y. Guo and G. S. Frankel. Characterization of trivalent chromium process coating on AA2024-T. *Surf. Coat. Technol.* **2012,** *206*, 3895-3902.

14. Y. Guo and G. S. Frankel. Active corrosion inhibition of AA2024-T3 by trivalent chrome process treatment, *Corrosion* **2012**, *68*, 045002-1-045002-10.

15. L. L. Li, D. Y. Kim and G. M. Swain. Transient formation of chromate in trivalent chromium process (TCP) coatings on AA2024, *J. Electrochem. Soc.* **2012**, *159*, C326-C333.

16. L. L. Li and G. M. Swain, Formation and structure of trivalent chromium process coatings on aluminum alloys 6061 and 7075, *Corrosion*, **2013**, *69*, 1205-1219.

17. L. L. Li, K. P. Doran and G. M. Swain. Electrochemical characterization of trivalent chromium process (TCP) coatings on AA6061 and 7075, *J. Electrochem. Soc.* **2013**, *160*, C396-C401.

18. L. L. Li and G. M. Swain. Effects of aging temperature and time on the corrosion protection provided by trivalent chromium process coatings on AA2024-T3. *ACS Appl. Mater. Interfaces* **2013**, *5*, 7923-7930.

19. J. T. Qi, T. Hashimoto, J. R. Walton, X. Zhou, P. Skeldon and G. E. Thompson. Trivalent chromium conversion coating formation on aluminum, *Surf. Coat. Technol*. **2015**, *280*, 317-329.

20. J. Qi, T. Hashimoto, J. Walton, X. Zhou, P. Skeldon and G. E. Thompson. Formation of a trivalent chromium conversion coating on AA2024-T351 alloy, *J. Electrochem. Soc*. **2016,** *163*, C25-C35.

21. J. Qi, T. Hashimoto, G. E. Thompson and J. Carr. Influence of water immersion post-treatment parameters on trivalent chromium conversion coatings formed on AA2024-T351 alloy, *J. Electrochem. Soc.* **2016**, *163*, C131 -138.

22. Z. Feng, G. S. Frankel and C. A. Matzdorf. Quantification of accelerated corrosion testing of coated AA7075-T6, *J. Electrochem. Soc.* **2014**, *161*, C42-C49.

23. Z. Feng, J. Boerstler, G. S. Frankel and C. A. Matzdorf. Effect of surface pretreatment on galvanic attack of coated Al alloy panels, *Corrosion* **2015**, *71*, 771-783.

24. J. R. Davis, International, A. S. M.; Handbook, C. *Aluminum and aluminum alloys*. ASM International: Materials Park, Ohio, 1994.

25. S. Dardona and M. Jaworowski. In situ spectroscopic ellipsometry studies of trivalent chromium coating on aluminum, *Appl. Phys. Lett.* **2010**, *97*, 181908-1 – 181908-3.

26. S. Dardona, L. Chen, M. Kryzman and M. Jaworowski. Polarization controlled kinetics and composition of trivalent chromium process coatings on aluminum, *Anal. Chem.* **2011**, *83*, 6127-6131.

27. M. Gao, C. R.Feng and R. P. Wei. An analytical electron microscopy study of constituent particles in commercial 7075-T6 and 2024-T3 alloys, *Metall. Mater. Trans. A* **1998**, *29*, 1145-1151.

28. N. Birbilis and R. G. Buchheit. Electrochemical characteristics of intermetallic phases in aluminum alloys - An experimental survey and discussion. *J. Electrochem. Soc.* **2005**, *152*, B140-B151.

29. N. Birbilis, M. K.. Cavanaugh and R. G. Buchheit. Electrochemical behavior and localized corrosion of Al_7Cu_2Fe particles in aluminum alloy 7075-T651, *Corros. Sci.* **2006**, *48*, 4202-4215.

30. S. Dey, M. K. Gunjan and I. Chattoraj. Effect of temper on the distribution of pits in AA7075 alloys, *Corros. Sci.* **2008**, *50*, 2895-2901.

31. R. G. Buchheit and N. Birbilis. Electrochemical microscopy: An approach for understanding localized corrosion in microstructurally complex metallic alloys, *Electrochim. Acta* **2010**, *55*, 7853-7859.

32. S. S. Singh, E. Y. Guo, H. X. Xie and N. Chawla. Mechanical properties of intermetallic inclusions in AA7075 alloys by micropillar compression, *Intermetallics* **2015**, *62*, 69-75.

33. G. S. Frankel, *2015 W.R. Whitney Award Lecture:* The Effects of Microstructure and Composition on Al Alloy Corrosion, *Corrosion* **2015,** *71*, 1308-1320.

34. N. Birbilis and R. G. Buchheit. Investigation and discussion of characteristics for intermetallic phases common to aluminum alloys as a function of solution pH, *J. Electrochem. Soc.* **2008**, *155*, C117-C126.

35. L. Li, A. L. Desouza and G. M. Swain. In situ pH measurement during the formation of conversion coatings on aluminum alloy (AA2024), *Analyst*, **2013**, *138*, 4398-4402.

36. J. Qi, J. Walton, G. E. Thompson, S. P. Albu and J. Carr. Spectroscopic studies of chromium VI formed in the trivalent chromium conversion coatings on aluminum, *J. Electrochem. Soc.*, **2016**, *163*, C357-C363.

37. B. M. Weckhuysen and I. E. Wachs. In situ raman spectroscopy of supported chromium oxide catalysts: reactivity studies with methanol and butane, *J. Phys. Chem.*, **1996**, *100*, 14437-14442.

38. B. L. Hurley and R. L. McCreery. Raman spectroscopy of monolayers formed from chromate corrosion inhibitor on copper surfaces, *J. Electrochem. Soc.* **2003**, *150*, B367-B373.

39. L. Xia and R. L. McCreery. Chemistry of a chromate conversion coating on aluminum alloy AA2024-T3 probed by vibrational spectroscopy, *J. Electrochem. Soc.* **1998**, *145*, 3083-3089.

40. J. D. Ramsey and R. L. McCreery. Raman microscopy of chromate interactions with corroding aluminum alloy 2024-T3, *Corros. Sci.*, **2004**, *46*, 1729-1739.

41. Z. Feng, J. Boerstler, G. S. Frankel and C.A. Matzdorf. Effect of surface pretreatment on galvanic attack of coated Al alloy panels, *Corrosion* **2015**, *71*, 771-783.

42. Z. Feng, G.S. Frankel and C.A. Matzdorf. Quantification of accelerated corrosion testing of coated AA7075-T6, *J. Electrochem. Soc.* **2014,** *161*, C42-C49.

43. M. Rumyantsev, A. Shauly, S. G. Yiantsios, D. Hasson, A. J. Karabelas and R. Semiat. Parameters affecting the response of dynamic membranes formed by Zr hydroxide colloids, *Desalination* **2000**, *131*, 189-200.

44. G. A. Carter, R. D. Hart, M. R. Rowles, C. E. Buckley and M. I. Ogden. The effect of processing parameters on particle size in an ammonia-induced precipitation of zirconyl chloride under industrial relevant conditions, *Powder Technol.* **2009**, *191*, 218-226.

45. J. Qi and G. E. Thompson. Comparative studies of thin film growth on aluminum by AFM, TEM and GDOES characterizaton, *Appl. Sur. Sci.* **2016**, *377*, 109-120.

46. J. D. Ramsey and R. L. McCreery. In situ Raman microscopy of chromate effects on corrosion pits in aluminum alloy, *J. Electrochem. Soc.* **1999**, *146*, 4076-4081.

47. E. Akiyma, A. J. Markworth, J. K. McCoy. G. S. Frankel, L. Xia and R. L. McCreery. Storage and release of soluble hexavalent chromium from chromate conversion coatings on Al alloys: kinetics of release, *J. Electrochem. Soc.* **2003**, *150*, B83-B91.

48. J. E. Maslar, W. S. Hurst, W. J. Bowers Jr., H. Hendricks, M. I. Aquino and I. Levin. In situ Raman spectroscopic investigation of chromium surfaces under hydrothermal conditions, *Appl. Surf. Sci.* **2001**, *180*, 102-118.

49. J. D. Ramsey and R. L. McCreery. Raman microscopy of chromate interactions with corroding aluminum alloy 2024-T3, *Corros. Sci.* **2004**, *46*, 1729-1739.

CHAPTER 3: ELECTROCHEMICAL CHARACTERIZATION OF DIFFERENT VARIANTS OF A COMMERCIAL TRIVALENT CHROMIUM PROCESS (TCP) COATING ON ALUMINUM ALLOY 7075-T6

3.1. Electrochemical Introduction

Multi-layer coating systems (conversion coating + primer + topcoat) are used to protect aerospace aluminum alloys from corrosion while in service. Environmental and health concerns are driving the aerospace industry to transition away from the traditional chromated conversion coatings and primers to more environmentally-friendly non-chromated coating systems.[1-5] Conversion coatings are generally thin, hydrated metal oxide films formed on a metal surface that ideally provide adhesion promotion with primers, anti-corrosion properties to the base metal, and a reservoir of inhibitor ions during the coating lifetime.[4-7] To this end, the Naval Air Systems Command (NAVAIR) has formulated some novel coating chemistries for metal finishing and developed associated application processes. Two of these for aluminum alloys are the (i) non-chromated process (NCP) and (ii) trivalent chromium process (TCP) conversion coatings. NCP is a non-chromium, zirconium and zinc-based aqueous coating that can be applied by both immersion and spray.[5,8,9] TCP is a non-chromated, trivalent chromium and zirconium-based coating that can also be applied by immersion or spray.[5,10,11] Both have undergone field testing on some assets, however, much remains to be learned about the mechanism(s) by which these coatings inhibit corrosion on different alloys in a variety of test environments, and how combinations of non-chromated conversion coatings with non-chromated primers maintain high corrosion resistance and good physical properties.

TCP is the leading candidate to replace the chromated pretreatment conversion coatings on aerospace aluminum alloys.[10-24] TCP has been licensed by several vendors and is currently marketed under different names: Bonderite M-Cr T5900 from Henkel, TCP-HF from Chemeon

(formerly Metalast), 650 ChromitAL from SurTec and Aluminescent from Luster-on. These coating baths have chemical compositions that differ to some extent from the original NAVAIR formulation so each should be treated as a separate coating system. Generally speaking, while these commercial TCP coatings have been qualified for use on selected aircraft components, differences are often observed in their anti-corrosion properties on aluminum alloys, particularly during accelerated corrosion testing and environmental exposure. The physical structure and chemical composition of a TCP coating depend on the coating bath composition, the cleanliness of the alloy surface, the chemical composition of the alloy surface namely the number density of intermetallic phases present, and the alloy surface morphology (*i.e.*, pit size and density). Improvements in the TCP coating's anti-corrosion performance could be realized with more fundamental knowledge regarding the physical structure and chemical composition of the coating, how the coating structure depends on the surface pretreatment of the alloy and the corrosion inhibition mechanism(s).

There has been some recent published work on fundamental investigations of the TCP coating formation mechanism, the physical and chemical structure of the coating on different aluminum alloys, and correlation of these properties with the anti-corrosion behavior. We have reported on the Bonderite M-Cr T5900 coating from Henkel on AA2024-T3, AA6061-T6 and AA7075-T6.[13,16-19] There have also been other reports on the 650 ChromitAl from SurTec.[20-26] The electrochemical data reported in the literature indicate that the TCP coating provides barrier layer protection on AA2024-T3, AA6061-T6 and AA7075-T6 suppressing both anodic and cathodic currents near the OCP by 10-100x, depending on the alloy, in zero or low-chloride electrolytes.[13,16-19] In other words, the coating acts as both an anodic and cathodic inhibitor. In high chloride electrolyte, the anodic protection diminishes while the cathodic protection remains in

place. The coating provides cathodic protection by functioning, in part, as a diffusional barrier for O_2, even though very thin (~100 nm).[13,16-19,20,27]

In the previous chapter, the physical and chemical properties of three different variants of a commercial TCP conversion coating (650 ChromitAl, SurTec), formed by immersion and spray on aluminum alloy AA7075-T6, were described.[26] The properties of conversion coatings applied by immersion and spray on degreased and deoxidized alloys were compared. Electrochemical testing (open circuit potentials, anodic and cathodic polarization currents, and polarization resistances) was performed in oxygenated 0.5 M Na_2SO_4 (mild electrolyte) and 3.5% NaCl (aggressive electrolyte). Evaluation of the stand-alone corrosion protection was made using a 14-day thin-layer mist test (3.5% NaCl and 55 ^{o}C). This chapter represents the first comprehensive investigation of how effectively these different TCP coatings inhibit corrosion on this aluminum alloy.

3.2. Experimental

3.2.1. Reagents

The 133 degreaser and 495L deoxidizer (SurTec, Inc., Brunswick, OH) were prepared to 4 wt. % and 20 vol. %, respectively, with ultrapure water. The ChromitAl 650 coating baths, versions E, V and C, were prepared to 20 vol. % with ultrapure water. The pH of the coating solution was adjusted to 3.85 using 0.1 M NaOH or 0.1 M H_2SO_4, as needed. The ultrapure water was obtained from a Barnstead E-Pure system and had a resistivity >17 MΩ·cm.

3.2.2. Specimen Preparation

AA7075-T6 was obtained as 2-mm thick sheets (**www.onlinemetals.com**) that were cut into 1 cm^2 specimens. The composition of the alloy was determined by x-ray fluorescence (XRF) using known sensitivity factors for the different elements (Bruker S2 Ranger). The semi-

quantitative results were presented in Table 1 of Chapter 2. All values are within the expected range[26,28], except for Mg which is a little higher than expected.

The specimens were prepared for the conversion coating by first wet sanding for 4 min using 1500 grit aluminum oxide paper to smooth the surface and expose fresh alloy. This was followed by ultrasonic cleaning in ultrapure water for 20 min in a covered glass beaker. The specimens were then hand polished for 4 min using a 0.3-μm diam. alumina powder (Buehler) slurry on a felt polishing pad. The alumina paste was prepared by mixing the powder with ultrapure water directly on the polishing pad. The polished specimens were then ultrasonically cleaned for 20 min in ultrapure water. After polishing, the specimens were degreased by a 5-min immersion in 4 wt. % SurTec 133 at 60°C in a glass beaker. This is an alkaline (pH 9.0-9.5) and silicate-free degreaser that contains phosphate and borate surfactants. The specimens were gently agitated each minute of the cleaning. The specimens were then rinsed for 2 min under gently flowing city tap water that contained ~0.1 ppm Zr, ~0.2 ppm Cu, Fe, Zn, ~0.4 ppm Al, and 30-45 ppm Ca, Mg, and S, as determined by ICP-OES analysis (July 2016).[9] This was followed by deoxidation for 2 min in 20 vol. % SurTec 495L at room temperature. The deoxidation was performed in a glass beaker without any specimen agitation. This fluoride-containing deoxidizer has a sulfuric acid base with added Fe salts. The specimens were then rinsed for 2 min under gently flowing city tap water. At this point, the pretreated specimens were dried under a stream of nitrogen gas and stored in a petri dish until further use. These specimens are referred to as “uncoated”.

The TCP coating was applied to degreased and deoxidized specimens by immersion and spray, for comparison. Immersion-coated specimens were placed in a 20 vol. % solution of 650 E, C or V at 30°C for 4 min without any agitation. The physical and chemical properties of the three different conversion coatings was reported on previously.[26] Spray-coated conversion

coatings were applied every 30 s for a 3-min period at room temperature, ~21-25°C. The coating conditions employed were ones recommended by the supplier. The spray coating was applied using an inexpensive nebulizer spray bottle. The immersion-coated specimens were then rinsed by immersion in city tap water for 2 min followed by a final soak in ultrapure water for 30 s. The spray-coated specimens were then rinsed with a city tap water spray every 30 s for a 2-min period followed by a final immersion in ultrapure water for 30 s. The coated specimens were allowed to dry in the laboratory atmosphere overnight before further testing. The drying, or aging, was performed at room temperature in a covered petri dish.

Quantitative inorganic chemical analysis of the city tap water and the coating baths was performed on a Varian 710-ES ICP-OES.[26] Quantitation was performed using response curves generated with external standards. The major chemical differences (inorganic composition) in the coatings are Zn in 650 V and C and not in E, the greater level of S in 650 V and C, and the greater level of Fe in 650 C. The Zr/Cr ratio is approximately 2:1 for all three coating variants. SurTec 650 (650 E) is the first-generation of the coating based on the original NAVAIR formulation with Zr^{+4} and Cr^{+3} salts. 650 V is the second-generation of the coating with the same general composition as 650 E plus some added complexing agents. 650 V is designed to produce a heavier coating than 650 E with more coloration for visible detection. 650 C is generally similar to 650 V in chemical composition, with some different complexing agents added. During the course of this work, it was learned that the 650 C has been discontinued from the company's product line.

3.2.3. Alloy and Coating Characterization

Detailed analysis of the coating bath compositions and the physical and chemical properties of the different conversion coatings were reported previously .[26]

3.2.4. Electrochemical Measurements

All electrochemical measurements were conducted in a single-compartment glass cell using a computer-controlled electrochemical workstation (Gamry Instruments, Inc, Reference 600, Warminster, PA).[29] An aluminum panel was mounted at the bottom of the cell with a Viton® O-ring defining the exposed geometric area. The area of the exposed aluminum panel was 0.20 cm^2. Currents for the aluminum panel are normalized to this area. The counter electrode was a Pt wire. The reference was a home-made Ag/AgCl electrode (3 M KCl, E^0 = 0.197 V vs. NHE) that was housed in a Luggin capillary with a cracked glass tip. All solutions were prepared by oxygenation with bubbling pure oxygen (0.5 M Na_2SO_4 or 3.5% NaCl (0.6 M)) for 30 min and then blanketing the solution with the gas during a measurement. All measurements were made at room temperature (23 ± 2).

The following electrochemical testing protocol was used: (i) measurement of the open circuit or corrosion potential (E_{corr}) for at least 30 min in oxygenated electrolyte (stability was most often achieved within this period); (ii) recording the impedance spectrum at E_{corr} from 10,000 to 0.01 Hz using a 10 mV rms AC voltage; (iii) recording a linear polarization curve ± 25 mV vs. E_{corr}, (iv) recording a potentiodynamic cathodic scan from E_{corr} to a potential limit of −0.8 to -1.2 V vs Ag/AgCl, depending on the electrolyte; and (v) recording a potentiodynamic anodic scan from E_{corr} to a potential limit of -0.5 to -0.2 V vs Ag/AgCl, depending on the electrolyte. The potentiodynamic scans were recorded at 1 mV/s (0.060 V/min). Separate specimens were used for the cathodic and anodic polarization curves. The polarization resistance, R_p, was determined by three methods: (i) recording the low frequency (0.01 Hz) total impedance at the E_{corr}, (ii) fitting the experimental EIS data recorded at the E_{corr} to an equivalent circuit using ZView software, and (iii) linear polarization curves recorded ±25 mV vs. E_{corr}.

The rotating disk voltammetric measurements were performed on home-made rotating aluminum alloy electrodes along with an Autolab rotator. The disk electrode was prepared by press fitting a rod into a Teflon shroud. The diameter of the disk electrode (AA7075-T6) was 0.6 cm. The dimensions of the shroud were 1.2 cm in diameter and 5 cm in length. The disk electrode was pretreated and coated with TCP exactly as described above for the aluminum alloy plates.

3.2.5. Thin-Layer Mist Degradation Test

A thin-layer mist (TLM) test was employed to assess the protective properties of the conversion coatings. In this accelerated degradation test, droplets of electrolyte solution are applied by misting the specimen surface with 3.5% NaCl using a conventional spray bottle. The test configuration is shown in Figure 11. The specimens (3 during a test run) were positioned horizontally on a platform above ultrapure water in a sealed polypropylene container. The temperature was maintained at 55 ^{o}C by placing the container in an oven. One test cycle was 24 h during which period the specimens were continuously exposed to the salty, humid environment. The air in the container and the electrolyte spray were replenished each 24-h cycle by (i) removing the container from the oven and cooling to room temperature for 0.5 h, and (ii) opening the container to the laboratory air for this cooling period during which time the specimen surface was re-sprayed with 3.5% NaCl. There was some droplet evaporation during each 24-h cycle and some thermal cycling (25-55 ^{o}C), but the specimen surface never went to complete dryness. The coverage of the water layer on the coated specimen changed over time due to changes in the wettability of the coating.[26] The entire test lasted for 14 cycles (*i.e.*, 14 days). At the end of the test period, the specimens were copiously rinsed with ultrapure water before being dried under a stream of N_2. The specimens were stored in covered petri dishes until subsequent analysis.

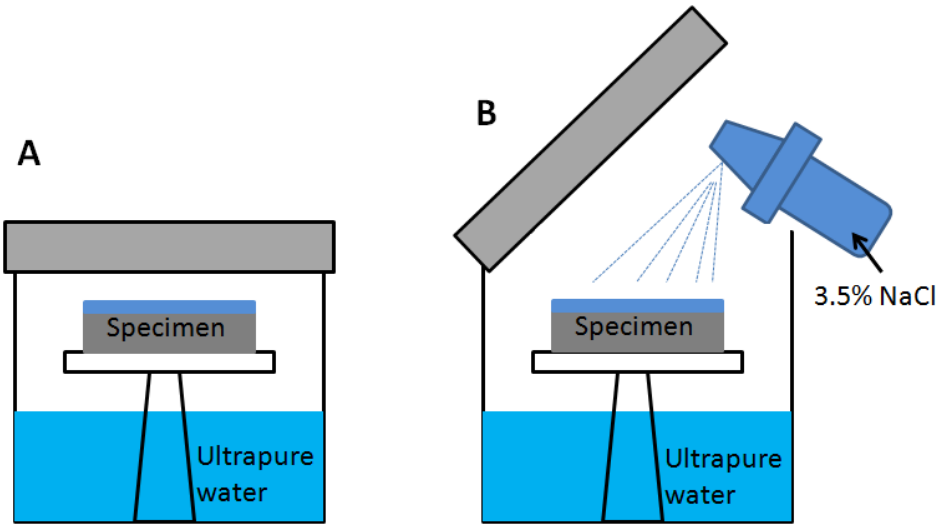

Figure 11. Schematic of the thin-layer mist (TLM) polypropylene test chamber and protocol: (A) specimen configuration during a test cycle and (B) reapplication of the 3.5% NaCl spray at the beginning of a test period. The polypropylene container was sealed during a test period but opened daily to re-apply the spray and to equilibrate with the laboratory air for 30 min at room temperature. The container was placed in an oven at 55 ^{o}C during the test. Each test cycle was 24 h over a 14-day period.

3.3. Results

3.3.1. Open Circuit or Corrosion Potentials

Figure 12 presents (A) representative open circuit potential (OCP)-time transients and (B) nominal values of the OCP or E_{corr} for TCP-coated (immersion) and uncoated specimens in oxygenated 0.5 M Na_2SO_4. The potentials for the 650 E-coated and uncoated 7075 specimens stabilized quickly upon immersion in this electrolyte solution, while the potentials for both 650 V and C-coated specimens were slower to equilibrate. Both started at negative potentials and drifted positive over time consistent with some surface passivation. There was also greater variability in the E_{corr} values for these two coating variants. The E_{corr} values are significantly more negative (more active) for all coated alloys as compared to the uncoated alloy at the $p \leq 0.15$ level, with 650 E exhibiting the most negative shift, nominally about 150 mV. It is unclear if the rather large variability in the values (n=3) for the coated alloys are due to chemical or process variables. The

trends seen for these TCP coatings, more active E_{corr} values as compared to uncoated controls, are different from what has been observed for another TCP coating variant. For this TCP coating (Bonderite T5900), unchanging E_{corr} for coated and uncoated controls was observed.[9,13,16-19]

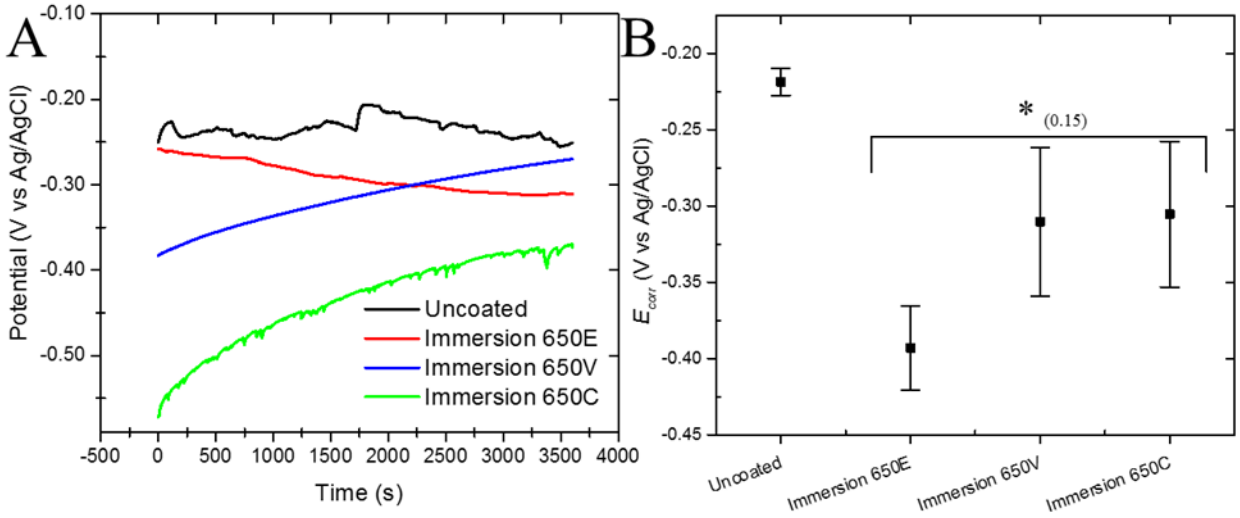

Figure 12. (A) Open circuit potential (OCP)-time transients for immersion-coated 650 E (red), 650 V (blue), 650 C (green), and uncoated AA7075-T6 (black) specimens in oxygenated 0.5 M Na_2SO_4. (B) Nominal values of the E_{corr} for the TCP-coated and uncoated specimens. Values are displayed as mean ± standard error of the mean (n = 3). Asterisk indicates data significantly different from the uncoated control ($p \leq 0.15$).

Figure 13 presents (A) representative OCP-time transients and (B) nominal values of E_{corr} for immersion-TCP-coated and uncoated specimens in oxygenated 3.5% NaCl. The potentials for all the coated specimens stabilized quickly upon immersion. The potentials in this aggressive electrolyte are considerably more negative than the values in the less aggressive Na_2SO_4. Compared to the results in 0.5 M Na_2SO_4, the immersion-coated specimens in NaCl exhibit less variability in E_{corr} from sample to sample. The higher rate of metal oxidation in this electrolyte must be compensated for a higher rate of dissolved oxygen reduction under open circuit conditions. This is achieved by a shift of the alloy potential toward more negative potentials. The nominal E_{corr} values for all the TCP-coated specimens are slightly more positive than the values for the uncoated specimens. Nominally, the most positive shift is seen for 650 E.

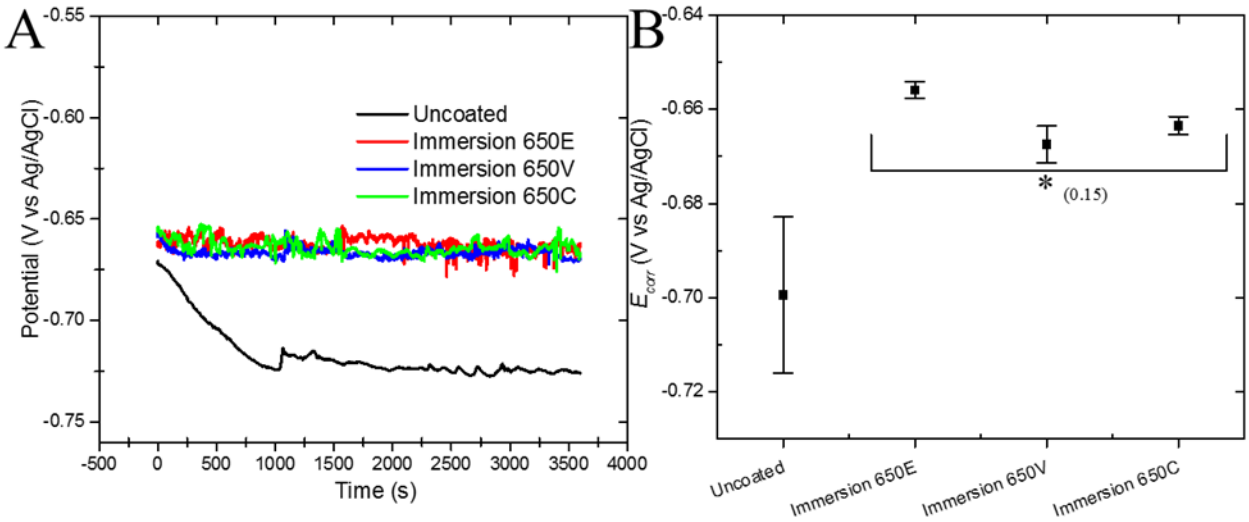

Figure 13. (A) OCP-time transients for immersion-coated 650 E (red), 650 V (blue), 650 C (green), and uncoated AA7075-T6 (black) specimens in oxygenated 3.5% NaCl. (B) Nominal values of Ecorr for the TCP-coated and uncoated specimens. Values are displayed as mean ± standard error of the mean (n = 3). Asterisk indicates data significantly different from the uncoated control ($p \leq 0.15$).

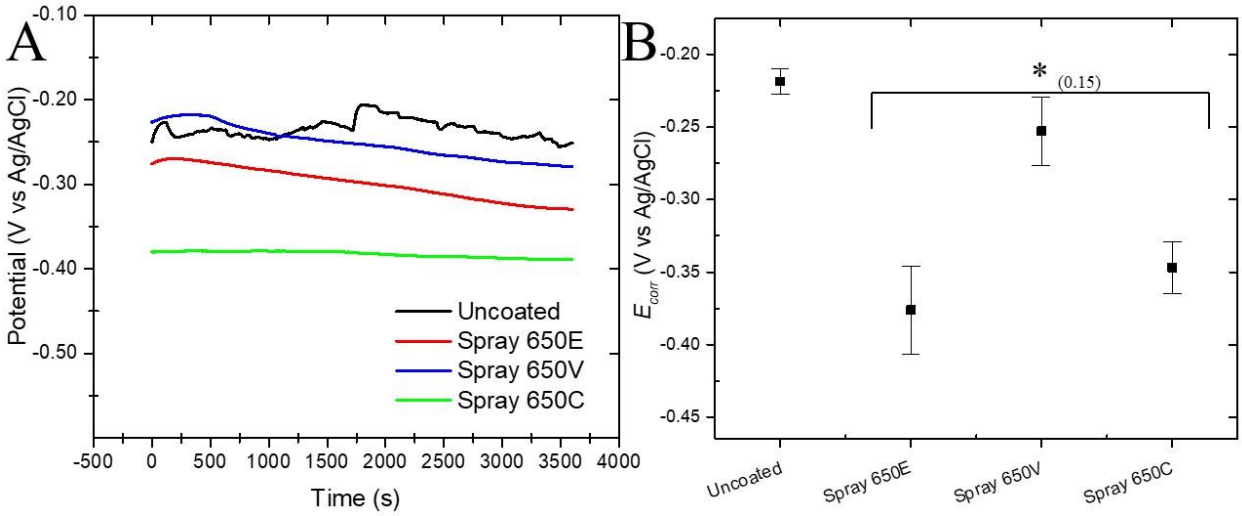

Figure 14. (A) Open circuit potential (OCP)-time transients for spray-coated 650 E (red), 650 V (blue), 650 C (green), and uncoated AA7075-T6 (black) specimens in oxygenated 0.5 M Na_2SO_4. (B) Nominal values of the E_{corr} for the TCP-coated and uncoated specimens. Values are displayed as mean ± standard error of the mean (n = 3). Asterisk indicates data significantly different from the uncoated control ($p \leq 0.15$).

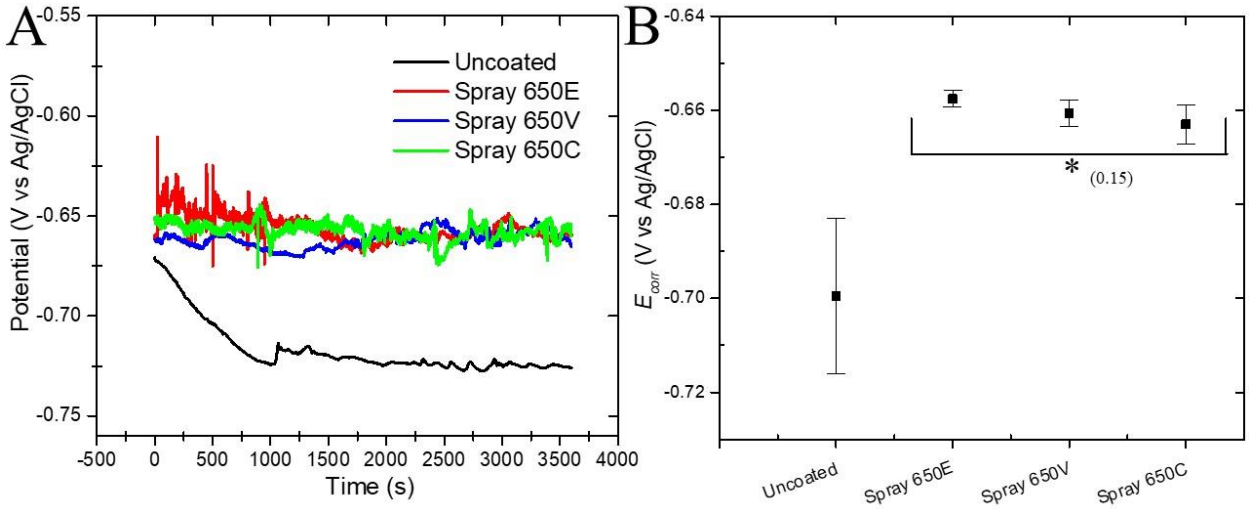

Figure 15. (A) OCP-time transients for spray-coated 650 E (red), 650 V (blue), 650 C (green), and uncoated AA7075-T6 (black) specimens in oxygenated 3.5% NaCl. (B) Nominal values of Ecorr for the TCP-coated and uncoated specimens. Values are displayed as mean ± standard error of the mean (n = 3). Asterisk indicates data significantly different from the uncoated control ($p \leq 0.15$).

3.3.2. Potentiodynamic Polarization Curves

Potentiodynamic polarization curves were recorded to investigate what effect the TCP coatings have on anodic and cathodic currents. Figure 16 presents representative (A) cathodic and (B) anodic polarization curves along with (C) nominal anodic and cathodic currents at two comparison potentials for immersion-coated and uncoated AA7075-T6 specimens in oxygenated 0.5 M Na_2SO_4. It can be seen that there is some variation in E_{corr} for these particular samples, especially for 650 V and C (Fig. 14A). E_{corr} for these two coated specimens is outside the range of values reported in Figure 2B for reasons that are unclear. The coating suppresses cathodic currents at potentials negative of E_{corr}, as compared to the uncoated control (Fig. 16A). The greatest suppression is seen for 650 E and the least is seen for 650 C (Fig. 16C). The current at potentials immediately negative of E_{corr} is attributable to the reduction of dissolved oxygen. At the most negative potentials, both dissolved oxygen reduction and hydrogen evolution contribute to the cathodic current. The currents decrease in the order: 650 C > V > E.

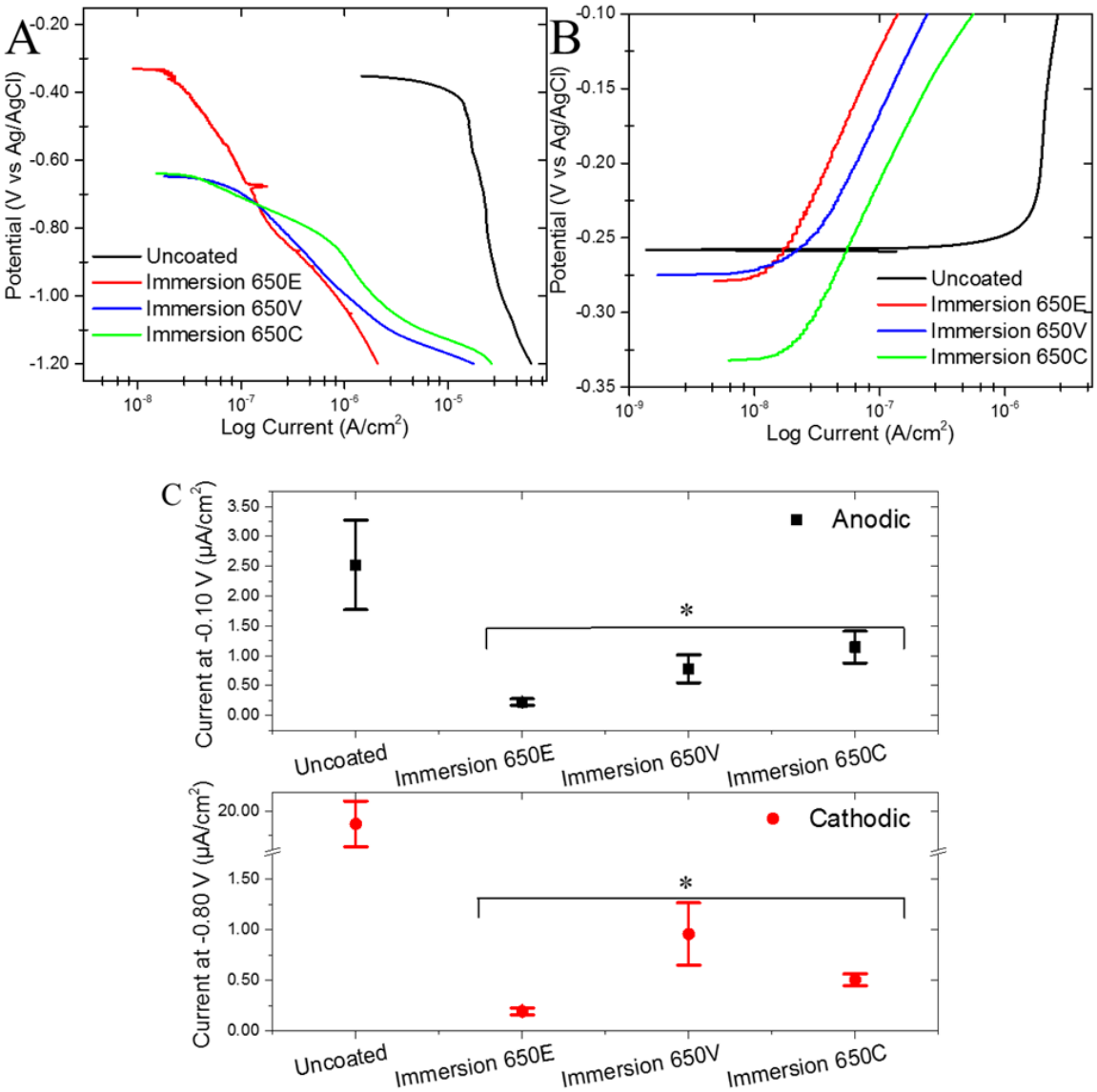

Figure 16. (A) Cathodic and (B) anodic potentiodynamic polarization curves for immersion-coated and uncoated AA7075-T6 specimens in oxygenated 0.5 M Na_2SO_4. (C) Plots of the nominal anodic (top, black, at -0.10 V) and cathodic (bottom, red, at -0.80 V) currents for the TCP-coated and uncoated alloys. Values are displayed as mean ± standard error of the mean (n = 3). Asterisk indicates data significantly different from the uncoated control ($p \leq 0.05$).

The TCP coatings also provide anodic protection (Fig. 16B), as evidenced by the suppressed currents around the E_{corr}. The currents decrease in the order: 650 C > V > E. The level of current suppression is greater for the cathodic than for the anodic currents. Figure 16C presents values (mean ± S.E.M.) of the cathodic current measured at -0.80 V and the anodic current at -0.10

V for the TCP-coated and uncoated alloys. All values for the coated specimens are statistically lower than the values for the uncoated controls. The cathodic current suppression is greatest for 650 E (100x) and less for C (36x) and V (18x). The anodic current suppression is greatest for 650 E (10x) and less for V (3x) and C (2x). Overall, immersion-coated 650 E provides the greatest suppression of both currents in oxygenated 0.5 M Na_2SO_4.

Figure 17 presents representative (A) cathodic and (B) anodic polarization curves along with (C) nominal anodic and cathodic currents for immersion-coated and uncoated AA7075-T6 specimens in oxygenated 3.5% NaCl. At potentials negative of E_{corr}, the current suppression is greatest for 650 E followed by 650 V and C (Fig. 18A). There is a progressive increase in the cathodic current for all the coated specimens as the potential becomes more negative with the level of suppression decreasing. At -0.9 V, the curves for the TCP-coated specimens all cross. Opposite trends are then seen for the three coatings at potentials more negative with 650 V providing the greatest current suppression, followed by 650 C and E. At potentials positive of E_{corr}, currents are suppressed in the following order: 650 E > V and C (Fig. 17B). The breakdown or pitting potential, E_{pit}, is within 25-50 mV of E_{corr} and is shifted positive by only a few millivolts by any of the coatings. Overall, the level of current suppression is less in this aggressive electrolyte as compared to the less aggressive Na_2SO_4. At -0.65 V, the nominal anodic current, as compared to the uncoated control, is suppressed more or less equivalently by all three coatings, 20x (Fig. 17C). At -0.80 V, the nominal anodic current is suppressed equivalently by all three coatings, 9x (Fig. 17C).

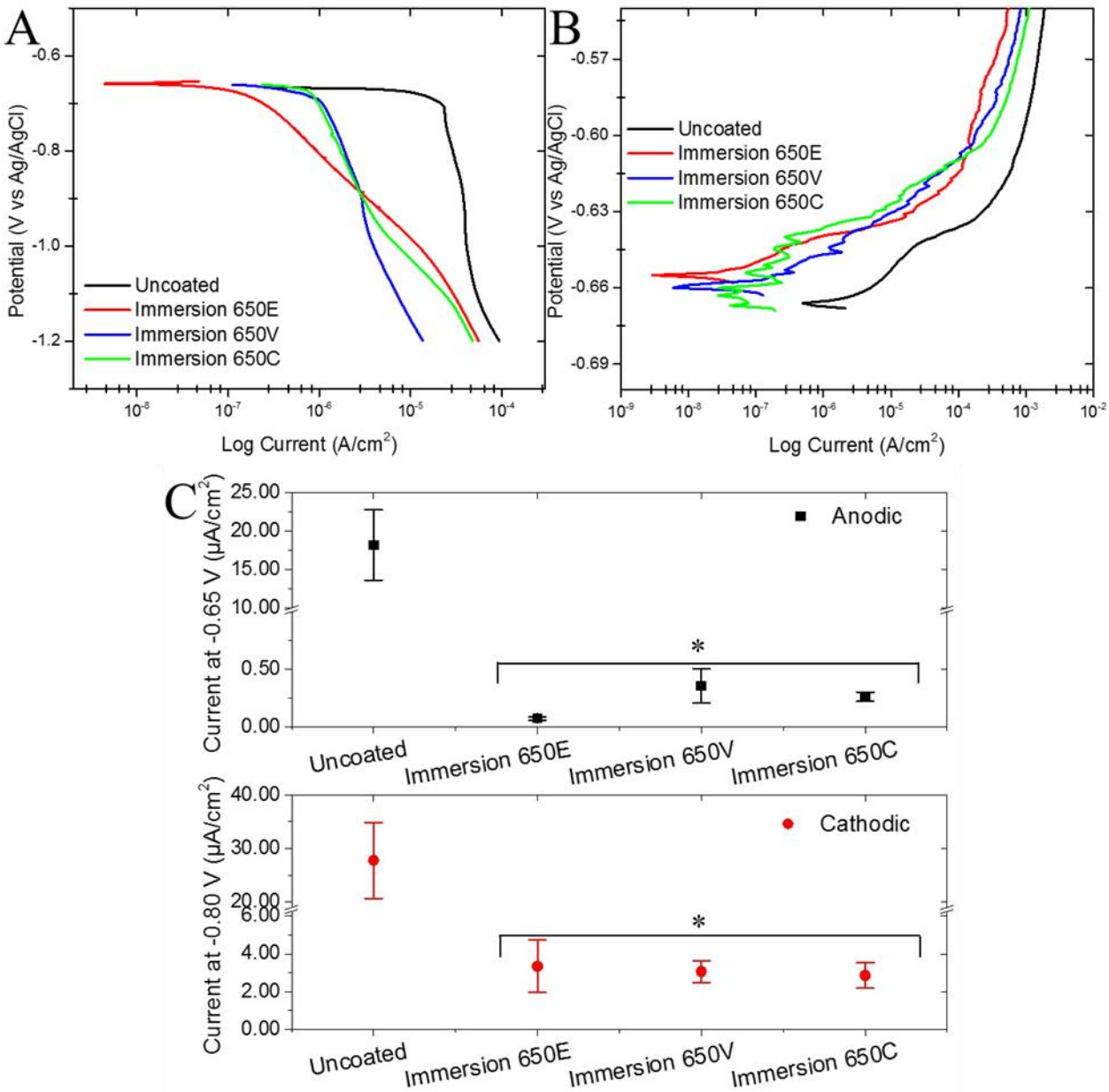

Figure 17. (A) Cathodic and (B) anodic potentiodynamic polarization curves for immersion-coated and uncoated AA7075-T6 specimens in oxygenated 3.5% NaCl. (C) Plots of the nominal anodic (top, black, at -0.65 V) and cathodic (bottom, red, at -0.80 V) currents for the TCP-coated and uncoated alloys. Values are displayed as mean ± standard error of the mean (n = 3). Asterisk indicates data significantly different from the uncoated control ($p \leq 0.05$).

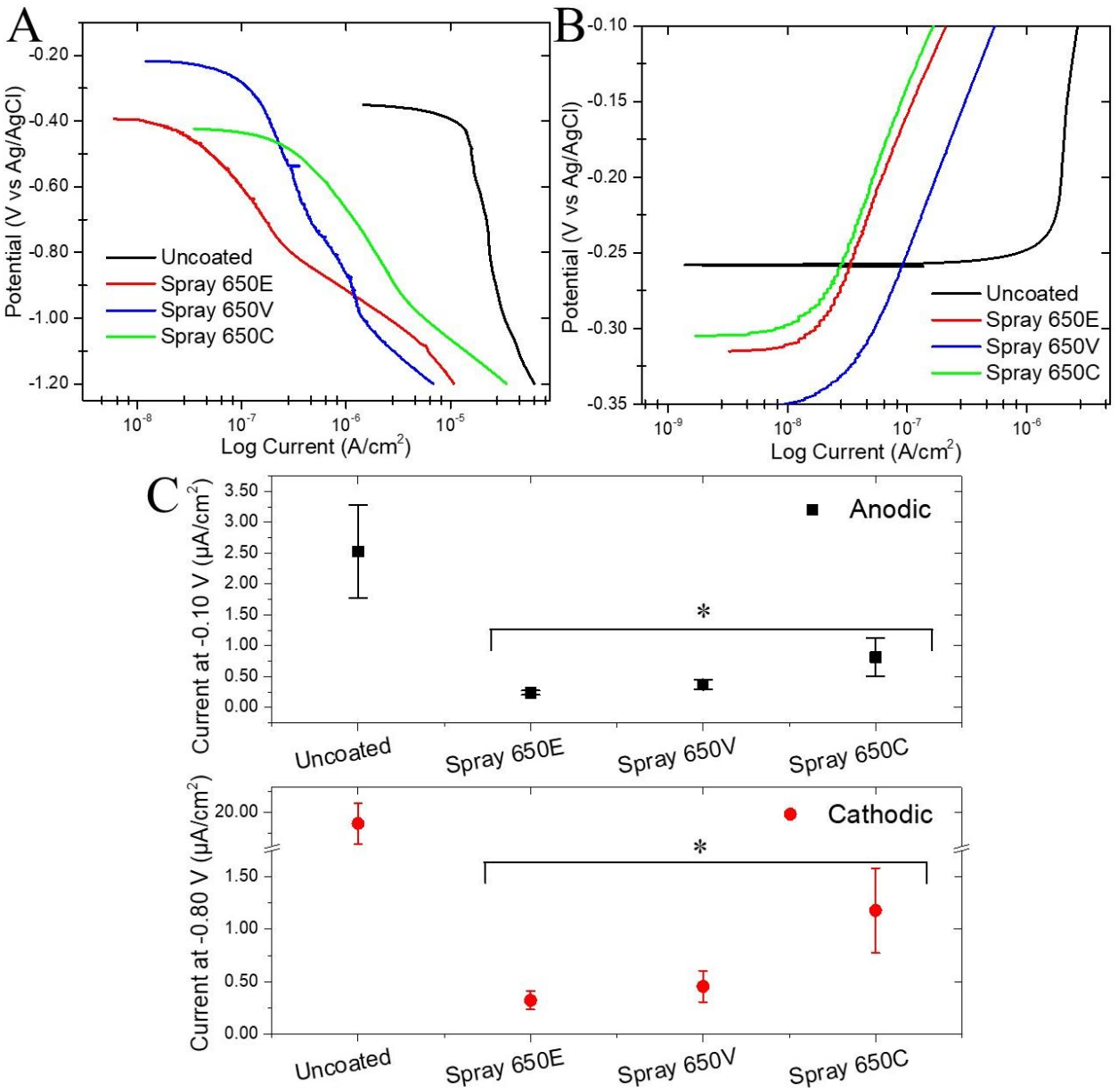

Figure 18. (A) Cathodic and (B) anodic potentiodynamic polarization curves for immersion-coated and uncoated AA7075-T6 specimens in oxygenated 0.5 M Na_2SO_4. (C) Plots of the nominal anodic (top, black, at -0.10 V) and cathodic (bottom, red, at -0.80 V) currents for the TCP-coated and uncoated alloys. Values are displayed as mean ± standard error of the mean (n = 3). Asterisk indicates data significantly different from the uncoated control ($p \leq 0.05$).

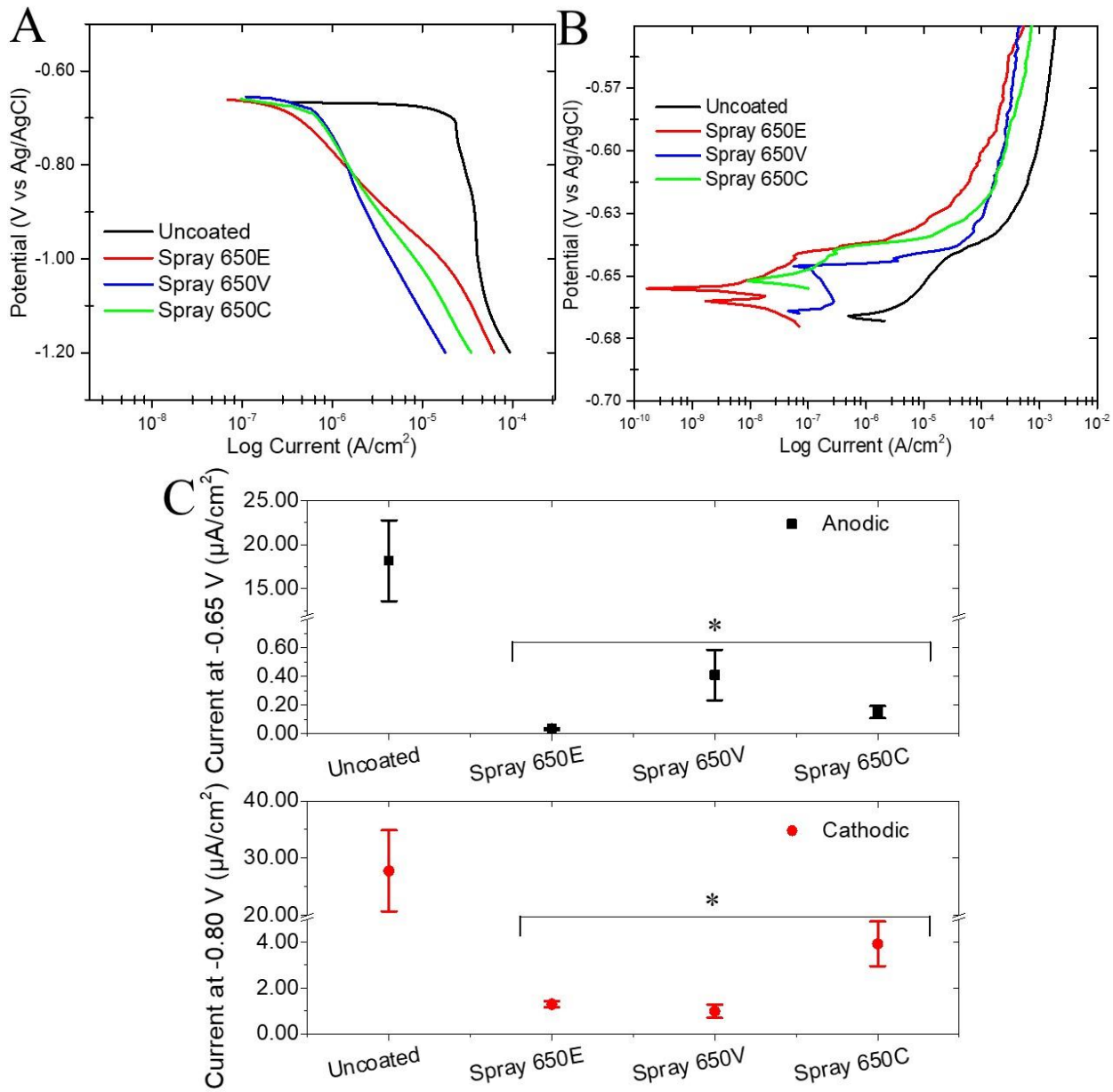

Figure 19. (A) Cathodic and (B) anodic potentiodynamic polarization curves for spray-coated and uncoated AA7075-T6 specimens in oxygenated 0.5 M Na_2SO_4. (C) Plots of the nominal anodic (top, black, at -0.10 V) and cathodic (bottom, red, at -0.80 V) currents for the TCP-coated and uncoated alloys. Values are displayed as mean ± standard error of the mean (n = 3). Asterisk indicates data significantly different from the uncoated control ($p \leq 0.05$).

Figure 20 shows values (mean ± S.E.M.) for E_{pit} measured for the TCP-coated and uncoated specimens. Data for immersion and spray coatings are compared. In all cases in 3.5 % NaCl, E_{pit} is within 25-50 mV of the E_{corr} for all the specimens and the TCP coatings shift the potential

equivalently positive by only a few tens of millivolts. At high chloride anion concentrations, the TCP coating has minimal effect on E_{pit}. However, at lower concentrations, there is a more dramatic effect. Figure 20 shows plots of E_{pit} versus the solution concentration of chloride for TCP-coated and uncoated AA2024-T3. The alloy is different from the AA7075-T6 used in most of this work and the TCP coating is different (Bonderite T5900), but the trend is clear. E_{pit} at lower chloride concentrations (0.01 M) is over 400 mV more positive of the value for the uncoated alloy. There is a linear decrease in E_{pit} with increasing chloride concentration for both the coated and uncoated specimens. At the higher concentration (0.1 M), the curves merge and E_{pit} is the same for both the uncoated and coated alloys, and is only a few tens of millivolts more positive of the open circuit or corrosion potential, E_{corr}. It would appear that at the higher chloride concentration either the coating's ability to inhibit contact of the anion with the surface is reduced or the behavior is dominated by chloride ion/solution penetration through native defects in the coating to the underlying alloy.

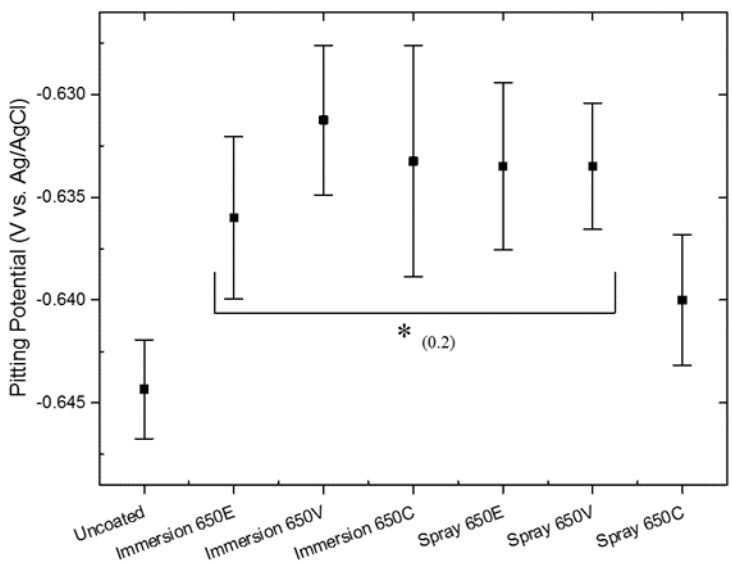

Figure 20. Pitting or breakdown potentials, E_{pit}, for the TCP-coated and uncoated AA7075-T6 alloys in oxygenated 3.5% NaCl. Values are displayed as mean ± standard error of the mean (n = 3). Asterisk indicates data significantly different from the uncoated control ($p \leq 0.2$).

3.3.3. Rotating Disk Voltammetry Studies of ORR

Polarization curve data for this and other commercial TCP coatings[13,16-19,20,21] indicate that cathodic currents at potentials where the reduction of dissolved oxygen occurs are suppressed by the conversion coating. To investigate this further, rotating disk voltammetry was used to investigate the oxygen reduction reaction (ORR) at uncoated (bare) and TCP–coated AA7075-T6. The TCP coating was SurTec 650 E. Figure 21 shows (A) cathodic polarization curves as a function of rotation rate for uncoated and coated electrodes in oxygenated 3.5 % NaCl and (B) limiting current (i_l)-rotation rate $(\omega)^{1/2}$ plots (Levich plots) for uncoated (bare) and TCP-coated AA7075-T6. It can be seen in the polarization curves (semi-log plot) that the currents increase with rotation rate for the uncoated electrode while the currents for the TCP-coated electrode are largely invariant of rotation rate. At these potentials, the current is mainly due to the reduction of dissolved oxygen. The limiting current (i_l) – rotation rate$^{1/2}$ plots, using the current at -0.85 V, reveal an increasing linear trend for the uncoated electrode as predicted from the Levich equation:

$$i_l = 0.62nAFC_{O_2}D_{O_2}^{0.67}\upsilon^{-0.167}\omega^{0.5}$$

where i_l is the limiting current, A is the electrode area, C is the concentration of dissolved oxygen, D is the diffusion coefficient for dissolved oxygen, υ is the kinematic viscosity and ω is the electrode rotation rate. n and F have their usual meanings. In contrast, the curve for the TCP-coated electrode is largely independent of the rotation rate$^{1/2}$. Clearly, the TCP coating is inhibiting the ORR, in part, through hindered mass transport.

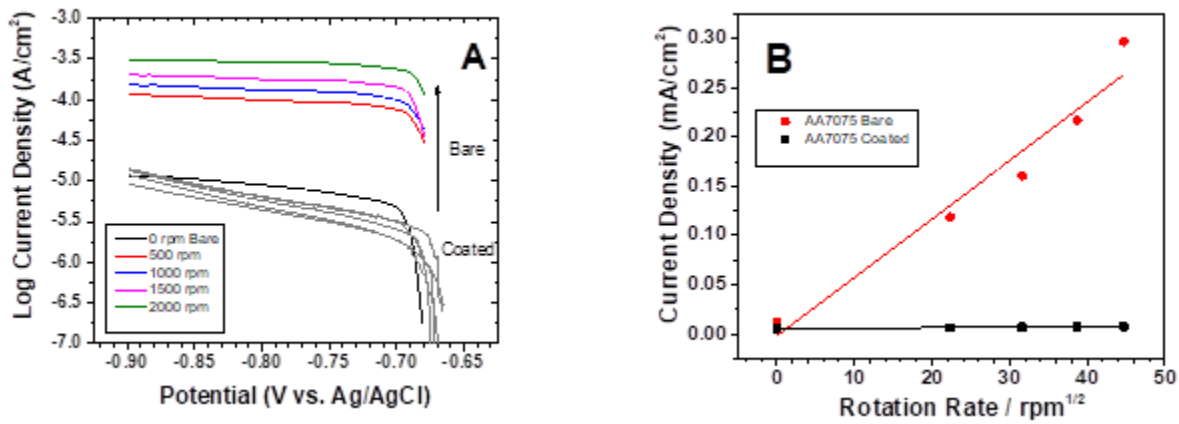

Figure 21. (A) Cathodic polarization curves for bare/uncoated (black) and TCP-coated (colored) AA7075-T6 disk electrodes in oxygenated 3.5% NaCl. The TCP coating was SurTec 650 E. The rotation rates were 500, 1000, 1500 and 2000 rpm. (B) Plots of the limiting current at -0.85 V, i_l, versus the rotation rate$^{1/2}$. Values are displayed as mean ± standard error of the mean (n = 3).

Figure 22 shows Levich plots for the limiting current at -0.85 V versus rotation rate$^{1/2}$ for TCP-coated AA2024-T3, 6061-T6 and 7075-T6 alloys. The TCP coating was SurTec 650 E, applied in the same way for each. Each of the curves is shown to have a very slight increase in current with rotation rate$^{1/2}$. The slopes of these curves are considerably lower than that for the uncoated alloy (see Fig. 22). The slopes of the curves are approximately the same for all three alloys but the current magnitude decreases in the following order: 2024 > 7075 > 6061. This trend results because of the difference in activity of each alloy for oxygen reduction, i.e., the amount of

available Cu from intermetallic phases present at the surface and available to participate in the reduction reaction.[30-34]

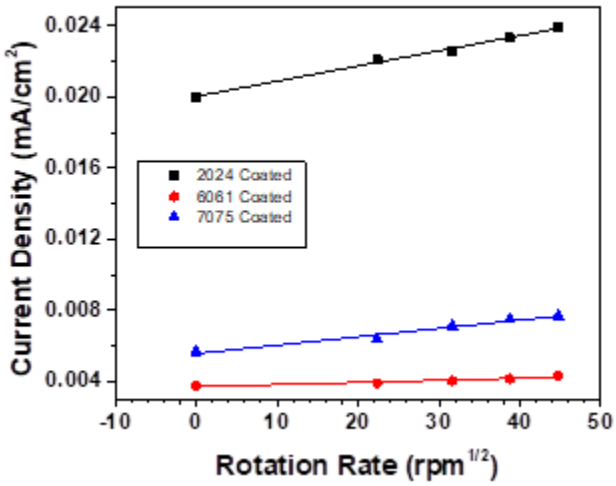

Figure 22. Plots of the limiting current at -0.85 V, i_l, versus the rotation rate$^{1/2}$ for TCP-coated AA2024-T3, 6061-T6 and 7075-T6 alloys in oxygenated 3.5% NaCl. The TCP coating was SurTec 650 E. The rotation rates were 500, 1000, 1500 and 2000 rpm.

3.3.4. Polarization Resistance

Figure 23 presents polarization resistance, R_p, data for immersion-coated and uncoated AA7075-T6 specimens in oxygenated 0.5 M Na_2SO_4. The values were determined from ac impedance data recorded at E_{corr} and linear polarization curves recorded around the E_{corr}. Figure 19A shows Bode plots of the total impedance data recorded at E_{corr}. vs. log frequency. The low frequency impedance at 0.01 Hz can be used as a measure of the resistance to charge transfer or R_p. The highest $Z_{0.01\ Hz}$ is seen for 650 E followed by 650 C and V. All of values for the coated specimens are larger than the impedance for the uncoated control. For example, the value for 650 E is *ca.* 1200 kΩ-cm^2, which is 60x larger than the value for the uncoated specimen, *ca.* 20 kΩ-cm^2. This trend is consistent with that seen in the polarization curve currents. Figure 19B shows Nyquist plots of the impedance data recorded at E_{corr}. It can be seen that the width of the semi-circle, which is reflective of R_p, is greatest for 650 E followed by 650 C, 650 V and the uncoated

specimen. Figure 23C shows linear polarization curve data for the three coated specimens and the uncoated control. Good linearity is seen in the *i-E* plots ± 25 mV vs. E_{corr}. The lower the slope is, the higher R_p is. The curve slope is smallest for 650 E and increases in the following order: 650 V < 650 C < the uncoated specimen. Figure 23D compares R_p data for the three methods. There is reasonable agreement among the three methods as the maximum difference is 2-3x in the data for 650 E. The linear polarization curve measurements give the largest values of R_p for each of the coatings. The largest nominal R_p values are seen for 650 E, measured by all three methods. All R_p values for the coated specimens are larger than the values for the uncoated specimens by a factor of 10-100x ($p \leq 0.05$). This is consistent with the magnitudes of the attenuated polarization curve currents. Nominal values are 3,100 k$\Omega \cdot cm^2$ (3.1×10^6 $\Omega \cdot cm^2$) for 650 E, 1,500 k$\Omega \cdot cm^2$ (1.5×10^6 $\Omega \cdot cm^2$) for 650 V, 800 k$\Omega \cdot cm^2$ (8.0×10^5 $\Omega \cdot cm^2$) for 650 C and 65 k$\Omega \cdot cm^2$ (5.6×10^4 $\Omega \cdot cm^2$) for the uncoated control.

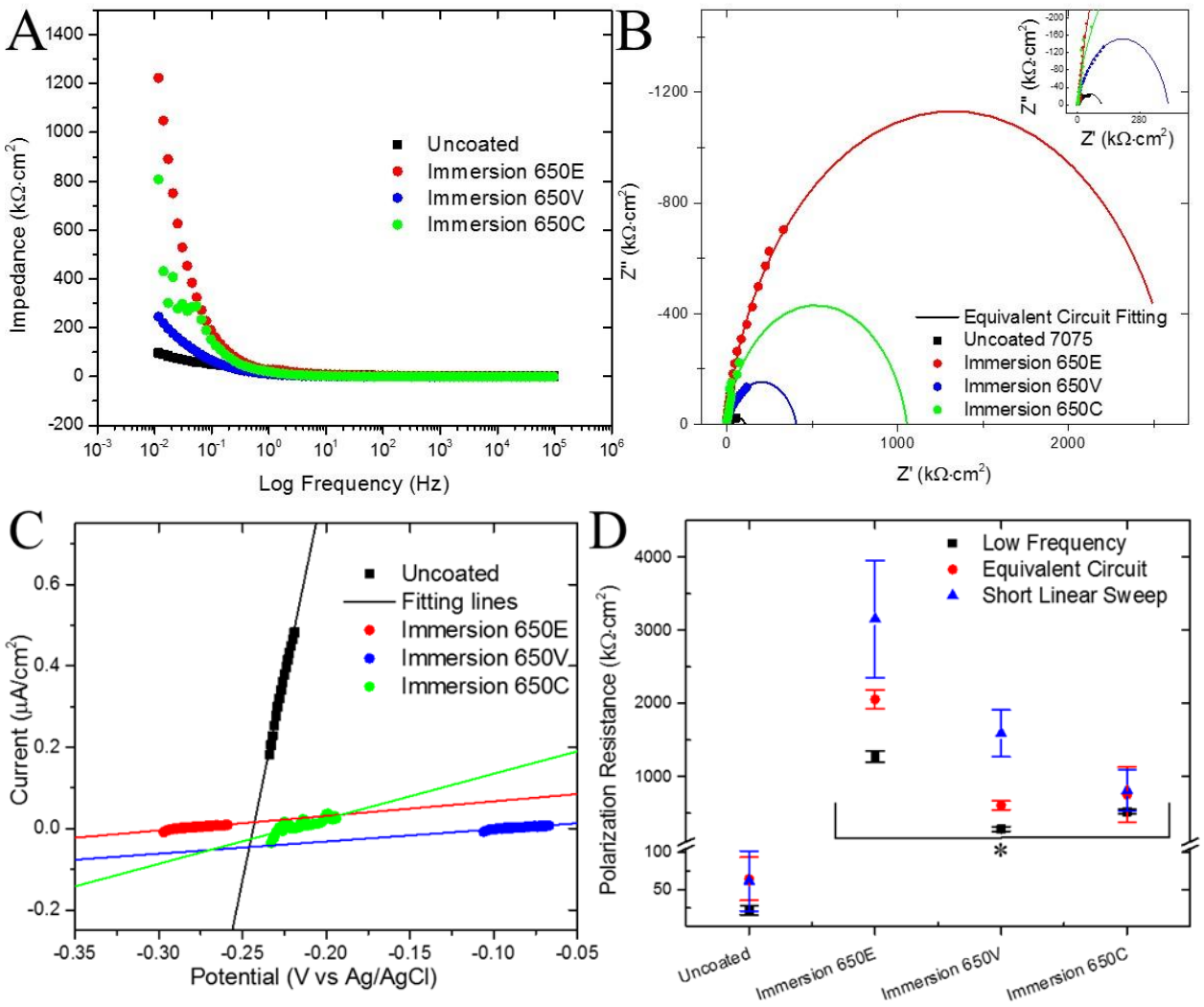

Figure 23. Polarization resistance, R_p, determined from (A) Bode plots of the total impedance recorded at E_{corr} ($Z_{0.01Hz}$), (B) equivalent circuit fitting of Nyquist plots of the impedance data recorded at E_{corr}, and (C) linear polarization curves recorded at ± 25 mV vs. E_{corr} for immersion-coated and uncoated AA7075-T6 specimens in oxygenated 0.5 M Na_2SO_4. (D) Plots of the R_p values determined by the three methods for the coated and uncoated specimens displayed as mean ± standard error of the mean (n = 3). Asterisk indicates data significantly different from the uncoated control ($p \leq 0.05$).

The full impedance spectrum can be fit to an approximate equivalent circuit. Figure 24 shows the equivalent circuits used to fit the impedance data for the uncoated (left) and TCP-coated (right) specimens, based off of circuit previous proposed for other TCP coatings.[35] The uncoated circuit represents the electrolyte resistance (R1), double layer capacitance (CPE1), and charge transfer resistance (R2) found at the electrolyte-metal interface. When the TCP coating is applied,

the circuit still contains the electrolyte resistance (R2), double layer capacitance (CPE2), and charge transfer resistance (R3), while gaining a capacitance due to the coating (CPE1) and a resistance due to electron movement through any pores or cracks in the coating (R2).

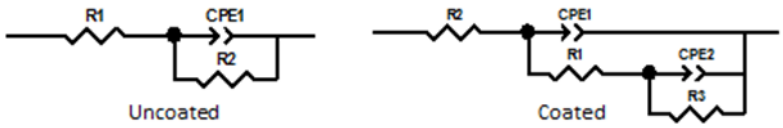

Figure 24. Equivalent circuits used for fitting Nyquist plots of impedance data recorded at E_{corr} for uncoated (left) and TCP-coated (right) specimens.

Figure 25 presents R_p data for immersion-coated and uncoated AA7075-T6 specimens in oxygenated 3.5% NaCl obtained by impedance analysis and linear polarization curves. Figure 25A shows Bode plots of the total impedance data recorded at E_{corr} versus log frequency. The highest $Z_{0.01\ Hz}$ is seen for 650 C followed by 650 E and V. However, the magnitude of $Z_{0.01\ Hz}$ is a factor of 10-100x lower than the values in the less aggressive 0.5 M Na_2SO_4. All values for the coated specimens are larger than the $Z_{0.01\ Hz}$ for the uncoated control. For example, the value for 650 C is *ca.* 100 kΩ-cm^2, which is 20x larger than the value for the uncoated specimen, *ca.* 5 kΩ-cm^2. Figure 21B shows Nyquist plots of the impedance data recorded at E_{corr}. The largest semi-circle width is seen for 650 C followed by 650 E, 650 V and the uncoated specimen. Figure 25C shows linear polarization curve data for the coated and uncoated specimens. Good linearity is seen in the *i-E* plots ± 25 mV vs. OCP. The trends in these data are opposite those seen in the impedance data. The curve slope is smallest for 650 E (*i.e.*, largest R_p) and decreases in the following order: 650 V > 650 C > uncoated specimen. Figure 25D compares data for the three methods. The R_p values for the coated specimens, determined by all three methods, are statistically larger than the values for the uncoated specimens by 10-50x, depending on the method. There is reasonable agreement among the three methods for 650 V but there is larger divergence in the data for 650 E and C. The nominal R_p values obtained by the linear polarization method are 110 kΩ·cm^2 (1.1 x 10^5 Ω·cm^2)

for 650 E, 20 k$\Omega \cdot cm^2$ (2.0 x 10^4 $\Omega \cdot cm^2$) for 650 V, 15 k$\Omega \cdot cm^2$ (1.5 x 10^4 $\Omega \cdot cm^2$) for 650 C and 5 k$\Omega \cdot cm^2$ (5.0 x 10^3 $\Omega \cdot cm^2$) for the uncoated control. The reason for the differences in trends for the three coatings, observed by ac impedance and linear polarization, is unclear.

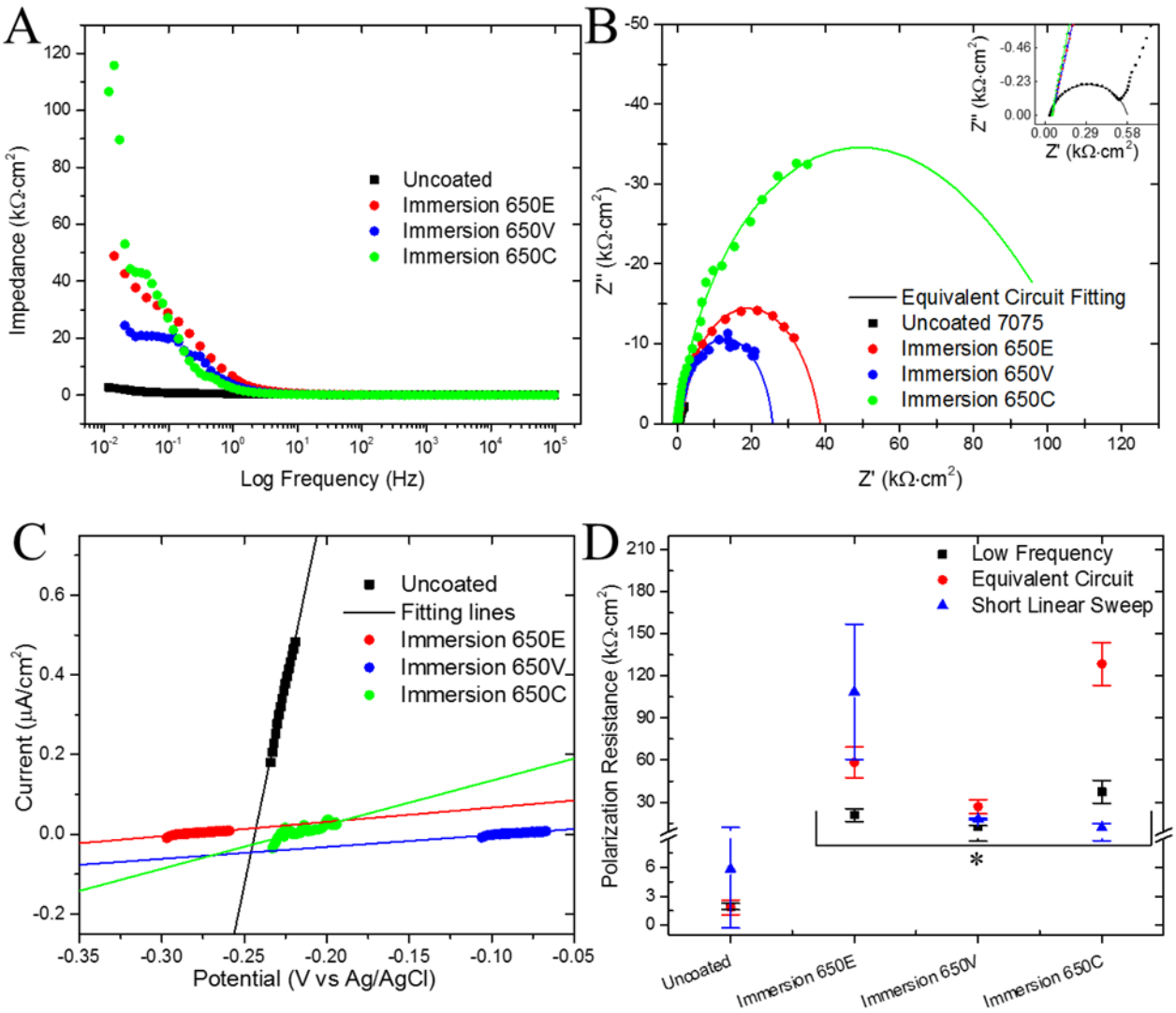

Figure 25. Polarization resistance determined from (A) Bode plots of the total impedance recorded at E_{corr} ($Z_{0.01\ Hz}$), (B) equivalent circuit fitting of Nyquist plots of the impedance data recorded at E_{corr}, and (C) linear polarization curves recorded at ± 25 mV vs. E_{corr} for immersion-coated and uncoated AA7075-T6 specimens in oxygenated 3.5 % NaCl. (D) Plots of the R_p values determined by the three methods for the coated and uncoated specimens displayed as mean ± standard error of the mean (n = 3). Asterisk indicates data significantly different from the uncoated control ($p \leq 0.05$).

3.3.5. Electrochemical Parameter Comparisons

Table 2 summarizes electrochemical parameter data in oxygenated 0.5 M Na_2SO_4 for AA7075-T6 immersion coated with the three TCP coatings as well as data for the untreated control. For all three coatings, the nominal E_{corr} values are slightly more negative of the value for the

uncoated control. The most negative shift (174 mV) is seen for 650 E. The cathodic (-0.80 V) and anodic (-0.10 V) currents are lower for all the TCP-coated specimens than for the uncoated control. The greatest suppression of both currents is seen for 650 E. The cathodic current is suppressed in the following order: 650 E (90x) > 650 C (35x) > 650 V (18x). The anodic current is suppressed in the following order: 650 E (115x) > 650 V (32x) > 650 C (22x). The R_p values are greatest for 650 E (60x increase) followed by 650 C and 650 V. Overall, in this electrolyte solution, 650 E provides the greatest anti-corrosion properties with the coating providing both anodic and cathodic protection to the alloy.

Table 2. Comparison of electrochemical parameters for uncoated and immersion-coated AA7075-T6 specimens in oxygenated 0.5 M Na_2SO_4. Data are presented for 650 E, V, and C coatings. Values are reported as mean ± standard error of the mean (n=3).

0.5 M Na_2SO_4	**Uncoated 7075**	**Immersion 650 E**	**Immersion 650 V**	**Immersion 650 C**
E_{corr} (V vs. Ag/AgCl)	-0.219 ± 0.009	-0.393 ± 0.028	-0.310 ± 0.049	-0.305 ± 0.048
Cathodic Current @ -0.80 V (μA/cm^2)	17.37 ± 4.77	0.19 ± 0.03	0.96 ± 0.31	0.50 ± 0.06
Anodic Current @ -0.10 V (μA/cm^2)	25.22 ± 0.75	0.22 ± 0.05	0.78 ± 0.23	1.15 ± 0.27
Polarization Resistance (R_p) $Z_{0.01Hz}$ (kΩ·cm^2)	22 ± 6	1,275 ± 79	284 ± 34	521 ± 32

Table 3 summarizes electrochemical parameters for uncoated and immersion-coated AA7075-T6 specimens in oxygenated 3.5% NaCl. Data are presented for 650 E, V and C. For all three coatings, the E_{corr} is shifted positive of the value for the uncoated alloy by 40-50 mV. Anodic currents are suppressed more or less equivalently by the three coatings by a factor of 9x. Cathodic currents, on the other hand, are suppressed more in the following order: 650 C (69x) > 650 V (47x) > 650 E (25x). These results indicate that all three TCP coatings provide greater cathodic than

anodic protection in this aggressive electrolyte. The R_p values are more or less the same for all three coatings, a factor of 5-18x greater with 650 C exhibiting the largest nominal value.

Table 3. Comparison of electrochemical parameters for uncoated and immersion-coated AA7075-T6 specimens in oxygenated 3.5% NaCl. Data are presented for 650 E, V, and C coatings. Values are reported as mean ± standard error of the mean (n=3).

3.5% NaCl	**Uncoated 7075**	**Immersion 650 E**	**Immersion 650 V**	**Immersion 650 C**
E_{corr} **(V vs. Ag/AgCl)**	-0.699 ± 0.017	-0.656 ± 0.002	-0.667 ± 0.004	-0.663 ± 0.002
Cathodic Current @ -0.80 V (μA/cm^2)	27.77 ± 1.39	3.33 ± 1.39	3.06 ± 0.59	2.86 ± 0.68
Anodic Current @ -0.65 V (μA/cm^2)	18.18 ± 4.60	0.76 ± 0.16	0.36 ± 0.15	0.26 ± 0.04
Polarization Resistance (R_p) $Z_{0.01\ Hz}$ (kΩ·cm^2)	2 ± 0.3	21 ± 5	11 ± 2	37 ± 8

Table 4 summarizes the E_{corr} values, cathodic (-0.80 V) and anodic (-0.10 V) currents, and R_p values for uncoated, immersion- and spray-coated 650 E in oxygenated 0.5 M Na_2SO_4. The low frequency polarization resistance ($Z_{0.01\ Hz}$) was used as a measure of R_p. E_{corr} for the immersion- and spray-coated specimens is some 150 mV more negative of the value for the uncoated specimen even though the anodic and cathodic currents are both equivalently suppressed (50-100x). The R_p data presented above indicate 650 E applied by both immersion and spray produce similar anti-corrosion properties with R_p increasing by a factor of 50-60x. The higher R_p values are consistent with the suppressed anodic and cathodic currents, as compared to the values for the uncoated specimen. The immersion-coated 650 E inhibits anodic and cathodic currents by 114 and 89%, respectively. The spray coating inhibits anodic and cathodic currents by 109 and 53%. The R_p values determined for this TCP coating are in agreement with values for another commercial TCP coating (Bonderite T5900, Henkel) on this same alloy in naturally-aerated 0.5 M Na_2SO_4.[12,13-

[16,36,37] Overall, the immersion coating provides slightly superior anti-corrosion performance than does the spray coating. The suppressed anodic and cathodic currents indicate the coating provides both anodic and cathodic protection.

Table 4. Comparison of electrochemical parameters for uncoated and conversion-coated AA7075-T6 specimens in oxygenated 0.5 M Na_2SO_4. Data are presented for immersion and spray-coated 650 E. Values are reported as mean ± standard error of the mean (n=3). †TCP coating values are for Bonderite T5900 (Henkel)[17] in naturally-aerated 0.5 M Na_2SO_4. NR = not reported.

0.5 M Na_2SO_4	**Uncoated 7075**	**Immersion 650 E**	**Spray 650 E**	**TCP Coating†**
E_{corr} (V vs. Ag/AgCl)	-0.219 ± 0.009	-0.393 ± 0.028	-0.376 ± 0.031	-0.390 ± 0.030
Cathodic Current @-0.80 V (μA/cm^2)	17.37 ± 4.77	0.193 ± 0.034	0.320 ± 0.090	NR
Anodic Current @-0.10 V (μA/cm^2)	25.22 ± 0.75	0.224 ± 0.053	0.238 ± 0.034	NR
Polarization Resistance (R_p) $Z_{0.01\ Hz}$ (kΩ·cm^2)	22 ± 6	1,275 ± 79	1,078 ± 76	1,260 ± 227

Table 5 summarizes E_{corr} values, cathodic (-0.80 V) and anodic (-0.65 V) currents, and low frequency polarization resistances ($Z_{0.01\ Hz}$) for uncoated, immersion- and spray- coated 650 E on AA7075-T6 in oxygenated 3.5% NaCl. E_{corr} is basically pinned at the breakdown or pitting potential, E_{pit}, for the alloy in this aggressive electrolyte. The TCP coating shifts E_{pit} positive by only about 50 mV from the value for the uncoated specimen. The cathodic (-0.80 V) currents are suppressed by 8-20x and the anodic (-0.65 V) currents are suppressed by 20-60x by the TCP coating. Nominally, the currents are suppressed to a slightly greater extent for the spray-coated 650 E. The R_p values are the same for both coatings and are 10x larger than the value for the uncoated specimen. In the more aggressive 3.5% NaCl, the stand-alone corrosion protection of the coating on this alloy is less (R_p increased 10x) than the corrosion protection provided in the less

aggressive 0.5 M Na_2SO_4 (R_p increase 50x). The suppressed anodic and cathodic currents in both electrolytes suggest that the coating functions as both an anodic and cathodic inhibitor.

Table 5. Comparison of electrochemical parameters for uncoated and conversion-coated AA7075-T6 specimens in oxygenated 3.5% NaCl. Data are presented for immersion- and spray-coated 650 E. Values are reported as mean ± standard error of the mean (n=3).

3.5% NaCl	**Uncoated 7075**	**Immersion 650 E**	**Spray 650 E**
E_{corr} (V vs. Ag/AgCl)	-0.699 ± 0.017	-0.656 ± 0.002	-0.658 ± 0.002
Cathodic Current @-0.80 V (μA/cm^2)	27.77 ± 1.39	3.33 ± 1.39	1.29 ± 0.15
Anodic Current @ -0.65 V (μA/cm^2)	18.18 ± 4.60	0.76 ± 0.16	0.32 ± 0.01
Polarization Resistance (R_p) $Z_{0.01\ Hz}$ (kΩ·cm^2)	2 ± 0.3	21 ± 5	22 ± 2

3.3.6. Thin-Layer Mist Accelerated Degradation Test

This accelerated degradation test was used to determine how well the electrochemical parameters predict the actual anti-corrosion performance of the coating during an aggressive environmental exposure. Uncoated and TCP-coated specimens were exposed to a 14-day (336 h) thin-layer mist test (3.5 % NaCl, 55 ^{o}C). The optical images shown in Figure 26 of the uncoated specimen reveal significant corrosion damage over the entire alloy surface after 14 days. This particular test is quite aggressive to the alloy as there is a change in wetting during each cycle, high chloride concentration that increases with droplet evaporation, temperature changes from 55°C to room temperature during each cycle and a high flux of dissolved oxygen to the surface due to a relative thin solution layer. The images also reveal that there is less corrosion protection offered by 650 V and C as compared to 650 E. The 650 E-coated alloy has far fewer pits and discolored regions as compared to the 650 C-coated panel, in particular. For example, large

discolored and damaged regions are seen in the upper right of the image panel for 650 C after 14 days. The 650 V-coated panel also has minimal visible damage. The stand-alone corrosion protection provided by the 650 E during this accelerated degradation test is qualitatively consistent with the trends in the electrochemical data.

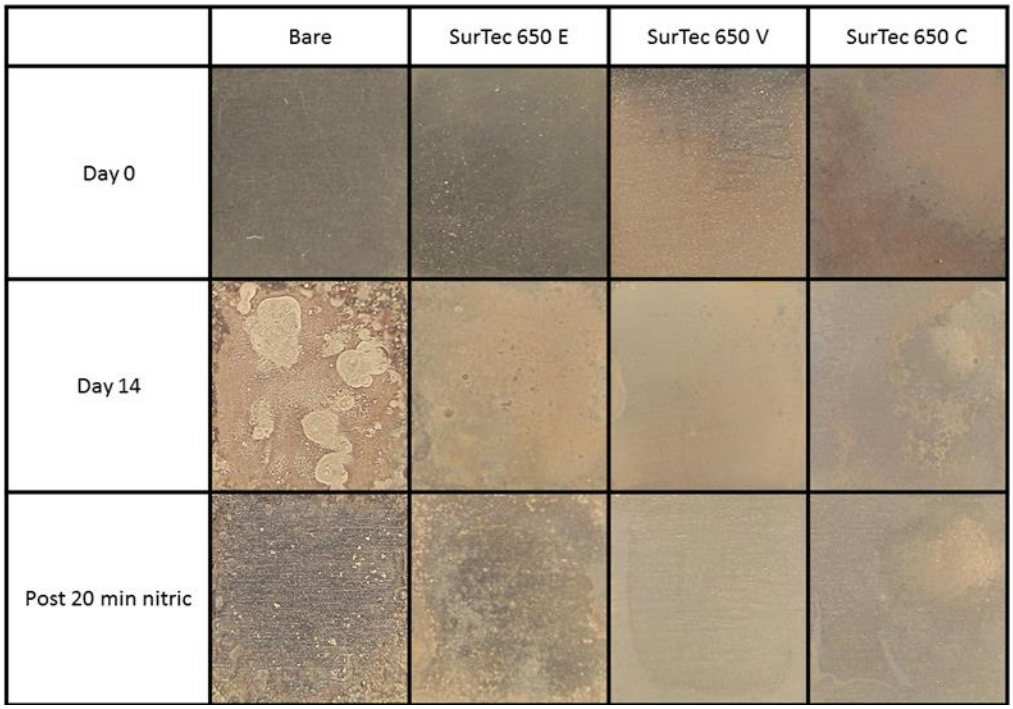

Figure 26. Optical micrographs of uncoated and TCP-coated specimens before and after exposure to a 14-day (336 h) thin-layer mist test (3.5 % NaCl, 55 ^{o}C). Image dimensions are 1 x 1 cm^2.

After the exposure, the corrosion product and conversion coating were removed by exposure to nitric acid for 20 min. This time was probably longer than necessary as both the corrosion product and coating as well as some of the underlying alloy were dissolved, leading to a weight loss that does not reflect just the loss of corrosion product. Nevertheless, the weight loss data are consistent with the qualitative assessment of the panels by microscopy and the predictions based on the electrochemical data: 1.61 ± 0.18 mg (uncoated), 0.36 ± 0.04 mg (650 E), 0.70 ± 0.06 mg (650 V) and 0.68 ± 0.02 mg (650 C). The best corrosion protection, based on the weight loss data, is offered by 650 E.

3.4. Discussion

In order to understand the trends in the electrochemical data and the accelerated degradation test results for the three TCP coating variants, it is useful to review what is known about the physical and chemical properties of the coatings on this alloy formed by immersion and spray.[26] The following are conclusions reached from previously reported characterization:

1. The Cr concentration is similar for all three coating baths at ~150 ppm. The nominal Zr concentration in all three baths is higher than the Cr concentration by about a factor of *ca.* 2x. The nominal Zr concentration is slightly greater in 650 V and C (350 and 340 ppm) than in 650 E (275 ppm). 650 V and C contain significant levels of Zn while the Fe level is greatest in 650 C as compared to 650 E and V.

2. The conversion coatings (immersion or spray) form over all regions of the alloy surface with some enrichment on and around intermetallic particles. Conversion coatings formed by immersion consist of coating aggregates. The number density of the aggregates is greater for 650 E and C than 650 V. Based on EDXS elemental intensities, greater coating coverage is seen for 650 E and C. The 650 C coating is characterized by cracks and delamination.

3. Conversion coatings formed by spray are characterized fewer coating aggregates than their immersion-coated counterparts. There is increased alloy pitting and trenching around intermetallic particles when the coatings are spray applied. This is attributed to a thin solution layer and increase flux of dissolved oxygen to the cathodically-active intermetallic particles.

4. AES depth profiling indicates the 650 E conversion coating (immersion and spray) consists of a biphasic structure. An outer layer (30-50 nm) exists that is rich in Zr and Cr. There is also an interfacial region (~50 nm) rich in Al, O, F and some Cr. The maximum Zr/Cr atomic concentration ratio is *ca.* 3:1 in the coatings.

5. The conversion coatings (immersion or spray) become more hydrophobic over a 7-day aging period in the laboratory air. For both the immersion and spray-on coatings, 650 E and 650 C are quite hydrophilic ($\theta \sim 10^o$) at day 1, more so that 650 V ($\theta \sim 60\text{-}80^o$). There may be more organic content in 650 V, which would explain the more hydrophobic character. Static water contact angles at day 7 are $60\text{-}90^o$ for all the coatings.

6. Ellipsometry data indicate 650 E is the thickest of the three coatings. At the 7-day point, the final mean thicknesses of the immersion coatings are 95, 50 and 75 nm for 650 E, C and V, respectively. For the spray coatings, the final mean thickness at the 7-day point was 75, 62 and 53 nm, respectively, for 650 E, C and V. Overall, the thickness of the spray-coated films (3 min) is less than the immersion-coated films (4 min).

Overall, the electrochemical data indicate that 650 E provides the greatest level of stand-alone corrosion protection, as compared to 650 V and C, and that there are no major differences in the level of protection provided by coatings (650 E) applied by immersion or spray, at least under the test conditions used herein (*e.g.*, see Tables 2-5). The coatings can be reproducibly applied by immersion or spray based on the low variability in the electrochemical parameters from sample to sample. The 650 E coating bath contains the greatest ratio of Cr/Zr and this translates into superior corrosion protection. The coatings formed from 650 E are more complete and less defective than those formed from 650 V and C based on previously reported SEM images.[26] Even though conversion coatings formed by spray (< 80 nm nominally) are a little thinner, based on ellipsometry data, than are coatings formed by immersion (~100 nm nominally), the corrosion protection is comparable. A previously reported for other commercial TCP coatings (Bonderite T5900, Henkel), the SurTec 650 E coating has a biphasic structure with an outer layer (30-50 nm) rich in Zr and Cr, and an interfacial region (~50 nm) rich in Al, O, F and some Cr. The coating

forms over most areas of the alloy surface with some thickening on and around intermetallic phases.[9,13,14,16,18,20] The spray-coated films have less of the coating aggregates formed on the surface, which may beneficially impact primer adhesion, but there is more trenching around intermetallic particles and pitting of the alloy surface during the coating application as compared to immersion coatings. Overall, the electrochemical results are consistent with what is predicted based on the physical structure of the coatings.[26]

The coatings provide both anodic and cathodic protection in low chloride electrolytes and work as more of a cathodic inhibitor in high chloride electrolytes. This assessment is based on the fact that both anodic and cathodic currents are suppressed around the OCP or E_{corr} in both 0.5 M Na_2SO_4 and 3.5% NaCl. For 650 E, the cathodic current is suppressed by 90x and the anodic current by 115x in the less aggressive 0.5 M Na_2SO_4, as compared to the currents for the uncoated alloy. In the more aggressive 3.5% NaCl, the cathodic current is suppressed by 9x and the anodic current by 23x, as compared to currents for the uncoated alloy. Nominal R_p values are some 60x greater in Na_2SO_4 for the 650 E-coated as compared to the uncoated alloy. Nominal R_p values are only 10x greater for the coated than for the uncoated alloy in NaCl. The conversion coating clearly provides some barrier layer protection. The fact that the coating forms on both the aluminum matrix and the intermetallic phases explains the fact that both anodic and cathodic currents are suppressed. The stand-alone corrosion protection afforded by TCP coating is reduced in the more aggressive 3.5% NaCl. This could be because of penetration by the electrolyte through defects and pinholes in the coating, which leads to breakdown of the passivating oxide layer on the exposed aluminum, pitting corrosion and undercutting of the conversion coating. Breakdown of the passivating oxide on the exposed aluminum does not occur in the less aggressive Na_2SO_4. In fact, there might even be some additional passivation in this electrolyte.[38] Consistent with the reduced

corrosion protection by the conversion coating in high chloride-containing electrolytes is the fact that at low chloride concentrations (see Fig. 7), the breakdown potential or E_{pit} is more noble for the TCP-coated alloy than for the uncoated alloy by some 400 mV. However, at high concentrations E_{pit} for the coated alloy is the same as that for the uncoated alloy. These data are for a different alloy (AA2024-T3) and a commercial conversion coating (Bonderite T5900, Henkel) but the trend is clear. The electrochemical data are merely predictive about corrosion protection. Such data should also be coupled with tests of the coated specimens under environmental exposure or exposure to accelerated degradation. The results presented herein for the thin-layer mist exposure reveal that, as predicted from the electrochemical data, 650 E provides superior corrosion protection.

Rotating disk voltammetric data are presented for the first time for TCP-coated AA7075-T6. The data reveal that the reduction of dissolved oxygen proceeds via a diffusion-controlled process on the uncoated alloy based on the linearity of the i_l vs. $\omega^{1/2}$ (see Fig. 8); however, on the TCP-coated alloy limiting currents are largely invariant with the rotation rate. Similar trends have been observed for oxygen reduction on AA2024-T3 in chromate-containing solutions.[31,32] This indicates that the conversion coating functions as a diffusional barrier. This a bit surprising given the thin nature of the coating (~100 nm) and the fact that the coating consists of some native defects (cracks and pinholes). Therefore, we also believe that the invariance of i_l with ω is due to blockade of O_2 chemisorption sites on the cathodic intermetallic particles where the kinetics for the reduction reaction are expected to be highest. EDXS data reveal that the conversion coating thickness is greater on and around intermetallic phases and that both Zr and Cr are present. The formation of relatively insoluble $Cr(OH)_3$ on the intermetallic surface appears to block chemisorption sites. Evidence for the important role of Cr species at inhibiting oxygen reduction

comes from preliminary rotating disk voltammetric data for AA2024-T3 coated with a normal TCP coating (Bonderite T5900, Henkel) and coated with the same conversion coating devoid of any added chromium species. The voltammetic data for oxygen reduction showed linear increases in i_l with $\omega^{1/2}$ for the uncoated alloy and an unchanging i_l with $\omega^{1/2}$ for the alloy coated with normal TCP. For the alloy coated with TCP devoid of Cr species, i_l increased linearly with $\omega^{1/2}$ albeit with a slope about half that for the uncoated alloy. The reduced slope is due to a lower apparent diffusion coefficient for oxygen through the coating and a reduced area available for the reaction. Rotating disk voltammetric data (see Fig. 9) indicate that the TCP coating inhibits oxygen reduction on multiple aluminum alloys (AA2024-T3, AA6061-T6 and AA7075-T6). The limiting current for oxygen reduction is close to being invariant with $\omega^{1/2}$ for all three alloys. The difference in current magnitude (2024 > 7075 > 6061) trends with the level of Cu in the alloys.[17,18]

3.5. Conclusions

Detailed electrochemical investigations were performed on three commercial variants of a trivalent chromium process (TCP) conversion coating on AA7075-T6. Prior work reported on the physical and chemical properties of these same coatings on this alloy.[26] The key findings from the present were can be summarized as follows:

1. The TCP conversion coatings can be formed reproducibility on this alloy by both immersion and spray application. The electrochemical properties of alloys coated by immersion were not significantly different than the properties of coatings formed by spray, even though the spray coatings a nominally thinner.
1. The conversion coatings provide both anodic and cathodic protection in low chloride-containing electrolytes and function more as a cathodic inhibitor in high chloride-containing electrolytes.

2. The greatest corrosion protection is provided by 650 E based on electrochemical data and a 14-day thin-layer mist test.

3. The breakdown potential or E_{pit} is shifted noble by some 400 mV in low chloride-containing electrolytes, as compared to values for the uncoated alloy. In high chloride-containing electrolytes, E_{pit} is nominally the same for the coated and uncoated alloy.

4. Rotating disk voltammetric data reveal that the limiting current for oxygen reduction is largely invariant with the rotation rate. The result indicates the TCP coating provides cathodic protection by functioning as a diffusional barrier and blocking O_2 chemisorption sites on the cathodically-active Cu-rich intermetallics.

REFERENCES

REFERENCES

Currently in the process of publication in Corrosion.

1. J. LaScala, Non-chromate/no-VOC coating systems for DoD applications, (WP-1521), Final Report, SERDP, 2009.

2. M. Costa. Toxicity and carcinogenicity of Cr(VI) in animal models and humans, *Critical Rev. Toxicol*. **1997**, *27*, 431-442.

3. S. Mishra, R. N. Bharagava. Toxic and genotoxic effects of hexavalent chromium in environment and its bioremediation strategies. *J. Environ. Sci. Health C. Environ. Carcinog. Ecotoxicol. Rev.* **2016**, *34*, 1-32.

4. R. L. Twite, G. P. Bierwagen. Review of alternatives to chromate for corrosion protection of aluminum aerospace alloys, Prog. *Org. Coat*. **1998**, *33*, 91-100.

5. S. A. Kulinich, A. S. Akhtar. On conversion coating treatments to replace chromating for Al alloys: recent developments and possible future directions, *Russ. J. Non-Ferrous Metals*, **2012**, *53*, 176-203.

6. M. W. Kendig, R. G. Buchheit. Corrosion inhibition of aluminum and aluminum alloys by soluble chromates, chromate coatings, and chromate-free coatings, *Corrosion*, **2003**, *59*, 379 -400.

7. H. Guan, R. G. Buchheit. Corrosion protection of aluminum alloy 2024-T3 by vanadate conversion coatings, *Corrosion*, **2004**, *60*, 284-296.

8. C. A. Matzdorf, W. C. Nickerson, Jr., E. N. Beck, A. S. Schwartz and J. L. Green. U.S. Patent Application Publication, *Non-Chromium Coatings for Aluminum*, US2007/0095436 A1, May 3, **2007**.

9. L. Li, B. W. Whitman, C. A. Munson, R. Estrada, C. A. Matzdorf, G. M. Swain. Structure and corrosion performance of a non-chromium process (NCP) Zr/Zn pretreatment conversion coating on aluminum alloys, *J. Electrochem. Soc*., **2016,** *163*, C1-11.

10. S. L. Suib, J. LaScala, W. Nickerson, A. Fowler, N. Zaki. Determination of hexavalent chromium in NAVAIR trivalent chromium process (TCP) coatings and process solutions, *Metal Finishing* **2009**, *107*, 28, 31-34.

11. A. Iyer, W. Willis, S. Frueh, W. Nickerson, A. Fowler, J. Bames, L. Hagos, J. Escarsega, J. La Scala, S.L. Suib. Characterization of NAVAIR trivalent chromium process (TCP) coatings and solutions, *Plating and Surface Finishing*, **2010**, *5*, 32-42.

12. X. C. Dong, P. Wang, S. Argekar and D. W. Shaefer. Structure and composition of trivalent chromium process (TCP) films on Al alloy, *Langmuir* **2010,** *26*, 10833-10841.

13. L.L. Li, G. P. Swain, A. Howell, D. Woodbury, G. M. Swain. The formation, structure, electrochemical properties and stability of trivalent chromium process (TCP) coatings on AA2024, *J. Electrochem. Soc.*, **2011**, *158*, C274-283.

14. Y. Guo, G. S. Frankel. Characterization of trivalent chromium process coating on AA2024-T3, *Surf. Coat. Technol.* **2012**, *206*, 3895-3902.

15. Y. Guo, G. S. Frankel. Active corrosion inhibition of AA2024-T3 by trivalent chrome process treatment, *Corrosion*, **2012**, *68*, 045002-1-045002-10.

16. L. L. Li, D. Y. Kim, G. M. Swain. Transient formation of chromate in trivalent chromium process (TCP) coatings on AA2024, J. *Electrochem. Soc*. **2012**, *159*, C326-C333.

17. L. L. Li and G. M. Swain. Formation and structure of trivalent chromium process coatings on aluminum alloys 6061 and 7075, *Corrosion*, **2013**, *69*, 1205-1219.

18. L. L. Li, K. P. Doran, G. M. Swain. Electrochemical characterization of trivalent chromium process (TCP) coatings on AA6061 and 7075, *J. Electrochem. Soc*., **2013**, *160*, C396-C401.

19. L. L. Li, G. M. Swain. Effects of aging temperature and time on the corrosion protection provided by trivalent chromium process coatings on AA2024-T3, *ACS Appl. Mater. Interfaces* **2013**, *5*, 7923-7930.

20. J. T. Qi, T. Hashimoto, J. R. Walton, X. Zhou, P. Skeldon, G. E. Thompson. Trivalent chromium conversion coating formation on aluminum, *Surf. Coat. Technol*., **2015**, *280*, 317-329.

21. J. Qi, T. Hashimoto, J. Walton, X. Zhou, P. Skeldon and G. E. Thompson. Formation of a trivalent chromium conversion coating on AA2024-T351 alloy, *J. Electrochem. Soc.*, **2016**, *163*, C25-C35.

22. J. Qi, T. Hashimoto, G. E. Thompson and J. Carr. Influence of water immersion post-treatment parameters on trivalent chromium conversion coatings formed on AA2024-T351 alloy, *J. Electrochem. Soc.*, **2016**, *163*, C131 -138.

23. Z. Feng, J. Boerstler, G. S. Frankel, C. A. Matzdorf. Effect of surface pretreatment on galvanic attack of coated Al alloy panels, *Corrosion*, **2015**, *71*, 771-783.

24. J. Qi, A. Nemcova, J. R. Walton, X. Zhou, P. Skeldon, G. E. Thompson. Influence of pre- and post-treatments on the formation of a trivalent chromium conversion coating on AA2024 alloy, *Thin Solid Films*, **2016**, *616*, 270-278.

25. J. Qi, J. Walton, G. E. Thompson, S. P. Albu, J. Carr. Spectroscopic studies of chromium VI found in the trivalent chromium conversion coatings on aluminum, *J. Electrochem. Soc.* **2016**, *163*, C357-C363.

26. C. A. Munson, G. M. Swain. Structure and chemical composition of different variants of a commercial trivalent chromium process (TCP) coating on aluminum alloy 7075-T6, *Surf. Coat. Technol.*, **2017**, *315*, 150-162.

27. L. L. Song, J. F. Li, C. Cai. Corrosion resistance and self-repairing behavior of Cr(III) containing conversion coating on AA2024-T3, *Corrosion Engr. Sci. Technol*., **2016**, *51*, 263-271.

28. ASM Aerospace Specification Metals Inc. Accessed August 2015: http://asm.matweb.com/search/SpecificMaterial.asp?bassnum=MA7075T6.

29. M. C. Granger, M. Witek, J. S. Xu, J. Wang, M. Hupert, A. Hanks, M. D. Koppang, J. E. Butler, G. Lucazeau, M. Mermoux, G. M. Swain. Standard electrochemical behavior of high-quality, boron-doped polycrystalline diamond thin-film electrodes, *Anal. Chem.*, **2000**, *72*, 3793-3804.

30. G. O. Ilevbare, J. R. Scully. Oxygen reduction reaction kinetics on chromate conversion coated Al-Cu, Al-Cu-Mg and Al-Cu-Mn-Fe intermetallic compounds, *J. Electrochem. Soc.* **2001**, *148*, B196-B207.

31. G. O. Ilevbare, J. R. Scully. Mass transport limited oxygen reduction reaction on AA2024-T3 and selected intermetallic compounds in chromate-containing solutions, *Corrosion* **2001**, *57*, 134-152.

32. K. D. Ralston, T. L. Young, R. G. Buchheit. Electrochemical evaluation of constituent intermetallics on aluminum alloy 2024-T3 exposed to vanadate inhibitors, *J. Electrochem. Soc.* **2009**, *153*, C135-C146.

33. A. L. Colley, J. V. Macpherson, P. R. Unwin. Effect of high rates of mass transport on oxygen reduction at copper electrodes: implications in aluminum corrosion, *Electrochem. Comm.* **2008**, *10*, 1334-1336.

34. M. A. Jakab, F. Presuel-Moreno, J. R. Scully. Effect of molybdate, cerium and cobalt ions on the oxygen reduction reaction on AA2024-T3 and selected intermetallics, *J. Electrochem. Soc.* **2006**, *153*, B244-B252.

35. M. E. Orazem, B. Tribollet. Electrochemical Impedance Spectroscopy, 1st ed.; Wiley-Interscience: Hoboken, NJ, **2008**; pp.156−162.

36. L. Li, A. L. Desouza, G. M. Swain. Effect of deoxidation pretreatment on the corrosion inhibition provided by a trivalent chromium process (TCP) conversion coating on AA2024-T3, *J. Electrochem. Soc.*, **2014**, *161*, C246-C253.

37. L. Li, G. M. Swain. Effects of aging temperature and time on the corrosion protection provided by trivalent chromium process coatings on AA2024-T3, *ACS Appl. Mater. Interfaces*, **2013**, *5*, 7923-7930.

38. P. Klomjit, R. G. Buchheit. Localized corrosion inhibition of AA7075-T6 by calcium sulfate, *Corrosion*, **2016**, *72*, 486-499.

CHAPTER 4: CROSS COMPARISON OF TCP- AND NCP-COATED AA7075-T6 DURING THIN-LAYER MIST AND SALT-SPRAY ACCELERATED DEGRADATION TESTING: SURFACE PROFILOMETRY AND OPTICAL MICROSCOPY

4.1. Introduction and Research Objectives

The anti-corrosion properties of SurTec 650 E, formed by standard immersion, were directly compared to the anti-corrosion properties of the three other commercial TCP coatings [Bonderite T5900 (Henkel), TCP-HF (Chemeon), and Aluminescent (Luster-on)] on AA7075-T6. The performance of the TCP coatings was also compared to that of a non-chromated conversion coating, NCP developed by NAVAIR. The commercial TCP coatings are all licensed from NAVAIR and are based on the original formulation.[1-4] However, each contains a slightly different chemical composition, so from a research perspective, each should be treated as a separate coating system. Studies were conducted on panels subjected to a 7-day neutral salt-spray (ASTM B117, 5 wt. % NaCl) and a 7-day thin-layer mist (3.5 wt.% NaCl, 55 ^{o}C) accelerated degradation test. The alloys were inspected for damage using optical and scanning electron microscopy after removal of the corrosion product layer with a nitric acid etch.[5]. The material lost due to corrosion was quantified by weight loss measurements and contact scanning profilometry. A 7-day (169 h) exposure period was used for coating evaluation because this time is required by the DoD when qualifying chemical conversion coating performance on aluminum and aluminum alloys, as described in the military document, MIL-DTL-5541F.

4.2. Experimental Procedures

4.2.1. ICP-OES Analysis of Coating Baths

Quantitative inorganic chemical analysis of all coating baths was performed on a Varian 710-ES ICP-OES. Quantitation was accomplished using response curves generated by external standards (0.001-100 ppm).

Specimen Preparation

The aluminum alloy specimens (www.onlinemetals.com) were used as received with no mechanical grinding or polishing. The specimens were marked on the back for easy identification. The thin-layer mist (TLM) test utilized square specimens 1 cm^2 in area while the salt-spray (SS) test utilized square specimens 1 in^2 (2.54 cm^2) in area. All as received alloy specimens were cleaned with a Kimwipe and acetone prior to the degreasing step. In most cases, three specimens were degreased, deoxidized and immersion coated at the same time during a test run.

Uncoated Control Specimens

A specimen was degreased with 20 vol. % Turco 6849 (Henkel) in a glass beaker (50 mL) at 55°C for 10 min with periodic agitation accomplished by careful solution swirling. This was followed by a 2-min flowing city tap water rinse. The water flowed along the sides of the beaker containing the specimens and not directly onto the specimen surface. The water was then allowed to continuously overflow the beaker for a 2-min period. This is referred to as the overflow method. The specimen was then deoxidized/desmutted with 20 vol. % Turco Liquid Smut-Go (Henkel) at room temperature (~23 ^{o}C) for 2 min in the glass beaker. This was also followed by a city tap water soak for 2 min and then an ultrapure water soak for 30 s. After the immersion, excess water was wicked off the uncoated surface using the edge of a Kimwipe. This was followed by drying the specimen with a stream of N_2 gas. The pretreated specimen was then used immediately in the accelerated degradation tests.

Bonderite T-5900 (Henkel) TCP Coating

A specimen was degreased with 20 vol. % Turco 6849 at 55°C for 10 min using periodic agitation. This was followed by a city tap water overflow rinse for 2 min. The specimen was then deoxidized with 20 vol. % Turco Liquid Smut-Go at room temperature (~23 ^{o}C) for 2 min. This

was also followed by a city tap water overflow rinse for 2 min. To form the conversion coating, the degreased and deoxidized specimen was immersed face up in the RTU Bonderite T-5900 coating bath (pH 3.63) at room temperature for 10 min, with very gentle periodic beaker agitation, as needed, to remove any gas bubbles (H_2) that formed on the metal surface. This was followed by a 2-min city tap water soak and then a 30-s soak in ultrapure water. Excess water was carefully wicked off the coated surface using the edge of a Kimwipe. This was followed by overnight drying in a covered petri dish at room temperature. These and all the other coating conditions described below were performed as per the recommendations of the suppliers.

chromitAL 650E (SurTec) TCP Coating

A specimen was degreased with 4 wt. % SurTec 133 at 55°C for 5 min using periodic beaker agitation. This was followed by a city tap water overflow rinse for 2 min. The specimen was then deoxidized with 20 vol. % SurTec 495L at room temperature (~23 ^{o}C) for 2 min. This was also followed by a 2-min city tap water overflow rinse. To form the conversion coating, the specimen was immersed face up in a 20 vol. % SurTec E (pH = 3.85) coating bath at 30°C for 10 min, with very gentle beaker agitation, as needed, to remove any bubbles that formed on the metal surface. This was followed by a 2-min city tap water soak and then a 30-s ultrapure water soak. Excess water was carefully wicked off the coated surface using the edge of a Kimwipe. This was followed by overnight drying in a covered petri dish at room temperature. In this work, only the 650 E coating was studied extensively.

TCP-HF (Chemeon) TCP Coating

A specimen was degreased with 4.5 wt. % Chemeon Cleaner 1000 at 43-49°C for 10 min using periodic beaker agitation. This was followed by a city tap water overflow rinse for 2 min. The specimen was then deoxidized using 35 vol. % nitric acid at room temperature (~23 ^{o}C) for 1

min. This was followed by a city tap water overflow rinse for 2 min. To form the conversion coating, the specimen was immersed face up in a 30 vol. % TCP-HF (pH = 3.85) coating bath at 30°C for 10 min with very gentle beaker agitation, as needed, to remove any gas bubbles that formed on the metal surface. The coating bath was prepared at least 24 h and not more than 2 months before use. After immersion coating, the specimen was followed by a city tap water soak for 2 min, then a 30-s soak in ultrapure water. Excess water was carefully wicked off the coated surface using the edge of a Kimwipe. This was followed by overnight drying in a covered petri dish at room temperature.

Aluminescent (Luster-on) TCP Coating

A specimen was degreased with 4 wt. % Luster-On 401 at 60°C for 5 min using periodic beaker agitation. This was followed by a city tap water overflow rinse for 2 min. The specimen was then deoxidized with 3.9 vol. % Luster-On 485 at room temperature (~23 ^{o}C) for 2 min. This was also followed by a 2-min city tap water overflow rinse. To form the conversion coating, the specimen was placed face up in a 1 wt. % Luster-On Aluminescent (pH = 3.5-4) coating bath at room temperature for 10 min, with very gentle beaker agitation, as needed, to remove any gas bubbles that formed on the metal surface. This was followed by a city tap water soak for 2 min and then a 30-s soak in ultrapure water. Excess water was carefully wicked off the coated surface using the edge of a Kimwipe. This was followed by overnight drying in a covered petri dish at room temperature.

NCP (NAVAIR) Conversion Coating

A specimen was degreased with 20 vol. % Turco 6849 at 55°C for 10 min with periodic beaker agitation. This was followed by a city tap water overflow rinse for 2 min. The specimen was then deoxidized with 20 vol. % Turco Liquid Smut-Go at room temperature (~23 ^{o}C) for 2

min. This was followed by a 2-min city tap water overflow rinse. To form the conversion coating, the specimen was immersed face up in a 100% NAVAIR NCP (RTU) coating bath at room temperature for 10 min, with gentle beaker agitation, as needed, to remove any gas bubbles that formed on the metal surface. This was followed by a city tap water soak for 2 min and then a 30-s soak in ultrananopure water. Excess water was carefully wicked off the coated surface using the edge of a Kimwipe. This was followed by overnight drying in a covered petri dish at room temperature.

4.2.3. Accelerated Degradation Tests

Thin-Layer Mist Test

Specimens were placed horizontal (coated side up) on plastic lids inside a sealed 16-oz. propylene carbonate screw-top container ¼ filled with 100 mL of ultrapure water. Three specimens were positioned above the water layer. A spray bottle (*e.g.*, plant mister) was used to wet the coated specimens with 5 sprays of a 3.5 wt. % NaCl solution (*ca.* 1 cm^2 area) once per day over a 7-day test period (168 h). The mist was applied with the samples at room temperature. The water in the bottom of the container ensured that a humid atmosphere was maintained inside the container during the test. Once the specimens were sprayed and the container opened to the atmosphere for 30-60 min, the container was tightly sealed to limit water evaporation and placed in an oven at 55°C. Exposure was then for 23 h. At the end of each daily test cycle, the container was removed, the specimens cooled and the mist reapplied over a 30-60 min period. There was presumably a decreasing dissolved oxygen concentration in solution over the period because the container was sealed. Oxygen is consumed in the overall corrosion reaction:

$$4(Al \leftrightarrow Al^{+3} + 3e^{-}) \text{ anodic (11)}$$

$$3(O_2 + 4H^{+} + 4e^{-} \leftrightarrow 2H_2O) \text{ cathodic (12)}$$

$$4Al + 3O_2 + 12H^+ \leftrightarrow 4Al^{+3} + 6H_2O \text{ net (13)}$$

At the end of the test period, the specimens were removed, rinsed thoroughly with ultrapure water, and dried under a stream of N_2 gas. After photos were taken, accumulated corrosion product on the surfaces was removed by exposure concentrated nitric acid for 20 min in a covered glass beaker, replacing the nitric acid after 10 min to prevent aluminum dissolution.[5]

Salt-spray (ASTM B117) Test

Specimens were placed at a ~20° angle (with respect to the vertical axis) on plastic racks inside the salt-spray chamber (Associated Environmental Systems, MX-04, 4 ft^3). The chamber was filled with a 5 wt. % NaCl solution. The salt fog test was conducted according to ASTM B117 for the 7-days (35 ºC). At the end of the test period, the specimens were removed, rinsed thoroughly with ultrapure water, and dried under a stream of N_2 gas. After photos were taken, any corrosion product was removed by ultrasonication in concentrated nitric acid for 20 min. The acid exposure was performed in a covered glass beaker, replacing the nitric acid after 10 min to prevent nitric acid photochemical decomposition, which could lead to increased matrix dissolution.[5] Nitric acid-treated specimens were then rinsed thoroughly with ultrapure water and dried using a stream of N_2 gas prior to any analysis.

4.2.4. Visual Analysis

Photographs were taken using a Canon PowerShot SD1300IS 12 MP digital camera with 4x wide-angle optical image stabilized zoom using the macro image setting. Photographs were processed using paint.net photo processing software into black and white images with enhanced contrast for improved visualization of features. All images encompass an area slightly less than the total specimen surface area, to prevent edge lighting differences from influencing the specimen visualization. Specimen surface areas (coated surface) were 1 cm^2 for the thin-layer mist test and

1 in^2 for salt-spray test. Images of water droplets across the surface, for the purpose of assessing hydrophobicity, show the entire 1 cm^2 specimen.

4.2.5. Optical Microscopy and Image Analysis

Optical microscope images were taken with an Olympus BX50 microscope with a 100x objective. Pits were determined and manually counted in the image frame (areas of ~10,000 μm^2 $\approx$ 0.01 mm^2). The images were analyzed with ImageJ software. Specifically, the particle analysis feature was used to determine the pit size (in μm^2) and pit number in the imaged area. From the number of pits in the image area, the pit density was calculated (in pits/mm^2). Micrographs were imported, an internal scale was established in the software using a reference micrometer-sized grid, and pits were identified visually. The image was then converted to a black and white photograph with only the pits darkened. The particle analysis feature determined the number of pits in addition to the individual size of each pit.

4.2.6. Contact Mode Scanning Profilometry

Profilometry maps and surface topography profiles were obtained over a 1 mm^2 area in three selected regions of each sample where a pit was visible in the optical micrographs. Profilometry analysis was performed using a NanoMap-500LS Contact Surface Profilometer with 0.5 nm resolution along the z-axis. The stylus has a sharp, pointed 2-micron tip made of tungsten carbide, with a 60º taper. The maps were obtained with 10 µm resolution along the x- and y-axes, using a standard contact load of 10 mg. The contact load was not optimized, but should be in future work. The depth profile maps were analyzed using SPIP software to determine the deepest pits and RMS roughness in each region on 3 specimens in a treatment group. The data presented are pooled from the results from all three specimens. The line profiles shown were chosen along the deepest pitting spot visible in each map. The maximum value of the line scan was used to

establish the zero point, as maps were conducted from the lowest point on the surface upwards, centered around a pit or damaged site, meaning that the highest point on the scan should be at the alloy surface. When this maximum value is subtracted from the other line scan values, the values are representative of the distance penetrated into the alloy surface.

4.2.7. Statistical Analysis and Graphs

All statistical analysis was performed using OriginPro 9.0, with values reported as mean ± standard error of the mean. The Gibbs test was used to remove any outlying values. Statistical differences between sample sets were determined with a two-sample t-test at the 0.05 confidence level. All graphs were created in OriginPro 9.0.

4.3. Cross Comparison Results

4.3.1. Coating Bath Elemental Analysis

All coating baths were examined using ICP-OES to determine the inorganic elemental composition. Particular attention was paid to the coating elements (Cr, Zr, and Zn) and relative amounts in each coating. The nominal values are included in Table 6. A comparison of the elemental composition of the coating baths (Figure 27) shows the highest Cr concentration in Luster-On (416 ppm), which should, in theory, produce the best corrosion protection. The second highest Cr content was found in Chemeon (332 ppm), then Henkel (327 ppm), with SurTec having a >2x lower amount (119 ppm). The anti-corrosion properties of these coatings are expected to follow this trend. The non-chromium process coating (NAVAIR NCP) contained no Cr. The ratio of Zr/Cr is also important, since these elements co-precipitate to form the coating. The Zr oxide formation reaction probably has faster reaction kinetics than the Cr oxide formation reaction, so a lower Zr/Cr ratio should lead to films with more Cr compounds available to provide active corrosion protection.[8] The Zr/Cr ratio trend is Chemeon (0.9:1) < Henkel (1.74:1) < SurTec (2:1)

< Luster-On (2.1:1). The nominal amount of Cr is probably an important factor, since the more Cr present in the bath, the more $Cr(OH)_3$ that is possible in the coating. Therefore, the anti-corrosion behavior is predicted to decrease in the following order: Luster-On > Chemeon > Henkel > SurTec > NCP.

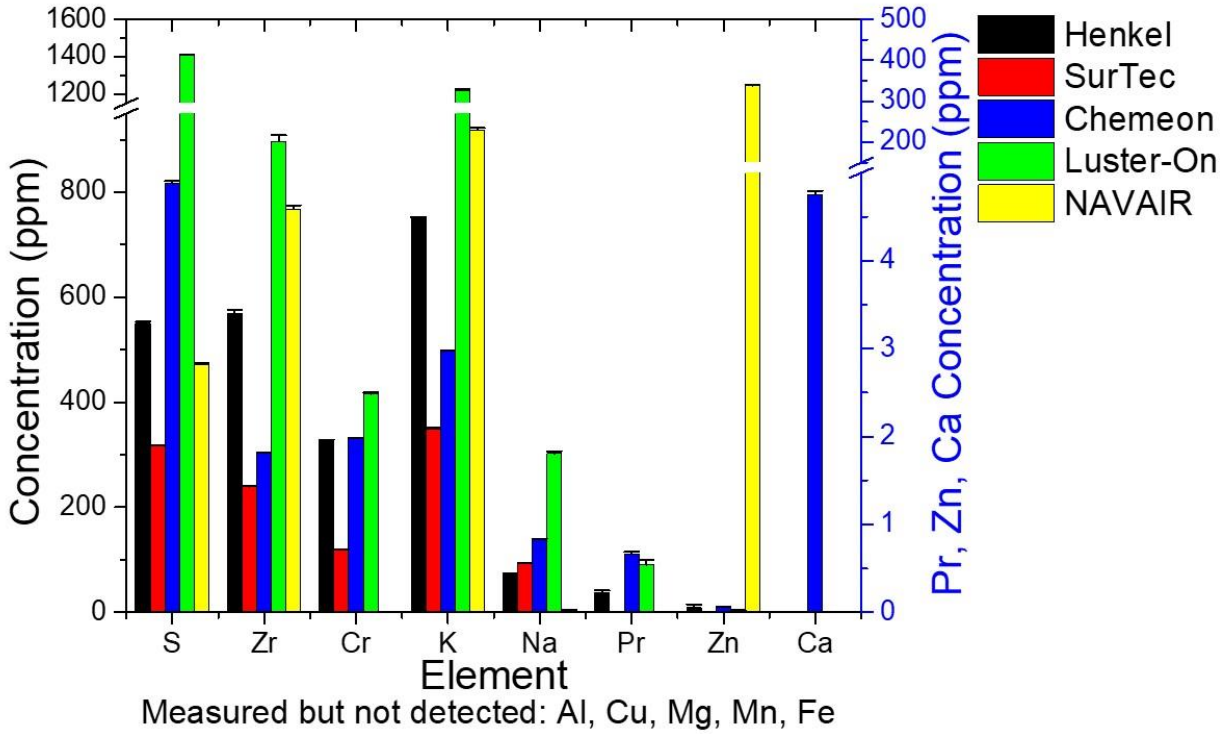

Figure 27. Elemental analysis of all TCP and NCP coating baths as determined by ICP-OES analysis. Data are presented as mean ± S.E.M. for n = 3.

Table 6. The elemental composition (ppm) of all coating baths as determined using ICP-OES analysis.

Coating Elemental Composition (ppm)	Henkel	SurTec E	Chemeon	Luster-On	NCP
Ca	0	0	4.8 ± 0.1	0	0
Cr	327.4 ± 1.4	119.4 ± 0.4	332.5 ± 0.5	416.1 ± 2.4	0
K	750.3 ± 2.3	349.9 ± 1.5	497.6 ± 0.9	1,219.0 ± 6.1	918.4 ± 4.0
Na	74.1 ± 0.2	93.9 ± 0.7	139.6 ± 0.6	302.3 ± 4.2	3.7 ± 0.3
Pr	0.2 ± 0.02	0	0.7 ± 0.02	0.5 ± 0.1	0
S	550.7 ± 2.9	318.0 ± 0.9	816.7 ± 4.6	1,407.8 ± 2.2	472.0 ± 3.0
Zn	0	0	0	0	338.5 ± 1.3
Zr	568.8 ± 7.7	239.5 ± 1.4	302.9 ± 1.1	896.9 ± 11.6	767.4 ± 7.4

Values are reported as mean ± standard error of the mean for n = 3 specimens. Values of 0 represent undetectable amounts in that coating bath.

4.3.2. Profilometry Analysis

Profilometry maps were used to determine the RMS roughness (1 mm^2 area) and deepest pits on all specimens before testing (Fig. 28). The RMS roughness of the uncoated AA7075-T6 was equivalent to the coated specimens, with the exception of Luster-On. This is not surprising as the specimens were not ground and polished smooth, so the large rolling grooves dominate over any smaller surface damage resulting from the different coating processes. The average pit depths measured were all statistically equivalent, as expected.

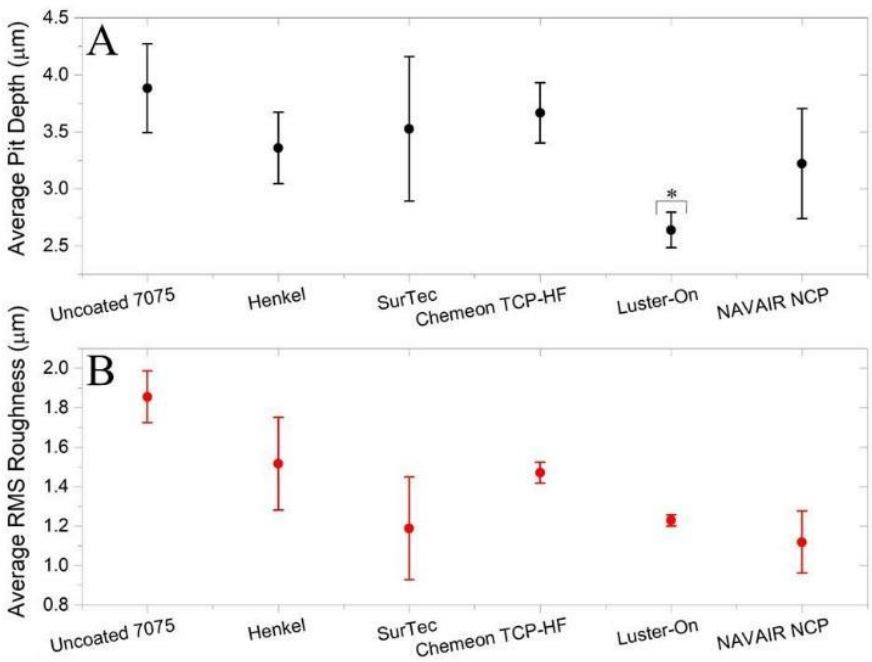

Figure 28. (A) Average pit depths (seen in the 1 mm^2 area) and (B) RMS roughness (over 1 mm^2) determined from contact profilometry. Data are presented for uncoated, TCP-coated, and NCP-coated AA7075-T6 before any testing or environmental exposure. Values are displayed as mean ± standard error of the mean (n = 3). Asterisks indicate data significantly different from the uncoated control ($P < 0.05$).

Surface profilometry was also used to image the coated and uncoated specimens before any testing. Images were recorded over a 1 mm^2 area. Representative images are presented in Figure 29. All specimens showed some higher and lower regions in repeating patterns, which are due to the ridges formed during alloy processing (metal rolling). There were no major differences

in the surface topography of the different alloy specimens prior to any accelerated degradation tests.

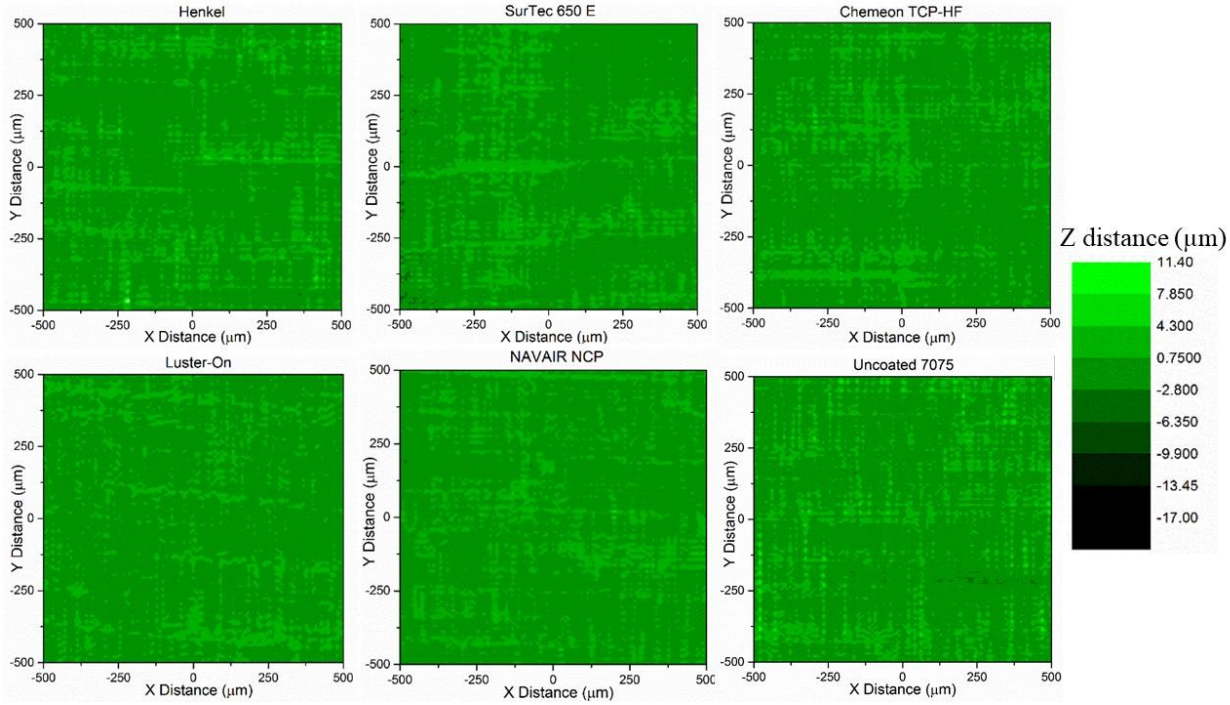

Figure 29. Surface profilometry maps of the TCP- and NCP-coated AA7075-T6 specimens as well as an uncoated control before any testing. The images were recorded over a 1 mm^2 area. The z-axis scale ranges from -17 μm (dark green) to 11.4 μm (light green).

Contact profilometry line scans across the TCP- and NCP-coated AA7075-T6 specimens as well as the uncoated control are shown in Figure 30. The line scans were recorded across the deepest points found in each 1 mm^2 map. All images show the undulating texture produced during the rolling processing. The height changes are in the range of 1-3 μm. All specimens showed similar surface roughness and no visible pits. Table 7 presents nominal values for the surface roughness and average pit depth.

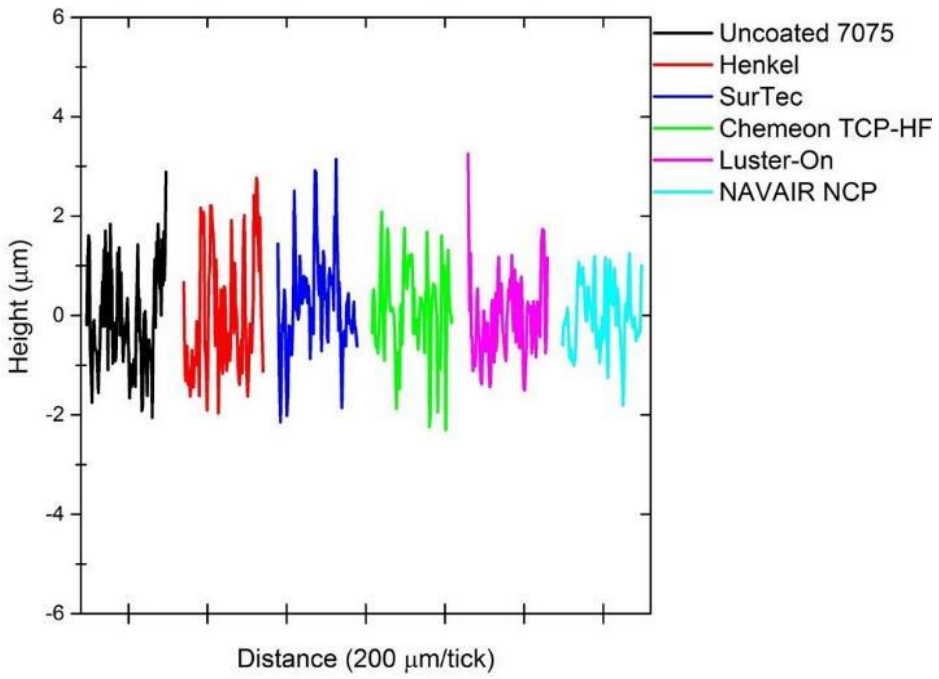

Figure 30. Line scan profiles across the deepest pits visible for uncoated, TCP-coated, and NCP-coated AA7075-T6 specimens before any testing.

Figure 31 shows surface roughness and pit depth data for uncoated, TCP-coated, and NCP-coated AA7075-T6 specimens after a 7-day neutral salt-spray test. The RMS roughness of the uncoated AA7075-T6 was 5x greater than the roughness for all the conversion-coated specimens after the test. This indicates the coated specimens experienced less surface damage and roughening during the corrosion test. The average pit depth was 6x deeper on the uncoated specimens compared to the NCP-coated specimens, and more than 8x deeper compared to the TCP-coated specimens. Nominal values for the pit depth and RMS surface roughness are presented in Table 7. In summary, all TCP and NCP-coated specimens had significantly shallower pits than the uncoated control and reduced surface roughness by a factor of 5-8x.

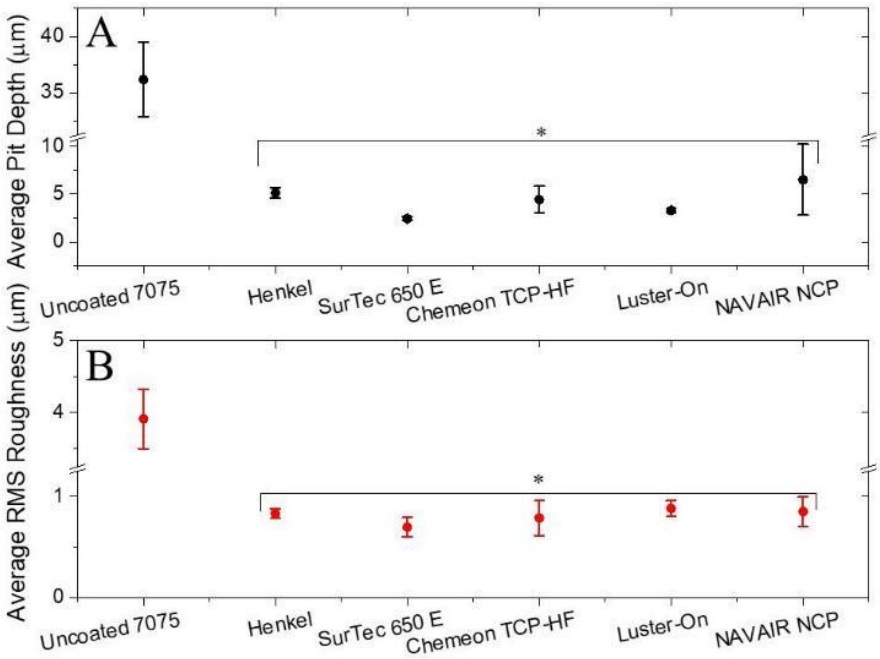

Figure 31. (A) Average pit depth (seen in the 1 mm^2 area) and (B) RMS roughness (over 1 mm^2) determined from contact profilometry. Data are presented for uncoated, TCP-coated, and NCP-coated AA7075-T6 after 7 days of a neutral salt-spray test. All panels were sonicated in nitric acid for 20 min to remove corrosion product. Values are displayed as mean ± standard error of the mean (n = 3). Asterisks indicate data significantly different from the uncoated control ($P < 0.05$).

Table 7. Nominal values for the RMS surface roughness (over 1 mm^2) and average pit depth determined from profilometry maps. Data are presented for uncoated, TCP-coated, and NCP-coated AA7075-T6 before any testing. Values are presented as mean ± S.E.M (n=3).

Specimen	RMS Roughness (μm)	Average Pit Depth (μm)
Uncoated AA7075-T6	3.9 ± 0.4	36.2 ± 3.4
Henkel	0.8 ± 0.1	5.7 ± 0.6
SurTec	0.7 ± 0.1	2.4 ± 0.2
Chemeon	0.8 ± 0.2	4.4 ± 1.4
Luster-On	0.9 ± 0.1	3.3 ± 0.3
NCP	0.8 ± 0.1	6.5 ± 3.7

Surface profilometry was used to image the coated and uncoated specimens after the 7-day neutral salt spray test. Images were recorded over a 1 mm^2 area. Representative images are presented in Figure 32. All of the TCP-coated specimens show no pits or corrosion damage. The slightly raised features (bright green) are produced by the rolling process during panel production. In contrast, the NCP-coated specimen shows a large pit and corrosion damage region (dark green) in the upper right. The pit depth is on the order of 10 μm. The uncoated specimen has considerably greater corrosion damage with large deep pitted regions. Pit depths are greater than 10 μm. There is also some evidence for intergranular corrosion as evidenced by the finger-like features that extend outward from the main pit areas.

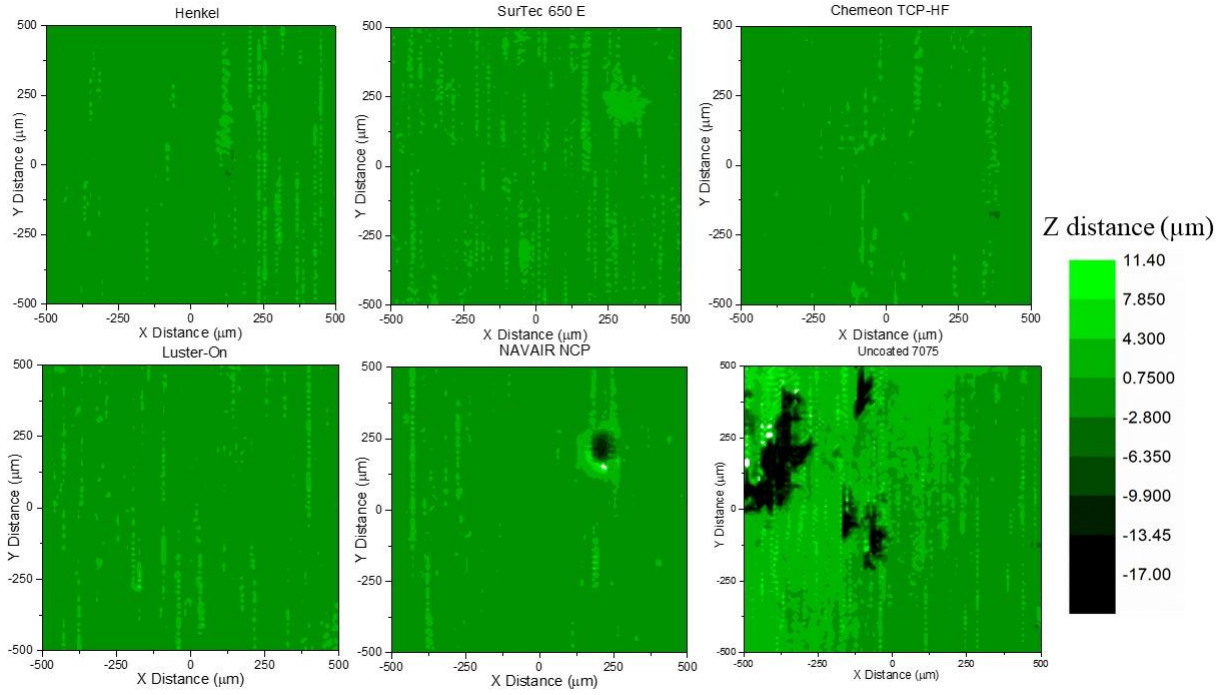

Figure 32. Surface contact profilometry maps of the TCP- and NCP-coated AA7075-T6 specimens as well as an uncoated control after a 7-day neutral salt-spray test. The images were recorded over a 1 mm^2 area. All panels were sonicated in nitric acid for 20 min to remove corrosion product. The z-axis scale ranges from -17 μm (dark green) to 11.4 μm (light green).

Figure 33 shows contact profilometry line scans recorded across the TCP- and NCP-coated AA7075-T6 specimens as well as the uncoated control after the 7-day neutral salt-spray test. The

line scans were recorded across the deepest pitted region found on each 1 mm^2 map. All images show some raised feature that are associated with the rolling grooves produced during the alloy processing. These are in the range of 1-3 μm. The increased surface roughness of the uncoated specimen is evident based on the large increase in surface height of the features, 5-7 μm. The uncoated specimen has the deepest pits, upwards of 20 μm. The SurTec-coated panel has the shallowest pits, on the order of 2 μm. The other TCP-coated specimens showed pits on the order of 3-5 μm. The NCP-coated specimen has increased surface roughness from corrosion damage and one moderately deep pit of 14 μm. The surface roughness of the TCP- and NCP-coated specimens is less than that for the uncoated control. Pit depths are deepest for the uncoated control followed by the NCP-coated and the TCP-coated specimens. The SurTec and Luster-on-coated specimens have the shallowest pits. Overall, the results reveal the superior stand-alone corrosion protection imparted to this alloy by all of the different TCP coatings.

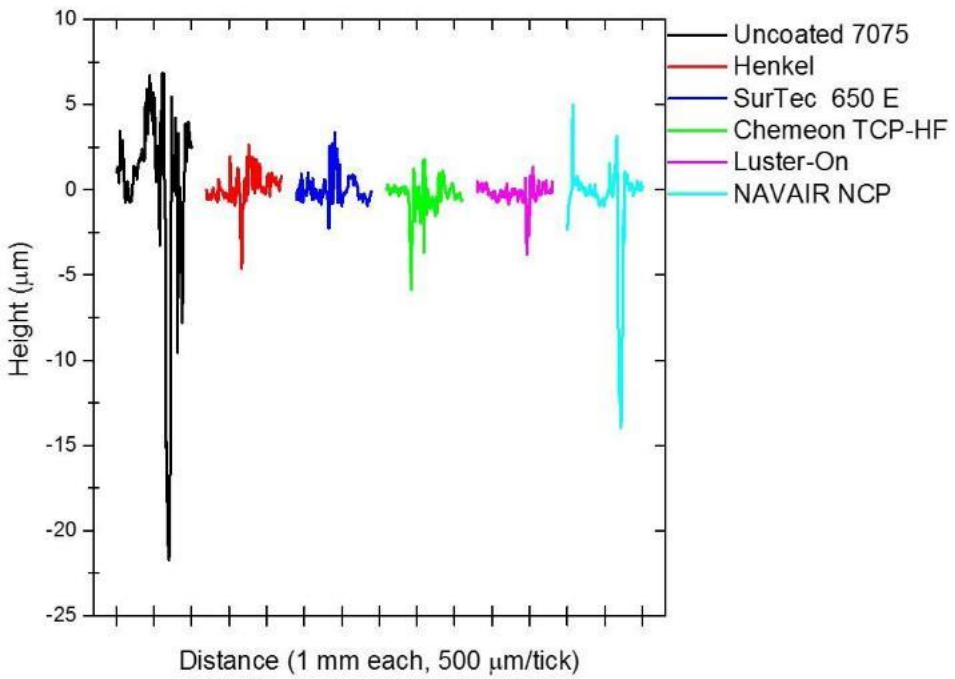

Figure 33. Line profiles across the deepest pits visible on the maps shown in Figure 32. Data are presented for uncoated, TCP-coated, and NCP-coated AA7075-T6 after 7 days of a salt-spray test. All panels were sonicated in nitric acid to remove corrosion product for 20 min.

Figure 34 shows surface roughness and pit depth data for uncoated, TCP-coated, and NCP-coated AA7075-T6 specimens after a 7-day thin-layer mist test. The roughness of the uncoated AA7075-T6 is significantly different from the roughness for the conversion-coated specimens after the 7-day test. The one exception is Luster-On, which is significantly lower, indicating less surface damage and roughening. The average pit depth for the uncoated specimen is ~2x deeper compared to the TCP-coated specimens. Nominal values for the pit depth and RMS surface roughness are presented in Table 8. These results show much less surface roughening and shallower pits when compared to specimens exposed to the salt-spray test. These results are perhaps reflective of a laboratory test that is more reflective of true environmental exposure, which the salt-spray test questionably provides.[45]

Table 8. Nominal values for the surface roughness (over 1 mm^2) and average pit depth determined from contact profilometry maps. Data are presented for uncoated, TCP-coated, and NCP-coated AA7075-T6 after a 7-day salt-spray test. All panels were sonicated in nitric acid for 20 min to remove corrosion product. Values are presented as mean ±S.E.M (n=3).

Specimen	RMS Roughness (µm)	Average Pit Depth (µm)
Uncoated AA7075-T6	1.8 ± 0.1	22.6 ± 3.1
Henkel	1.6 ± 0.3	7.4 ± 1.6
SurTec	2.1 ± 0.1	12.3 ± 2.2
Chemeon	1.8 ± 0.1	11.4 ± 5.8
Luster-On	1.3 ± 0.1	2.9 ± 0.1
NCP	1.7 ± 0.2	16.4 ± 2.2

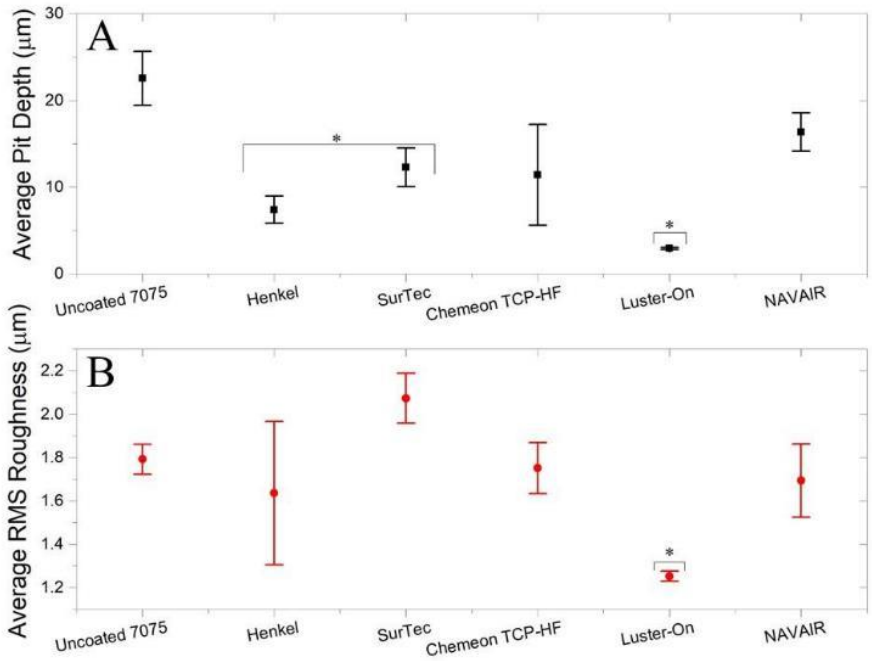

Figure 34. (A) Average pit depths (seen in the 1 mm^2 area) and (B) RMS surface roughness (over 1 mm^2) for uncoated, TCP-coated, and NCP-coated AA7075-T6 after 7 days of a thin-layer mist test. All panels were sonicated in nitric acid for 20 min to remove corrosion product. Values are displayed as mean ± standard error of the mean (n = 3). Asterisks indicate data significantly different from the uncoated control ($P < 0.05$).

The profilometry surface maps shown in Figure 35 reveal the Chemeon and Luster-On-coated specimens experienced minimal pitting and the least apparent corrosion damage. The Henkel-coated specimen has one wide but shallow pit, while the SurTec-coated specimen has a few small but deep pits visible. The rolling grooves from the alloy processing are still present across all samples. In contrast, the NCP-coated specimen shows several large pits across the surface. The pit depth is on the order of 15 μm. The uncoated specimen has considerably greater corrosion damage with a large number of deep pits. Pit depths are greater than 20 μm. The intergranular corrosion seen on the uncoated specimen after salt-spray testing is not evident after the thin-layer mist test.

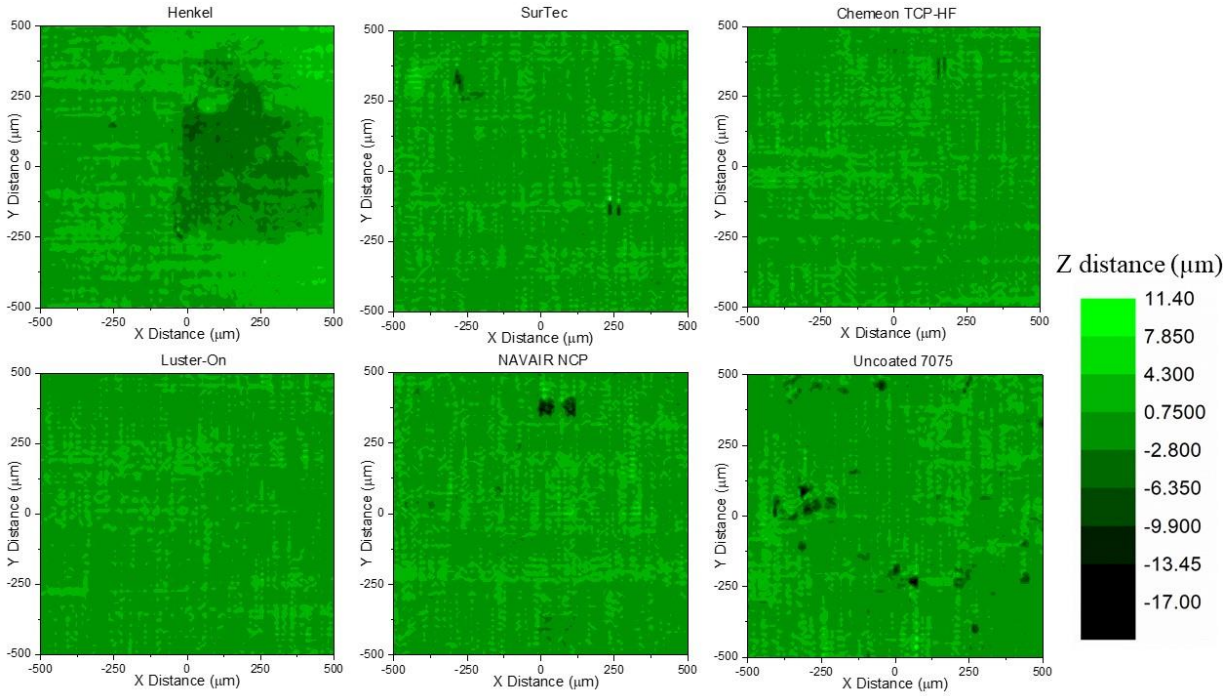

Figure 35. Surface contact profilometry maps of uncoated, TCP-, and NCP-coated AA7075-T6 specimens after a 7-day thin-layer mist test. The images were recorded over a 1 mm^2 area. All panels were sonicated in nitric acid for 20 min to remove corrosion product. The z-axis scale ranges from -17 μm (dark green) to 11.4 μm (light green).

Contact profilometry line scans across the TCP- and NCP-coated specimens as well as the uncoated control are shown in Figure 36. The line scans were recorded across the deepest pitted

region found in each 1 mm^2 map. All images show some raised features (rolling grooves produced during the alloy processing). These are in the range of 1-3 μm. The uncoated specimen has the deepest pitting, upwards of 15 μm. Three of the TCP-coated panels (Henkel, Chemeon and Luster-on) have shallow pits on the order of 3-5 μm. The SurTec-coated specimen has minimal pitting. The NCP-coated specimen has a moderately deep pit of 15 μm. Table 9 presents nominal values for the surface roughness and average pit depth. The surface roughness of the TCP- and NCP-coated specimens is not significantly different from the uncoated control. Pit depths, however, are deepest for the uncoated control followed by the NCP-coated and the TCP-coated specimens. The SurTec and Luster-on-coated specimens have the shallowest pits.

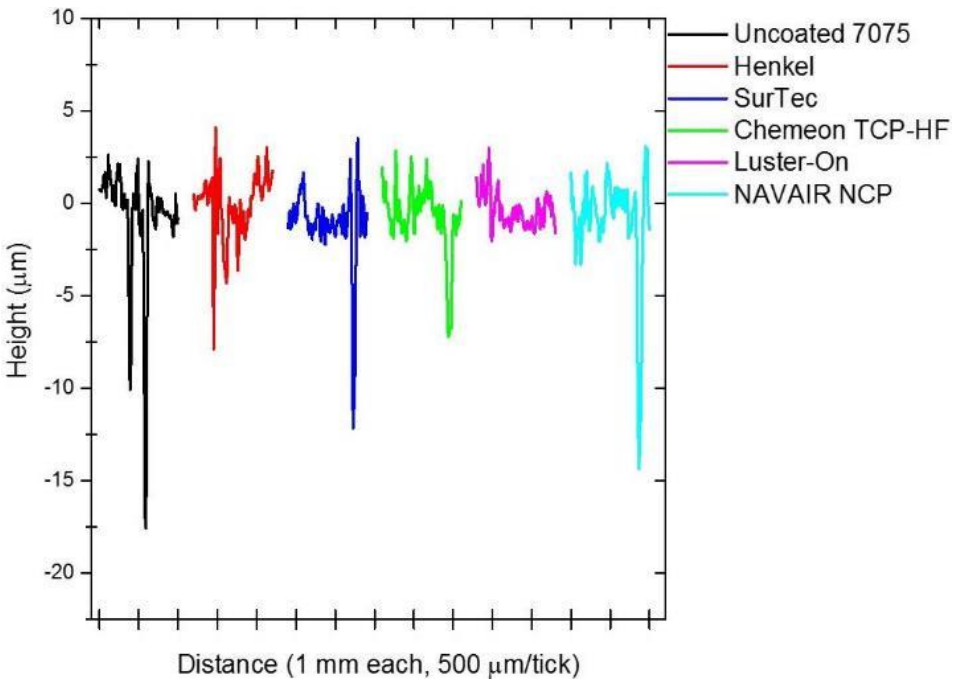

Figure 36. Line profiles across the deepest pits visible on the maps shown in Figure 8. Data are presented for uncoated, TCP-coated, and NCP-coated AA7075-T6 after 7 days of a thin-layer mist test. All panels were sonicated in nitric acid for 20 min to remove corrosion product.

Table 9. Nominal values for the surface roughness (over 1 mm^2) and average pit depth determined from contact profilometry maps. Data are presented for uncoated, TCP-coated, and NCP-coated AA7075-T6 after a 7-day thin-layer mist test. All panels were sonicated in nitric acid to remove corrosion product for 20 min. Values are presented as mean ±S.E.M (n=3).

Specimen	RMS Roughness (μm)	Average Pit Depth (μm)
Uncoated AA7075-T6	1.8 ± 0.1	22.6 ± 3.1
Henkel	1.6 ± 0.3	7.4 ± 1.6
SurTec	2.1 ± 0.1	12.3 ± 2.2
Chemeon	1.8 ± 0.1	11.4 ± 5.8
Luster-On	1.3 ± 0.1	2.9 ± 0.1
NCP	1.7 ± 0.2	16.4 ± 2.2

4.3.3. Weight Change Analysis

Figure 37 shows weight loss data for the TCP- and NCP-coated specimens as well as for the uncoated control after the 7-day neutral salt-spray test. All specimens were subjected to a 20-min ultrasonication in nitric acid to remove corrosion product following by drying prior to weighing. All the coated specimens showed statistically significant lower mass loss than the uncoated control. The reduced mass loss indicates the coatings provide corrosion protection in this environment. Surprisingly, the NCP-coated specimen exhibits similarly reduced mass loss, as compared to the TCP-coated specimens, even with a greater average pit depth. Of the different TCP coatings, the specimens coated with the Luster-on product had the lowest normalized mass loss (uncoated = 33.9 ± 1.4%, Henkel = 11 ± 0.4%, SurTec = 10.4 ± 1.0%, Chemeon = 7.2 ± 1.0%, Luster-On = 4.6 ± 1.0%, NCP = 7.7 ± 1.0%). The normalized mass loss was calculated by dividing each mass loss by the mass of the specimen before exposure. After corrosion product removal, the uncoated specimens had a 3-4x greater weight loss as compared to the coated specimens. The Chemeon and Luster-On coatings provided the best performance based on weight loss.

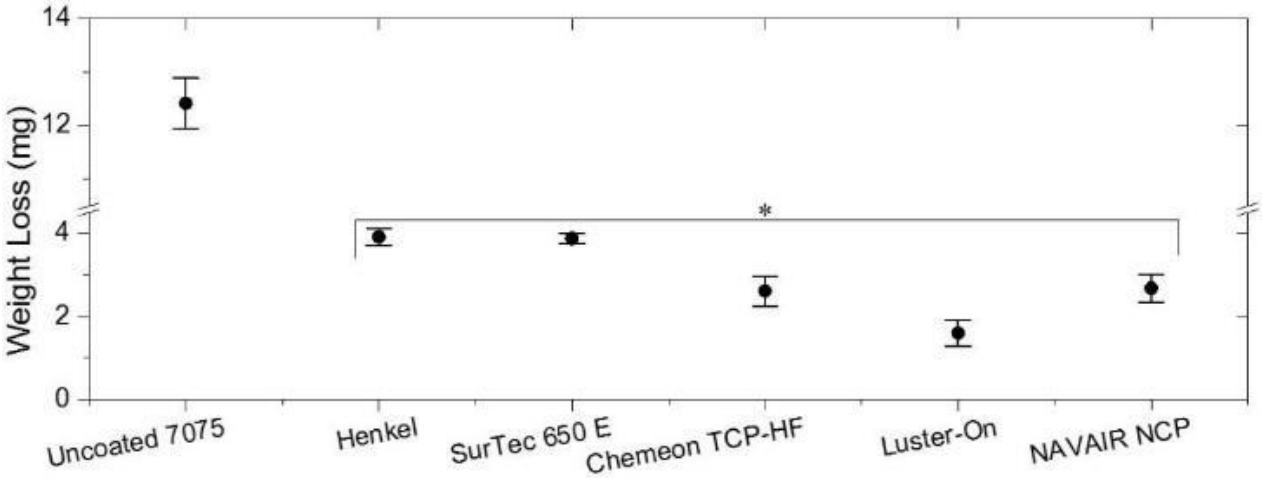

Figure 37. Weight loss data for uncoated, TCP-coated and NCP-coated AA7075-T6 panels after a 7-day neutral salt-spray test. All panels were ultrasonicated in nitric acid for 20 min to remove corrosion product. Panels used had a one square inch surface area. Values are displayed as mean ± standard error of the mean (n = 3 tested panels). Asterisks indicate data significantly different from the uncoated control ($P < 0.05$).

Figure 38 shows weight loss data for the uncoated, TCP-coated, and NCP-coated AA7075-T6 panels after the 7-day thin-layer mist test. The overall magnitude of the weight loss is less that the magnitude seen for the specimens used in the salt-spray testing by a factor of 10x. This is because the panel size was considerably smaller. Unlike the salt-spray test data where all the coatings performed in a more or less similar manner, differences in the performance of the TCP and NCP coatings are more apparent after the thin-layer mist test. There is no statistical difference in the weight loss seen for the specimens coated with the Henkel product as compared to the uncoated control. Weight loss was significantly less for the specimens coated with the SurTec and NCP coatings, as compared to the uncoated control. The specimens coated with the Chemeon and Luster-on products exhibited the least normalized weight loss in this test (Uncoated = 28.4 ± 0.5%, Henkel = 23.3 ± 5.1%, SurTec = 19.6 ± 2.9%, Chemeon = 10.2 ± 1.7%, Luster-On = 7.3 ± 3.0%, NAVAIR = 14.6 ± 1.0%). Again, the normalized mass loss was calculated by dividing each mass loss by the mass of the specimen before exposure. Overall, the normalized magnitude of the mass loss is significantly higher for the coated specimens during the thin-layer mist test compared to the neutral salt-spray test, indicating a more aggressive test perhaps more reflective of real-world specimen corrosion.

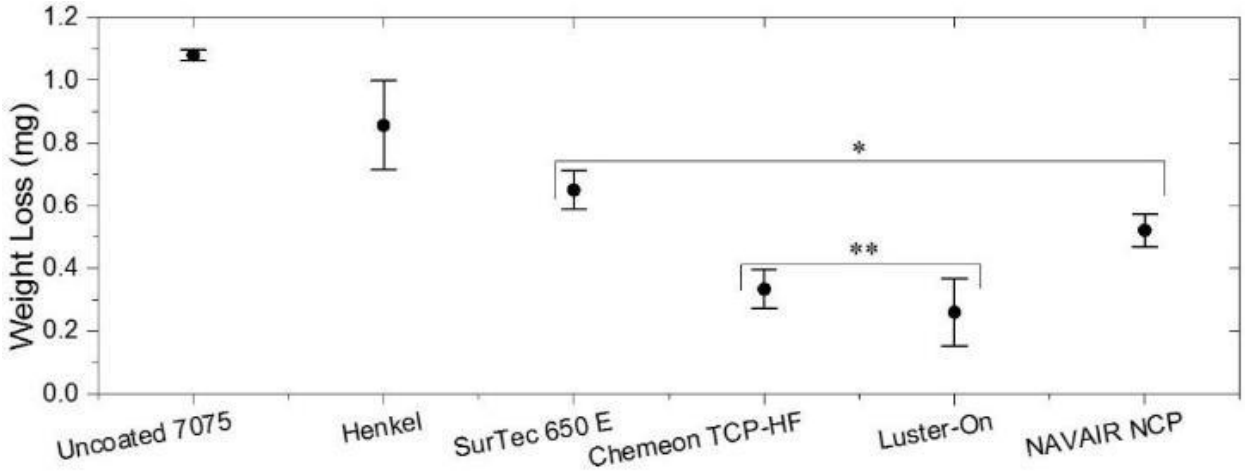

Figure 38. Weight loss data for uncoated, TCP-coated and NCP-coated AA7075-T6 panels after the 7-day thin-layer mist test. Panels used had a one square centimeter surface area. Values are displayed as mean ± standard error of the mean (n = 3). Asterisks indicate data significantly different from the uncoated control ($P < 0.05$). Double asterisks indicate data significantly different from the single asterisk data ($P < 0.05$).

4.3.4. Microscopy Analysis

Optical microscopy was used to analyze the pits formed in a small area (~10,000 μm^2 = 0.01 mm^2). Three of these damage regions were examined on each of three panels for every coating, yielding a total of nine sampled areas for each. While this allows for a more accurate representation of the pit sizes, it will not capture large pits indicative of major corrosion. Figure 39 A and B show data for the average pit area and average pit density for uncoated, TCP-coated, and NCP-coated panels after the 7-day salt-spray test. All coated specimens had smaller pit areas compared to uncoated AA7075-T6. The difference in area is over 10x for the coated panels. There are no differences in the average pit area of all of the coated panels. The average pit density is similar statistically for all of the coated panels and for the uncoated panel (40-100 pits/mm^2) except for the Chemeon-coated specimens. The pit density on these panels (10 pits/mm^2) is significantly smaller than the density on the uncoated panels. This could indicate that the aggressive conditions with a higher Cl^- ion concentration are leading to more pit initiation and film undercutting with all

coatings except Chemeon. Values for the pit density and area are provided for reference in Table 10.

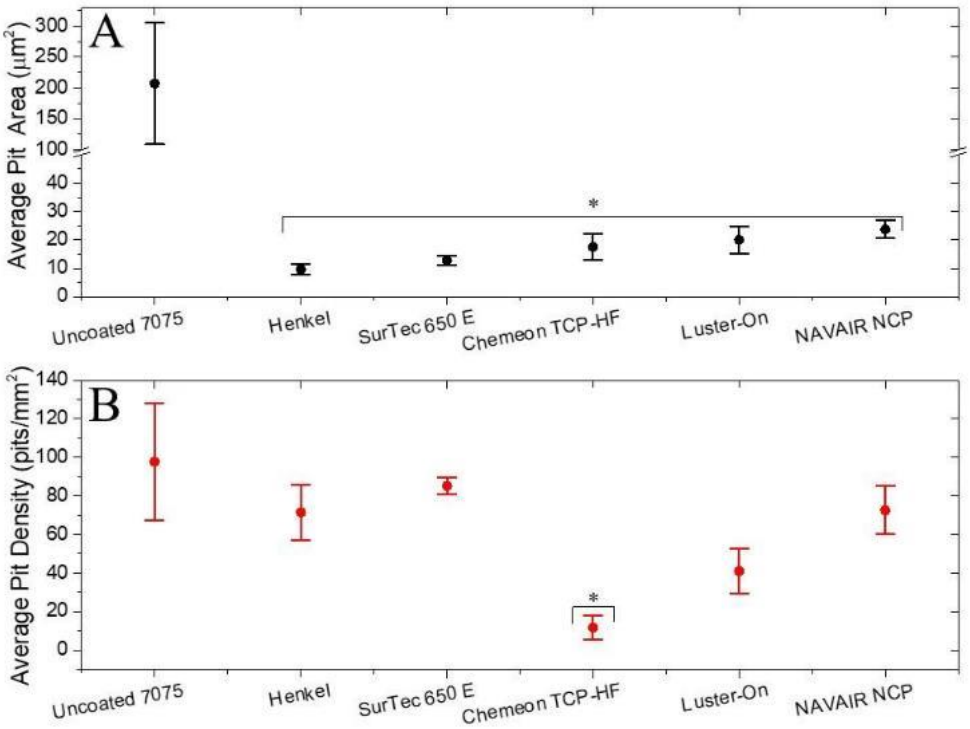

Figure 39. Pit areas and pit densities were determined from optical micrographs measured over at least 3 imaging areas of 0.001 mm^2 in various spots across the overall 1 mm^2 panel surface. Data are presented for uncoated, TCP-coated, and NCP-coated AA7075-T6 panels after 7 days of a salt-spray test. All panels were sonicated in nitric acid for 20 min to remove corrosion product. Values are displayed as mean ± standard error of the mean (n = 3). Asterisks indicate data significantly different from the uncoated control ($P < 0.05$).

Figure 40 A and B show data for the average pit area and average pit density for the uncoated, TCP-coated, and NCP-coated panels after the 7-day thin layer mist (TLM) test. Smaller pits for all coated specimens and smaller pit densities for Henkel, Chemeon, and Luster-On-coated panels are evident as compared to uncoated AA7075-T6. **Pit densities for the SurTec TCP and NCP-coated panels are significantly higher than the other coatings, and even the uncoated specimen in the case of the NCP-coated panel. Perhaps this indicates a larger number of small pits initiating across the surface, which can lead to film undercutting and performance degradation. Additionally, the uncoated specimens showed very large pits, sometimes larger**

than the imaging area, leading to fewer pits counted in one significantly damaged region of the panel surface. Values for the pit area and density are included for reference in Table 10.

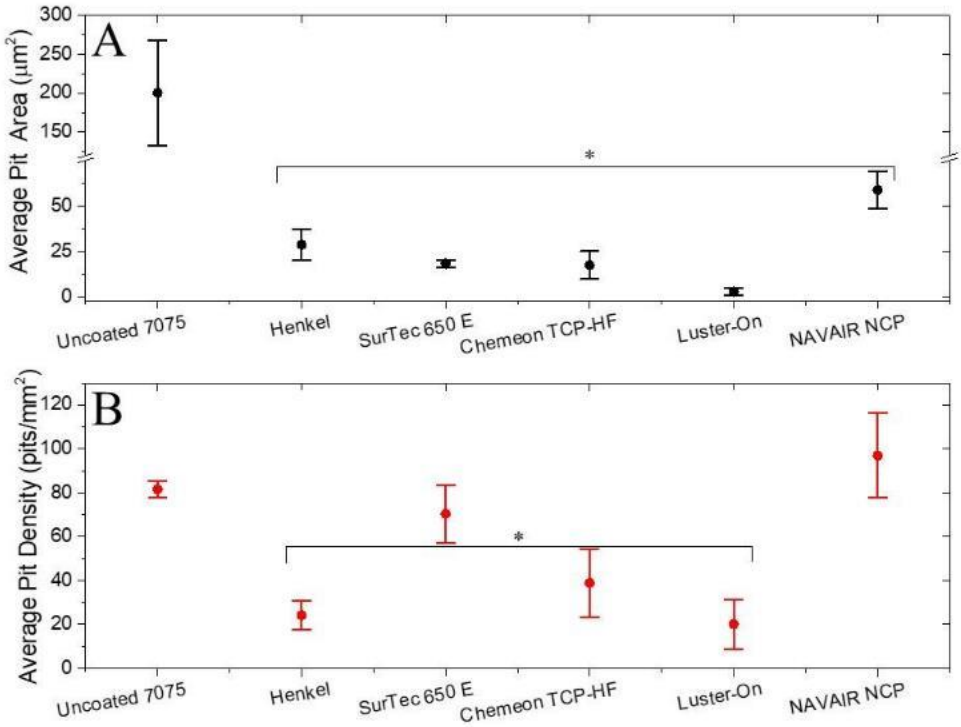

Figure 40. Pit areas and pit densities were determined from optical micrographs measured over at least 3 imaging areas of 0.001 mm^2 in various spots across the overall 1 mm^2 panel surface. Data are presented for uncoated, TCP-coated, and NCP-coated AA7075-T6 panels after 7 days of a thin-layer test. All panels were sonicated in nitric acid for 20 min to remove corrosion product. Values are displayed as mean ± standard error of the mean (n = 3). Asterisks indicate data significantly different from the uncoated control ($P < 0.05$)**.**

Table 10. Pit density and pit diameter data for uncoated, Henkel, SurTec E, Chemeon, Luster-On, and NAVAIR NCP-coated AA7075-T6 after corrosion product removal with 20-min nitric acid after 7-day thin-layer mist (TLM) and 7-day salt-spray (SS) tests. Values are presented as mean ±S.E.M (n=3).

Specimen	SS Pit Density (pits/mm^2)	SS Average Pit Area (μm^2)	TLM Pit Density (pits/mm^2)	TLM Average Pit Area (μm^2)
Uncoated AA7075-T6	98 ± 30	207 ± 98	82 ± 4	201 ± 68
Henkel	71 ± 14	10 ± 2	24 ± 7	29 ± 8
SurTec	85 ± 4	13 ± 2	70 ± 13	31 ± 9
Chemeon	12 ± 6	18 ± 5	39 ± 15	17 ± 8
Luster-On	41 ± 12	20 ± 5	20 ± 11	6 ± 4
NAVAIR	125 ± 13	24 ± 3	97 ± 19	59 ± 10

4.3.5. Visual Analysis

Camera photographs of the entire 1 cm^2 (thin-layer mist) or 1 $inch^2$ (salt-spray) surface of the exposed specimens were used to identify corrosion product build-up and surface damage caused by the two accelerated degradation tests. Photoshop software was then used to convert the photographs into black and white images with enhanced contrast to better visualize the white and dark corrosion product formations, and the dark pits after 20 min nitric acid cleaning. The images also reveal how reproducible the corrosion damage is across multiple panels.

Figure 41 shows black and white images of three uncoated AA7075-T6 specimens before exposure, after a 7-day neutral salt-spray test, and after acid dissolution of the corrosion product. All three uncoated specimens look very similar with the rolling grooves apparent. These specimens were degreased and deoxidized so there are pits (small black spots) decorating the surface. Some of these spots are also likely intermetallic particles and inclusions. There is significant damage to all three specimens after the test. Large mounds of corrosion product are visible over all areas of the panel with significant pitting (black areas). After acid dissolution, the large corrosion product mounds are gone but the surface roughness and large pitted areas (black spots) are apparent.

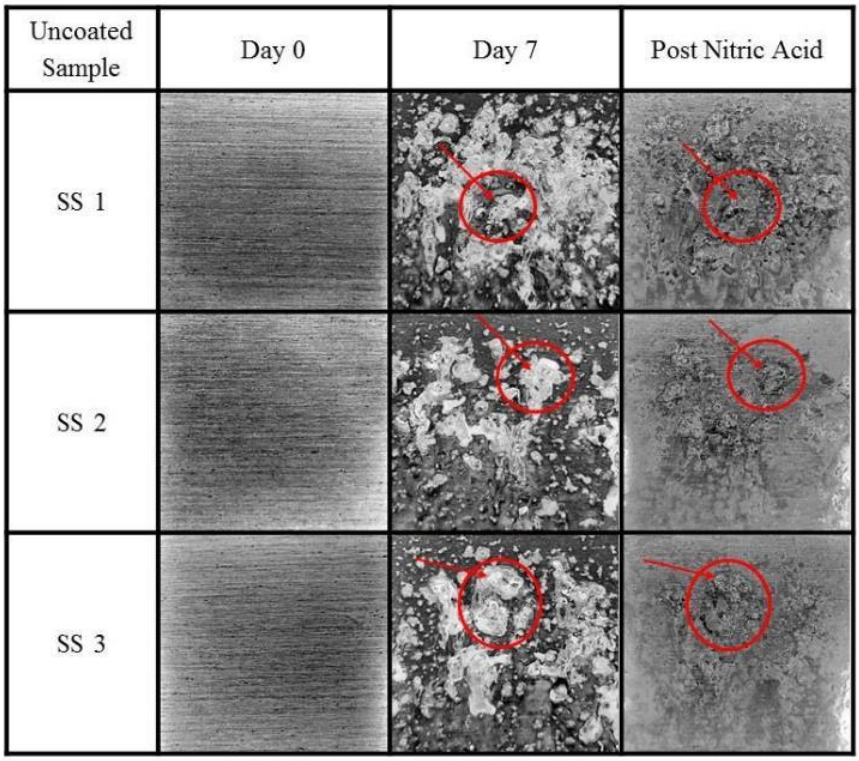

Figure 41. Black and white images of replicate uncoated AA7075-T6 specimens before (Day 0), after 7 days of a neutral salt-spray test (Day 7), and after nitric acid dissolution of corrosion product (Post Nitric Acid). Red circles demark regions of corrosion product formation seen on day 7, and red arrows demark regions of surface pitting. Image size = one square inch (entire panel shown in image).

Figure 42 shows black and white images of three replicate specimens coated with NCP before and after the 7-day neutral salt-spray test. All three coated panels are featureless before the start of the test with only the rolling grooves present. No pits are present (no small black spots). This conversion coating, as well as the other TCP coatings, were continuous in appearance on the alloy and visibly discernible (due to coloration). All surfaces are devoid of powdery areas or loose coating, voids, scratches, flaws, and other defects or damage. After salt-spray exposure, all three specimens have clearly visible corrosion product formation. The large areas of discoloration are regions where corrosion product has formed and the small black spots are pits that have formed. The pits are greatest in number in the middle panel (SS2) but form over the entire panel. The largest black regions (red circles) are locations of significant pitting and corrosion. After acid dissolution of the

corrosion product, the large and small-scale corrosion damage is visible. Overall, the exposed specimens and the acid-cleaned specimens look very different from the uncoated panels, which have clear and extensive corrosion damage.

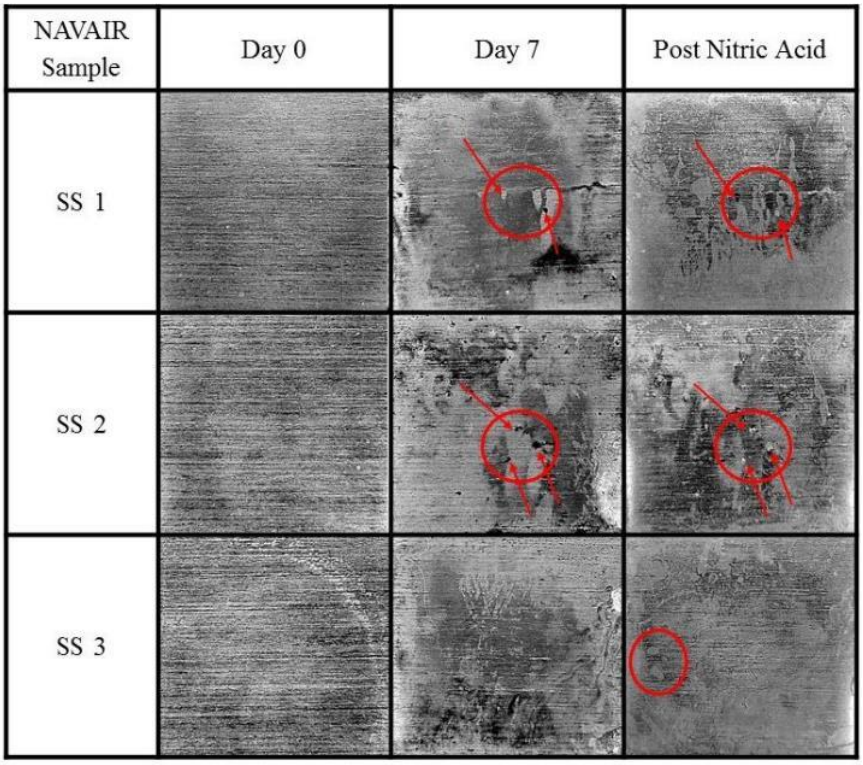

Figure 42. Black and white images of replicate NCP-coated (NAVAIR) AA7075-T6 specimens before (Day 0), after 7 days of a neutral salt-spray test (Day 7), and after nitric acid dissolution of corrosion product (Post Nitric Acid). Red circles demark regions of corrosion product formation seen on day 7, and red arrows demark regions of surface pitting. Image size = one square inch (entire panel shown in image).

Figure 43 shows replicate black and white images of three specimens coated with the Luster-On product before, after a 7-day neutral salt-spray test and after acid dissolution of corrosion product. Aside from the rolling grooves, all three coated specimens are largely featureless before the corrosion test. The specimens after the salt-spray test are also largely featureless and unchanged as compared to the unexposed controls. There is no large-scale discoloration, surface roughening, pitting or corrosion product formation, at least on this image scale. There are some slight discolorations on the side of each panel. After acid dissolution, one

of the panels (SS2) has four small damage regions near the bottom of the image. These are likely very shallow pits just beginning to form. Overall, the exposed specimens and the acid-cleaned specimens have few localized damage sites visible, that were clearly introduced during the test.

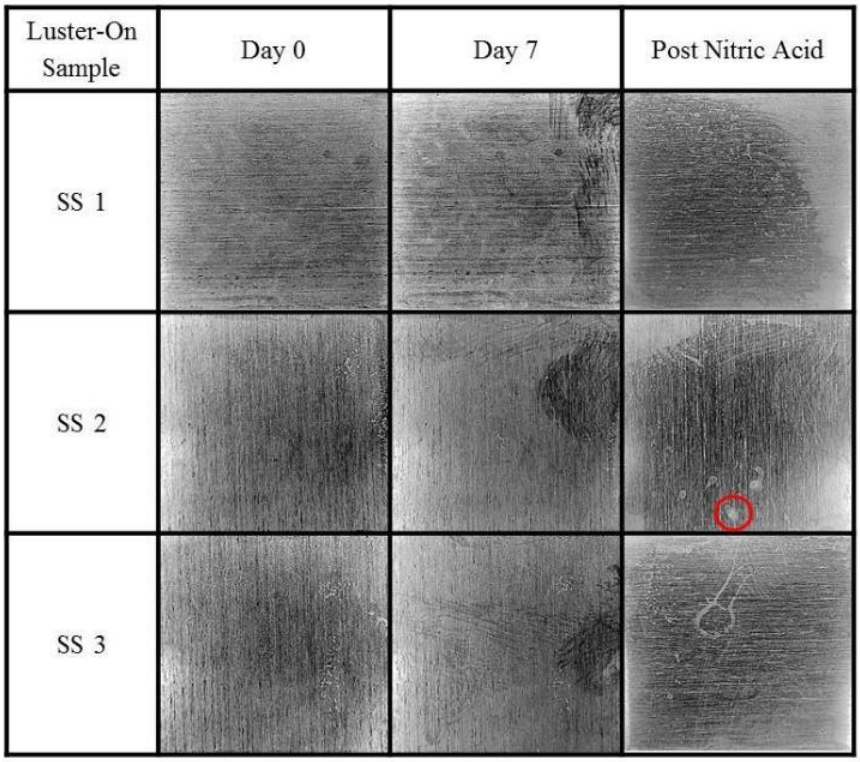

Figure 43. Black and white images of replicate TCP-coated (Luster-On) AA7075-T6 specimens before (Day 0), after 7 days of a neutral salt-spray test (Day 7), and after nitric acid dissolution of corrosion product (Post Nitric Acid). Red circles demark regions of surface pitting. Image size = one square inch (entire panel shown in image).

Figure 44 shows black and white images of three TCP-coated AA7075-T6 panels (Chemeon) before and after a 7-day neutral salt-spray test. Images of the exposed specimens after acid dissolution of the corrosion product are also shown. The images reveal no significant changes in the surface condition after the salt-spray test. There is no obvious corrosion product formation or pitting on any of the three panels. The only difference is in SS3 as there is a discolored region that developed in the lower right. After acid dissolution of any corrosion product, the surfaces are largely unchanged except for some discoloration around the edges. SS3 has two small depressed features in the center of the image. These maybe small shallow pits in the very early stages of

growth. Overall, there is very little damage on these three specimens, indicating the Chemeon TCP coating provides good stand-alone corrosion protection in this environment.

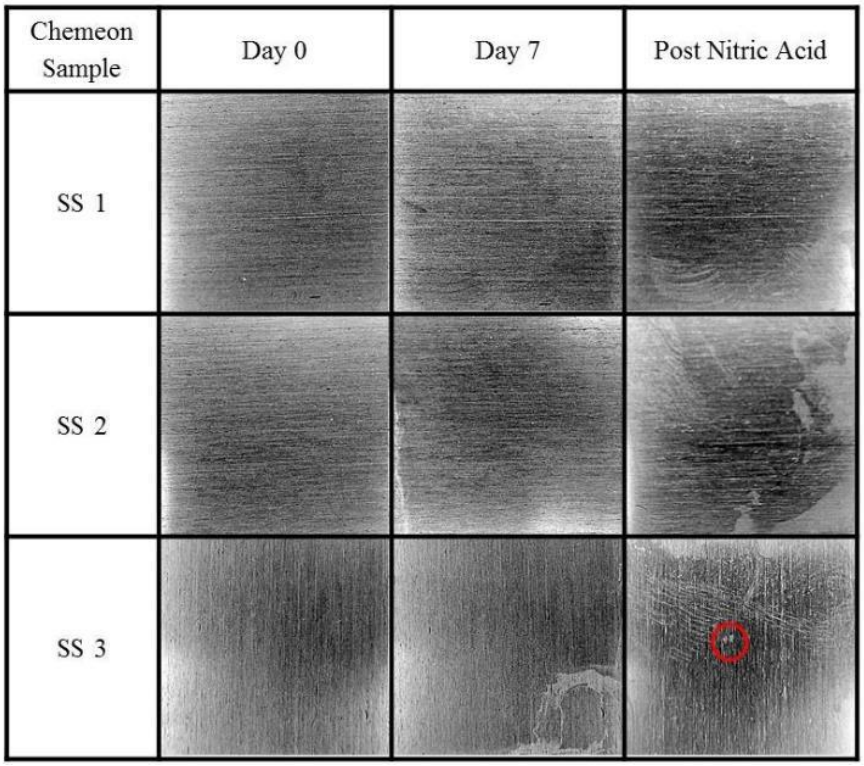

Figure 44. Black and white images of replicate TCP-coated (Chemeon) AA7075-T6 specimens before (Day 0), after 7 days of a neutral salt-spray test (Day 7), and after nitric acid dissolution of corrosion product (Post Nitric Acid). Red circles demark regions of surface damage. Image size = one square inch (entire panel shown in image).

Figure 45 shows black and white images of TCP-coated (SurTec) AA7075-T6 specimens before (Day 0), after a 7-day neutral salt-spray test (Day 7) and after acid dissolution of any corrosion product. Prior to exposure and generally after exposure, all three specimens are devoid of significant corrosion product formation, pitting, voids, scratches and flaws. There are discolored regions on the right side of SS2 and 3. After acid dissolution, SS2 has a surface defect that develops in the center of the panel but other than this the panels are devoid of major surface roughening and pitting. Overall, there is little damage introduced during the exposure, reflective of good stand-alone corrosion protection.

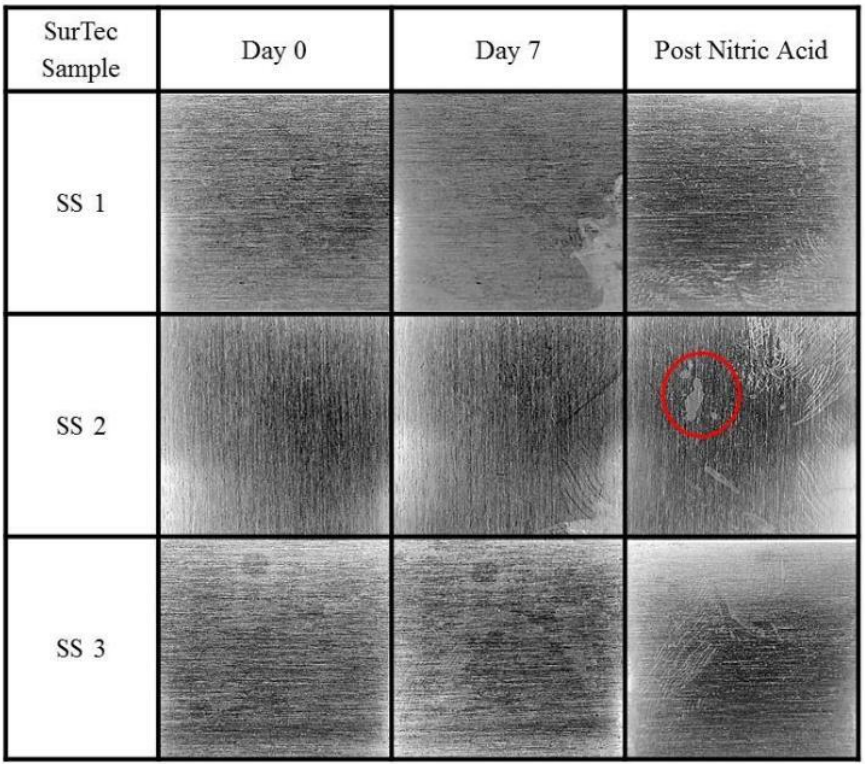

Figure 45. Black and white images of replicate TCP-coated (SurTec 650 E) AA7075-T6 specimens before (Day 0), after 7 days of a neutral salt-spray test (Day 7), and after nitric acid dissolution of corrosion product (Post Nitric Acid). Red circles demark regions of corrosion product formation seen on day 7, and red arrows demark regions of surface pitting. Image size = one square inch (entire panel shown in image).

Figure 46 shows black and white images of TCP-coated (Henkel) AA7075-T6 panels before (Day 0), after a 7-day neutral salt-spray test (Day 7) and after acid dissolution (Post Nitric Acid). This coating, as was the case for the other conversion coatings, was visibly discernible. However, these coated surfaces had some discoloration, as evidenced by the features on the right side of SS3. The main difference is that the surface features seen in SS3 prior to testing are gone after the salt-spray exposure. After acid dissolution, the surfaces have a few discolored regions (top of SS2 and 3) and a small damaged region in the center of SS1. Overall, this TCP coating, as well as the other three commercial variants, provide good stand-along corrosion protection under these test conditions.

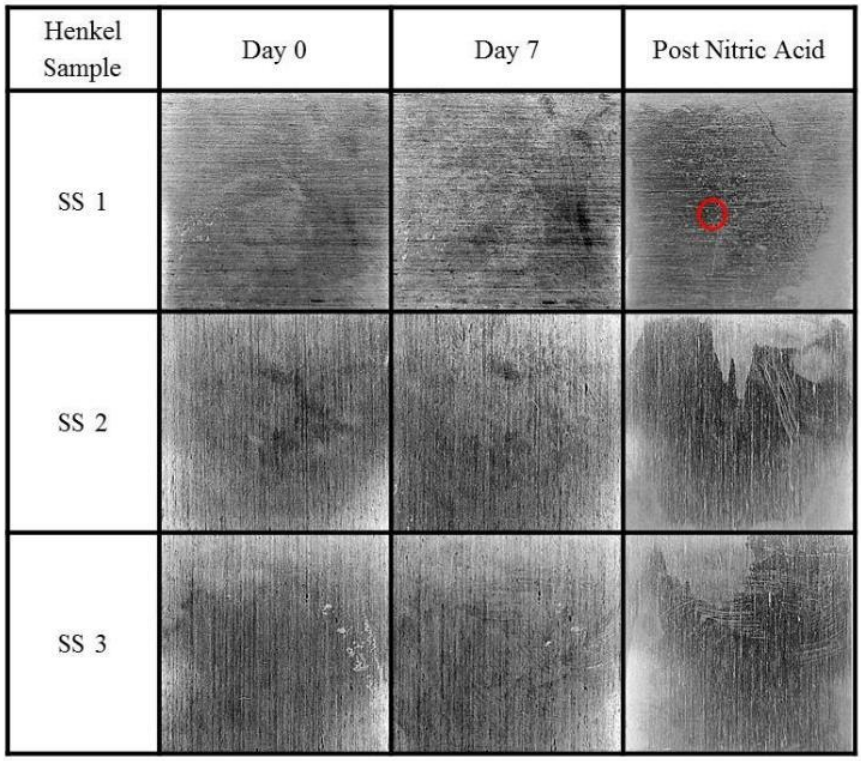

Figure 46. Black and white images of replicate TCP-coated (Henkel) AA7075-T6 panels before (Day 0), after a 7-day neutral salt-spray test (Day 7), and after nitric acid dissolution of any corrosion product (After Nitric Acid). Red circle marks a region of slight surface damage. Image size = one square inch (entire panel shown in image).

Figure 47 shows black and white images of three uncoated AA7075-T6 specimens before exposure, after a 7-day thin-layer mist test and after acid dissolution of the corrosion product. All three uncoated specimens look very similar with the rolling grooves apparent. These specimens were degreased and deoxidized so there are pits (small black spots) decorating the surface. Some of these spots are also likely intermetallic particles and inclusions. There is significant damage to all three specimens after the test. Large mounds of corrosion product are visible over all areas of the panel with significant pitting (black areas). After acid dissolution, the large corrosion product mounds are gone but the surface roughness and large pitted areas (white spots) remain.

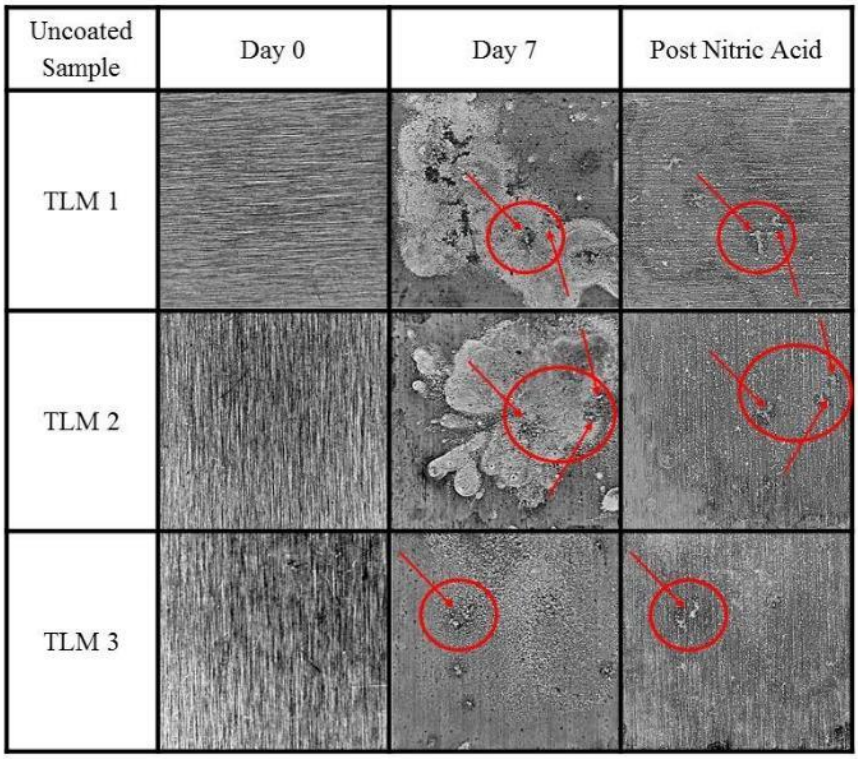

Figure 47. Black and white images of replicate uncoated AA7075-T6 specimens before (Day 0), after 7 days of a thin-layer mist test (Day 7), and after nitric acid dissolution of corrosion product (Post Nitric Acid). Red circles demark regions of corrosion product formation seen on day 7, and red arrows demark regions of surface pitting. Image size = one square centimeter (entire panel shown in image).

Figure 48 shows black and white images of three replicate specimens coated with NCP before and after the 7-day thin-layer mist test. All three coated panels are again featureless before the start of the test with only the rolling grooves and no pits present. This conversion coating was continuous in appearance and visibly discernible. After the thin layer mist test, all three specimens have visible large white corrosion product patches and small black pits. The pits are greatest in number for the top panel (TLM 1) and form over the entire panel. After acid dissolution of the corrosion product, the surface roughness is visible as are pits. Overall, the exposed specimens and the acid-cleaned specimens look very different from the untreated panels, with visible corrosion damage.

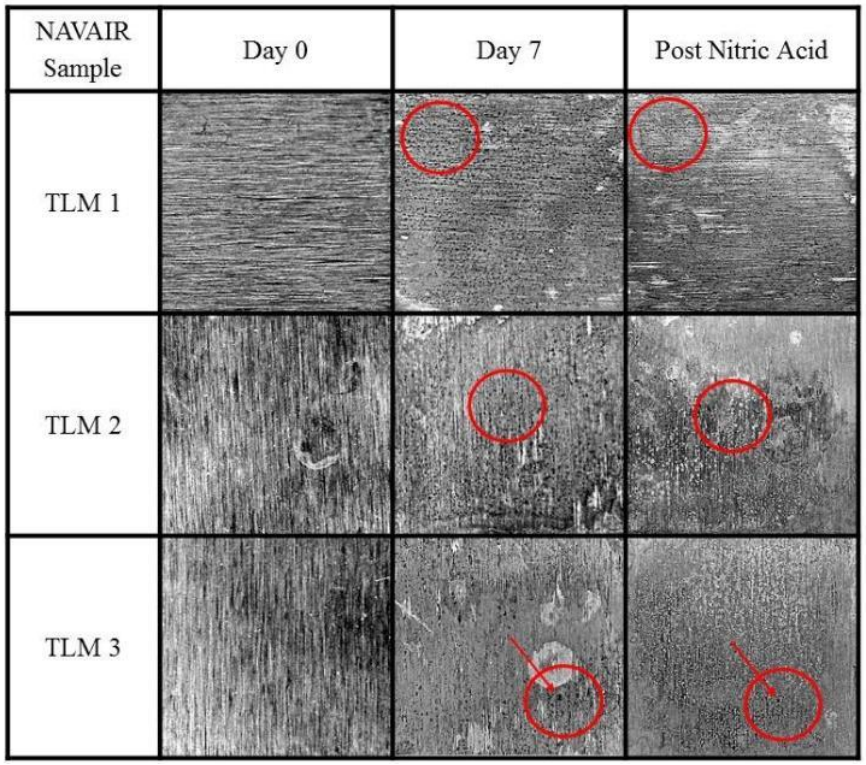

Figure 48. Black and white images of replicate NCP-coated (NAVAIR) AA7075-T6 specimens before (Day 0), after 7 days of a thin-layer mist test (Day 7), and after nitric acid dissolution of corrosion product (Post Nitric Acid). Red circles demark regions of corrosion product formation seen on day 7, and red arrows demark regions of surface pitting. Image size = one square centimeter (entire panel shown in image).

Figure 49 shows replicate black and white images of three specimens coated with the Luster-On product before, after a 7-day thin-layer mist test, and after acid dissolution of corrosion product. Before the test, two of the three coated specimens show some visible coating flaws near the specimen edge. After the test, there are some visible surface marks but these seem to be discoloration and not corrosion damage. After acid dissolution, one of the panels (TLM 1) has a large region of apparent corrosion product buildup. After acid dissolution, the product is gone and there is minimal corrosion damage, only a small apparent pit. Overall, the coating provides good stand-alone corrosion protection to this alloy and in these test conditions.

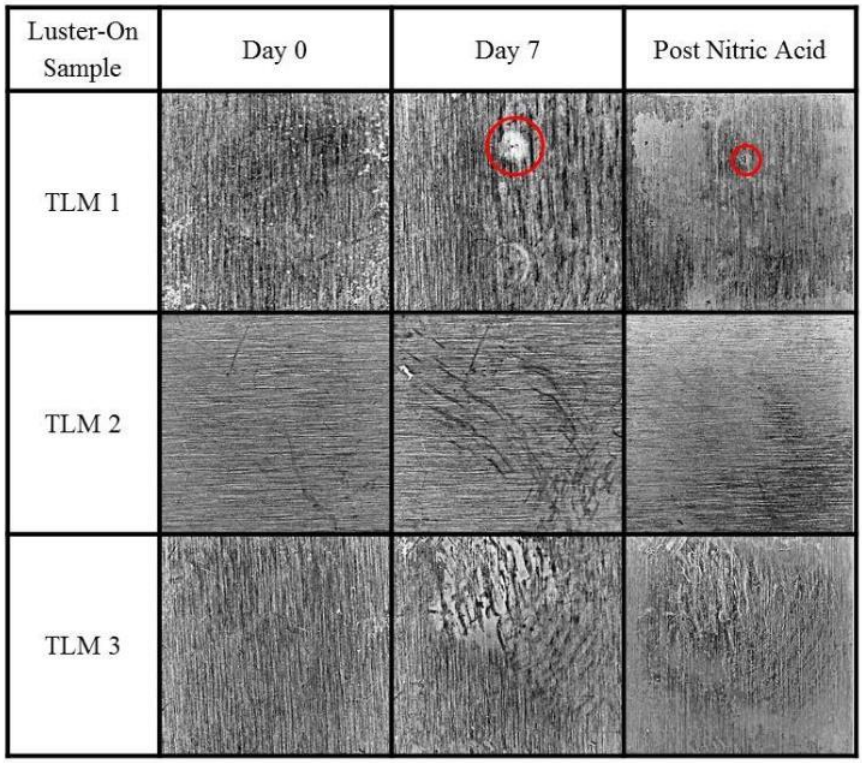

Figure 49. Black and white images of replicate TCP-coated (Luster-On) AA7075-T6 specimens before (Day 0), after 7 days of a thin-layer mist test (Day 7), and after nitric acid dissolution of corrosion product (Post Nitric Acid). Red circles demark regions of corrosion product formation and surface pitting. Image size = one square centimeter (entire panel shown in image).

Figure 50 shows black and white images of three TCP-coated AA7075-T6 panels (Chemeon) before and after a 7-day thin-layer mist test. Images of the exposed specimens after acid dissolution of the corrosion product are also shown. The images reveal no significant changes in the surface condition after the test. There is no obvious corrosion product formation or pitting on any of the three panels. All specimens show some slight coloration changes, which are assumed to be purely cosmetic or even due to illumination differences. After acid dissolution, the surfaces are unchanged. Surface features are less prominent, probably due to removal of any coating present on the surface. Overall, there is no damage on these three specimens, indicating the Chemeon TCP coating provides excellent stand-alone corrosion protection in this environment.

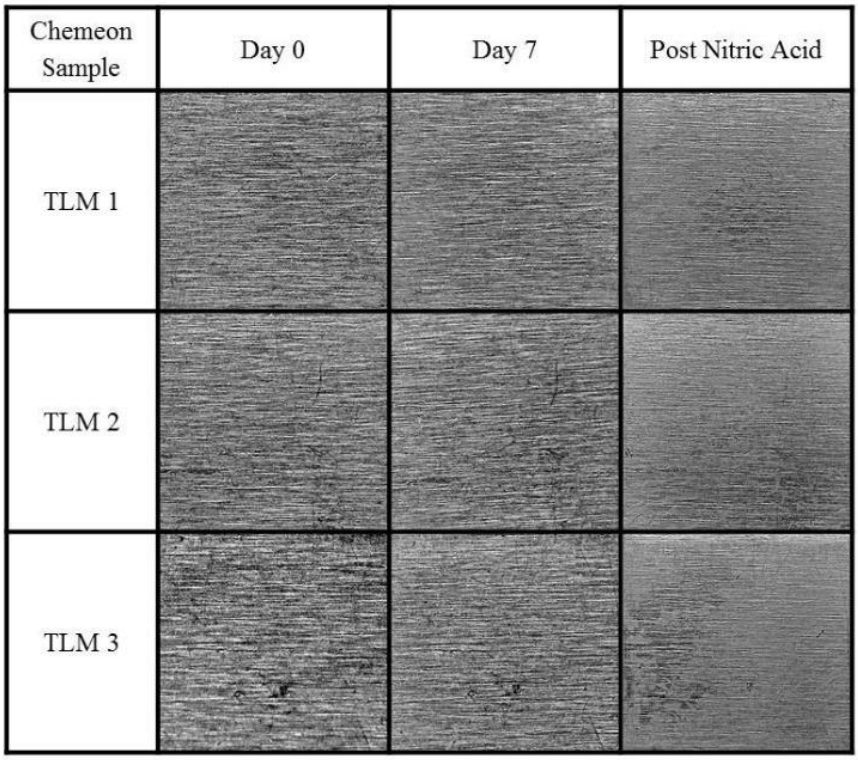

Figure 50. Black and white images of replicate TCP-coated (Chemeon) AA7075-T6 specimens before (Day 0), after 7 days of a thin-layer mist test (Day 7), and after nitric acid dissolution of corrosion product (Post Nitric Acid). No corrosion product or surface pitting was seen after the 7-day test. Image size = one square centimeter (entire panel shown in image).

Figure 51 shows black and white images of TCP-coated (SurTec) AA7075-T6 specimens before (Day 0), after a 7-day thin-layer mist test (Day 7), and after acid dissolution of any corrosion product (Post Nitric Acid). Prior to exposure, all three specimens are devoid of significant corrosion product, pitting, voids, scratches and flaws. After acid dissolution, TLM 2 has a large amount of discoloration, but no significant surface damage. TLM 3 has some surface defects that develop in the center of the panel, which lead to two large damaged regions. The other the panels are devoid of major surface roughening and pitting, with the exception of some superficial scratches and discoloration.

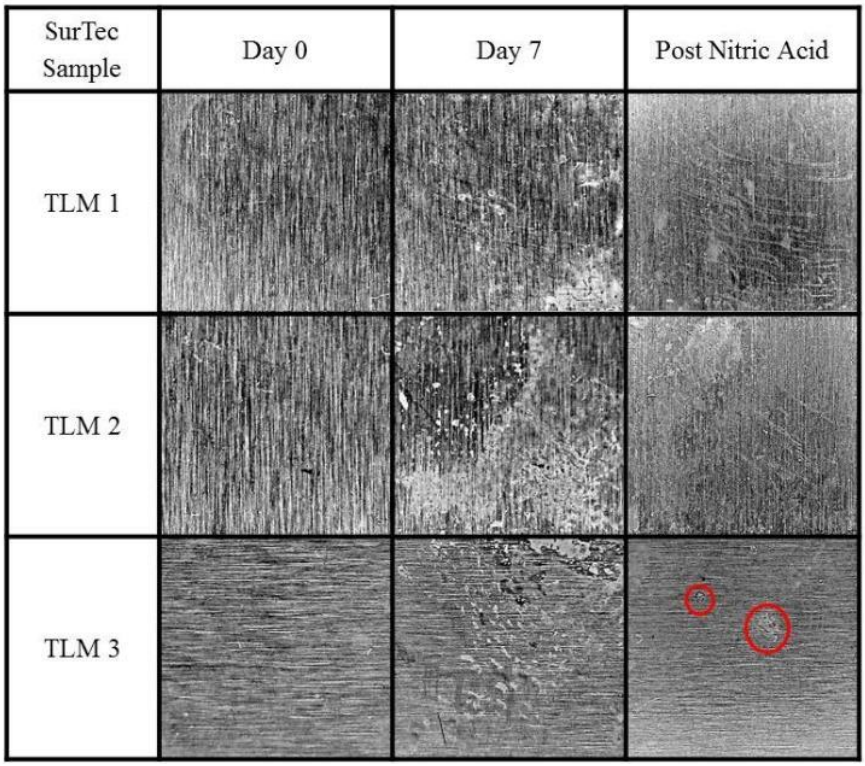

Figure 51. Black and white images of replicate TCP-coated (SurTec 650 E) AA7075-T6 specimens before (Day 0), after 7 days of a thin-layer mist test (Day 7), and after nitric acid dissolution of corrosion product (Post Nitric Acid). Red circles demark regions of surface damage. Image size = one square centimeter (entire panel shown in image).

Figure 52 shows black and white images of TCP-coated (Henkel) AA7075-T6 panels before (Day 0), after a 7-day thin-layer mist test (Day 7) and after acid dissolution (Post Nitric Acid). Of all the TCP and NCP coatings, the panels coated with this conversion coating showed the most surface features. The coating, as was the case for the other conversion coatings, was visible on the surface. There are many color variations across the specimen surfaces, as seen through the dark and light patches on TLM 2 and TLM 3. There is no significant visible change to the coated surfaces after the thin-layer mist exposure, with the exception of TLM 1 where one large pit is visible. All coated surfaces showed no visible corrosion product formation or major pitting. The main difference is that the surface features seen in SS3 prior to testing are gone after the salt-spray exposure. After acid dissolution, the surfaces have some discolored regions, which again are not

necessarily indicative of damage. Overall, this TCP coating, as well as the other three commercial variants, provide good stand-along corrosion protection to this aluminum alloy.

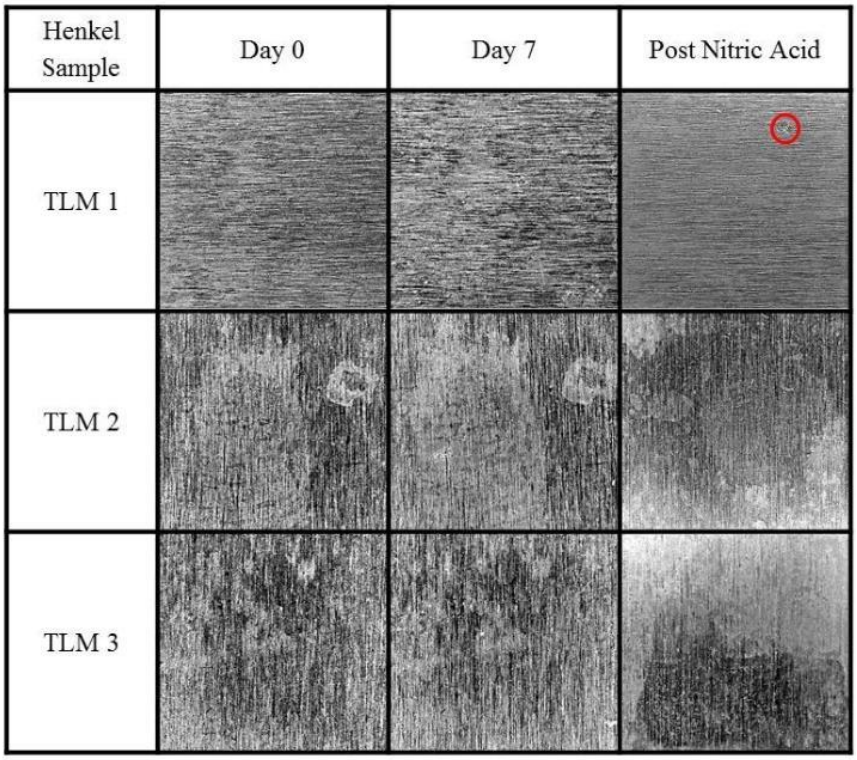

Figure 52. Black and white images of replicate TCP-coated (Henkel) AA7075-T6 specimens before (Day 0), after 7 days of a thin-layer mist test (Day 7), and after nitric acid dissolution of corrosion product (Post Nitric Acid). Red circles demark regions of surface pitting. Image size = one square centimeter (entire panel shown in image).

Overall, the TCP coatings protect the alloy against pitting and surface damage (with only a few pits seen) during the thin-layer mist 7-day test. The NCP coating had a significant amount of dark corrosion product buildup and surface damage, while the uncoated alloy experienced severe corrosion damage. These results also reveal that the coatings are all reproducibly applied by immersion, and their anti-corrosion properties (TCP) are apparent from sample to sample.

Figure 53 compares optical images of the uncoated, TCP-coated, and NCP-coated aluminum alloy panels before and after the 7-day neutral salt-spray exposure. Clearly, all four commercial TCP coatings provide good stand-alone corrosion protection in this environment. After exposure and acid dissolution, the images reveal negligible corrosion damage, discoloration

or flaws. Additionally, the NCP-coated and particularly the uncoated panels have significant corrosion damage. Both panels are decorated with large and small pits (black spots) after exposure and removal of the corrosion product.

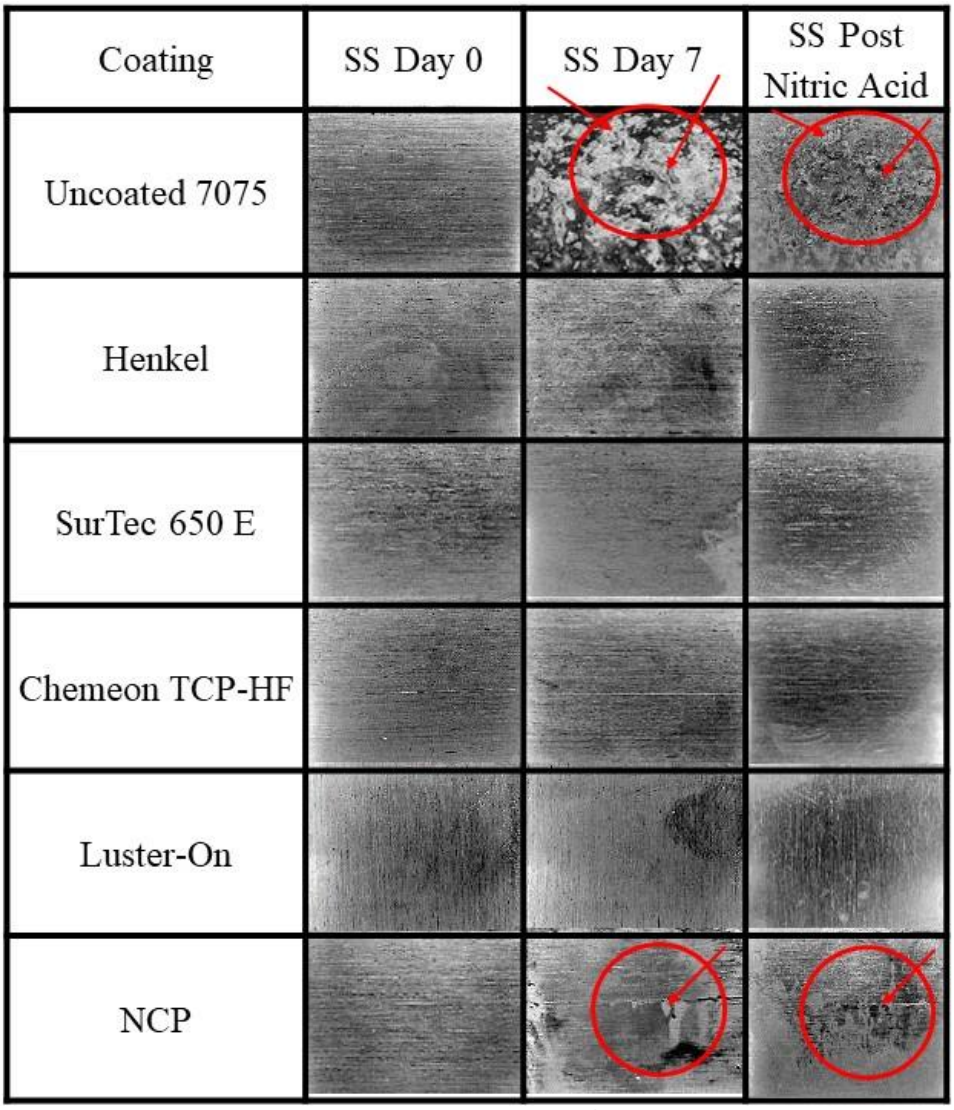

Figure 53. Comparison of optical images of the full 1 inch^2 surface area for NCP- and TCP-coated as well as uncoated AA7075-T6 before and after the 7-day neutral salt-spray test. Images for the panels after acid dissolution of any corrosion product are also presented. Red circles demark regions of corrosion product formation seen on day 7, and red arrows demark regions of surface pitting.

Figure 54 compares optical images of the uncoated, TCP-coated, and NCP-coated alloy panels before and after a 7-day thin-layer mist test. This particular test introduces more discoloration and flaws in the coating appearance as compared to the salt-spray test, but the TCP

coatings generally provide good stand-alone protection. The two exceptions were for the SurTec and Luster-On coatings, as these two panels had some pitting and damaged regions. This damage on the TCP-coated panels is far less than that seen on the NCP-coated and uncoated panels.

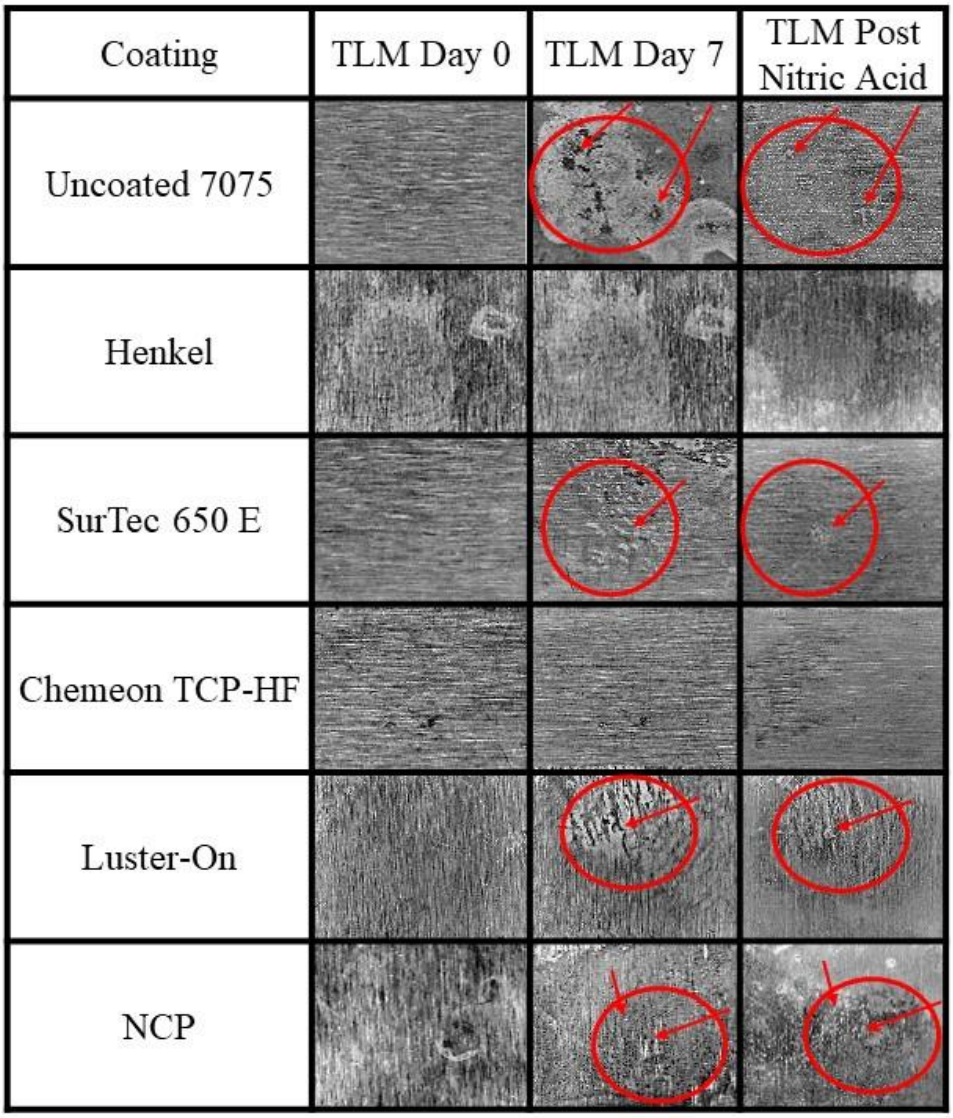

Figure 54. Comparison of optical images of the full 1 cm^2 surface area for NCP- and TCP-coated as well as uncoated AA7075-T6 before and after a 7-day thin-layer mist test. Images for the panels after acid dissolution of any corrosion product are also presented. Red circles demark regions of corrosion product formation seen on day 7, and red arrows demark regions of surface pitting.

Figure 55 shows the droplets of salt spray and how they exist on the surface of uncoated, TCP-, and NCP-coated AA7075-T6 panels before and after 2 days of thin-layer mist test exposure. While we refer to this as a thin-layer of mist, actually rather large droplets exist over the surface

after the application of five “sprays”. The droplets vary in size from larger regions of aggregated droplets to isolated regions of smaller droplets. These images reveal the surface condition prior to the start of the test. Generally speaking, the TCP-coated panels are more hydrophobic than both the uncoated and NCP-coated panels. For these specimens, the water layer wets the surface and spreads out as a more-or-less continuous layer. During the TLM test, some solvent evaporation occurs so he droplet volume will decrease, but the surface never reaches complete dryness. There is also an element of temperature fluctuation, as the specimens experience 23h of 35°C heat and then are cooled back to room temperatures, ~23°C, for one hour each day when the specimens are re-sprayed with the 3.5% NaCl. Images from days 3 - 7 showed the same hydrophobicity as day 2, so these are not shown. The uncoated, Henkel-, and NCP-coated specimens began hydrophilic, with the aqueous solution covering the surface with little to no breaks. SurTec E, Chemeon, and Luster-On were at least half hydrophobic at day 0. After one day of exposure, the images of all coatings showed at least one specimen with highly increased hydrophobicity apparent from the beading of salt solution droplets on the surface. The NCP coating showed the most hydrophilic films, with little water repellent properties, appearing similar to the uncoated specimen. After one day, damage to the uncoated specimen is evident, either through surface roughening or specimen darkening with corrosion product (uncoated and NCP panels).

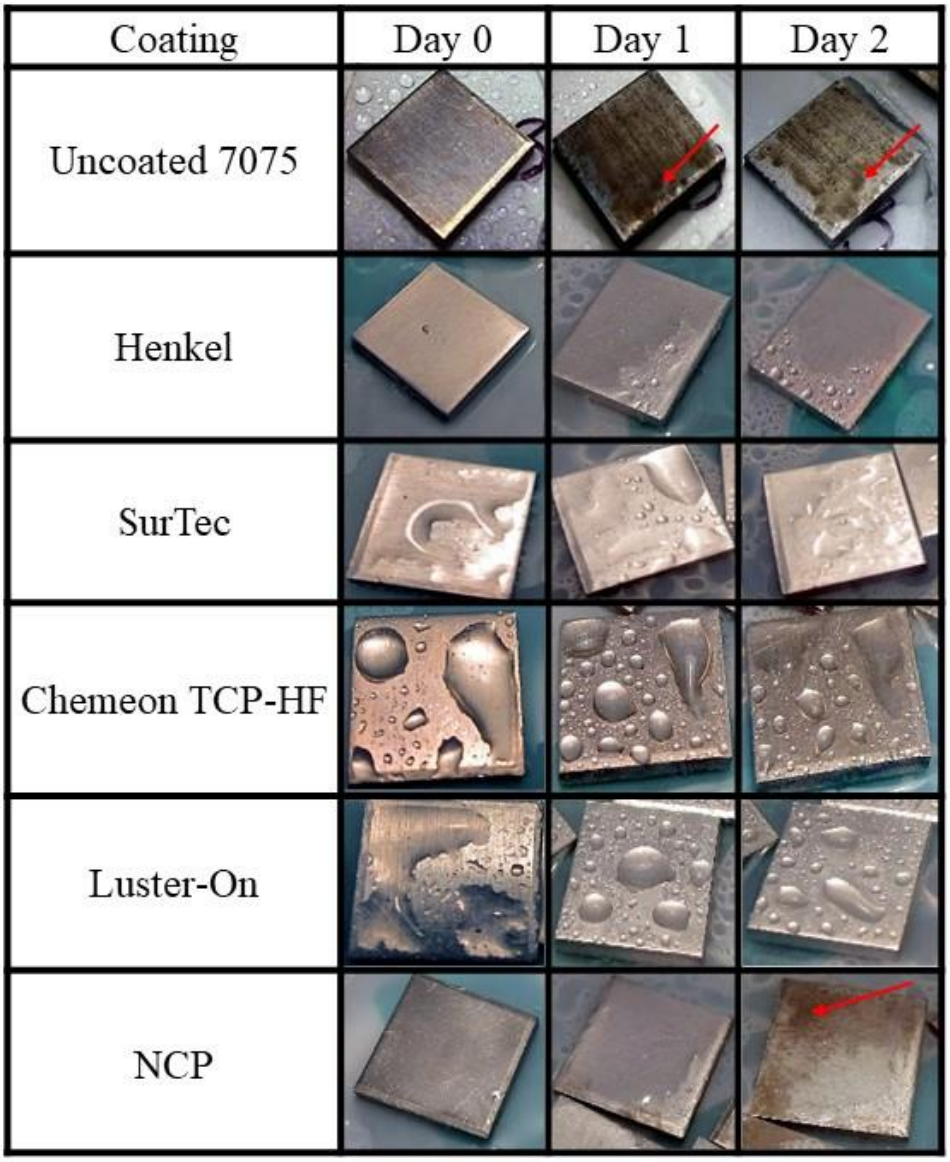

Figure 55. Photographs of the full 1 cm^2 surface area for NCP-coated, TCP-coated, and uncoated AA7075-T6 before (Day 0), after 1 day (Day 1), and after 2 days (Day 2) of a thin-layer mist test. The droplet distribution is shown for the 3.5% NaCl spray immediately after application. Red arrows mark regions of corrosion initiation, seen after 1 day for uncoated specimens and after 2 days for NCP-coated specimens.

4.4. Cross Comparison Discussion

A review of all the results leads to some important points for discussion:

The pit depths and surface roughness were significantly increased for the uncoated specimens after both the 7-day salt-spray (10x and 2x) and thin-layer mist tests (<10x and <2x), as compared to unexposed specimens. All the TCP-coated specimens showed no changes in

roughness after both tests. Pit depths increased during the salt-spray test for Henkel (<2x) and during the thin-layer mist test for Henkel (>2x), SurTec (>3x), and Chemeon (>3x). The NCP-coated specimens also showed no changes in surface roughness after both tests. Pit depths increased more noticeably for the NCP-coated specimens after both the salt-spray (2x) and the thin-layer mist tests (>4x). The changes in pit depth reveal damage to the aluminum alloy, with greater pit depths indicating more metal dissolution due to corrosion. As expected, the uncoated specimens experienced major pit deepening and damage. Specimens conversion coated with NCP containing no Cr showed greater pitting and surface damage, as compared to the TCP-coated specimens. This difference is attributed to the protective action of $Cr(OH)_3$ in the TCP coating. The NCP coating provided much better protection than no coating at all, so the hydrated zirconia, ZrO_2, and $Zn(OH)_2$ precipitates in the coating provide a decent amount of corrosion protection. The variations between TCP coatings were unexpected, but reveal some interesting differences that follow trends in coating bath composition. The Cr bath content is highest for Luster-On, which showed the shallowest pit depths. Chemeon had the next highest Cr content in the bath and specimens coated with it also had shallow pit depths. The Henkel and SurTec coating baths were close in Cr content and specimens coated with these conversion coatings had similar pit depths, but greater than those for the Luster-on and Chemeon-coated specimens. The panels without any Cr present (NCP and uncoated specimens) showed the deepest pits and greatest surface roughening.

The weight changes after both tests are consistent with trends in the coating bath Cr concentration. The Luster-On-coated specimens showed the lowest weight loss, followed by the Chemeon, SurTec and Henkel-coated specimens. Surprisingly, NCP provided an equivalent level of weight loss to the TCP coatings during the thin-layer mist test. Again, this indicates that even

the barrier coating without any possible active corrosion protection provides excellent stand-alone corrosion protection to this aluminum alloy.

While an analysis of pit density did not correlate with the in the Cr concentration in the coating baths, the pit areas were decreased for all coatings after both tests, as compared to the uncoated controls. Luster-On-coated specimens had the lowest pit areas after the thin-layer mist test, with Chemeon providing the second lowest. There were no statistical differences in nominal pit area between the TCP coatings and NCP coating after a salt-spray test, but NCP-coated specimens had a larger nominal pit area compared to the TCP-coated specimens after a thin-layer mist test. Overall, the TCP coatings protect well against pitting and surface damage (with only a few pits seen) during the salt-spray 7-day test. The NCP coating showed little visible white corrosion product, but still had a significant amount of dark corrosion product and surface damage, while uncoated AA7075-T6 had a severe buildup of corrosion product and a large amount of surface damage after the salt-spray test. The corrosion product is likely composed of $AlCl_3$, $NaAlCl_2$, and Al_2O_3.

The confocal microscopy map images reflect the damage detected through the microscopy and profilometry, with trends matching the Cr trends: Luster-On showed the least visible damage after any testing, followed by Chemeon, Henkel, and SurTec. The visual analysis revealed large amounts of white corrosion product on the uncoated specimens, large amounts of dark corrosion product on the NCP-coated specimens, and little to no corrosion product on any of the TCP-coated specimens.

4.5. Conclusions

Overall, the Luster-On and Chemeon coatings provided better corrosion protection as compared to the SurTec and Henkel coatings in thin-layer mist and salt-spray accelerated

degradation tests. This assessment is based on the quantitative analysis of surface topography and specimen mass loss. The SurTec and Henkel TCP coatings provided corrosion protection to AA7075-T6 in both tests but these specimens had greater pitting. NCP provided a lower level of corrosion protection. All coatings provided improvements in the corrosion resistance of the alloy as compared to the uncoated control. This protection was evidenced qualitatively through a decrease in visible white and dark corrosion product on the specimen surface, and quantitatively through decreased surface damage seen through topographical analysis. This protection was quantified through statistically significant decreases in weight loss indicating less aluminum matrix degradation and pit statistics indicating smaller, shallower pits. All of these results agree well with the coating bath analysis, which predicted these trends based on the concentrations of Cr in each.

REFERENCES

REFERENCES

1. Polmear, I. J., 2 - Physical metallurgy of aluminium alloys. In *Light Alloys (Fourth Edition)*, Polmear, I. J., Ed. Butterworth-Heinemann: Oxford, **2005**; pp 29-96.

2. Birbilis, N.; Buchheit, R. G., Electrochemical characteristics of intermetallic phases in aluminum alloys - An experimental survey and discussion. *Journal of the Electrochemical Society* **2005,** *152* (4), B140-B151.

3. Costa, M., Toxicity and carcinogenicity of Cr(VI) in animal models and humans. *Critical Reviews in Toxicology* **1997,** *27* (5), 431-442.

4. Shanker, A. K.; Cervantes, C.; Loza-Tavera, H.; Avudainayagam, S., Chromium toxicity in plants. *Environment International* **2005,** *31* (5), 739-753.

5. Dardona, S.; Chen, L.; Kryzman, M.; Goberman, D.; Jaworowski, M., Polarization Controlled kinetics and composition of trivalent chromium coatings on aluminum. *Analytical Chemistry* **2011,** *83* (16), 6127-6131.

6. Li, L.; Swain, G. M., Formation and structure of trivalent chromium process coatings on aluminum alloys 6061 and 7075. *Corrosion* **2013,** *69* (12), 1205-1216.

7. La Scala, J., Non-Chromate/ no VOC conversion coatings. *SERDP Report* **2009**, 68.

8. Feng, Z.; Frankel, G. S.; Matzdorf, C. A., Quantification of Accelerated corrosion testing of coated AA7075-T6. *Journal of The Electrochemical Society* **2014,** *161* (1), C42-C49.

9. Feng, Z.; Boerstler, J.; Frankel, G. S.; Matzdorf, C. A., Effect of surface pretreatment on galvanic attack of coated al alloy panels. *Corrosion* **2015,** *71* (6), 771-783.

10. Qi, J. T.; Hashimoto, T.; Walton, J. R.; Zhou, X.; Skeldon, P.; Thompson, G. E., Trivalent chromium conversion coating formation on aluminium. *Surface and Coatings Technology* **2015,** *280*, 317-329.

11. Dardona, S.; Jaworowski, M., In situ spectroscopic ellipsometry studies of trivalent chromium coating on aluminum. *Applied Physics Letters* **2010,** *97* (18), 181908.

12. Li, L.; Swain, G. P.; Howell, A.; Woodbury, D.; Swain, G. M., The formation, structure, electrochemical properties and stability of trivalent chrome process (TCP) coatings on AA2024. *Journal of The Electrochemical Society* **2011,** *158* (9), C274-C283.

13. Li, L.; Swain, G. M., Effects of aging temperature and time on the corrosion protection provided by trivalent chromium process coatings on AA2024-T3. *ACS Applied Materials & Interfaces* **2013,** *5* (16), 7923-7930.

14. Li, L.; Doran, K. P.; Swain, G. M., Electrochemical characterization of trivalent chromium process (TCP) coatings on aluminum alloys 6061 and 7075. *Journal of The Electrochemical Society* **2013,** *160* (8), C396-C401.

15. Qi, J.; Hashimoto, T.; Thompson, G. E.; Carr, J., Influence of water immersion post-treatment parameters on trivalent chromium conversion coatings formed on AA2024-T351 alloy. *Journal of The Electrochemical Society* **2016,** *163* (5), C131-C138.

16. Qi, J.; Hashimoto, T.; Walton, J.; Zhou, X.; Skeldon, P.; Thompson, G. E., Formation of a trivalent chromium conversion coating on AA2024-T351 alloy. *Journal of The Electrochemical Society* **2016,** *163* (2), C25-C35.

17. Qi, J.; Thompson, G. E., Comparative studies of thin film growth on aluminium by AFM, TEM and GDOES characterization. *Applied Surface Science* **2016,** *377*, 109-120.

18. Qi, J.; Walton, J.; Thompson, G. E.; Albu, S. P.; Carr, J., Spectroscopic Studies of chromium VI formed in the trivalent chromium conversion coatings on aluminum. *Journal of The Electrochemical Society* **2016,** *163* (7), C357-C363.

19. Munson, C. A.; Swain, G. M., Structure and chemical composition of different variants of a commercial trivalent chromium process (TCP) coating on aluminum alloy 7075-T6. *Surface and Coatings Technology* **2017,** *315*, 150-162.

20. Committee, A. S. M. I. H., ASM Handbook, Volume 05 - Surface Engineering. ASM International.

21. Li, L.; Desouza, A. L.; Swain, G. M., Effect of deoxidation pretreatment on the corrosion inhibition provided by a trivalent chromium process (TCP) conversion coating on AA2024-T3. *Journal of The Electrochemical Society* **2014,** *161* (5), C246-C253.

22. Li, L.; Desouza, A. L.; Swain, G. M., In situ pH measurement during the formation of conversion coatings on an aluminum alloy (AA2024). *Analyst* **2013,** *138* (15), 4398-4402.

23. Xue, T.; Cooper, W. C.; Pascual, R.; Saimoto, S., Effect of fluoride ions on the corrosion of aluminium in sulphuric acid and zinc electrolyte. *Journal of Applied Electrochemistry* **1991,** *21* (3), 238-246.

24. Li, L.; Whitman, B. W.; Munson, C. A.; Estrada, R.; Matzdorf, C. A.; Swain, G. M., Structure and corrosion performance of a non-chromium process (NCP) Zr/Zn pretreatment conversion coating on aluminum alloys. *Journal of The Electrochemical Society* **2016,** *163* (13), C718-C728.

25. Ramsey, J. D.; McCreery, R. L., Raman microscopy of chromate interactions with corroding aluminum alloy 2024-T3. *Corrosion Science* **2004,** *46* (7), 1729-1739.

26. Feng, Z.; Frankel, G. S., Galvanic test panels for accelerated corrosion testing of coated Al alloys: Part 2—measurement of galvanic interaction. *CORROSION* **2014,** *70* (1), 95-106.

27. Feng, Z.; Frankel, G. S.; Abbott, W. H.; Matzdorf, C. A., Galvanic attack of coated al alloy panels in laboratory and field exposure. *Corrosion* **2016,** *72* (3), 342-355.

28. Frankel, G. S.; Newman, R. C.; Jahnes, C. V.; Russak, M. A., On the pitting resistance of sputter-deposited aluminum alloys. *Journal of The Electrochemical Society* **1993,** *140* (8), 2192-2197.

29. Guo, Y.; Frankel, G. S., Characterization of trivalent chromium process coating on AA2024-T3. *Surface and Coatings Technology* **2012,** *206* (19–20), 3895-3902.

30. Guo, Y.; Frankel, G. S., Active corrosion inhibition of AA2024-T3 by trivalent chrome process treatment. *CORROSION* **2012,** *68* (4), 045002-1-045002-10.

31. Clark, W. J.; Ramsey, J. D.; McCreery, R. L.; Frankel, G. S., A galvanic corrosion approach to investigating chromate effects on aluminum alloy 2024-T3. *Journal of The Electrochemical Society* **2002,** *149* (5), B179-B185.

32. Standard practice for immersion testing of industrial protective coatings and linings. ASTM International: 2015.

33. Standard practice for operating salt spray (fog) apparatus. ASTM International: 2016.

34. Leggat, R. B.; Taylor, S. R.; Zhang, W.; Buchheit, R. G., Corrosion performance of field-applied chromate conversion coatings. *CORROSION* **2002,** *58* (3), 283-291.

35. Mishra, S.; Bharagava, R. N., Toxic and genotoxic effects of hexavalent chromium in environment and its bioremediation strategies. *Journal of Environmental Science and Health, Part C* **2016,** *34* (1), 1-32.

36. (a) Twite, R. L.; Bierwagen, G. P., Review of alternatives to chromate for corrosion protection of aluminum aerospace alloys. *Progress in Organic Coatings* **1998,** *33* (2), 91-100; (b) Kendig, M. W.; Buchheit, R. G., Corrosion inhibition of aluminum and aluminum alloys by soluble chromates, chromate coatings, and chromate-free coatings. *CORROSION* **2003,** *59* (5), 379-400; (c) Guan, H.; Buchheit, R. G., Corrosion Protection of Aluminum Alloy 2024-T3 by Vanadate Conversion Coatings. *CORROSION* **2004,** *60* (3), 284-296.

37. C. A. Matzdorf, W. C. N., Jr., E. N. Beck, A. S. Schwartz and J. L. Green, Non-chromium coatings for aluminum. *Us. Patent Application Publication* **2007**.

38. Suib, S. L.; La Scala, J.; Nickerson, W.; Fowler, A.; Zaki, N., Determination of hexavalent chromium in NAVAIR trivalent chromium process (TCP) coatings and process solutions. *Metal Finishing* **2009,** *107* (2), 28-34.

39. A. Iyer, W. W., S. Frueh, W. Nickerson, A. Fowler, J. Bames, L. Hagos, J. Escarsega, J. La Scala and S.L. Suib, Characterization of NAVAIR trivalent chromium process (TCP) coatings and solutions. *Plating and Surface Finishing* **2010,** *5* 32-42.

40. Dong, X.; Wang, P.; Argekar, S.; Schaefer, D. W., Structure and composition of trivalent chromium process (TCP) films on Al alloy. *Langmuir* **2010,** *6* (13), 10833-10841.

41. Li, L.; Kim, D. Y.; Swain, G. M., Transient formation of chromate in trivalent chromium process (TCP) coatings on AA2024 as probed by Raman spectroscopy. *Journal of The Electrochemical Society* **2012,** *159* (8), C326-C333.

42. Davis, J. R.; International, A. S. M.; Handbook, C., *Aluminum and aluminum alloys*. ASM International: Materials Park, Ohio, 1994.

43. (a) Gao, M.; Feng, C. R.; Wei, R. P., An analytical electron microscopy study of constituent particles in commercial 7075-T6 and 2024-T3 alloys. *Metall Mater Trans A* **1998,** *29* (4), 1145-1151; (b) Birbilis, N.; Cavanaugh, M. K.; Buchheit, R. G., Electrochemical behavior and localized corrosion associated with Al7Cu2Fe particles in aluminum alloy 7075-T651. *Corrosion Science* **2006,** *48* (12), 4202-4215; (c) Dey, S.; Gunjan, M. K.; Chattoraj, I., Effect of temper on the distribution of pits in AA7075 alloys. *Corrosion Science* **2008,** *50* (10), 2895-2901; (d) Buchheit, R. G.; Birbilis, N., Electrochemical microscopy: An approach for understanding localized corrosion in microstructurally complex metallic alloys. *Electrochimica Acta* **2010,** *55* (27), 7853-7859; (e) Singh, S. S.; Guo, E.; Xie, H.; Chawla, N., Mechanical properties of intermetallic inclusions in Al 7075 alloys by micropillar compression. *Intermetallics* **2015,** *62*, 69-75.

42. (a) Frankel, G. S., 2015 W.R. Whitney Award Lecture: The effects of microstructure and composition on Al alloy corrosion. *CORROSION* **2015,** *71* (11), 1308-1320; (b) Birbilis, N.; Buchheit, R. G., Investigation and discussion of characteristics for intermetallic phases common to aluminum alloys as a function of solution pH. *Journal of The Electrochemical Society* **2008,** *155* (3), C117-C126.

43. (a) Weckhuysen, B. M.; Wachs, I. E., In situ Raman spectroscopy of supported chromium oxide catalysts: reactivity studies with methanol and butane. *The Journal of Physical Chemistry* **1996,** *100* (34), 14437-14442; (b) Hurley, B. L.; McCreery, R. L., Raman spectroscopy of monolayers formed from chromate corrosion inhibitor on copper surfaces. *Journal of The Electrochemical Society* **2003,** *150* (8), B367-B373; (c) Xia, L.; McCreery, R. L., Chemistry of a Chromate Conversion Coating on Aluminum Alloy AA2024-T3 Probed by Vibrational Spectroscopy. *Journal of The Electrochemical Society* **1998,** *145* (9), 3083-3089.

44. Carter, G. A.; Hart, R. D.; Rowles, M. R.; Buckley, C. E.; Ogden, M. I., The effect of processing parameters on particle size in ammonia-induced precipitation of zirconyl chloride under industrially relevant conditions. *Powder Technology* **2009,** *191* (1), 218-226.

45. Roudabush, L. A.; Townsend, H. E.; McCune, D. C., Update on the development of an improved cosmetic corrosion test by the automotive and steel industries. SAE International: 1993.

46. Ferrer, K. S.; Kelly, R. G., Comparison of Methods for Removal of Corrosion Product from AA2024-T3. *CORROSION* **2001,** *57* (2), 110-117.

CHAPTER 5: CROSS COMPARISON OF TCP- AND NCP-COATED AA7075-T6 DURING SALT-SPRAY ACCELERATED DEGRADATION TESTING: SCANNING ELECTRON MICROSCOPY AND ENERGY DISPERSIVE X-RAY SPECTROSCOPY

5.1. Introduction and Research Objectives

The performance of SurTec 650 E, formed by standard immersion, was directly compared to the performance of three other commercial variants of the TCP coating [Bonderite T5900 (Henkel), TCP-HF (Chemeon), and Aluminescent (Luster-on)] on AA7075-T6. The performance of a non-chromate conversion coating (NCP) developed by NAVAIR was also compared.[24, 37-38] The commercial TCP coatings are all licensed from NAVAIR and are based on the formulation described in the original patent. As already mentioned, each contains a slightly different chemical composition and will be treated as a separate coating. Studies were performed to directly evaluate the anti-corrosion performance of each of the coatings on immersion-coated panels when subjected to a 7-day neutral salt-spray (ASTM B117, 5 wt. % NaCl) accelerated degradation test. The alloys were inspected for corrosion damage using scanning electron microscopy (SEM) after removal of the corrosion product with a nitric acid etch.[46] The exposure period was used for coating evaluation because a 7-day (168 h) neutral salt-spray test (5 wt. % NaCl, 35 ^{o}C) is required by DoD when evaluating chemical conversion coating performance on aluminum and aluminum alloys as described in the military document, MIL-DTL-5541F.

5.2. Experimental Procedures

5.2.1. Scanning Electron Microscopy

Scanning electron microscopy and energy dispersive x-ray analysis (EDXS) were performed using a field emission microscope (JEOL 6610LV) with an EDXS microanalysis attachment (AZtecEnergy analysis). These studies were performed to assess the metallographic

condition of the coated specimen surfaces before and after accelerated degradation testing. All maps were collected at 3,000x using a 15kV accelerating voltage, 10 mm working distance, and spot size of 30 nm. The x-ray emission lines from EDXS spectra were used to determine the presence of the conversion coating (Zr, Cr, F and O) near intermetallic particles and away from these particles on the aluminum matrix. The measurements were made at the Center for Advanced Microscopy (MSU).

Specimen Preparation

The specimen preparation is detailed in Chapter 4.

5.2.3. Accelerated Degradation Tests

Salt-spray (ASTM B117) Test

The ASTM B117 salt-spray test performed is in Chapter 4.

5.3. Cross Comparison Results

5.3.1. Scanning Electron Microscopy Analysis Before and After Accelerated Degradation Tests

Scanning electron microscopy was performed on the coated and uncoated specimens, before and after the 7-day salt-spray test, and after nitric acid removal of any corrosion product. Figure 56 shows secondary electron (SE) micrographs on the top and backscattered electron micrographs on the bottom for an uncoated panel (degreased and deoxidized) before (Day 0) and after the 7-day test (Day 7). Two separate regions are shown after the test, one region contains localized damage, visible through the large regions with increased surface roughness and visibly powdery corrosion product (Damage). The other region shows much less corrosion (Little Damage). The SE micrographs reflect differences in surface height through brightness, with regions containing higher points providing a greater density of secondary electrons to escape the

surface, leading to a higher intensity and brightness. The surface before testing shows regular ridges due to the alloy rolling process into sheets, seen through the repeating light and dark lines. There are some white spots that could be surface debris or intermetallic particles (IMPs). To determine if these white spots are in fact IMPs, the backscattered electron signal was examined. Backscattered electrons (BSE) show differences in brightness due to elemental differences (Z-number contrast) instead of topographical differences. Regions with elements of higher atomic mass (Z number) will show up as brighter spots on the micrograph, so the Cu and Fe IMPs will reveal as white spots in the grey Al background. Conversely, any regions of lower atomic weight (C or O rich areas) will reveal as dark spots in the grey Al background. The white spots in the SE for Day 0 align with the bright spots in the BSE, indicating they contain elements with a higher atomic mass than Al, and are therefore probably IMPs. After the nitric acid etching, the secondary electron micrograph reveals one large cluster of pits in the center of the image and smaller isolated pits over the remainder of the surface.

The uncoated AA7075-T6 control performed poorly during the salt-spray test (Figure 56), with a generally rough appearance over the entire panel. Additionally, a light powdery product is visible in most areas (Day 7- Damage). This product does not have a different elemental composition from the rest of the alloy surface (Al and O as $Al(OH)_3$). This indicates the rougher surface and increased features are due to aluminum oxide corrosion product build-up. The corrosion product is wide spread over the surface (several hundred micrometers) and visible even in the least changed areas of the panel. In order to determine the extent of the aluminum alloy damage under the corrosion product, the layer was removed by short ultrasonic treatment in concentrated nitric acid. After product removal, the uncoated surface exhibited large regions of rough topography due to the rolling process. There is a large pitted region in the center of the

secondary electron micrograph. The backscattered electron micrograph reveals bright spots reflective of non-Al intermetallic phases (Post Nitric-Damage) as well as some small black spots that are likely pits. Pits spanning hundreds of micrometers were visible across the entire surface with a total of 20 seen, and are in the same regions as the corrosion product seen before acid treatment. Additionally, these pits are seen in the same areas as the pits that were identified and examined using profilometry in Chapter 4. The surface is also covered with smaller pits spanning less than 50 µm, which were too numerous to count with the naked eye. To examine the surface damage more in depth, a closer view is necessary.

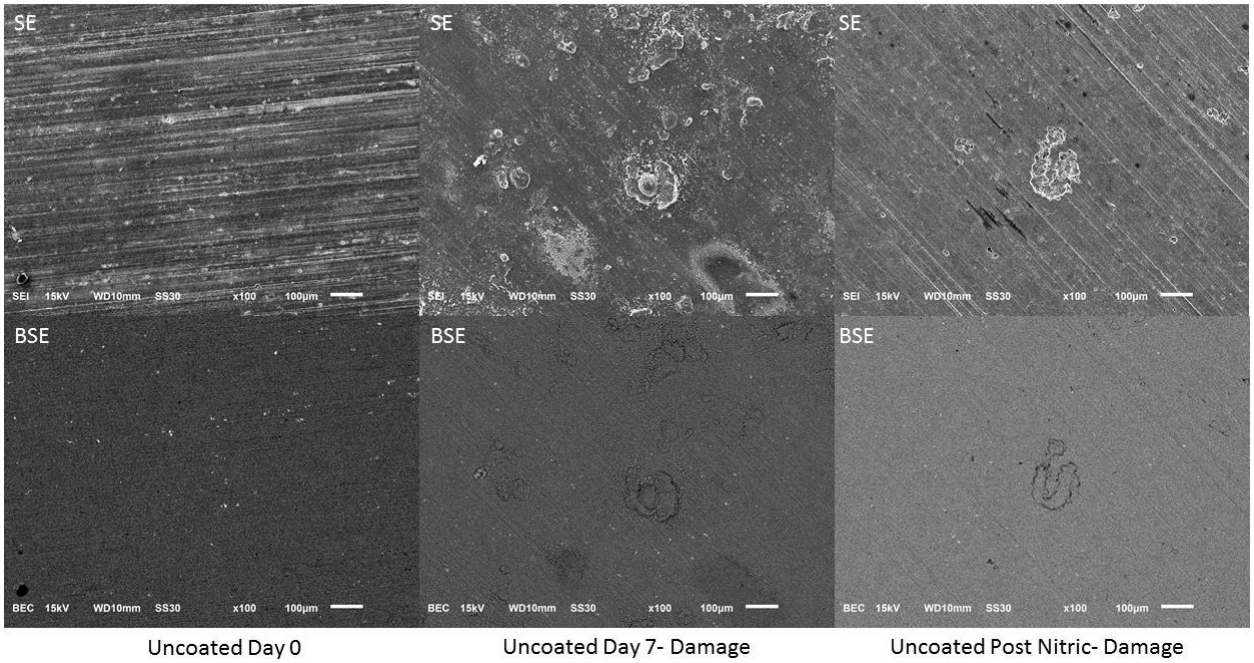

Figure 56. Scanning electron micrographs of uncoated AA7075-T6. Top images show secondary electron micrographs and bottom images show back-scattered electron micrographs. Images on the left are before testing (Day 0), images in the center are major damaged regions after the 7-day neutral salt-fog exposure (ASTM B117) (Day 7- Damage), and images on the right are the same regions as the center panels after nitric acid sonication to remove corrosion product (Post Nitric-Damage). All images have a 100 µm scale bar in the bottom right.

A closer examination of the surface is necessary to view more subtle changes, and is performed on the uncoated control both before (Figure 57) and after the salt-spray test. Before any testing, the image of the uncoated surface shows one of the bright regions from both the SE

and BSE (attributed to an IMP) in Figure 56. The rolling ridges due to the alloying process are evident, and seen to have widths from 5-15 µm. The ridges extend across the entire panel and are all parallel to each other. Along with ridges, some small pits and other surface features are visible. Energy dispersive x-ray spectroscopy was used to determine the elements present in each distinct region of the micrographs, and the results are presented as color-coded maps in Figure 57. The aluminum alloy itself is composed of Mg, Na, Al, Cr, and Zn, with some C and O present mainly on the surface. The carbon comes from adventitious hydrocarbon contaminants adsorbed from the air. Some Cu is also visible across the surface due to its dissolution from the IMPs during the deoxidation process and re-deposition onto the bulk alloy. The largest visible IMP is composed of Cu.

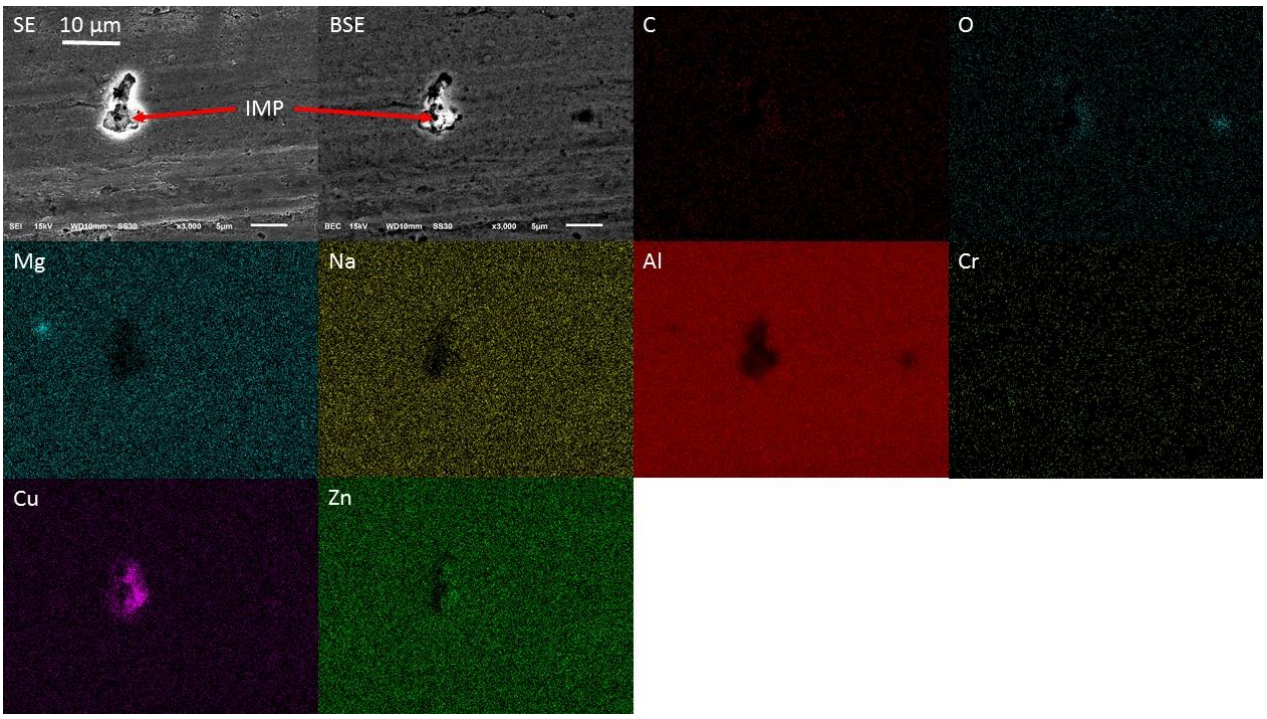

Figure 57. Scanning electron micrographs and corresponding energy dispersive x-ray spectral maps of uncoated AA7075-T6 before any testing. All images correspond to the 10 µm scale bar in the secondary electron (SE) image, next to the back-scattered (BSE) image. The element represented in each map is shown in the top left corner of each panel.

After the salt-spray testing, most of the uncoated surface is covered with a powdery, bright corrosion product, as seen in the SE and BSE micrographs (Figure 58). The surface is covered by

a film of aluminum oxide (Al_2O_3) corrosion product. The cracks seen resemble the mud cracking that often occurs with coatings due to dehydration in the vacuum chamber of the SEM. The cracks in the oxide layer allow for a higher aluminum signal in the elemental map for the element. The Cu IMP visible in this area (upper right corner) is co-localized with Zn, based on the elemental maps for the two. There is a large growth of nodular corrosion product formed around thus IMP. The corrosion product is composed of Al and O. The carbon present is presumably due to hydrocarbon contamination from exposure to the laboratory atmosphere. There is some Na and Cl detected on the surface. This is residual salt from the salt-spray test.

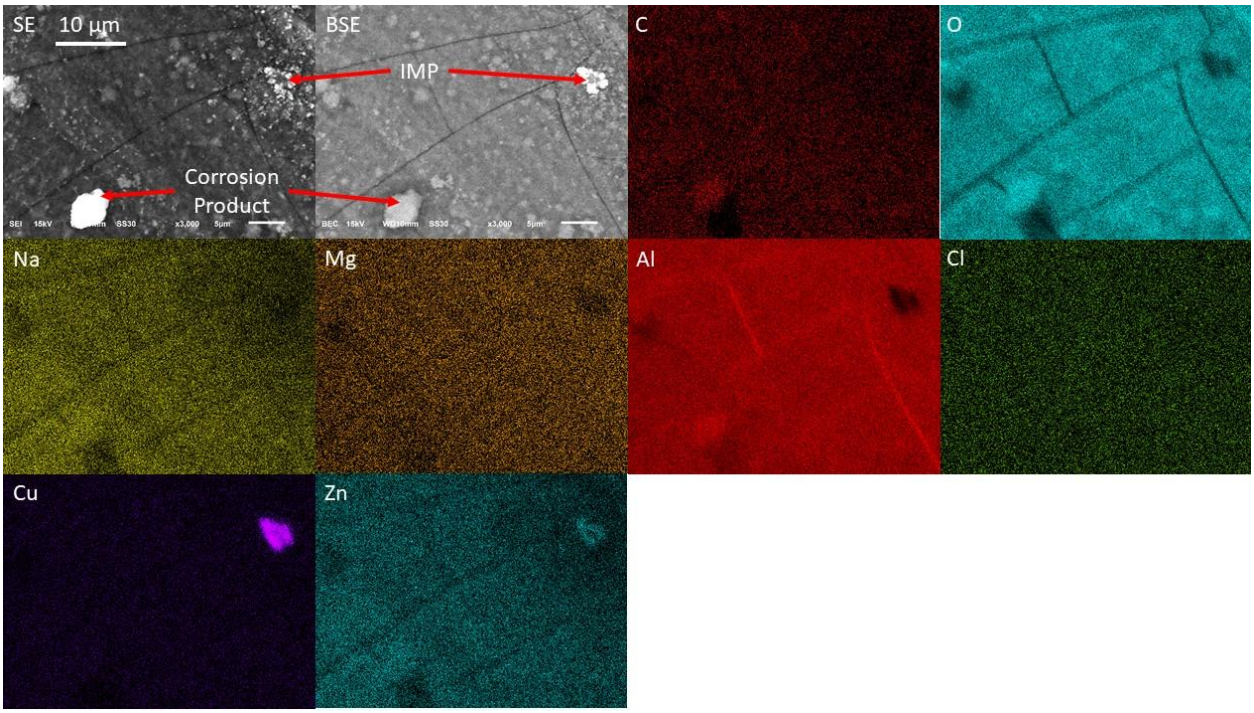

Figure 58. Scanning electron micrographs and corresponding energy dispersive x-ray spectral maps for uncoated AA7075-T6 after a 7-day neutral salt-fog test. All image dimensions are indicted by the 10 µm scale bar in the secondary electron (SE) image. The element represented in each map is shown in the top left corner of the panel.

The corroded regions after the salt-spray exposure show little difference in elemental composition from the bulk aluminum alloy after removal of the corrosion product. In a region with low surface damage (Figure 59) on the uncoated panel, one Fe IMP is visible. The periodic ridges from the alloy processing are no longer resolved due to the overall surface roughening.

There are cracks and voids in the Fe IMP probably due to some dealloying that occurred either during the deoxidation step or the salt-spray exposure. The major damage seen is the cracks extending away from the IMP, suggestive of intergranular corrosion.

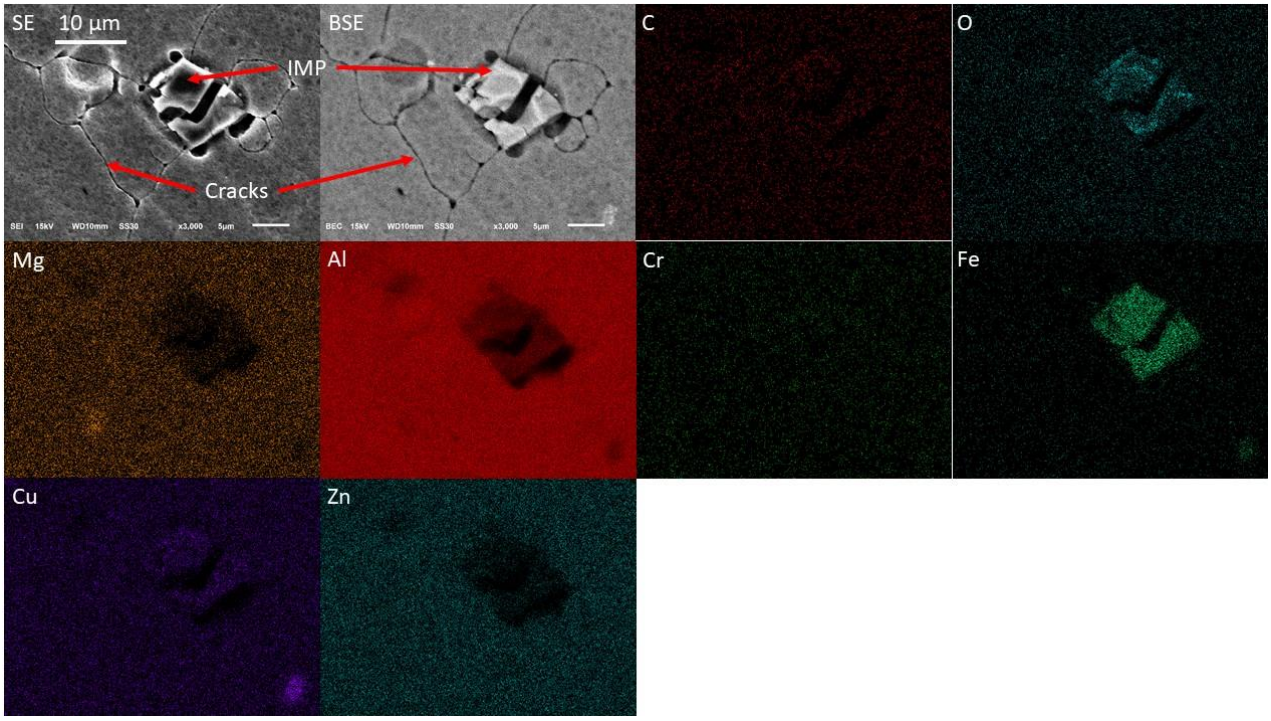

Figure 59. Scanning electron micrographs and corresponding energy dispersive x-ray spectral maps of uncoated AA7075-T6 after a 7-day neutral salt-fog test and subsequent removal of corrosion product with nitric acid. All image dimensions are indicated by the 10 µm scale bar in the secondary electron (SE) image. The element represented in each map is shown in the top left corner of the panel.

Electron micrographs elemental maps for one of the TCP-coated (Henkel) AA7075-T6 specimens reveal a very different surface topography after the 7-day salt-spray test, as compared to the exposed uncoated specimens (Figure 60). Before testing (Day 0), the secondary and backscattered electron micrographs show the grooves from the alloy rolling process, but the height variations are decreased due to the presence of the conversion coating. Additionally, there are numerous white precipitates seen decorating the surface. These are bright features in the backscattered electron image indicating a higher atomic number element than Al. These are TCP coating precipitates that consist of Cr and Zr oxides. These form across the alloy surface and

aggregate around IMPs.[6] After the salt-spray test (Day 7- Major Damage), the precipitates are less visible and lower in surface density, but are still present. The grooves from the rolling process are more visible, perhaps due to loss of some coating from the surface. Overall, there is very little noticeable change in the surface topography or evidence for corrosion on the specimen. There are some pits seen in the secondary electron micrograph of the specimen after nitric acid removal of corrosion product. It is unclear though if these pits formed during the salt-spray exposure or were generated during the degreasing and deoxidation pretreatment if the metal prior to applying the conversion coating. Unequivocally, there appears to be far less surface damage and corrosion of the TCP-coated specimen after 7 days of salt-spray exposure, as compared to the uncoated alloy.

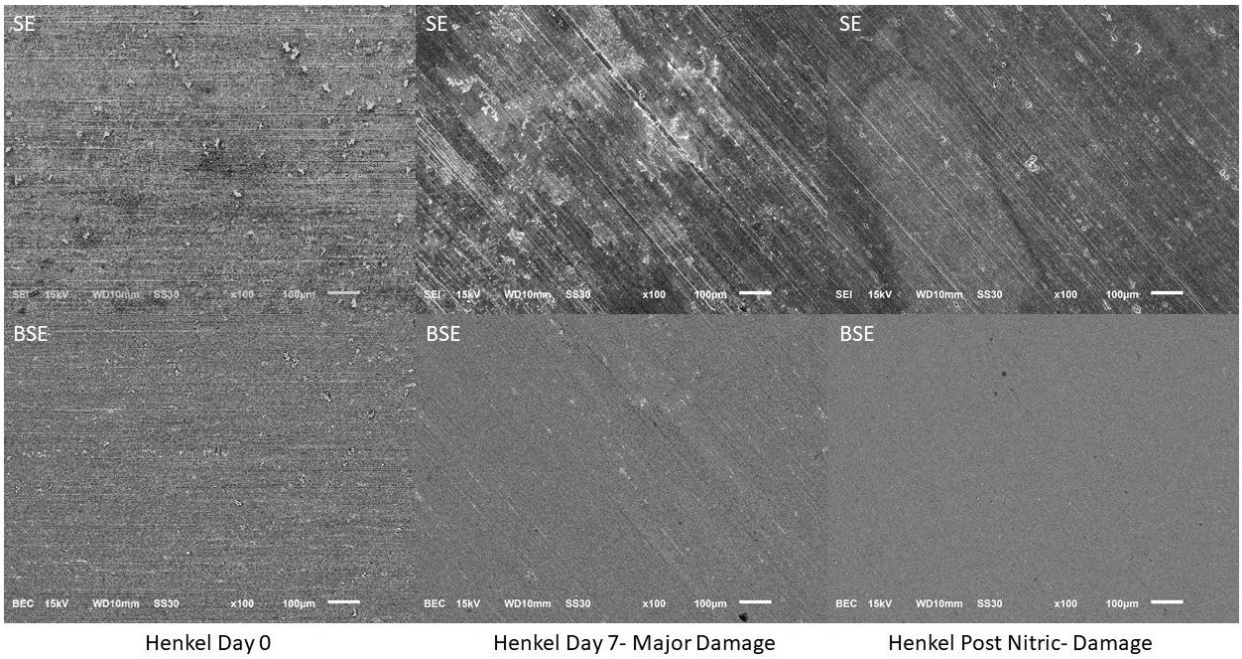

Figure 60. Scanning electron micrographs of TCP-coated (Henkel) AA7075-T6. Top images show secondary electron micrographs and bottom images show back-scattered electron micrographs. Images on the left are before testing (Day 0), images in the center are the major damaged regions after the 7-day neutral salt-fog exposure (Day 7- Major Damage), and images on the right are damaged regions after nitric acid removal of corrosion product (Post Nitric- Damage). All images are the same magnification and have a 100 µm scale bar in the bottom right.

Figure 61 shows electron micrographs and elemental maps for a TCP (Henkel)-coated AA7075-T6 alloy before salt-spray exposure. The secondary and backscattered electron

micrographs show evidence for the conversion coating in the form of elongated precipitates decorating the surface. There is a large aggregate of these precipitate particles in the center of the image. The elemental maps indicate the precipitates are comprised of Zr, Cr, F, and O, as indicated in the respective elemental maps. The large coating aggregate is localized around an unidentified intermetallic phase as evidenced by the dark void in the Al and Mg maps. A small Mg IMP is visible in the spectral map, but is not visible in the electron micrographs due to coverage by the TCP coating.

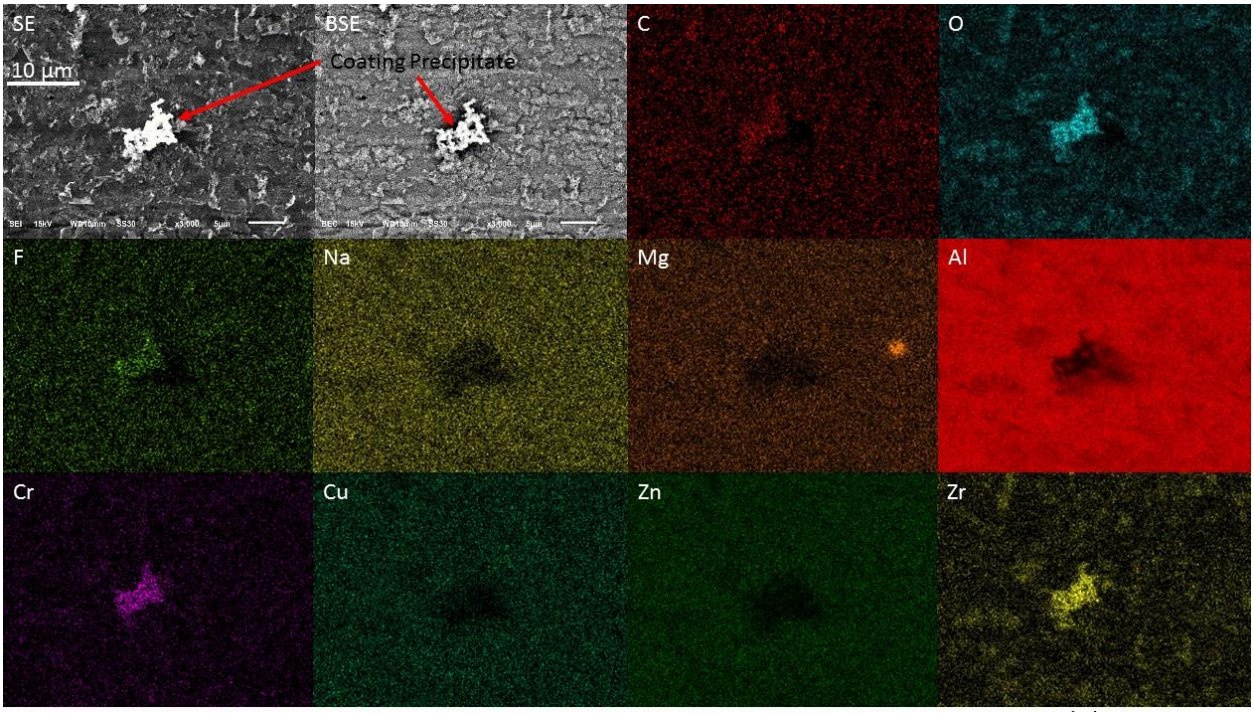

Figure 61. Scanning electron micrographs and corresponding energy dispersive x-ray spectral maps of TCP-coated (Henkel) AA7075-T6 before salt-spray testing. All images and maps are scaled equivalently with the corresponding 10 µm scale bar seen in the secondary electron (SE) micrograph. The element represented in each map is shown in the top left corner of the panel.

Figure 62 shows scanning electron micrographs and elemental maps for a TCP-coated (Henkel) AA7075-T6 specimen after the 7-day salt-spray exposure. A major difference in the electron micrographs is that there are fewer of the elongated coating precipitates present on the surface after exposure and the rolling grooves are more visible. There are two large intermetallic particles in the center of the image that are cracked presumably due to dealloying during the

exposure. Some of the TCP coating precipitates remain on and around the IMPs, as evidenced by the elemental maps for Zr, Cr, F, and O. There are also some pits and trenching around the IMPs, which appear to have occurred during the salt-spray exposure. It could be that there are more TCP coating defects around the intermetallic particles and these are the localized regions where the corrosion protection breaks down initially and corrosion commences.

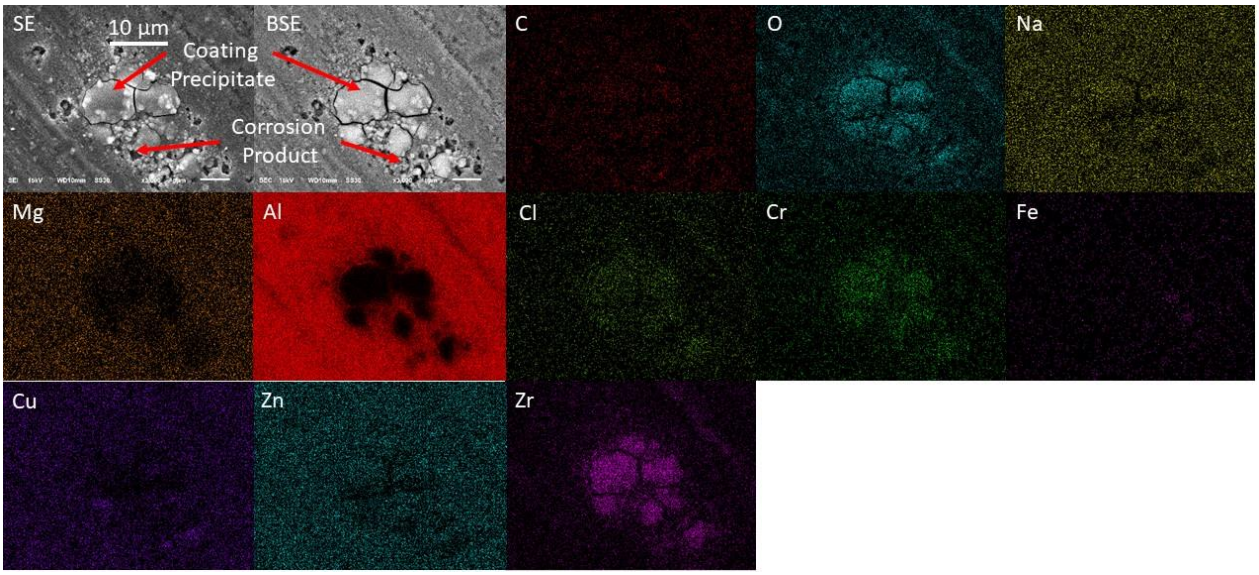

Figure 62. Scanning electron micrographs and corresponding energy dispersive x-ray spectral maps of TCP-coated (Henkel) AA7075-T6 after a 7-day salt-spray test. All images and maps are scaled equivalently with the corresponding 10 µm scale bar seen in the secondary electron (SE) micrograph. The element represented in each map is shown in the top left corner of the panel.

A closer view of the less damaged region on the Henkel-coated specimen after the nitric acid treatment reveals two Fe-containing IMPs in the lower right (Figure 63). The particles have a rough surface compared to IMPs seen on the uncoated specimen and there is trenching around the particles resulting from aluminum dissolution. The surface is rough with many divots and some small cracks, but the extensive intergranular cracking seen on the uncoated surface was not apparent. The corrosion damage is not as extensive as that seen for the uncoated AA7075.

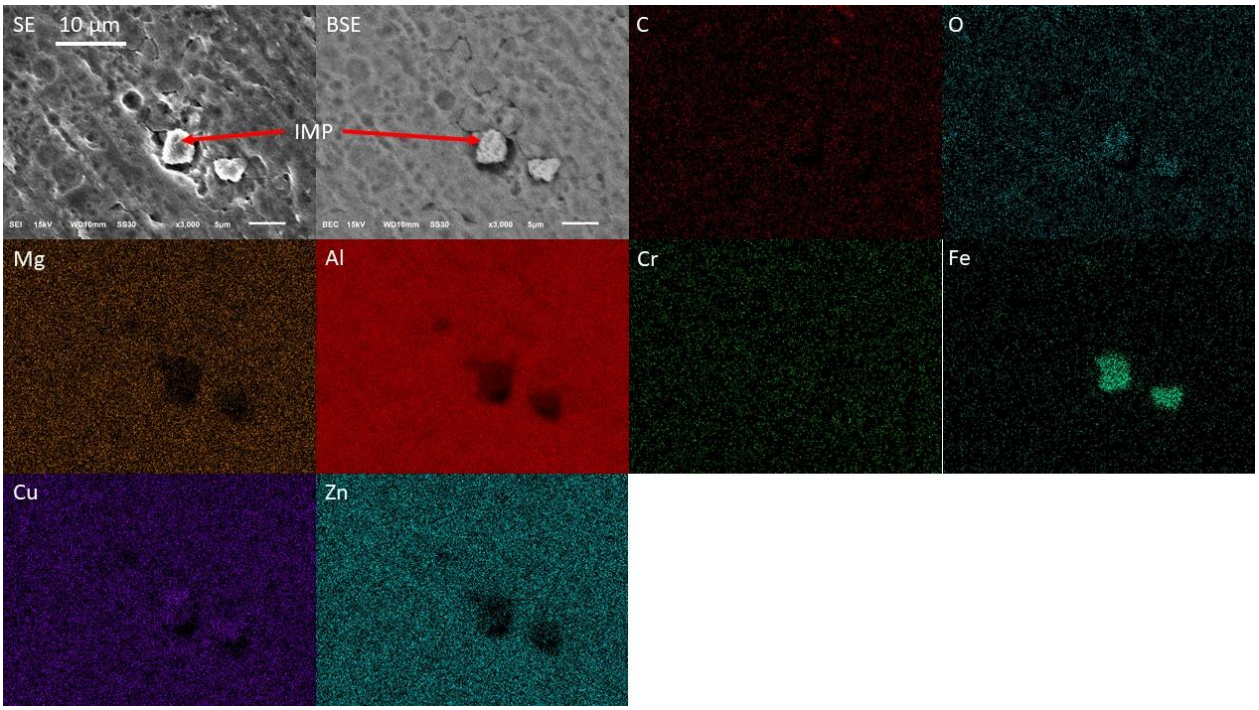

Figure 63. Scanning electron micrographs and corresponding energy dispersive x-ray spectral maps of TCP-coated (Henkel) AA7075-T6 after a 7-day salt-spray test and nitric acid removal of corrosion product. All images are the same scale correspond to the 10 µm scale bar in the secondary electron (SE) image. The element represented in each map is shown in the top left corner of each panel.

Other quantitative topographical analysis revealed that the Luster-On coating provides slightly superior corrosion protection as compared to the other commercial TCP and NCP coatings examined (Chapter 4). Figure 64 shows electron micrographs for the TCP (Luster-on)-coated AA7075-T6 before and after a 7-day neutral salt spray exposure and after nitric acid removal of the corrosion product. The Luster-On coating has a higher number density of the elongated coating precipitates (up to 50 µm diameters) than does the Henkel coating before testing (Figure 64- Day 0). The grooves from the alloy processing are visible after the coating formation. These large and high-density coating precipitates correlate with the highest concentration of Cr and Zr seen in the Luster-On coating baths, and could be a good predictor of coating performance. After the 7-day salt-spray exposure, none of the coating precipitates are visible and a few small regions of white corrosion product are seen (Day 7-Damage). The majority of the surface, however, is devoid

of both regions of metal dissolution and corrosion product formation (Day 7- No Damage). After corrosion product removal, the specimen (Figure 64- Post Nitric- Damage), the images revealed no large damaged regions like the 50 µm diameter pits seen on the Henkel and uncoated specimens. There are many small damaged sites (<20 µm), too many to count, but nothing larger on the entire panel. The conversion coating aggregates dissolved and the rolling pattern in visible across the panel. As seen with the Henkel coating, the rolling ridges are more pronounced both after the salt-spray test and after coating removal with nitric acid, suggestive of TCP coating removal. Overall, the results reveal that there is minimal damage on the Luster-On-coated panel after the 7-day salt-spray exposure, indicating the conversion coating offers excellent stand-alone corrosion protection.

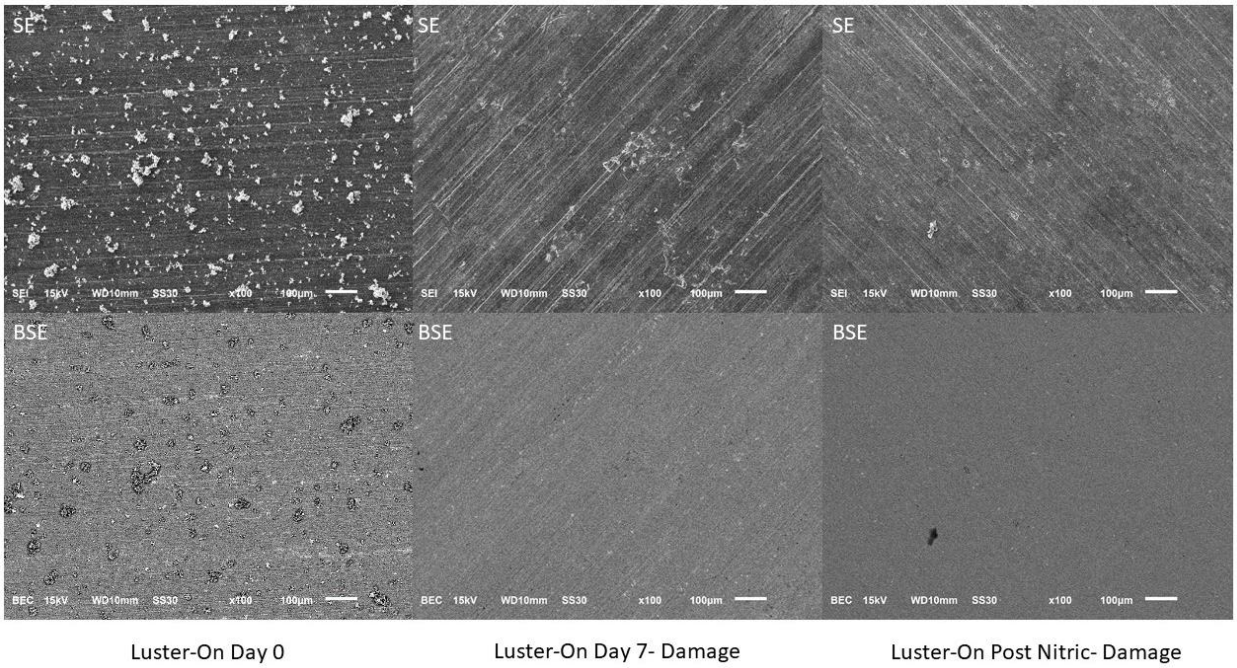

Figure 64. Scanning electron micrographs of TCP-coated (Luster-On) AA7075-T6. Top images show secondary electron micrographs and bottom images show back-scattered electron micrographs. Images on the left are before testing (Day 0), images in the center are major damaged regions after the 7-day test (Day 7- Major Damage), and images on the right are damaged regions after nitric acid sonication to remove corrosion product (Post Nitric- Damage). All images have a 100 µm scale bar in the bottom right.

Before any testing, the Luster-On coating consists of elongated precipitates (> 10µm) covering the majority of the surface, with a few IMPs visible (Figure 65). As the elemental maps in Figure 65 reveal, the coating precipitates are composed of F, S, K, Cr, Zr, and O, in agreement with the coating bath elemental composition. The visible IMP is composed of mainly Cu, with coating elements aggregating around it including Ca, Cr, Zr, and O. Some cracking in the coating surface is also visible, again probably due to the film dehydration under the SEM vacuum.

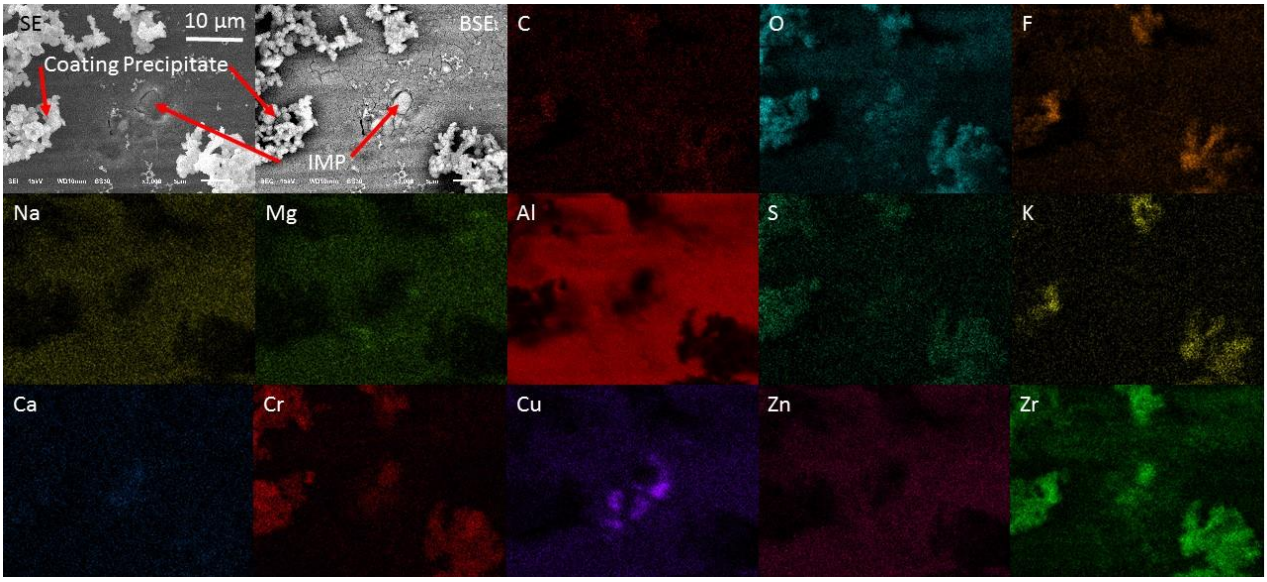

Figure 65. Scanning electron micrographs and corresponding energy dispersive x-ray spectral maps of TCP-coated (Luster-On) AA7075-T6 before testing. All images and maps are scaled equivalently with the corresponding 10 µm scale bar seen in the secondary electron (SE) micrograph. The element represented in each map is shown in the top left corner of each panel.

A possibly pre-existing defect is the only major damage seen on the Luster-On coated samples after the 7-day test, as seen in Figure 66. This defect looks like something related to the processing and handling of the specimen. The corrosion damaged regions tend to be round and centered around IMPs, with visible protective oxides forming around damaged edges. None of these features are seen with the Luster-On coating, but are viewed extensively on the uncoated and other TCP and NCP-coated specimens. Only a small amount of corrosion product is visible in this damaged site, that composed mainly of Zn, Na, and O. The alloy ridges are much more pronounced and visible after the 7-day test, indicating some coating loss.

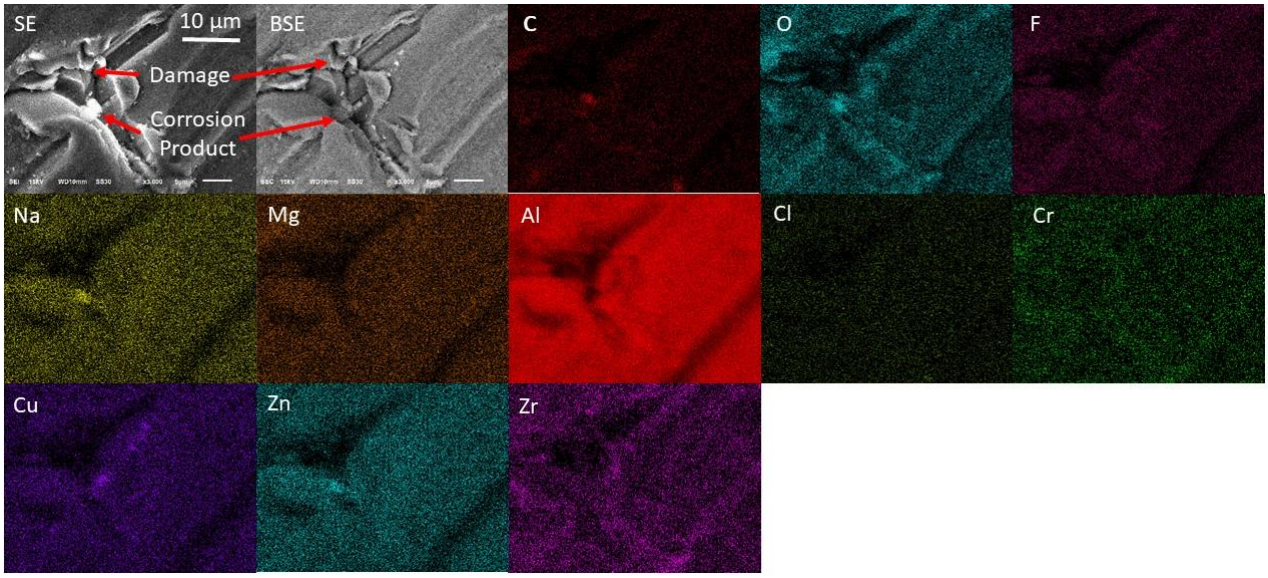

Figure 66. Scanning electron micrographs and corresponding energy dispersive x-ray spectral maps of TCP-coated (Luster-On) AA7075-T6 after a 7-day salt-spray test. All images and maps are scaled equivalently with the corresponding 10 µm scale bar seen in the secondary electron (SE) micrograph. The elements represented in each map are shown in the top left corner of each panel.

The large damaged regions look very similar to those seen on Henkel-coated 7075 and will not be shown, but areas with damage initiating look slightly different with the Luster-On coating after corrosion product removal (Figure 67). The Fe-Cu IMPs visible show some cracking damage, but are far less degraded compared to the Henkel-coated specimen. This may be because of increased coating coverage in the form of the elongated precipitates and better corrosion protection. The large number of intergranular cracks indicate surface damage occurred, but no significant pitting or surface roughening is seen. These cracks might be due to the nitric acid cleaning process, but varied drastically between coatings, despite the identical nitric acid cleaning process used for all specimens. It is postulated that these cracks are not due to the nitric acid cleaning process, but this should be studied in future research. Additionally, the cracks are very thin and shallow, indicating less severe corrosion damage than seen on the uncoated and Henkel-coated AA7075.

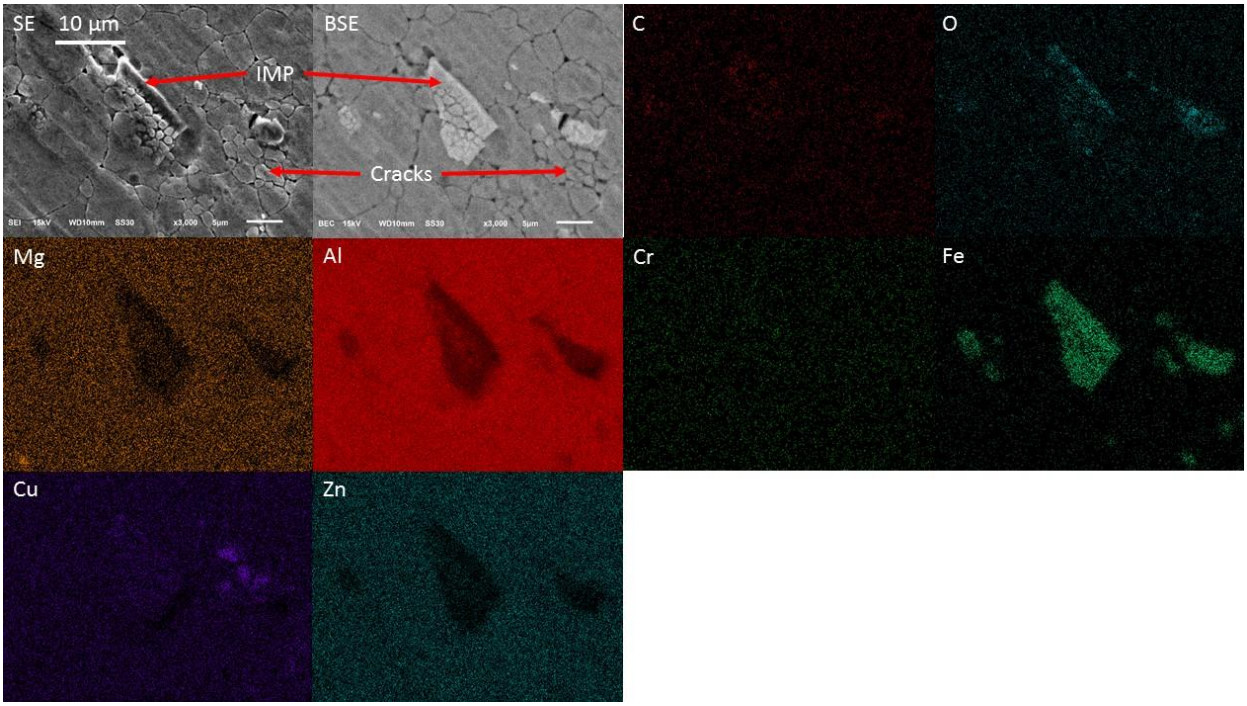

Figure 67. Scanning electron micrographs and corresponding energy dispersive x-ray spectral maps of TCP-coated (Luster-On) AA7075-T6 after a 7-day salt-spray test and nitric acid sonication to remove corrosion product. All images and maps are scaled equivalently with the corresponding 10 µm scale bar seen in the secondary electron (SE) micrograph. The elements represented in each map are shown in the top left corner of each panel.

The previous analysis (shown in Chapter 4) after the salt-spray accelerated degradation test showed Chemeon coated specimens to have the second least amount of corrosion damage. Again, this appears to correlate with the second highest Cr concentration and Cr/Zr ratio in the coating bath. Figure 68 shows the Chemeon-coated specimen before (Day 0) and after (Day 7) a 7-day salt-spray test. Before the test, the entire panel is decorated with a large number of coating precipitates (not as many or as large diameter as seen on Luster-On-coated 7075) with slightly obscured ridges. Some surface features present as dark spots in the BSE, which are regions of high carbon content. After the 7-day test, a large amount of finger-like corrosion product is seen across the entire panel, but no large corrosion product build-up or deep pits are visible. Some of the coating precipitates are still visible across the surface (bright spots running along ridges), which was not observed with the other two TCP coatings discussed above. The dark spots visible with

BSE are still present, though not as numerous or large diameter as seen before the test. After product removal from the surface, the micrographs reveal little corrosion damage (Figure 68). All coating precipitates present before the nitric acid cleaning (Day 7-Corrosion Product) are removed from the surface. This leaves the bare aluminum surface with some small (<25 µm) pits visible (Post Nitric- Damage). The surface ridges are more pronounced and similar in appearance to those seen on the uncoated specimen before testing, indicating very little coating still present. No large pits (>25 µm) are seen on the entire panel.

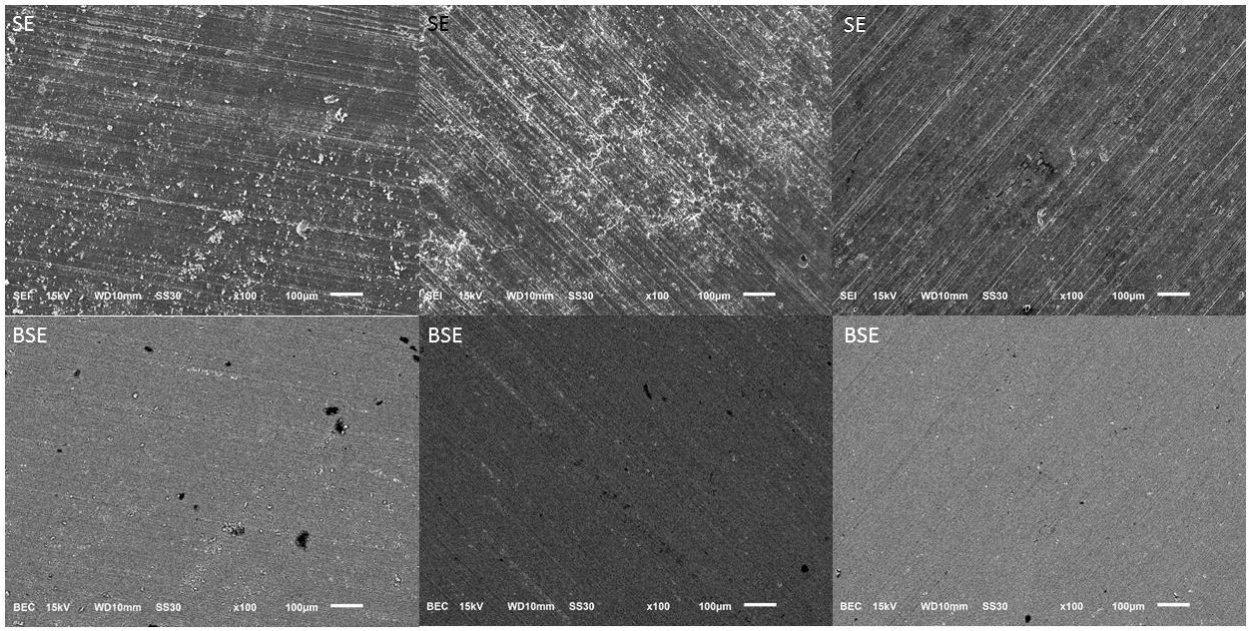

Figure 68. Scanning electron micrographs of TCP-coated (Chemeon) AA7075-T6. Top images show secondary electron micrographs and bottom images show back-scattered electron micrographs. Images on the left are before testing (Day 0), images in the center are major damaged regions after the 7-day test (Day 7- Major Damage), and images on the right are damaged regions after nitric acid sonication to remove corrosion product (Post Nitric- Damage). All images have a 100 µm scale bar in the bottom right.

Before any salt-spray exposure, a closer examination of the surface reveals compact coating precipitates composed of C, F, Cr, Zr, and O (Figure 69). These coating precipitates (<5 µm diameter) cover the entire specimen, presumably with coating enrichment around IMPs, several of which are visible that consist of Cu or Mg. The precipitates seen for the Chemeon TCP

are much smaller and show a less defined crystalline structure as compared to the precipitates of both the Henkel and Luster-On TCPs. This indicates the Chemeon coating structure is probably more amorphous than Henkel and Luster-On. The ridges due to rolling processing are visible, but are somewhat obscured due to coverage with the TCP coating.

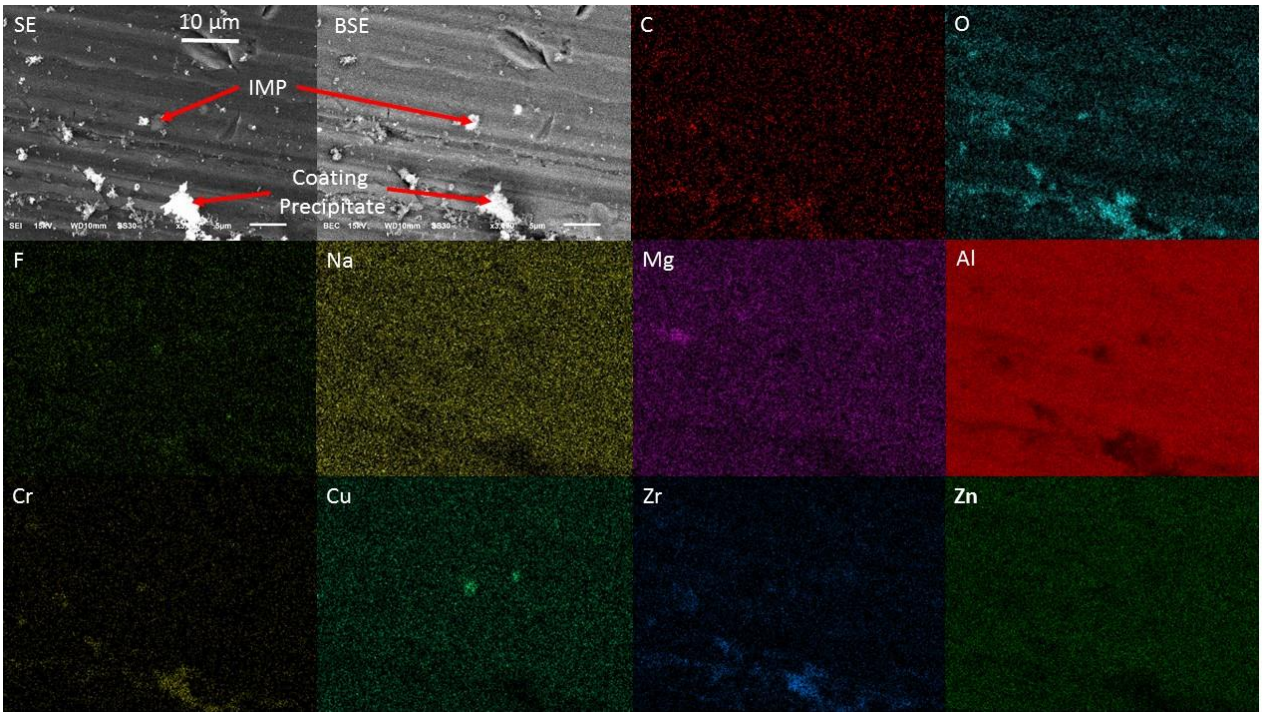

Figure 69. Scanning electron micrographs and corresponding energy dispersive x-ray spectral maps of TCP-coated (Chemeon) AA7075-T6 before testing. All images and maps are scaled equivalently with the corresponding 10 µm scale bar seen in the secondary electron (SE) micrograph. The element represented in each map is shown in the top left corner of each panel.

The majority of Chemeon-coated panel after the 7-day salt-spray test is undamaged with only a small amount of corrosion product formed that is composed of Na, Cl, Zn, O, F, Cr, and Zr (Figure 70). It seems like the coating elements are co-precipitating with the corrosion product or the corrosion product is forming specifically over the coating precipitate. The Cu-Fe IMP shows some visible cracking in the middle, but very little damage otherwise across the surface. The alloy ridges are much more apparent and defined, indicating some loss of the coating.

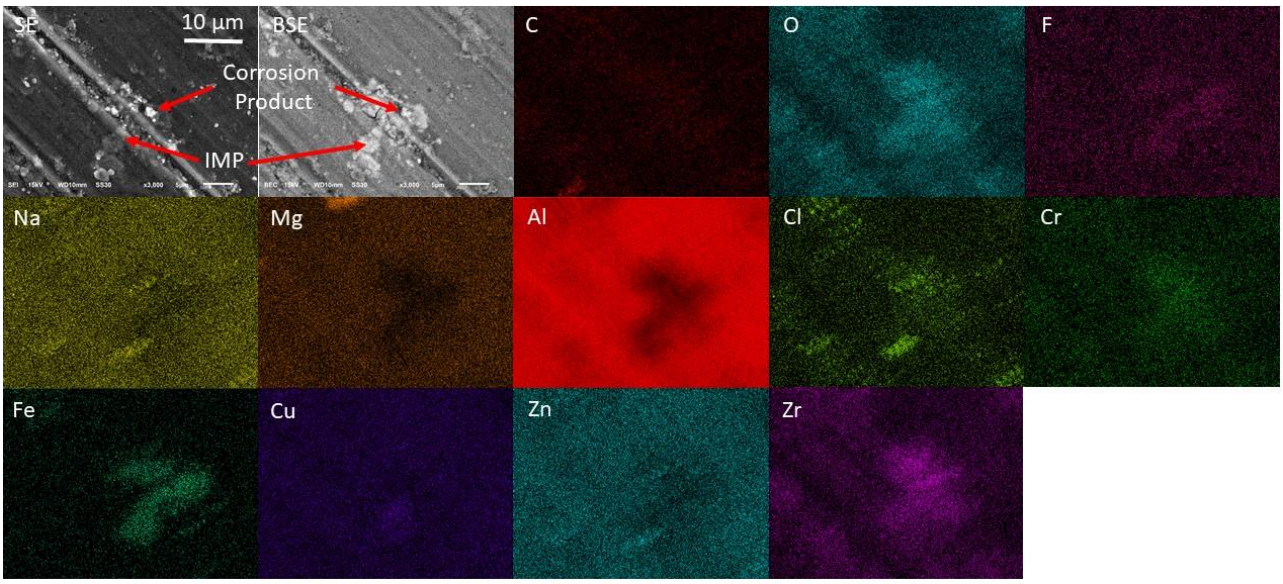

Figure 70. Scanning electron micrographs and corresponding energy dispersive x-ray spectral maps of TCP-coated (Chemeon) AA7075-T6 after a 7-day salt-spray test. All images and maps are scaled equivalently with the corresponding 10 µm scale bar seen in the secondary electron (SE) micrograph. The element represented in each map is shown in the top left corner of each panel.

A closer look at the Chemeon-coated surface shows damage similar to that seen on the Luster-On-coated specimen (Figure 71). Small pits (<1 µm) cover the surface, and shallow intergranular cracks extend away from the visible Cu-Fe and Mg IMPs. Oxygen is detected on the IMP, but the weakly intense Cr signal indicates this O is probably not from any coating precipitate or corrosion product. The Fe IMPs are intact and not degraded, especially when compared to the Henkel-coated panel.

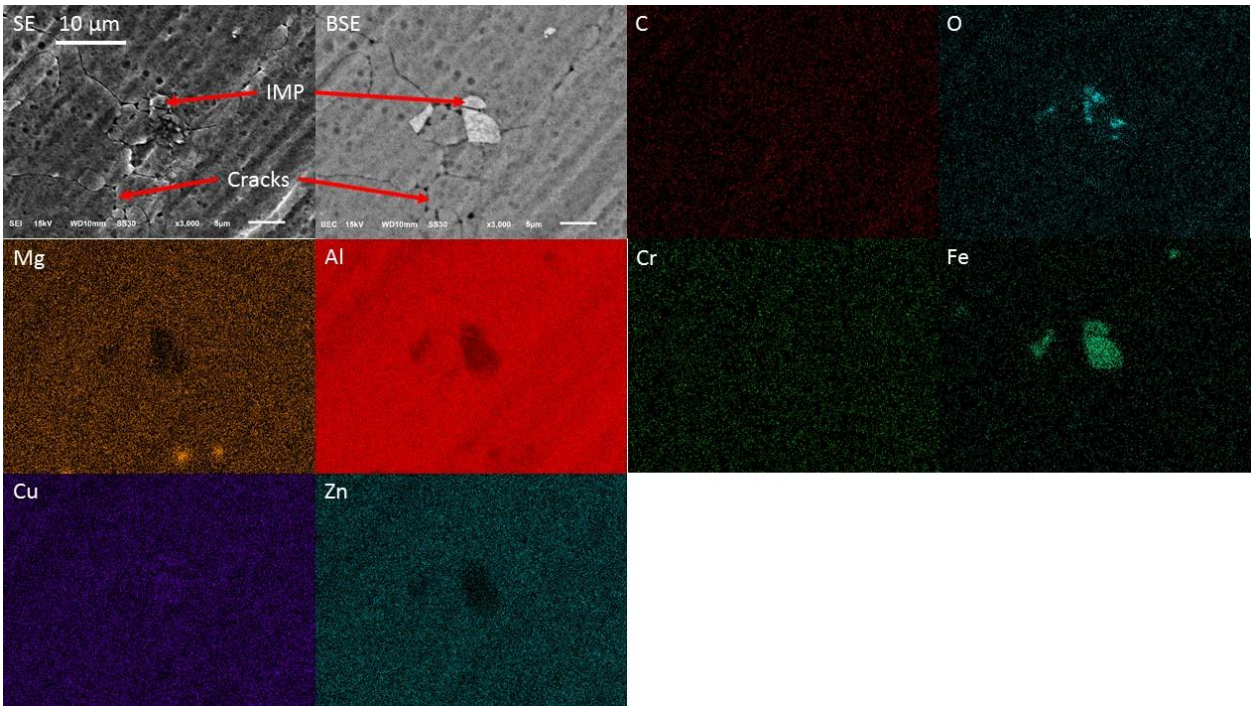

Figure 71. Scanning electron micrographs and corresponding energy dispersive x-ray spectral maps of TCP-coated (Chemeon) AA7075-T6 after a 7-day salt-spray test and nitric acid sonication to remove corrosion product. The element represented in each map is shown in the top left corner of each panel.

The SurTec 650E TCP coating performs similarly to the other TCP coatings examined (Figure 72). Before testing (Day 0), the surface shows well defined ridges, similar to the uncoated specimen, indicating a thinner coating than the other TCP brands. Coating precipitate is seen through the white spots in the BSE, and is smaller in diameter than those seen on the other TCP coatings, which follows the coating bath Cr content trend, as anticipated from Chapter 4. After the salt-spray test, the corrosion product is visually similar to Chemeon, with fingers of corrosion product forming over the entire surface (Day 7- Damage). Dark spots are seen, which correspond to dark spots in the BSE. These regions contain large amount of carbon, similar to those seen on the Chemeon coated specimen. There are some regions (like the upper right corner of Day 7- Damage) that reveal a grey dark spot on the BSE and reveal large amounts of rough corrosion product. There were 5 of these spots seen on the SurTec panel. The majority of the panel has small regions of carbon product and corrosion product fingers, as shown in Day 7- Little Damage.

After corrosion product was removed with nitric acid, the SurTec coated panel looks very similar to those seen with the other TCP coatings (Post Nitric- Damage). Two large pit regions (~100 µm) are visible on the surface, with numerous small pits (<50 µm) seen over the entire panel. Some large darker spots are seen with the SE in the vicinity of the damaged sites, but show no differences in the BSE micrograph and are assumed to be superficial discoloration.

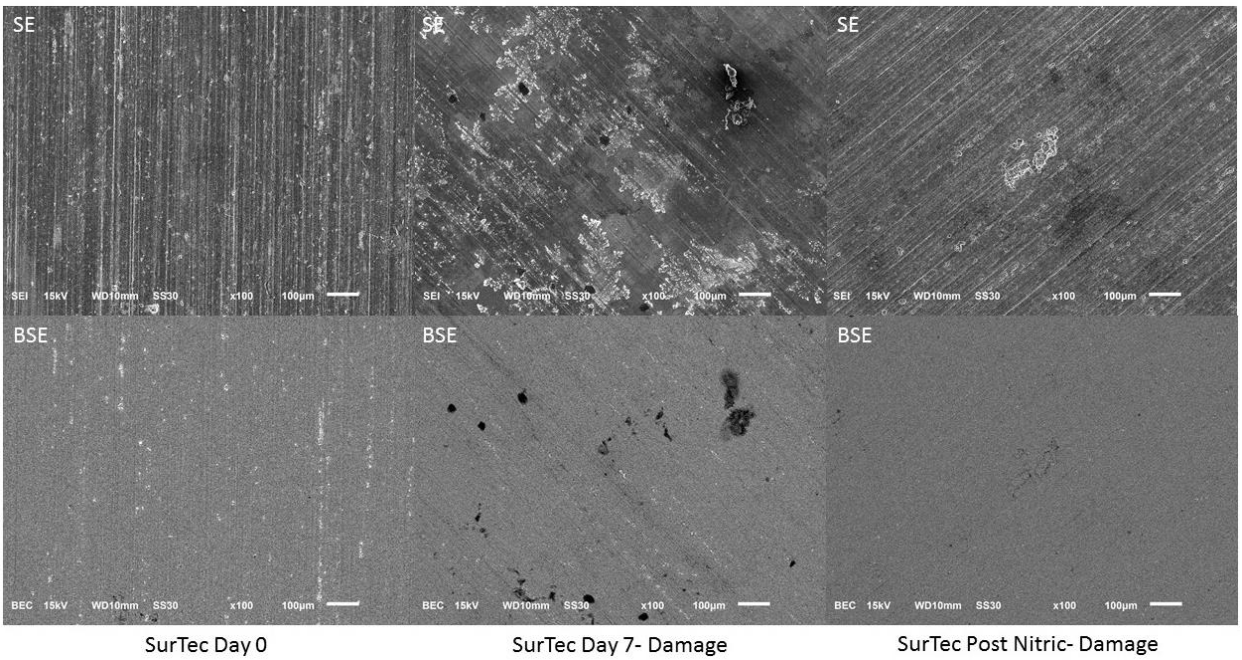

Figure 72. Scanning electron micrographs of TCP-coated (SurTec E) AA7075-T6. Top images show secondary electron micrographs and bottom images show back-scattered electron micrographs. Images on the left are before testing (Day 0), images in the center are major damaged regions after the 7-day test (Day 7- Major Damage), and images on the right are damaged regions after nitric acid sonication to remove corrosion product (Post Nitric- Damage). All images have a 100 µm scale bar in the bottom right.

Before any testing, the SurTec film shows the expected linear white precipitate which aggregates around IMPs, which have been discussed already in Chapter 2 (Figure 73). The thin coating over the entire surface adhere conformally to the specimen, allowing the appearance of the rolling ridges. The coating precipitate is composed of F, Cr, Zr, and O, which corresponds to the results of the coating bath analysis. The precipitates are significantly smaller and less dense than

those seen on the other TCP coated specimens, and the SurTec was not expected to perform as well as the other TCP coatings.

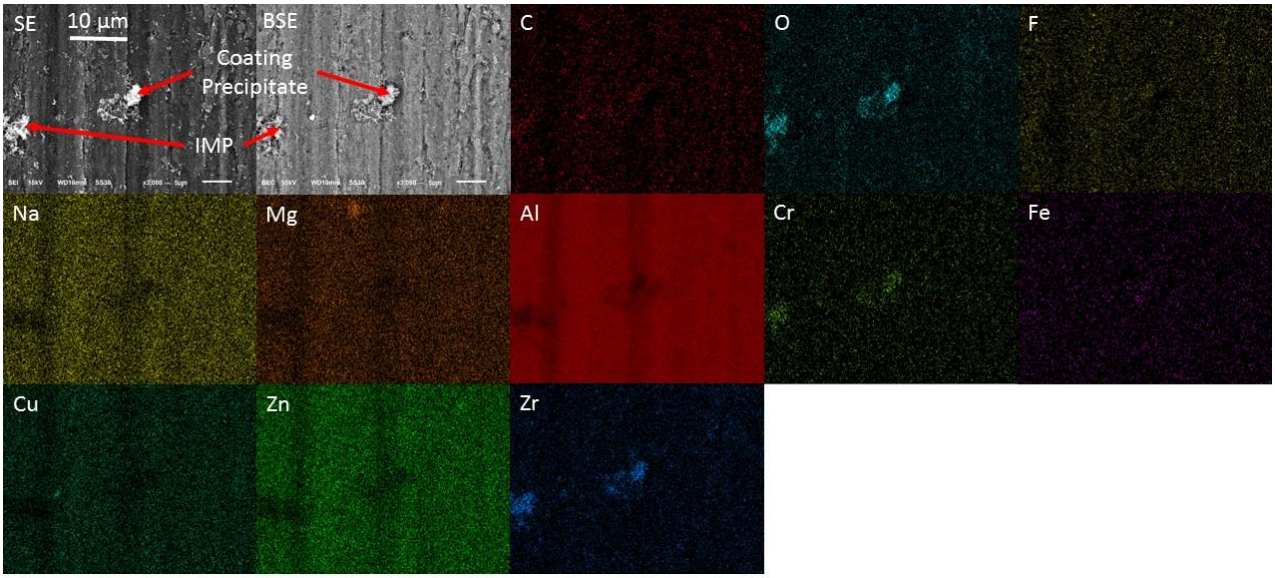

Figure 73. Scanning electron micrographs and corresponding energy dispersive x-ray spectral maps of TCP-coated (SurTec E) AA7075-T6 before testing. All images correspond to the 10 µm scale bar in the secondary electron (SE) image, next to the back-scattered (BSE) image the element represented in each map is shown in the top left corner of each panel.

After the salt-spray test, some regions on the SurTec surface show large amounts of tall and rough corrosion product buildup around IMPs (Figure 74). The IMPs in these areas show small amounts of cracking and surrounding damage. The corrosion product elemental analysis reveals Na, Cl, Zn, and O present, as seen for the other TCP coatings. Some coating precipitate is still visible around the IMPs, even those that are completely covered with corrosion product. The coating precipitate has the same composition as seen before the test, with the exception that F is no longer visible (Cr, Zr, O). The IMPs visible are composed of Fe and Cu, with major losses of Cu seen in these damaged regions.

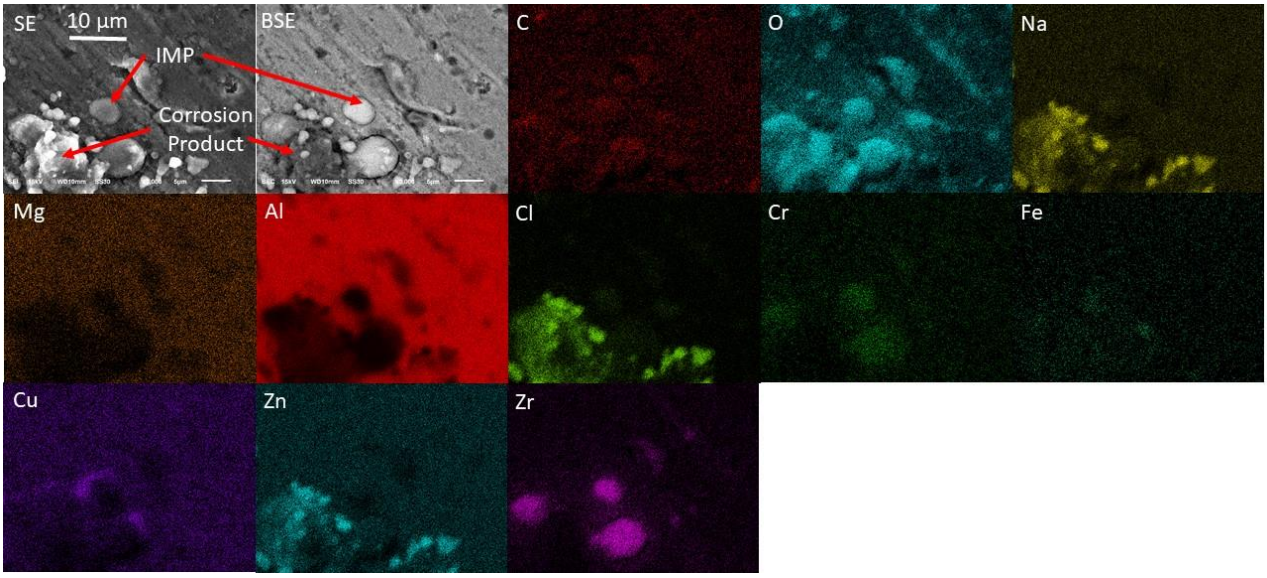

Figure 74. Scanning electron micrographs and corresponding energy dispersive x-ray spectral maps of TCP-coated (SurTec E) AA7075-T6 after a 7-day salt-spray test. All images correspond to the 10 µm scale bar in the secondary electron (SE) image, next to the back-scattered (BSE) image. The element represented in each map is shown in the top left corner of each panel.

Looking on a smaller scale, the SurTec surface shows similar results to Luster-On and Chemeon but with a larger amount of surface damage (Figure 75). The visible Fe and Cu IMPs are very damaged but less degraded and pitted than those seen with the Henkel coating. The overall surface pitting is less significant than on the Henkel specimen, with the majority of damage directly around the IMPs and a few ~ 5 µm pits across the surface. The visible cracks look similar to those on Chemeon, with obvious intergranular corrosion initiating. The cracks are less obvious and deep than those on the uncoated control, indicating less overall aluminum alloy damage with the SurTec coating.

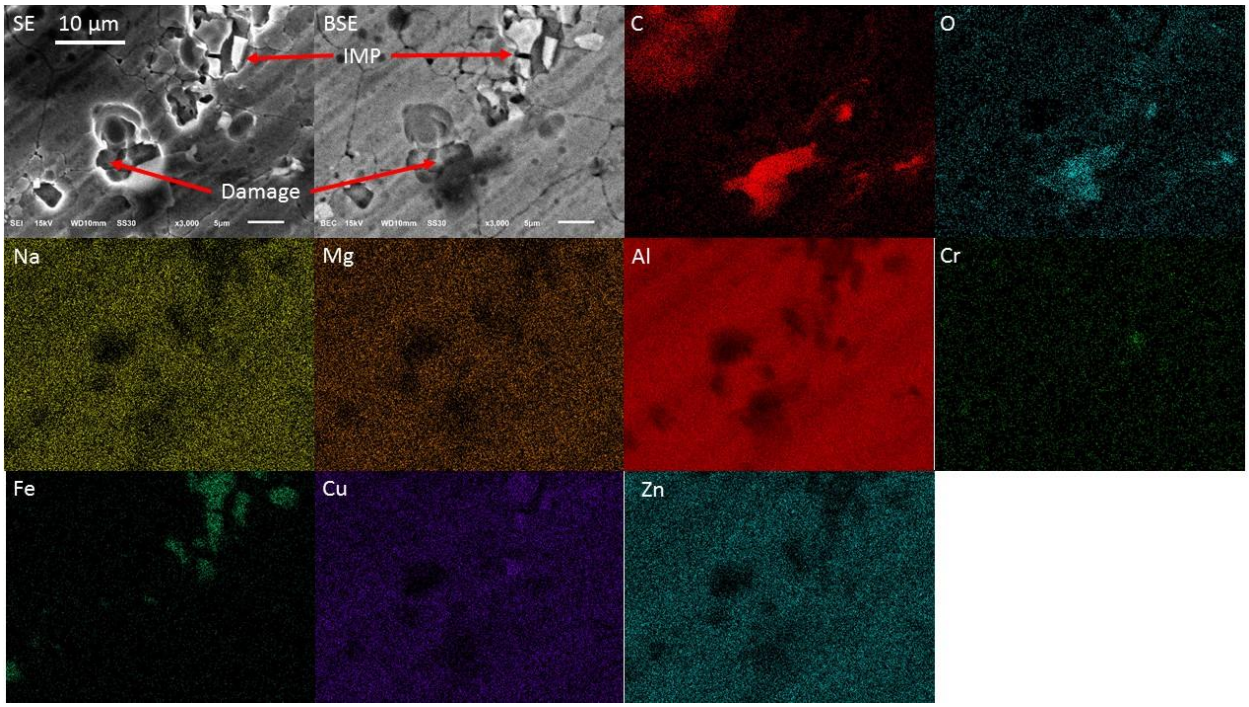

Figure 75. Scanning electron micrographs and corresponding energy dispersive x-ray spectral maps of TCP-coated (SurTec E) AA7075-T6 after a 7-day salt-spray test and nitric acid sonication to remove corrosion product. All images and maps are scaled equivalently with the corresponding 10 µm scale bar seen in the secondary electron (SE) micrograph. The element represented in each map is shown in the top left corner of each panel.

After the non-chromium process coating (NCP) was subjected to the salt-spray exposure, more drastic damage is finally seen for a coated specimen (Figure 76). Before the test (Day 0), the NAVAIR surface is studded with large, extremely linear white precipitates which aggregated into star-like structures. The rest of the surface has obviously apparent ridges, indicating a relatively thin coating. After the test (Day 7- Damage), there are regions of hundreds of micrometers of raised corrosion product surrounding large damaged sites. The surface is mottled with darker regions in the SE micrograph, which correspond to lighter regions in the BSE micrograph, indicating regions of exposed Al matrix. The surface areas on NAVAIR without a large amount of corrosion product visible (Day 7- Little Damage) still show smaller amounts (<20 µm) of corrosion product and visible surface roughening compared to the surface before testing. After corrosion product was removed with nitric acid, the NAVAIR surface looks very similar to

those seen with the TCP coatings (Post Nitric-Damage). Many small pits are seen (<20 µm), but no large damaged regions across the entire panel. To examine the surface damage differences, compared to the TCP coatings, a closer view is necessary.

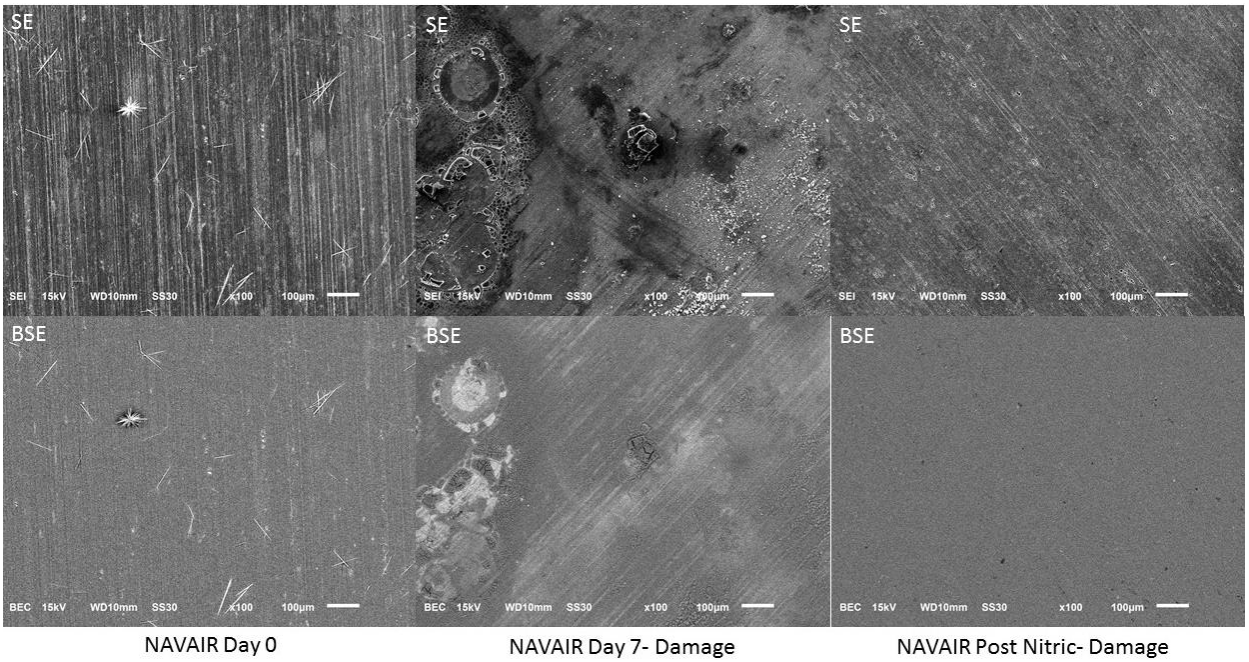

Figure 76. Scanning electron micrographs of NCP-coated (NAVAIR) AA7075-T6. Top images show secondary electron micrographs and bottom images show back-scattered electron micrographs. Images on the left are before testing (Day 0), images in the center are major damaged regions after the 7-day test (Day 7- Major Damage), and images on the right are damaged regions after nitric acid sonication to remove corrosion product (Post Nitric- Damage). All images have a 100 µm scale bar in the bottom right.

Before any testing, the NAVAIR NCP coating shows some very small, dense coating precipitates (~1 µm) near IMPs, as seen in Figure 77. The tightly adhered coating around the Cu IMP consists of F, Zr, C, and O. There seems to be a thin and conformal coating over the metal surface without many visible cracks or damaged regions. The few dark spots seen in both SE and BSE micrographs do not correspond to any elements in the spectra maps.

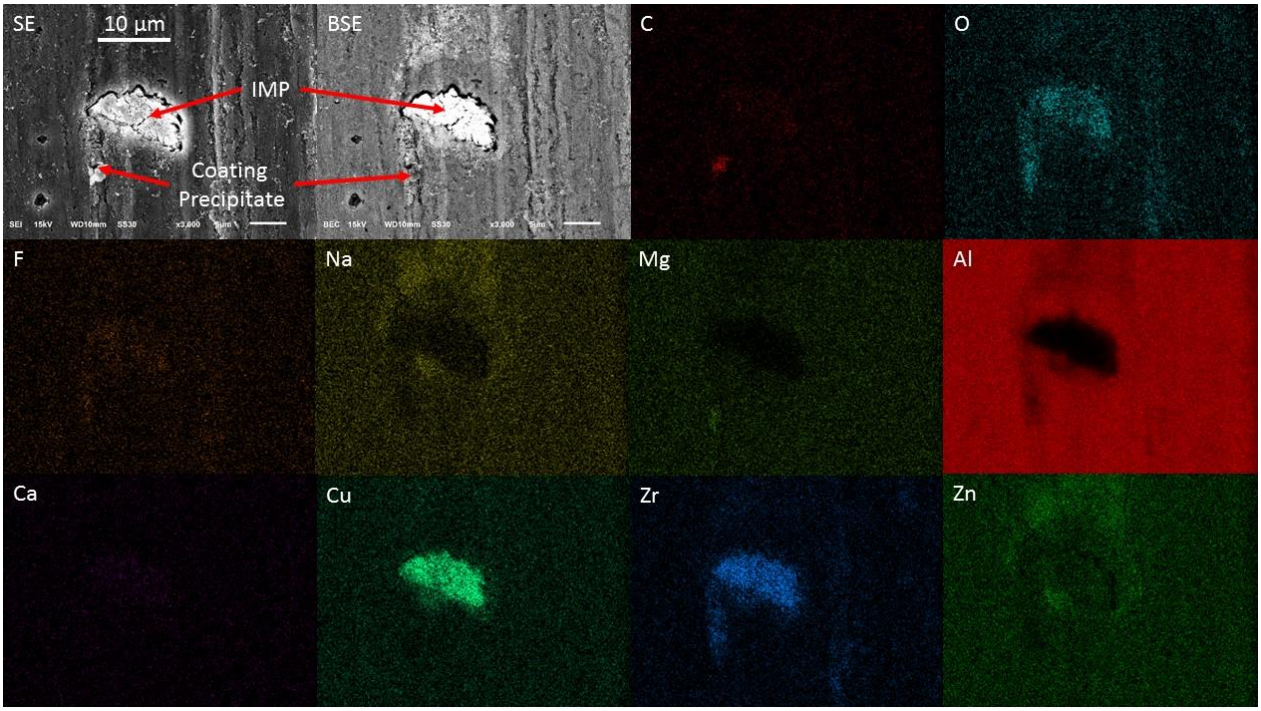

Figure 77. Scanning electron micrographs and corresponding energy dispersive x-ray spectral maps of NCP-coated (NAVAIR) AA7075-T6 before testing. All images and maps are scaled equivalently with the corresponding 10 µm scale bar seen in the secondary electron (SE) micrograph. The element represented in each map is shown in the top left corner of each panel.

The linear precipitates consist of elements in the coating bath, mainly C, F, K, Zr, and O, as seen in Figure 78. These precipitates are much larger in size than the elongated precipitates characteristic of the conversion coating, but less numerous across the NCP-coated surface.

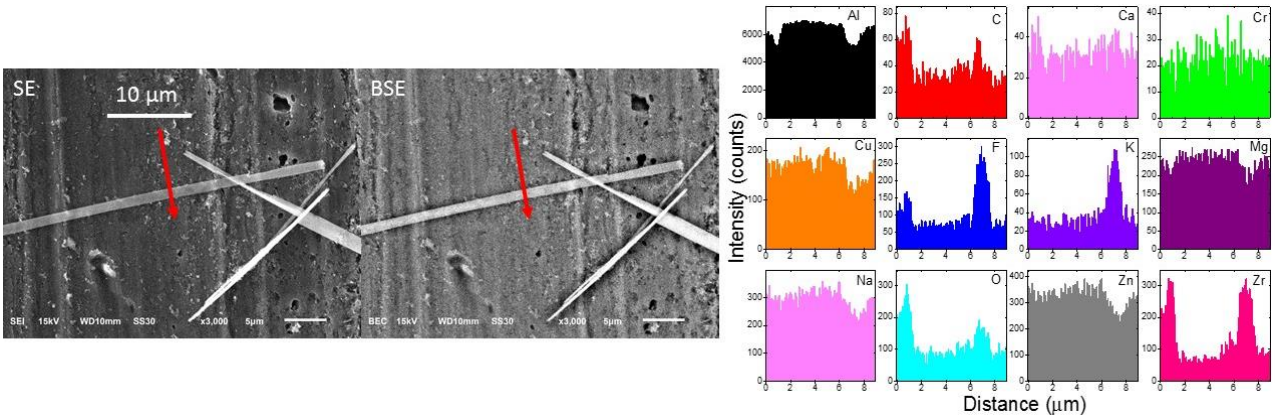

Figure 78. Scanning electron micrographs and corresponding energy dispersive x-ray spectral line scans along the red arrow. All images and maps are scaled equivalently with the corresponding 10 µm scale bar seen in the secondary electron (SE) micrograph. The elemental line scans are presented on the right for the red arrows going from 0 to 9 µm at the arrow tip.

One of the less damaged regions is examined for the NCP-coated AA7075 after the 7-day salt-spray test (Figure 79), which reveals a thick coating of corrosion product covering the entire surface, masking the signals from most other elements drastically. Some large aggregates of corrosion product are visible, composed of C, Na, Zn, and O. The rolling ridges are mostly obscured by the thick nodular corrosion product covering the surface of the panel. Some of the ridges are visible under the corrosion product through the lines of Zr present. The oxide layer does not contain as much water as the oxide layer on the uncoated specimen because there is no cracking of the oxide surface due to SEM dehydration.

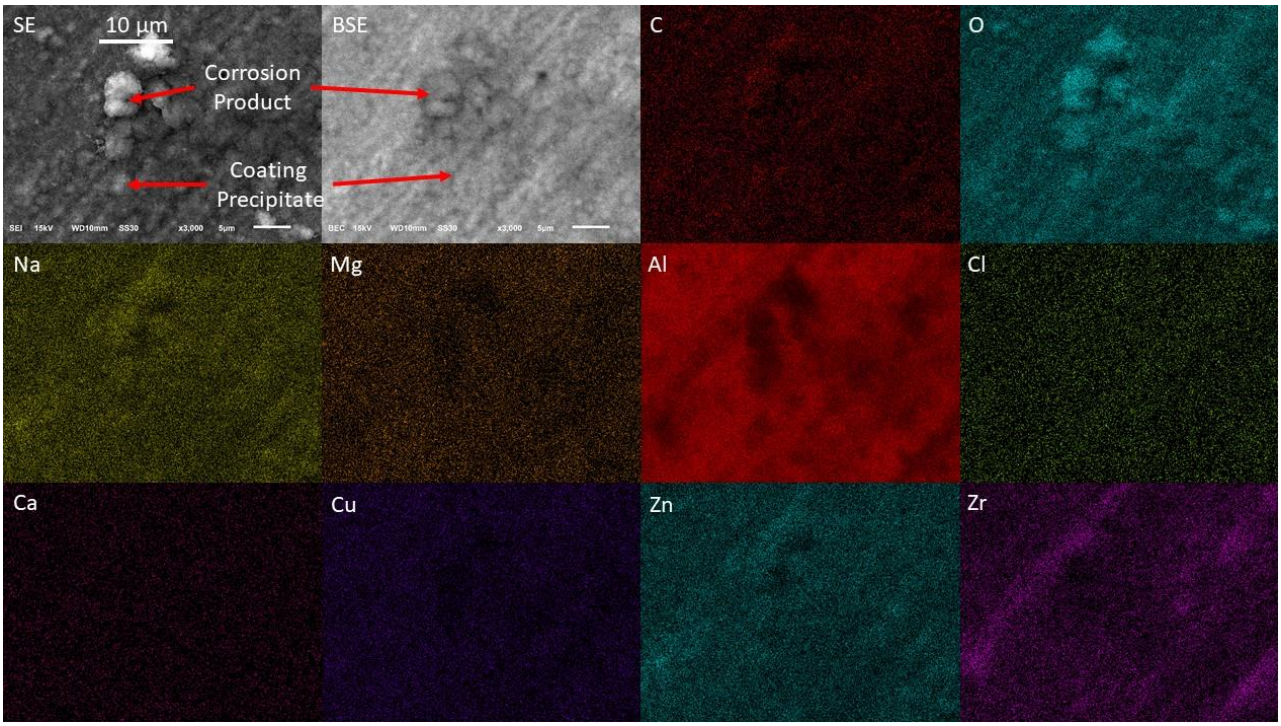

Figure 79. Scanning electron micrographs and corresponding energy dispersive x-ray spectral maps of NCP-coated (NAVAIR) AA7075-T6 after a 7-day salt-spray test. All images and maps are scaled equivalently with the corresponding 10 µm scale bar seen in the secondary electron (SE) micrograph. The element represented in each map is shown in the top left corner of each panel.

Looking on the tens of micrometers scale, the surface is reminiscent of the Henkel specimen. IMPs are severely damage and significantly smaller than seen with the Henkel coating, and the surface pitting is more substantial with a much higher pit density in the visible region (Figure 80). Additionally, more intergranular cracks are also seen, though nothing much more severe than seen on any of the TCP coated AA7075. This indicates the NAVIAR coating protects almost as well as the TCP coatings, with the exceptions of Chemeon and Luster-On which show very little surface pitting.

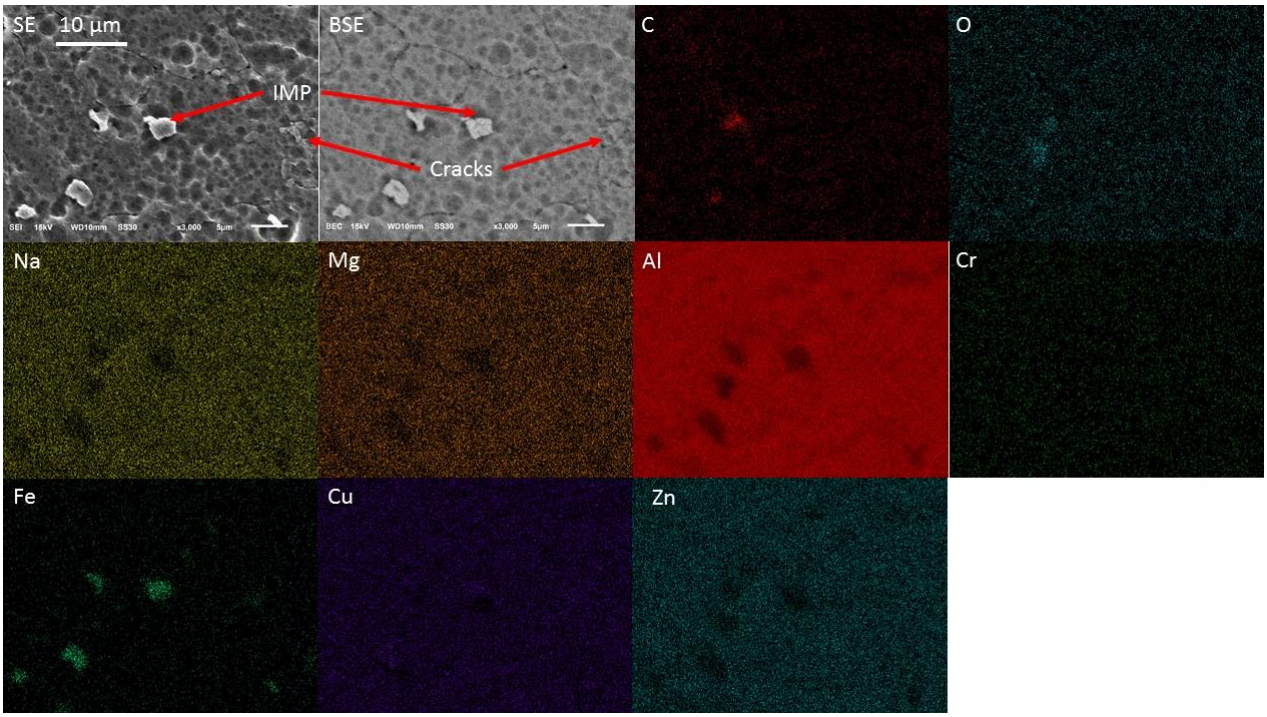

Figure 80. Scanning electron micrographs and corresponding energy dispersive x-ray spectral maps of NCP-coated (NAVAIR) AA7075-T6 after a 7-day salt-spray test and nitric acid sonication to remove corrosion product. All images correspond to the 10 µm scale bar in the secondary electron (SE) image, next to the back scattered (BSE) image. The element represented in each map is shown in the top left corner of each panel.

5.4. SEM Cross Comparison Discussion

Scanning electron microscopy (secondary and backscattered electron images) characterization of the alloy surface topography and EDXS analysis of the elemental composition were used to characterize uncoated, TCP-coated and NCP-coated AA7075-T6 panels before and after a 7-day neutral salt-spray exposure. The results indicate that the TCP conversion coatings provide greater stand-alone corrosion protection to the aluminum alloy as compared to the NCP conversion coating. Some of the key findings can be summarized as follows:

1. The coatings with the highest Cr concentrations (Luster-On and Chemeon) detected with ICP-OES showed the lowest amount of corrosion product buildup and the lowest large damaged regions (>50 µm), although many small pits were still seen. The coatings with the lowest Cr concentrations (Henkel and SurTec) showed large amounts

of corrosion product buildup and a high number of large damaged regions (>50 μm) across the panels. This shows the Cr content in the coatings is providing a considerable decrease in the corrosion damage, as qualified through corrosion product buildup, pit sizes, and pit numbers. The levels of Cr concentration in coating baths also correlates to the number and size of coating precipitates visible before testing, which could be used as an easy predictor of coating performance.

2. Intergranular cracking was seen on the majority of TCP coated specimens, but did not seem to be a good indicator of surface damage when these results were correlated with the quantitative detection of damage through weight loss and pit depths. As noted in Chapter 4, the weight loss and pit depth followed the trends in coating bath Cr content very well, which also agrees with the surface pitting seen here through microscopy.
3. The damage for TCP coatings initiated around IMPs, with pits forming in the close vicinity of the IMPs and the IMPs themselves degrading during more severe corrosion. This is in agreement with the known Cu site catalysis of aluminum alloy degradation.

The NCP coating also showed a decent amount of corrosion protection, during both the salt-spray and thin-layer mist tests, when compared to the TCP-coated specimens. The pure barrier protection provides decent protection against the major pitting and damage seen on the uncoated specimen, indicating that this is a less effective but still viable method for corrosion protection in real world coating applications. However, the TCP coatings with the highest Cr content provided the best corrosion protection from pit initiation, and are the recommended chromate conversion coating replacements for future corrosion protection.

5.5. Cross Comparison Conclusions

Overall, the Luster-On and Chemeon conversion coatings provided the best stand-alone corrosion protection to AA7075-T6 during the 7-day neutral salt-spray fog test. This protection was seen qualitatively through a decrease in white and dark corrosion product on the specimen surface, and decreased surface damage seen through IMP degradation and intergranular cracking indicating alloy damage. This protection was linked to the amount of Cr in coating baths and the subsequent number and size of coating precipitates, with higher Cr levels and larger more numerous precipitates associated with higher levels of corrosion protection. These results agree well with the results from Chapter 4 indicating these two coatings to perform the best in two separate accelerated degradation tests. SurTec and Henkel provided sufficient protection, but had some larger pitting (>50 μm) and possibly film undercutting. This lesser performance was predicted from the decreased Cr content compared to Luster-On and Chemeon, as well as from the lesser performance and increased variability in results seen from these coatings in Chapter 4. The NCP provided the lowest degree of corrosion prevention, but was still an improvement on uncoated AA7075-T6.

CHAPTER 6: CONCLUSIONS AND FUTURE WORK

6.1. SurTec Characterization Conclusions

Three different TCP coating variants (SurTec 650 E, V and C), formed by immersion and spray-on AA7075-T6 were characterized for morphology, coating chemistry, film thickness, and hydrophobicity. The results showed similar Cr concentrations for all coating baths (~150 ppm) with a similar Zr/Cr ratio in the two variants with added colorants (>2) and a slightly lower Zr/Cr ratio (1.8) in the standard E variant. Additionally, the variants with added colorant contained Zn and Fe. These additional components in the coating bath could deleteriously affect the formation and structure of the $Cr(OH)_3$ deposits in the conversion coating; hence the reduced anti-corrosion properties of the V and C variants. Both V and C variants did not perform as well as the E variant (as seen in Chapter 3), and the only major difference between these coatings is the additional components in the coating baths to add color.

All the conversion coating variants formed over all location on the AA7075-T6 surface, with some enhancement (increased coating thickness) around IMPs. The C variant had some visible cracking and delamination in the SEM micrographs, reflective of poor adhesion. Although it should be noted that one cannot say for sure that the damage sites are inherent to the formed coating or are produced by the high vacuum environment of the SEM; so-called mud cracking. The TCP coating E formed by immersion was thicker (95 nm) than the V and C variants (75 and 50 nm), while the spray application produced significantly thinner films for E, V, and C (75, 53, and 62 nm, respectively). The immersion application method produced a higher number of the elongated coating precipitates/aggregates on the alloy surface. The conversion coatings formed by spray had increased aluminum trenching and pitting around IMPs, as compared to the

immersion coatings presumably due to an increased flux of oxygen to Cu sites leading to increased aluminum dissolution nearby. A biphasic coating structure was confirmed depth-profiling XPS, with high levels of Zr and Cr in the outer 30-50 nm region of the coating and a 50-nm interfacial region consisting of Al, O, F, and some Cr. The Zr/Cr ratio in the conversion coating was higher than the concentration ratio in the coating bath, possibly due to faster precipitation kinetics for the $ZrO_2 \bullet nH_2O$ than for the $Cr(OH)_3$.

As the coatings dehydrated during a 7-day aging period in the laboratory atmosphere, all became more hydrophobic based on increasing static water contact angles. This could allow for more uniform formation and better adhesion of organic solvent-based primers. The SurTec conversion coating dehydration did not result in significant coating shrinkage and densification, as has been observed for the Henkel Bonderite T5900 conversion coating. The coating thickness was measured by ellipsometry in the air. The films with added colorants had more variation in the ellipsometrically-determined coating thickness due to the darker coatings, which reduced the light reflection.

Raman spectroscopy revealed localized regions of Cr(III)-O and evidence of transiently formed Cr(VI)-O species. A mixed Cr(III)/Cr(VI) species was often detected in the elongated aggregate particles that decorate the coating surface, particularly around IMPs. There is positive evidence for transient formation of Cr(VI)-O via the reduction of dissolved oxygen at intermetallic sites to H_2O_2 followed by the oxidation of nearby Cr(III) species to Cr(VI) species. Therefore, while there is no Cr(VI) species in the coating baths or in the initially formed conversion coatings, there is evidence for transient formation of Cr(VI) and possible active corrosion protection.

6.2. SurTec Electrochemical Characterization Conclusions

The three SurTec coating variants were examined electrochemically when applied immersion and spray to AA7075-T6. Both methods produced coatings with reproducible physical, chemical and electrochemical properties, with no statistically-significant differences in the corrosion inhibition provided in both low and high chloride electrolytes. This was quantitatively assessed by suppression of anodic and cathodic polarization curve currents, increased polarization resistance, and decreased oxygen reduction reaction kinetics. In the high chloride electrolyte, the conversion coatings provided more cathodic inhibition. The immersion coated 650 E variant provided the best anti-corrosion properties as assessed by electrochemical methods. Alloy specimens coated with this version of the TCP conversion coating also experienced the least topography changes and corrosion damage (weight loss and pit density) during a 14-day thin-layer mist accelerated degradation test. This correlation between the electrochemical test data and accelerated degradation test performance indicates that the electrochemical methods could be useful for predicting TCP coating performance in service applications.

6.3. Cross Comparison Conclusions

Cross comparison testing of the different commercial TCP coatings was performed in AA7075-T6. These include SurTec 650E, Henkel Bonderite T5900, Chemeon TCP-HF and Luster-on chromitAL. A non-chromium conversion coating, NAVAIR's NCP, was also evaluated. The coatings were formed by immersion on degreased and deoxidized alloy and tested for 7 days in a neutral salt fog (ASTM B117) and a thin-layer mist test. The results showed that the conversion coatings with the highest levels of Cr in their coating baths exhibited the best anti-corrosion performance. Luster-On and Chemeon had the highest Cr concentrations, which produced the highest density in coating precipitates decorating the alloy surface. Both TCP coatings showed

the least damage during the standard salt-spray testing and during more aggressive thin-layer mist testing. The Henkel and SurTec coatings provided excellent protection against corrosion when compared to the uncoated control, but larger pits and possible film undercutting were seen when compared to the other TCP coated specimens. The NCP coating provided a statistically-significant decrease in all quantitative measures of corrosion (weight loss, pit size, pit depth, pit density) during the testing period, but showed a higher degree of damage when compared to the TCP formulations.

6.4. Cross Comparison SEM Conclusions

This trend of increased Cr concentration in coating baths linking with increased corrosion protection was verified on a smaller scale using scanning electron microscopy. Damage initiation followed similar trends across all coatings, with intergranular cracking and pitting near IMPs visible first, followed by larger damage leading to extensive pits which are eventually visible with the naked eye. This extensive damage was the visible damage seen in Chapter 4, and only occurred to a significant extent on the NCP and uncoated specimens.

6.5. Future Work

Future work should focus on an in-depth examination of the damage initiation sites to determine the corrosion mechanisms occurring at the aluminum alloy surface. This should be undertaken with a focus on the time frames in which the coatings begin to experience significant damage and film undercutting, which seem to be less than 7 days. Major study should include how the TCP coatings slow and prevent this corrosion initiation, and how this process can be improved upon. This could be achieved through a very thorough analysis of the TCP surfaces on a smaller scale than presented here, with precise locations being examined both before and after accelerated degradation testing. This would allow the identification of corrosion initiation sites,

which could lead to coating formulation changes that promote increased protection of these regions.

Additionally, interactions between the non-chromate conversion coating and non-chromate primer need to be investigated and understood. This could involve tailoring the drying time to the primer solvents and including some analysis of damage mechanisms to the conversion coating and alloy beneath the primer. In order to do this, conversion coated and primed specimens are scribed to simulate pre-existing damage and subjected to accelerated degradation tests. After the testing period, the specimen could be cut and a cross section examined for alloy loss around the scribe with particular attention to the damage initiation sites (probably IMPs).

A final examination of the coating performance should include the accelerated degradation test analysis when panels are galvanically-coupled to rivets similar to those used in the aerospace industry. The electrical contact between the dissimilar metals of the rivet and the aluminum alloy promotes corrosion and damage of the panel. The corrosion mechanisms during this galvanic corrosion should also be examined in depth to determine initiation sites.

Hopefully, with a better understanding of the corrosion mechanisms and initiation sites, the conversion coating industry can produce more effective coatings free of toxic Cr (VI) that prevent loss of time, money, and lives due to catastrophic damage to aerospace aluminum alloys.

REFERENCES

REFERENCES

1. Li, L.; Whitman, B. W.; Munson, C. A.; Estrada, R.; Matzdorf, C. A.; Swain, G. M., Structure and corrosion performance of a non-chromium process (NCP) Zr/Zn pretreatment conversion coating on aluminum alloys. *Journal of The Electrochemical Society* **2016,** *163* (13), C718-C728.

2. Suib, S. L.; La Scala, J.; Nickerson, W.; Fowler, A.; Zaki, N., Determination of hexavalent chromium in NAVAIR trivalent chromium process (TCP) coatings and process solutions. *Metal Finishing* **2009,** *107* (2), 28-34.

3. A. Iyer, W. W., S. Frueh, W. Nickerson, A. Fowler, J. Bames, L. Hagos, J. Escarsega, J. La Scala and S.L. Suib, Characterization of NAVAIR trivalent chromium process (TCP) coatings and solutions. *Plating and Surface Finishing* **2010,** *5* 32-42.

4. C. A. Matzdorf, W. C. N., Jr., E. N. Beck, A. S. Schwartz and J. L. Green, Non-chromium coatings for aluminum. *Us. Patent Application Publication* **2007**.

5. Ferrer, K. S.; Kelly, R. G., Comparison of methods for removal of corrosion product from AA2024-T3. *CORROSION* **2001,** *57* (2), 110-117.

6. Li, L.; Swain, G. M., Formation and structure of trivalent chromium process coatings on aluminum alloys 6061 and 7075. *Corrosion* **2013,** *69* (12), 1205-1216.

7. Munson, C. A.; Swain, G. M., Structure and chemical composition of different variants of a commercial trivalent chromium process (TCP) coating on aluminum alloy 7075-T6. *Surface and Coatings Technology* **2017,** *315*, 150-162.